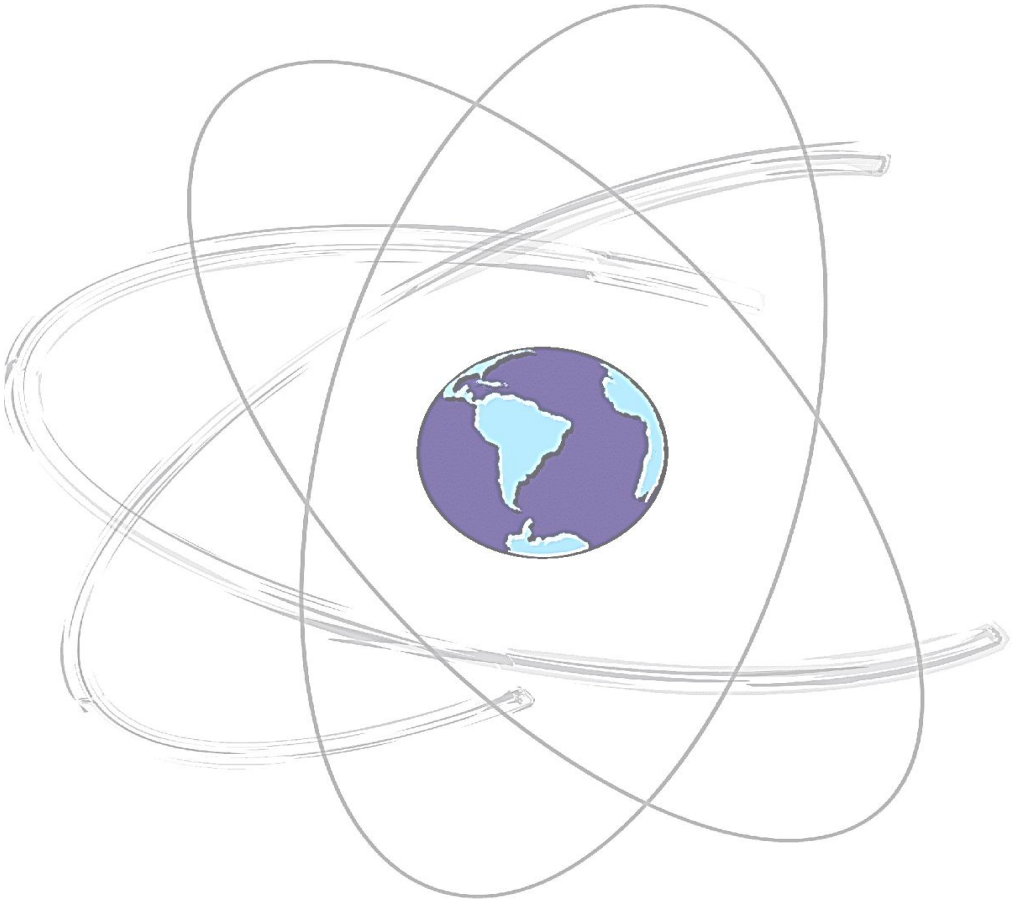
UNESP – UNIVERSIDADE ESTADUAL PAULISTA

FACULDADE DE CIÊNCIAS E TECNOLOGIA

PÓS-GRADUAÇÃO EM CIÊNCIAS CARTOGRÁFICA

WEVERTON DA COSTA SILVA

EXPLORING THE CONTRIBUTION OF GBAS DFDC IN ENHANCING PRECISION APPROACH



Presidente Prudente/SP

Julho/2025

WEVERTON DA COSTA SILVA

EXPLORING THE CONTRIBUTION OF GBAS DFDC IN ENHANCING PRECISION APPROACH

Doctoral thesis presented to the Graduate Program of Cartographic Sciences (PPGCC) at Sao Paulo State University (UNESP), School of Technology and Sciences, campus Presidente Prudente, SP, Brazil, for the fulfilment of the requirements for the grade of Doctor in Cartographic Sciences.

Supervisor: Dr. João Francisco Galera Monico

Co-Supervisor: Dr. Vinícius Amadeu Stuani Pereira

Presidente Prudente/SP

Julho/2025

S586e

Silva, Weverton da Costa
Exploring the contribution of GBAS DFDC in enhancing precision approach / Weverton da Costa Silva. -- Presidente Prudente, 2025
172 p.

Tese (doutorado) - Universidade Estadual Paulista (UNESP), Faculdade de Ciências e Tecnologia, Presidente Prudente
Orientador: João Francisco Galera Monico
Coorientador: Vinícius Amdeu Stuani Pereira

1. GBAS - Ground Based Augmentation System. 2. Aproximação de precisão. 3. Integridade. I. Título.

Sistema de geração automática de fichas catalográficas da Unesp. Dados fornecidos pelo autor(a).

POTENTIAL IMPACT OF THE RESEARCH

The development of a Dual-Frequency Dual-Constellation GBAS (GBAS DFDC) prototype, as presented in this research, holds transformative potential for aviation safety and precision approach operations in low-latitude regions such as Brazil. By addressing the challenges posed by ionospheric irregularities and a critical limitation of current single-frequency GBAS systems, this work paves the way for more reliable and resilient navigation solutions in low-latitude regions, where ionospheric scintillation frequently degrades GNSS signal quality.

The GBAS UNESP Experimental Test Bed, by utilizing GPS (L1/L5) and Galileo (E1/E5a) signals, represents a significant advancement in mitigating ionospheric errors through dual-frequency and dual-constellation processing. Performance analyses conducted under both high and low scintillation conditions enable the assessment of the feasibility of GBAS usage.

From a sustainability perspective, it is important to highlight that this research, by investigating GBAS performance and evaluating its feasibility, may contribute to more efficient, safer, and environmentally responsible aviation operations. By enabling high-precision approach procedures, the system reduces fuel consumption and, consequently, greenhouse gas emissions, contributing to climate change mitigation. Furthermore, GBAS allows for more optimized and flexible trajectories, reducing noise levels in urban areas surrounding airports.

IMPACTO POTENCIAL DA PESQUISA

O desenvolvimento de um protótipo GBAS DFDC, conforme apresentado nesta pesquisa, possui potencial transformador para a segurança da aviação e para operações de aproximação de precisão em regiões de baixa latitude, como o Brasil. Ao abordar os desafios impostos pelas irregularidades ionosféricas e uma limitação crítica dos sistemas GBAS atuais de frequência única, o trabalho abre caminho para soluções de navegação mais confiáveis e resilientes em regiões de baixas latitudes, onde a cintilação ionosférica frequentemente degrada a qualidade dos sinais GNSS.

O GBAS UNESP Experimental Test Bed, ao utilizar sinais GPS (L1/L5) e Galileo (E1/E5a), representa um avanço significativo na mitigação de erros ionosféricos por meio do processamento em dupla frequência e dupla constelação. As análises de desempenho conduzidas sob condições de alta e baixa cintilação permitem avaliar a viabilidade do uso de GBAS.

Do ponto de vista de sustentabilidade deve-se destacar que a pesquisa ao investigar o desempenho GBAS e analisar sua viabilidade, futuramente pode auxiliar em operações aeronáuticas mais eficientes, seguras e ambientalmente responsáveis. Ao possibilitar procedimentos de aproximação de alta precisão, o sistema reduz o consumo de combustível e, consequentemente, as emissões de gases de efeito estufa, contribuindo para a mitigação das mudanças climáticas. Além disso, o GBAS permite trajetórias mais otimizadas e flexíveis, diminuindo o ruído nas áreas urbanas próximas aos aeroportos.

UNIVERSIDADE ESTADUAL PAULISTA

Câmpus de Presidente Prudente

CERTIFICADO DE APROVAÇÃO

TÍTULO DA TESE: **EXPLORING THE CONTRIBUTION OF GBAS DFDC IN ENHANCING PRECISION APPROACH**

AUTOR: WEVERTON DA COSTA SILVA
ORIENTADOR: JOÃO FRANCISCO GALERA MONICO
COORIENTADOR: COORIENTADOR: VINICIUS AMADEU STUANI PEREIRA

Aprovado como parte das exigências para obtenção do Título de Doutor em Ciências Cartográficas, área: Aquisição, Análise e Representação de Informações Espaciais pela Comissão Examinadora:

gov.br Documento assinado digitalmente
JOAO FRANCISCO GALERA MONICO
Data: 01/04/2026 11:52:00-0300
Verifique em https://validar.iti.gov.br

Prof. Dr. JOÃO FRANCISCO GALERA MONICO (Participaçao Presencial)
Departamento de Cartografia / Faculdade de Ciencias e Tecnologia de Presidente Prudente - FCT/Unesp

Prof. Dr. LEONARDO MARINI PEREIRA (Participaçao Virtual)
Departamento de Controle do Espaço Aéreo – DECEA / Instituto de Controle do Espaço Aéreo – ICEA

Prof. Dr. TEDDY MODESTO SURCO ESPEJO (Participaçao Virtual)
Institute for Scientific Research / Boston College

Prof. Dr. ROBERTO SABATINI (Participaçao Virtual)
Khalifa University

Prof. Dr. PAULO SÉRGIO DE OLIVEIRA JÚNIOR (Participaçao Virtual)
Departamento de Geomática / Universidade Federal do Paraná

Presidente Prudente, 11 de julho de 2025.

Era mais um fim de tarde em que um jovem estudante seguia seu caminho para a escola. Ao passar em frente à casa de Dona Lerinda, uma simpática vizinha idosa, ela sempre me recebia com um afetuoso abraço, um sorriso e a seguinte frase: “Olha aí o nosso doutorzinho. Você vai ser nosso doutor”. Provavelmente, pensava que eu me tornaria médico ou advogado.

O tempo passou, não segui nenhuma dessas duas possibilidades, mas, 20 anos depois, a profecia de Dona Lerinda foi cumprida, e o título de doutor foi alcançado. Embora nunca tenha sido uma obsessão em minha vida, à medida que essa conquista se aproximava, era inevitável recordar essa profecia de Dona Lerinda (in memoriam).

Este trabalho também é dedicado a pessoas marcantes em minha vida, como os tios Ademar Sarmento e José Geraldo (Tio Baiano), e minha avó Geni Costa.

AGRADECIMENTOS

Gratidão a Deus pelo dom da vida em plenitude e cuidar daqueles que amamos para que possamos ter tranquilidade e concentração em nossos propósitos.

O presente trabalho foi realizado com apoio da Coordenação de Aperfeiçoamento de Pessoal de Nível Superior Brasil (CAPES) - Código de Financiamento 001.

Agradecimentos ao Instituto Nacional de Ciência e Tecnologia – Tecnologia GNSS no Suporte à Navegação Aérea (INCT GNSS-NavAer), financiado pelo CNPq (Conselho Nacional de Desenvolvimento Científico e Tecnológico – processo 465648/2014-2), FAPESP (Fundação de Amparo à Pesquisa do Estado de São Paulo – processo 2017/50115-0) e CAPES (Coordenação de Aperfeiçoamento de Pessoal de Nível Superior – processo nº 88887.137186/2017-00).

Gratidão ao meu orientador Prof. Dr. João Francisco Galera Monico, fonte de inspiração por sua trajetória nas ciências geodésicas, e por abrir as portas no PPGCC se colocando à disposição para me orientar desde o mestrado até o doutorado. Foram cerca de 6 anos em que pude beber de um referencial científico inestimável na ciência brasileira e internacional.

Agradeço ao Programa de Pós-Graduação em Ciências Cartográficas (PPGCC) da FCT - UNESP pela infraestrutura fundamental para o desenvolvimento deste trabalho, além do conhecimento compartilhado por professores e demais colegas pós-graduandos.

Agradeço ao amigo do Laboratório de Geodésia Espacial (LGE), Ítalo pela amizade, ajudas, discussões e dicas que contribuíram na realização desta pesquisa e de outras atividades realizadas durante o Doutorado.

Grande parte trabalho desenvolvido nesta tese foi realizado em parceria com os amigos Felipe Tintino e Crislaine Meneses. Com eles formamos um grupo de estudos de GBAS no qual produzimos o protótipo de processamento de dados GNSS para GBAS ajudando mutuamente em nossas atividades.

Agradeço a minha namorada Camila, pelo companheirismo, incentivo, compreensão das minhas ausências e me oferecer carinho e refúgio quando o necessário era descansar das atividades.

A meus pais, Lindomar Sarmento e Maria do Carmo, meu irmão Tiago, e familiares por toda a educação, amor e incentivo irrestrito que sempre tiveram comigo nessa longa caminhada, iniciada na nossa querida Cachoeira Escura – MG.

ABSTRACT

The Ground-Based Augmentation System (GBAS) is a type of Global Navigation Satellite System (GNSS) augmentation designed to enhance navigation and positioning accuracy and integrity during precision approach and landing operations. Architecture comprises a network of reference stations that generate differential corrections, which are transmitted to the aircraft to improve the aircraft's position. Currently, aviation regulations permit the use of GNSS signals only for the L1 carrier-phase of the GPS or GLONASS. GBAS employs differential GNSS positioning, wherein a significant portion of the systematic errors from satellite signals is mitigated by assuming spatial and temporal correlation between the data of the reference stations and the aircraft. However, in low latitude regions such as Brazil, the higher incidence of ionospheric irregularities leads to significant discrepancies in errors between ground and airborne receivers, as well as degrading signal quality. These conditions can increase positioning errors and degrade performance parameters, making precision approach operations using GBAS unfeasible. The modernization of GNSS, introducing new signals and satellite constellations, is seen as a promising strategy to mitigate or reduce ionospheric effects. Thus, this thesis presents the development of a GBAS Dual-Frequency Dual-Constellation (GBAS DFDC) system for processing, monitoring and evaluating GBAS performance in support of precision approach categories. The aim is to assess whether the performance achieved satisfies the requirements established for specific aviation operations. The implemented system, named GBAS UNESP Experimental Test Bed, is composed of six reference stations from the INCT GNSS-NavAer Network, located in the region of Presidente Prudente, Sao Paulo, Brazil. Four of these stations are configured as ground systems responsible for generating differential corrections and integrity parameters, while the remaining two stations simulate aircraft in static mode, thereby enabling GBAS performance analysis and ionospheric condition monitoring. The system utilizes GNSS data from GPS (L1/L5) and Galileo (E1/E5a), as well as linear combinations of these signals, including pseudorange smoothing, ionosphere-free (IFree), and divergence-free (Divergence Free) combinations. Two MATLAB implementations of GBAS CAT I were developed to support both Single Frequency (SF L1) and IFree modes, incorporating the following functionalities: GNSS data input, pseudorange smoothed via carrier-phase measurements, cycle slip detection, differential correction generation, B-values computation, ionospheric monitoring, aircraft, positioning error, and protection level calculation. GBAS performance was evaluated under both high and low ionospheric scintillation conditions for Single Frequency (SF) L1 and IFree modes. The results demonstrated that, in both ionospheric scenarios and for both simulated aircraft, the SF L1 mode support the CAT I performance requirements over 99% of the analyzed period. In contrast, the IFree mode exhibited reduced availability, achieving CAT I operational conditions for approximately only 90% of the time. The time series analysis of the vertical protection level (VPL) revealed integrity loss events, where VPL values exceeded the 10-meter alert limit. These occurrences were primarily associated with variations in the number of satellites used, which directly influence the VPL magnitude. The exclusion of satellites, resulting from GNSS signal quality monitoring, had a more detrimental impact on the IFree mode than on the SF L1 mode, further underscoring the trade-offs between signal diversity and system robustness in GBAS applications.

Key words: precision approach, differential corrections, protections levels, ionospheric gradient, performance requirements.

RESUMO

O Sistema de Aumento Baseado em Terra (GBAS) é um tipo de sistema de aumento do GNSS projetado para aprimorar a acurácia e a integridade do posicionamento e da navegação durante operações de aproximação e pouso de precisão. Sua arquitetura é composta por uma rede de estações de referência que geram correções diferenciais, as quais são transmitidas à aeronave com o objetivo de melhorar sua estimativa de posição. Atualmente, as regulamentações da aviação permitem o uso de sinais GNSS apenas na portadora L1 do GPS ou do GLONASS. O GBAS usa o posicionamento diferencial GNSS, no qual parte significativa dos erros sistemáticos dos sinais dos satélites é mitigada ao se assumir correlação espaço-temporal dos erros das estações de referência e da aeronave. Entretanto, em regiões de baixa latitude, como o Brasil, a maior incidência de irregularidades ionosféricas resulta em discrepâncias significativas entre os erros observados nos receptores em solo e os da aeronaves, além de degradar a qualidade dos sinais. Essas condições podem aumentar os erros de posicionamento e comprometer os parâmetros de desempenho, tornando inviáveis operações de aproximação de precisão utilizando o GBAS. A modernização dos sistemas GNSS, com a introdução de novos sinais e constelações de satélites, tem sido considerada uma estratégia promissora para mitigar ou reduzir os efeitos ionosféricos. Nesse contexto, esta tese apresenta o desenvolvimento de um sistema GBAS de Dupla Frequência e Dupla Constelação (GBAS DFDC) para o processamento, monitoramento e avaliação do desempenho do GBAS em suporte às categorias de aproximação de precisão. O objetivo é avaliar se o desempenho obtido atende aos requisitos estabelecidos para operações aeronáuticas específicas. O sistema implementado, denominado GBAS UNESP Experimental Test Bed, é composto por seis estações de referência da rede INCT GNSS-NavAer, localizadas na região de Presidente Prudente, São Paulo, Brasil. Quatro dessas estações são configuradas como sistemas em solo responsáveis pela geração de correções diferenciais e parâmetros de integridade, enquanto as duas restantes simulam aeronaves em modo estático, permitindo a análise do desempenho do GBAS e o monitoramento das condições ionosféricas. O sistema utiliza dados GNSS provenientes do GPS (L1/L5) e do Galileo (E1/E5a), bem como combinações lineares desses sinais, incluindo suavização de pseudodistância, combinações livres da ionosfera (IFree) e livres de divergência (Divergence Free). Foram desenvolvidas duas implementações em MATLAB do GBAS CAT I, capazes de operar tanto no modo de frequência única (SF L1) quanto no modo IFree, incorporando as seguintes funcionalidades: entrada de dados GNSS, suavização da pseudodistância via medições de fase da portadora, detecção de *cycle slips*, geração de correções diferenciais, cálculo dos B-values, monitoramento ionosférico, posicionamento da aeronave, cálculo do erro de posicionamento e dos níveis de proteção. O desempenho do GBAS foi avaliado sob condições de alta e baixa cintilação ionosférica para os modos SF L1 e IFree. Os resultados demonstraram que, em ambos os cenários ionosféricos e para ambas as aeronaves simuladas, o modo SF L1 atende aos requisitos de desempenho para CAT I em mais de 99% do período analisado. Em contraste, o modo IFree apresentou menor disponibilidade, atingindo condições operacionais de CAT I em aproximadamente 90% do tempo. A análise das séries temporais do nível de proteção vertical (VPL) evidenciou eventos de perda de integridade, nos quais os valores de VPL excederam o limite de alerta de 10 metros. Essas ocorrências estiveram principalmente associadas a variações no número de satélites utilizados, que influenciam diretamente a magnitude do VPL. A exclusão de satélites, decorrente do monitoramento da qualidade dos sinais GNSS, impactou de forma mais significativa o modo IFree do que o modo SF L1, evidenciando

os compromissos existentes entre diversidade de sinais e robustez do sistema em aplicações GBAS.

Palavras-chave: aproximação de precisão, correções diferenciais, níveis de proteção, gradiente ionosférico, requisitos de desempenho.

LIST OF TABLES

Table 1 – Precision approaches categories for ILS. 31
Table 2 – Requeriments for GBAS aproach services. 32
Table 3 – Ground Accuracy Designator or GAD Model for GPS satellites..... 40
Table 4 – AAD Model for GPS satellites. 40
Table 5 – Characterization of the services, messages and signals used in GBAS. 49
Table 6 – Message content planned for MT50. 50
Table 7 – Distribution of GBAS message transmission compartments by VDB antennas. 50
Table 8 – Uncertainty Models dual-frequency dual constellation ($\sigma prgnd$) associated with pseudorange from ground system GBAS for GPS and Galileo. 53
Table 9 – Uncertainty Models dual-frequency dual constellation ($\sigma prair$) associated with pseudorange from aircraft system GBAS for GPS and Galileo. 54
Table 10 – Classification of the amplitude scintillation event according to S4 index. .. 65
Table 11 – Ionospheric scintillation classification according to Sigma phi ($\sigma\varphi$). 65
Table 12 – Coordinate of the stations that compose the GBAS UNESP Experimental. 72
Table 13 – Range of values calculated by Ground System to be transmitted to aircraft.74
Table 14 – Average of the estimated multipath over the 11 days. 97
Table 15– Average of standard deviation of the multipath estimated for each station on the days analyzed. 98
Table 16– Average of the 95% percentile of the multipath estimated for each station on the days analyzed. 99
Table 17– Statistical indicators of the B-Values for the reference stations during periods of high ionospheric scintillation. 103
Table 18 – Statistical indicators of the Iono Test estimate for the STAV and STPZ stations in the period 033 to 035/2024. 107
Table 19 – Statistical indicators of the B-Values for the reference stations during periods of low ionospheric scintillation..... 117
Table 20 – Statistical indicators of the Iono Test estimate for the STAV and STPZ stations in the period 083 to 084/2024. 120
Table 21 – Statistical indicators of the B-Values IFree for the reference stations during periods from 033 to 035/2024. 129
Table 22 - Summary of the perfomance of experiments conducted using the GBAS UNESP Experimental prototype..... 137
Table 23 – HPE and VPE performance during flight in the low scintillation scenario.145
Table 24 – HPE and VPE performance during flight in the high scintillation scenario. 151

LIST OF FIGURES

Figure 1 – Illustration of the application of GNSS augmentation systems across flight phases. 30
Figure 2 – Conventional GBAS architecture. 33
Figure 3 – Pseudorange corrections calculated for 4 reference stations from GBAS Unesp Experimental using single frequency (L1/E1) GPS and Galileo on DOY 205/2024. 35
Figure 4 – Example of B-Values from a MOR3 station located in Presidente Prudente (São Paulo) on 033/2024. 36
Figure 5 – Integrity parameters in aircraft position domain. 42
Figure 6 – Integrity Diagram with the possible events for GBAS. 44
Figure 7 – Ionospheric delay monitoring for GAST F. 52
Figure 8 – Proposed architecture for GAST X approach service. 60
Figure 9 – Proposed architecture for GAST E approach service. 62
Figure 10 – Representation of the occurrence of Equatorial Plasma Bubbles. 64
Figure 11 – Representation of an ionospheric front that can generate ionospheric delay decorrelation. 67
Figure 12 – Representation of the Station Pair Method for determining the ionospheric gradient. 68
Figure 13 – Representation of the Time-Step Method for determining the ionospheric gradient. 69
Figure 14 – Estimated ionospheric gradients for Brazil in the ionospheric threat model study. 70
Figure 15 – GNSS stations comprising the GBAS UNESP Experimental project. 71
Figure 16 – Main activities proposed for the GBAS Monitoring Station. 72
Figure 17 – Multipath (L1/E1) values estimated for the PRU2 station by CMC DFree method. 77
Figure 18 – Multipath (L5/E5a) values estimated for the PRU2 station using the CMC DFree method. 78
Figure 19 – Multipath (L1/E1) values estimated for azimuth using the CMC DFree method at the PRU2 station. 79
Figure 20 – Multipath (L1/E1) values estimated for elevation using the CMC DFree method at the PRU2 station. 79
Figure 21 – Multipath (L1/E1) values estimated for PRU4 station by CMC DFree. 81
Figure 22 – Multipath (L1/E1) values estimated for PRU4 station by CMC DFree. 82
Figure 23 – Multipath (L1/E1) values estimated for azimuth using CMC DFree from PRU4 station. 83
Figure 24 – Multipath (L1/E1) values estimated for elevation using CMC DFree from PRU4 station. 83
Figure 25 – Multipath (L1/E1) values estimated for DMC1 station by CMC DFree. 84
Figure 26 – Multipath (L5/E5a) values estimated for DMC1 station by CMC DFree. 85

Figure 27 – Multipath (L1/E1) values estimated for azimuth using CMC DFree from DMC1 station. 86
Figure 28 – Multipath (L1/E1) values estimated for elevation using CMC DFree from DMC1 station. 86
Figure 29 – Multipath (L1/E1) values estimated for MOR3 station by CMC DFree. ... 87
Figure 30 – Multipath (L5/E5a) values estimated for MOR3 station by CMC DFree... 88
Figure 31 – Multipath (L1/E1) values estimated for azimuth using CMC DFree from MOR3 station. 89
Figure 32 – Multipath (L1/E1) values estimated for elevation using CMC DFree from MOR3 station. 89
Figure 33 – Multipath (L1/E1) values estimated for STPZ station by CMC DFree. 90
Figure 34 – Multipath (L5/Ea) values estimated for STPZ station by CMC DFree. 91
Figure 35 – Multipath (L1/E1) values estimated for azimuth using CMC DFree from STPZ station. 92
Figure 36 – Multipath (L1/E1) values estimated for elevation using CMC DFree from STPZ station. 93
Figure 37 – Multipath (L1/E1) values estimated for STAV station by CMC DFree. 94
Figure 38 – Multipath (L5/Ea) values estimated for STAV station by CMC DFree. 95
Figure 39 – Multipath (L1/E1) values estimated for azimuth using CMC DFree from STAV station. 96
Figure 40 – Multipath (L1/E1) values estimated for elevation using CMC DFree from STAV station. 97
Figure 41 – S4 index in the high ionospheric scintillation scenario..... 100
Figure 42 – S4 index in the low ionospheric scintillation scenario..... 101
Figure 43 – Pseudorange Corrections for L1/E1 for the period from 033 to 035/2025. 102
Figure 44 – Ground integrity parameter B-Values calculated by the ground system for the period from 033 to 035/2025. 103
Figure 45 – Ionospheric Gradient Monitoring for Ground System and Aircraft System for the period 033 to 035/2024. 104
Figure 46 – Spatial distribution of ionospheric gradients at STAV and STPZ stations for DOYs 033, 034 and 035/2024. 105
Figure 47 – Iono Test estimates for STAV and STPZ aircraft in DOYs 033 to 035/2024. 106
Figure 48 – GBAS performance CAT I SFL1 for the horizontal position at the STAV station during the period of high ionospheric scintillation. 107
Figure 49 – GBAS performance CAT I SFL1 for the vertical position at the STAV station during the period of high ionospheric scintillation. 108
Figure 50 – Integrity diagram for the horizontal and vertical components of GBAS CAT I SFL1 for the STAV station during the period of high ionospheric scintillation..... 109
Figure 51 – Histograms of positioning errors and protection levels for GBAS CAT I SFL1 at the STAV station during a period of high ionospheric scintillation. 110
Figure 52 – GBAS performance CAT I SFL1 for the horizontal position at the STPZ station during the period of high ionospheric scintillation. 111

Figure 53 – GBAS performance CAT I SFL1 for the vertical component at the STPZ station during the period of high ionospheric scintillation. 111
Figure 54 – Integrity diagram for the horizontal and vertical component of GBAS CAT I SFL1 for the STPZ station during the period of high ionospheric scintillation. 112
Figure 55 – Histograms of positioning errors and protection levels for GBAS CAT I SFL1 at the STPZ station during a period of high ionospheric scintillation. 113
Figure 56 – Number of satellites used in GBAS STAV (CAT I SF L1) in DOY 033 to 035/2024. 114
Figure 57 – Status of GNSS signals on the L1/E1 carrier-phase at the STAV station from days 033 to 035 of 2024. 115
Figure 58– Status of GNSS signals on the L1/E1 carrier-phase at the STPZ station from days 033 to 035 of 2024. 115
Figure 59 – Pseudorange Corrections for L1/E1 for the low ionospheric scintillation scenario. 116
Figure 60 – Ground integrity parameter B-Values calculated by the ground system for the period from 083 to 084/2025. 117
Figure 61 – Ionospheric Gradient Monitoring for Ground System and Aircraft System for the period 083 to 084/2024. 118
Figure 62 – Spatial distribution of ionospheric gradients at STAV and STPZ stations for DOYs 083 and 084/2024. 119
Figure 63 – Iono Test estimates for STAV and STPZ aircraft in DOYs 083 to 084/2024. 119
Figure 64 – GBAS performance CAT I SFL1 for the horizontal position at the STAV station during the period of low ionospheric scintillation. 121
Figure 65 – GBAS performance CAT I SFL1 for the vertical component at the STAV station during the period of low ionospheric scintillation. 121
Figure 66 – Integrity diagram for the horizontal and vertical component of GBAS CAT I SFL1 for the STAV station during the period of low ionospheric scintillation. 122
Figure 67 – Histograms of position errors and protection levels for GBAS CAT I SFL1 at the STAV station during a period of low ionospheric scintillation. 123
Figure 68 – GBAS performance CAT I SFL1 for the vertical component at the STPZ station during the period of low ionospheric scintillation. 123
Figure 69 – GBAS performance CAT I SFL1 for the vertical component at the STPZ station during the period of low ionospheric scintillation. 124
Figure 70 – Integrity diagram for the horizontal and vertical component of GBAS CAT I SFL1 for the STPZ station during the period of low ionospheric scintillation. 125
Figure 71 – Histograms of position errors and protection levels for GBAS CAT I SFL1 at the STPZ station during a period of low ionospheric scintillation. 126
Figure 72 – Number of satellites used in GBAS STAV (CAT I SF L1) in DOY 083 to 084/2024. 126
Figure 73 – Status of GNSS signals on the L1/E1 carrier at the STAV station from days 083 to 084 of 2024. 127
Figure 74– Status of GNSS signals on the L1/E1 carrier-phase at the STPZ station from days 083 to 084 of 2024. 127

Figure 75 – Pseudorange Corrections IFree estimated for the period from 033 to 035/2025. 128
Figure 76 – Ground integrity parameter B-Values calculated by the ground system for IFree modo to the period from 033 to 035/2025. 129
Figure 77 – GBAS performance CAT I IFree for the vertical component at the STAV station during the period of high ionospheric scintillation. 130
Figure 78 – GBAS performance CAT I IFree for the vertical component at the STAV station during the period of high ionospheric scintillation. 130
Figure 79 – Integrity diagram for the horizontal and vertical component of GBAS CAT I IFree for the STAV station during the period of high ionospheric scintillation. 131
Figure 80 – Histograms of position errors and protection levels for GBAS CAT I IFree at the STAV station during a period of high ionospheric scintillation. 132
Figure 81 – GBAS performance CAT I IFree for the horizontal position at the STPZ station during the period of high ionospheric scintillation. 133
Figure 82 – GBAS performance CAT I IFree for the vertical component at the STPZ station during the period of high ionospheric scintillation. 133
Figure 83 – Integrity diagram for the horizontal and vertical component of GBAS CAT I IFree for the STPZ station during the period of high ionospheric scintillation. 134
Figure 84 – Histograms of position errors and protection levels for GBAS CAT I IFree at the STPZ station during a period of l ow ionospheric scintillation. 135
Figure 85 – Number of satellites used in GBAS STAV (CAT I IFree) in DOY 033 to 035/2024. 136
Figure 86 – S4 index for ionospheric scintillation scenario on DOYs 145/2023 and 321/2023. 139
Figure 87 a) General view of the trajectory of the flight carried out in Presidente Prudente - SP. b) UAV Phantom 4 Pro model used in the GBAS kinematic experiment. 140
Figure 88 – Standard Deviation of Relative Kinematic Positioning during flight in low ionospheric scintillation. 142
Figure 89 – Discrepancies of the geocentric Cartesian coordinates estimated for flight by the GBAS and Kinematic Relative positioning during low scintillation. 142
Figure 90 – Position errors in the Local Geodetic System applied to flight in the low ionospheric scintillation scenario. 143
Figure 91 – GBAS performance for the horizontal component on DOY 145/2023..... 144
Figure 92 – GBAS performance for the vertical component on DOY 145/2023..... 144
Figure 93 – Integrity diagram on the 145/2023 flight. 146
Figure 94 – Number of satellites used in GBAS and Kinematic Relative positioning for the 145/2023 flight. 146
Figure 95 – Performance of VPL and NSU in GBAS positioning for day 145/2023. . 147
Figure 96 – Standard Deviation of Relative Kinematic Positioning during flight in high ionospheric scintillation. 148
Figure 97 – Discrepancies of the geocentric Cartesian coordinates estimated applied to flight by the GBAS and Kinematic Relative positioning during high scintillation. 149

Figure 98 – Position errors in the LGS for flight in the high ionospheric scintillation scenario. 149
Figure 99 – GBAS performance for the horizontal component on DOY 321/2023..... 150
Figure 100 – GBAS performance for the vertical component on DOY 321/2023..... 150
Figure 101 – Integrity diagram on the 321/2023 flight. 151
Figure 102 – Number of satellites used in GBAS and Kinematic Relative positioning for the 321/2023 flight. 152
Figure 103 – Performance of VPL and NSU in GBAS positioning for day 145/2023. 152

LIST OF ABBREVIATIONS AND ACRONYMS

AAD	Aircraft Accuracy Designator
ABAS	Aircraft-Based Augmentation System
APV	Approach with Vertical Guidance
CAT	Category Approach Type
CCD	Code-Carrier Divergence
CMC	Code Minus Carrier
DFDC	Dual Frequency Dual Constellation
DFMC	Dual Frequency e Multi Constellation
DFree	Divergence Free
DGNSS	Differential GNSS
DGPS	Differential GPS
DH	Decision Height
DIA	Detection, Identification, and Adaptation
DOY	Day Of Year
DSIGMA	Dual Smoothing Ionospheric Gradient Monitor Algorithm
E_{IG}	Error Ionosphere Gradient
EPB	Equatorial Plasma Bubble
EUROCAE	EURopean Organization for Civil Aviation Equipament
EUROCONTROL	European Organization for the Safety of Air Navigation
eVTOL	electric Vertical TakeOff and Landing
FAS	Final Approach Segment
GAD	Ground Accuracy Designator
GAST	GBAS Approach Service Type
GBAS	Ground-Based Augmentation System
GFS	Ground Facility Station
GLONASS	*Global'naya Navigatsionnaya Sputnikovaya Sistema*
GNSS	Global Navigation Satellite System
GPA	Glide Slope Angle
GPS	Global Positioning System
HAL	Horizontal Alert Limit
HMI	Hazardously Misleading Information

HPE	Horizontal Position Error
HPL	Horizontal Protection Level
ICAO	International Civil Aviation Organization
IFree	Ion Free
IGM	Ionospheric Gradient Monitor
ILS	Instrument Landing System
INCT	*Instituto Nacional de Ciência e Tecnologia* (National Institute of Science and Technology)
IPP	Ionospheric Pierce Point
Kffmd	Fault-Free Missed Detection
LGS	Local Geodetic System
LTP/FTP	Landing Threshold Point/ Fictitious Threshold Point
MDB	Minnimum Detectable Bias
M_{EIG}	Maximum Error Ionosphere Gradient
MFMC	Multi Frequency and Multi Constellation
MI	Misleading Information
MIEV	Maximum Ionosphere induced Error Vertical
MMQ	Método dos Mínimos Quadrados
MOPS	Minimum Operation Performance Specifications
MP	MultiPath index
MT	Message Type
NM	Nautical Miles
NSP	Navigation Systems Panel
NSU	Number of Satellites Used
PDOP	Positioning Dilution of Precision
PRC	Pseudorange Correction
RINEX	Receiver INdependent EXchange Format
RRC	Range Rate Correction
RTCA	Radio Technical Commission for Aeronautics
RTK	Real Time Kinematic
SARP	International Standards and Recommended Practices
SBAS	Satellite-Based Augmentation System
SESAR	Single European Skies Air Traffic Management Research
SF	Single Frequency

STEC	Slant Total Electron Content
SU	System Unavailable
TC	Tropospheric Correction
TEC	Total Electron Content
UAV	Unmanned Aerial Vehicle
UTC	Universal Time Coordinated
VAL	Vertical Alert Limit
VDB	VHF Data Broadcast
VHF	Very High Frequency
VIG	Vertical Ionospheric Gradient
VPE	Vertical Position Error
VPL	Vertical Protection Level
VTEC	Vertical Total Electron Content

SUMÁRIO

1. INTRODUCTION 24
1.1. Hypothesis and Objectives 26
1.2. Contents and Contributions 26
1.3. Potential Impact of the Research 28
2. GBAS APPROACH SERVICE TYPE 30
2.1. GAST C: Fundamentals 33
2.1.2 Integrity Parameters in the Aircraft Position Domain 42
2.2. GAST D 45
2.2.1. Monitor DSIGMA 46
2.2.2. Ionospheric Gradient Monitor 46
2.2.3. Monitor CCD 47
2.3. GAST F 48
2.3.1. GAST F Modes 51
2.3.2. Dual Frequency Ionospheric Delay Monitoring for GAST F 54
2.3.3 GNSS Multipath Estimate for GBAS Dual Frequency 56
2.3.4 Cycle Slip Monitor for Dual Frequency 57
2.4 State of the Art: from GAST X to GAST E 59
3. IONOSPHERIC EFFECTS ON GBAS 62
3.1 Ionospheric Gradient 66
4. GBAS UNESP EXPERIMENTAL 71
4.1 Main Task of Ground System 73
4.2 Aircraft System 74
5. MULTIPATH AND NOISE FROM GBAS STATIONS 76
5.1. PRU2 Station 76
5.2. PRU4 Station 80
5.3. DMC1 Station 83
5.4. MOR3 Station 86
5.5. STPZ Station 89
6. GBAS EXPERIMENTS AND RESULTS 100
6.1. GBAS CAT I SF L1: High Ionospheric Scintillation Scenario 101
6.2. GBAS CAT I SF L1: Low Ionospheric Scintillation Scenario 115
6.3. GBAS CAT I IFree: High Ionospheric Scintillation Scenario 128

6.4. GBAS CAT I SF L1: Kinematic Mode for UAV test 138
6.4.1. Kinematic GBAS processing 140
6.4.2. GBAS Kinematic: low Scintillation Scenario 141
6.4.3. GBAS Kinematic: high scintillation scenario 147
7. CONCLUSIONS 153
7.1 Recommendations for Future Research 156
8. REFERENCES 158
APPENDIX 164
APPENDIX A – Partial view of the surroundings of the PRU2 station (reference date 04/23/2024). 164
APPENDIX B – Partial view of the surroundings of the PRU4 station (reference date 01/17/2024). 165
APPENDIX C – Partial view of the surroundings of the DMC1 station (reference date 01/20/2024). 166
APPENDIX D – Partial view of the surroundings of the MOR3 station (reference date 11/03/2024). 167
APPENDIX E – Partial view of the surroundings of the STAV station (reference date 04/13/2024). 168
APPENDIX F – Partial view of the surroundings of the STPZ station (reference date 04/23/2024). 169
APÊNDICE G – Status of GNSS Signals on the L1/E1 Carrier-phase at the STAV station from Days 033 to 035 of 2024. 169
APÊNDICE H – Status of GNSS signals on the L5/E5a carrier-phase at the STAV station from days 033 to 035 of 2024. 170
APÊNDICE I – Status of GNSS Signals on the L1/E1 Carrier at the STPZ Station from Days 033 to 035 of 2024. 170
APÊNDICE J – Status of GNSS Signals on the L5/E5a Carrier-phase at the STPZ Station from Days 033 to 035 of 2024. 171
DADOS CURRICULARES 172

1. INTRODUCTION

GBAS (Ground-Based Augmentation System) is an augmentation system developed to ensure accuracy, integrity, continuity and availability of the use of GNSS (Global Navigation Satellite System) positioning to support aircraft precision approaches and landings.

GBAS is composed of a set of GNSS reference stations, usually 4, provides corrections to be applied to the aircraft positioning, aiming to improve its accuracy (PULLEN, 2017). A GBAS can provide different categories of approach services simultaneously to several users, with varying operational objectives. All these services are referred to GBAS Approach Service Type (GAST) and are defined according to the precision approach category and GNSS signal combinations (ROTONDO et al., 2015).

Currently, GAST categories A, B and C are approved with standards and procedures published by the International Civil Aviation Organization (ICAO). The first two categories provide the level of accuracy for the APV I and APV II (Approach with Vertical Guidance) service, and the third GAST C is the one that provides performance for the CAT I (Category Precision Approach) precision approach phase with a decision height of 60 m (approximately) or 200 feet. Some airports in the world already have GAST C certification, such as Bremen and Frankfurt in Germany, Newark and Houston in the United States, Malaga in Spain, Sydney in Australia and, Zurich in Switzerland.

Another service called GAST D, according to Song et al. (2020), has been standardized at the international level to support CAT II and III precision approaches with a decision height of up to 15 m (50 ft). These standards and procedures were added in 2018 in Annex 10 of the ICAO Conventions (SAITO et al., 2018). With the addition of new GNSS signals and constellations, standards are expected to be included in the future for services to support CAT II and III precision approaches using new satellite signals and constellations. These services have been investigated by ICAO working groups, and several architectures have been proposed, such as GAST F, GAST X, and GAST E.

GBAS is based on the DGPS (Differential GPS) positioning method, which assumes that the systematic errors of the ephemeris, ionosphere and troposphere are correlated; that is, it is assumed that these errors occur simultaneously at the reference stations and on the aircraft receiver. However, Yoon et al. (2019) state that in equatorial and low latitude regions, due to the greater variability of the ionosphere, this correlation

can be degraded and insert significant errors in the position. Furthermore, it has also been observed that the quality of the measurements is degraded, with the occurrence of cycle slip, for example, as it will be presented in this work. Thus, mitigating the effects of the ionosphere on GNSS signals is one of the main challenges to ensuring accuracy, integrity, continuity, and availability in GBAS, as well as in other real-time applications that require integrity.

Various errors and failures that occur in GNSS signals can be associated with the ionosphere, such as cycle slip, divergence of code and carrier-phase measurements (CCD – Code Carrier Divergence) and variation in the ionospheric gradient. In this scenario, with the advent of new GNSS constellations and frequencies, it is possible to use linear combinations that can minimize the effects caused by the ionosphere.

At this moment, the rules and procedures governing the use of GBAS have standardized the use of GNSS observations only for L1 frequency of the GPS (Global Positioning System) constellation. In the research level, several papers in the literature have recently evaluated the potential of using more frequencies and the addition of satellites from the GLONASS, Galileo and Beidou constellations.

Jiang et al. (2017) present a proposal for a CCD monitor using the IFree linear combination for the GBAS F service. In Rotondo (2016), Felux et al. (2017b), and Pullen et al. (2017) one can find analyses and methodologies that evaluate the impact of ionospheric gradients on the performance of GAST D and F using dual-frequency GNSS data. It is important to note that there are several controls being carried out at the level of the GBAS station, but there isn't, at least very clearly, at aircraft positioning level, nor an ionospheric scintillation monitor in the airport region. A new GBAS architecture proposed by Murphy et al. (2023), referred to as GAST-E, is based on the use of multi-frequency, multi-constellation data and prioritizes the use of the Divergence-Free linear combination. It is currently being studied for incorporation into aviation standards to enable the inclusion of new signals and constellations.

In these studies, promising results were obtained using the additional Galileo constellation for L5/E5a frequencies for mid-latitude regions, where the ionosphere problem does not behave as it does in low-latitude regions. Therefore, this thesis aims to conceptualize, implement and evaluate the performance of GBAS in a Brazilian region, considering the dual-frequency, dual-constellation (DFDC) scenario for precision approach services. Named GBAS Unesp Experimental, it will work as a Test Bed evaluating GBAS DFDC performance and will indicate the precision approach categories

that meet the performance requirements. It will also monitor anomalous ionospheric conditions to aid quality control of GNSS positioning performed at aircraft level.

1.1. Hypothesis and Objectives

The use of GNSS DFDC data through linear combinations will help minimize systematic effects and improve GBAS performance in the context of occurrence of ionospheric scintillation.

The general aim of this work is to investigate the use of data from a GBAS DFDC station to analyze the performance and integrity requirements for each category of precision approach. To accomplish this objective, the present study will proceed through the following stages:

- Development of a GBAS DFDC prototype using frequency observables from the GPS (L1 and L5) and Galileo (E1 and E5a) constellations.
- Implementation of fault identification monitors for anomalous ionospheric conditions, ionospheric scintillation, and position error estimation.
- Evaluation of GBAS performance with the linear combinations used to generate differential corrections and mitigate the effects of the ionosphere on GNSS signals.
- Multipath estimation of the reference stations and aircraft using the linear combinations Code Minus Carrier Divergence Free (CMCDF).

1.2. Contents and Contributions

This thesis evaluates the performance of dual-frequency and dual-constellation GNSS data in GBAS for the equatorial region of Brazil, an area frequently affected by ionospheric irregularities. Developed under the INCT GNSS-NavAer Project (MONICO et al., 2022), the study focuses on a prototype named GBAS UNESP Experimental, which comprises GNSS stations used for GBAS simulations and algorithms collaboratively developed by the GBAS research group within the INCT GNSS-NavAer Project.

The GBAS UNESP Experimental architecture consists of six GNSS stations, with four operating as ground systems providing differential corrections and ground integrity

parameters. The remaining two stations simulate aircraft in static mode, monitoring performance conditions to determine the feasibility of precision approach using GBAS.

The algorithms, implemented in MATLAB, utilize dual-frequency (L1/E1 and L5/E5a) and dual-constellation (GPS and Galileo) data, which are being investigated by the scientific community for potential integration into future precision approach services.

The thesis is structured into seven chapters. Chapter 1, which includes this section, provides an introduction to the proposed approach, its context within GBAS research, and the objectives and potential contributions of the study.

Chapters 2 and 3 present the theoretical fundamentals of the thesis. Chapter 2 discusses the categories of GBAS precision approach services (GAST C), highlighting the mathematical models of GAST C and D services, currently regulated by RTCA (Radio Technical Commission for Aeronautics) standards DO253-C and DO253-D, respectively. Since these services rely on single-frequency GNSS data, the chapter also introduces the architecture and models proposed in the literature for GAST F, X, ands E services, which align with the dual-frequency and dual-constellation approach of this thesis.

Chapter 3 addresses the theoretical fundamentals of ionospheric effects on GNSS signals and their implications for GBAS. It defines key ionospheric irregularity phenomena in equatorial and low-latitude regions, such as plasma bubbles, scintillation, and high ionospheric gradients.

Chapter 4 details the GBAS UNESP Experimental prototype, including the spatial architecture with the locations of the GNSS stations, as well as the configuration of the ground and aircraft systems, as defined within the INCT GNSS-NavAer Project for GBAS studies. Additionally, it presents the implementations for GBAS performance simulations, including the mathematical models and performance requirements adopted for the ground and aircraft systems.

Chapter 5 presents the initial results of the thesis, focusing on the nominal multipath conditions of the six GNSS stations used in the GBAS UNESP Experimental prototype. Using the Divergence-Free CMC (Code Minus Carrier) linear combination, multipath estimates were derived for the L1/E1 and L5/E5a frequencies and compared with conventional multipath estimation algorithms (referred to as MP1 and MP5 in this thesis). A descriptive analysis of the statistical indicators for each station is also provided.

Chapter 6 presents the GBAS simulation experiments in both static and kinematic modes. The static mode evaluates the GBAS DFDC (Dual-Frequency Dual-Constellation) performance of the GBAS UNESP Experimental during periods of high

and low ionospheric scintillation, comparing the ground and aircraft system performance against GBAS precision approach requirements. Additionally, given the prototype's potential as a monitoring station, integrity parameters related to ionospheric effects and positioning performance during the analyzed period are discussed.

The kinematic scenario in Chapter 6 involves performance analysis using UAV flights during periods of low and high ionospheric scintillation. Although this experiment was not conducted within the thesis implementations, it was simulated using the PEGASUS software developed by EUROCONTROL, adopting the GAST F SF L1 architecture to align with the static scenario implementation.

Finally, Chapter 7 presents the main conclusions, considerations, and insights gained from the study regarding the addition of dual-frequency signals and satellite constellations to GBAS performance in a region heavily impacted by ionospheric irregularities. It also discusses challenges and proposes a future research agenda to address the limitations of this work.

1.3.Potential Impact of the Research

The development of a GBAS DFDC prototype, as presented in this research, holds transformative potential for aviation safety and precision approach operations in low-latitude regions like Brazil. By addressing the challenges posed by ionospheric irregularities and a critical limitation of current single-frequency GBAS systems, this work paves the way for more reliable and resilient navigation solutions in equatorial areas, where ionospheric scintillation frequently degrades GNSS signal quality.

The GBAS UNESP Experimental Test Bed, leveraging GPS (L1/L5) and Galileo (E1/E5a) signals, represents a significant advancement in mitigating ionospheric errors through multi-frequency and multi-constellation processing. Performance analyses under both high and low scintillation conditions enable the assessment of the feasibility of employing modernized GNSS signals in safety-critical aviation applications.

One of the most impactful outcomes of this research is the empirical validation of SF L1's robustness in low-latitude environments. Despite severe ionospheric disturbances, the SF L1 mode-maintained compliance with CAT I requirements for over 99% of the analyzed period, outperforming the IFree mode (90% availability). This finding challenges the assumption that dual-frequency processing alone guarantees

superior performance, highlighting the nuanced trade-offs between ionospheric error mitigation and system availability.

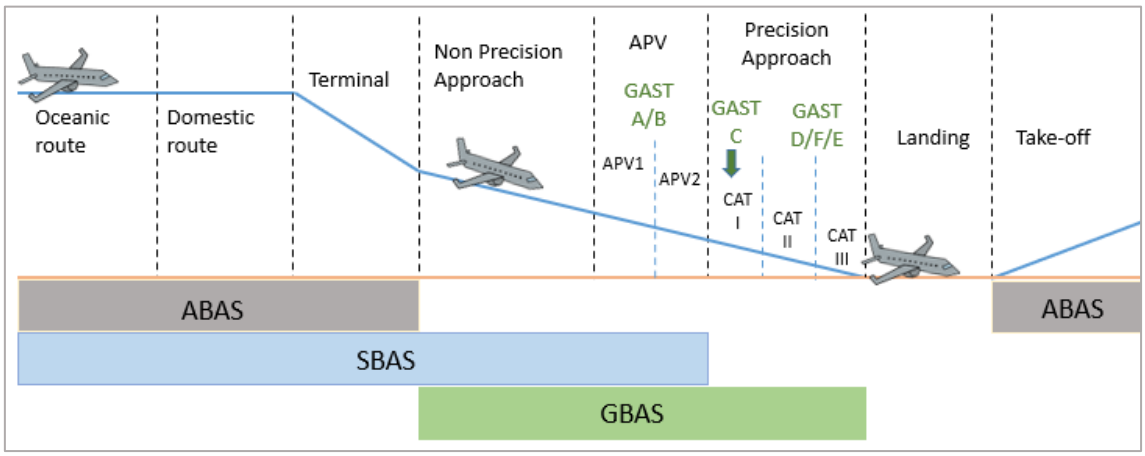
The research underscores that satellite exclusion due to signal quality monitoring disproportionately affects the IFree mode, emphasizing the need for adaptive algorithms to optimize satellite selection and weighting in GBAS operations. These insights are critical for regulatory bodies, such as ICAO and FAA, as they consider updates to GBAS standards to incorporate dual-frequency and multi-constellation capabilities.

Another important aspect of the research is the presentation of the nominal multipath conditions of the UNESP Experimental GBAS stations. This study provided information on the directions and times of day with the highest rates of multipath at each station. In addition, this survey may in future generate a multipath model for each station for application in GBAS or other GNSS positioning methods.

2. GBAS APPROACH SERVICE TYPE

GNSS technology has been adopted in aviation owing to its global navigation capabilities, high accuracy, low cost, compact size, and receiver flexibility. As illustrated in Figure 1, GNSS supports all phases of flight. Since this is a safety-critical, stringent performance requirements are imposed on GNSS to ensure accuracy, integrity, continuity, and availability at every stage of flight (PULLEN, 2017). Thus, augmentation systems were developed to provide corrections and integrity parameters to GNSS data, enabling fault detection and mitigating systematic effects on satellite signals. Among the GNSS augmentation systems used in aviation are ABAS (Aircraft-Based Augmentation System), SBAS (Satellite-Based Augmentation System), and GBAS. Details of each of these augmentation systems and the flight stages can be found in Rotondo (2016) and Farnworth (2017).

Figure 1 – Illustration of the application of GNSS augmentation systems across flight phases.



Source: Adapted from Rotondo (2016).

GBAS was developed to support precision approach and landing of aircraft by defining the landing path on the runway. At most international airports, this operation is conducted with the aid of the Instrument Landing System (ILS), particularly under low-visibility conditions. The ILS consists of two radio frequency transmitters that provide lateral and vertical guidance: the Localizer, which directs the aircraft to the centerline of the runway, and the Glide Slope, which indicates the descent path to the landing point on the runway. Distance markers and runway lights are also part of the ILS infrastructure,

which requires all equipment to be installed at each runway threshold (FARNWORTH, 2017). ILS approaches are classified into three categories (CAT I, II, and III) based on horizontal and vertical guidance error limits, runway visibility, and decision height (Table 1).

Table 1 – Precision approaches categories for ILS.

(*Category Approach Type* – CAT)		Decision Height	Runway visibility
CAT I		Higher than 60 m	Between 800 and 550 m
CAT II		Between 60 and 30 m	Between 550 and 300 m
CAT III	A	Less than 30 m	Between 300 and 175 m
	B	Less than 15 m	Between 175 and 50 m
	C	No decision height and runway visibility limit	

Source: ICAO (2018).

GBAS is an alternative to ILS, with the potential to enhance the efficiency of precision approaches and landings at an airport. A single GBAS station can provide approach services to all the airport's runways (FELUX et al., 2013). It also has the capability to perform curved approaches, which could lead to reduced travel and fuel costs in the future.

As seen in Figure 1, a GBAS station can simultaneously provide several types of approach services (GAST), depending on horizontal and vertical accuracy performance (Table 2). GAST categories A, B, C, and D are standardized by ICAO (RTCA DO-253C, 2008). GAST A and B refer to APV I and APV II services. GAST C provides guidance for the precision approach phase up to CAT I, while GAST D was developed to support CAT II and III with single frequency.

Table 2 – Requeriments for GBAS aproach services.

Approach service types	Horizontal accuracy (95%)	Horizontal Alert Limit	Vertical Accuracy (95%)	Vertical Alert Limit	GAST
APV – I	16 m	40 m	20 m	50 m	A
APV – II	16 m	40 m	8 m	20 m	B
CAT I	16 m	40 m	6 m to 4 m	10 m	C
CAT II	5 m	17 m	2.9 m	10 m	D, F
CAT III	5 m	17 m	2.9 m	10 m	D, F

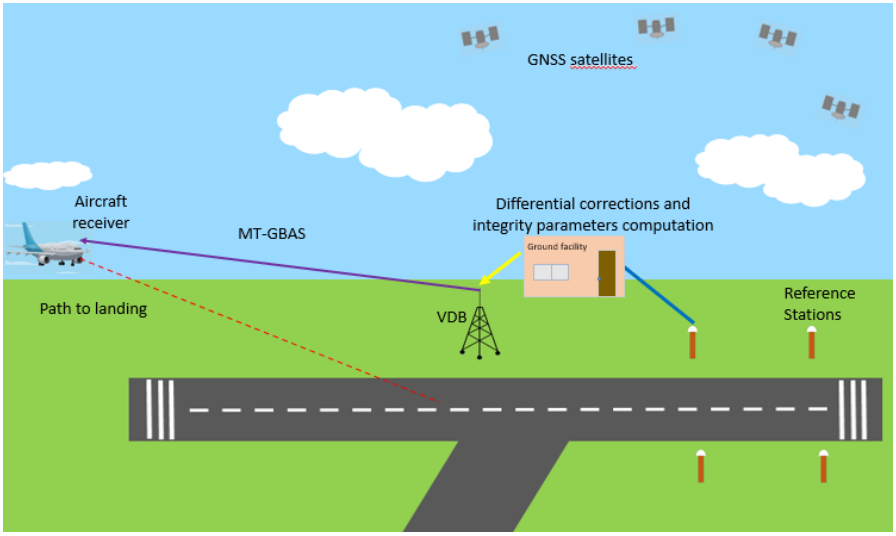
Source: Adapted ICAO (2018), Pullen (2017).

According to Rotondo et al. (2015), GAST C, D, and F can also be defined by signals and constellations used:

- GAST C: uses L1, GPS and GLONASS;
- GAST D: uses L1, GPS and GLONASS;
- GAST F: concept is being designed to be Dual Frequency (L1 and L5), Multi Constellation (GPS and Galileo), i.e. GBAS DFDC;
- GAST X and E: service proposed to be GBAS dual frequency multi-comstellation (DFMC) in different modes (MURPHY et al., 2021; MURPHY et al., 2023).

Mitigating ionospheric effects is the main challenge for GBAS to meet performance requirements, especially in low-latitude regions. Therefore, the use of GNSS DFDC data is an attempt to minimize ionospheric effects and enable the use of GBAS in these regions. The GBAS architecture (Figure 2) is based on the differential GNSS positioning method. The ground infrastructure consists of 2 to 4 GNSS reference stations (located within the airport) that continuously provide data to generate differential corrections, a master control station (or Ground Facility Station – GFS) that calculates the differential corrections, and a VHF (Very High Frequency) antenna that transmits data to the aircraft or VDB (VHF Data Broadcast). At the aircraft level, a GNSS receiver uses the corrections and integrity parameters sent by the ground segment to improve positioning accuracy.

Figure 2 – Conventional GBAS architecture.



Source: Silva and Monico (2022).

2.1. GAST C: Fundamentals

GAST C is the level of precision approach service provided by GBAS that is equivalent to the same service performed by ILS in the CAT I category, according to the performance requirements shown in Table 2.

As previously mentioned, GBAS is based on differential positioning and uses the GNSS-observable pseudorange smoothed by the carrier-phase, to minimize uncorrelated errors such as multipath and noise. This observable is obtained by applying the Hatch Filter, as expressed in Equation (1) (RTCA DO-253C, 2008):

$$\widehat{PD}_t^i = \frac{S}{\tau} PD_t^i + \left(1 - \frac{S}{\tau}\right)\left[\widehat{PD}_{t-1}^i + \lambda\left(\varphi_t^i - \varphi_{t-1}^i\right)\right] \quad (1)$$

where: $\widehat{PD}_t^i$ and $\widehat{PD}_{t-1}^i$ are respectively the pseudorange smoothed for satellite *i* at the current time (*t*) and the previous time (*t-1*); *S* is the GNSS data sampling interval; τ is the pseudorange smoothing time constant of the Hatch Filter; λ is the wavelength of the GNSS signal frequency used; φ_t^i and φ_{t-1}^i are the carrier-phase for satellite *i* at the current and previous time.

The smoothed pseudorange is calculated recursively and used to generate the PseudoRange Corrections (PRC) calculated for each reference station, according to Equation (2):

$$PRC_{CSC}^i(j,t) = R^i(j,\ t) - \widehat{PD}_t^i(j) - (c * \Delta t^i(t)) \quad (2)$$

where: $PRC_{CSC}^{i}(j,t)$ is the smoothed pseudorange correction from satellite *i* to receiver *j* at time *t*; $R^{i}(j,\ t)$ is geometric distance between satellite *i* at transmission time *t* and, receiver j, *c* is the speed of light in vacuum; and $\Delta t^{i}(t)$is the clock error of satellite *i* at time *t* (transmission time) calculated from the parameters present in the navigation messages (broadcast ephemeris).

Additionally, the receiver clock error is removed, because it is an uncorrelated systematic effect and therefore affects each reference station differently. Equation (3) shows the removal of the receiver clock error:

$$PRC_{SCA}^{i}(j,t) = PRC_{CSC}^{i}(j,t) - \sum_{i\in S_c}^{N_c} k_i * PRC_{CSC}^{i}(j,t) \quad (3)$$

where $PRC_{SCA}^{i}(j,t)$ is the smoothed pseudorange correction adjusted after removing the receiver clock error; k_i is the weighting factor, with $\sum_{i\in S_c}^{N_c} k_i = 1;\ S_c$ is the set of satellites tracked by all reference stations; N_c is the number of elements in the S_c set. The satellite weighting factor is not defined by the standards (RTCA DO-253C, and ED-114A), only the requirement that $\sum_{i\in S_c}^{N_c} k_i = 1$. The main possibilities are to use equal weights or weights based on the elevation of the satellites, but it is up to the ground subsystem to decide which method to apply (CIRCIU, 2020).

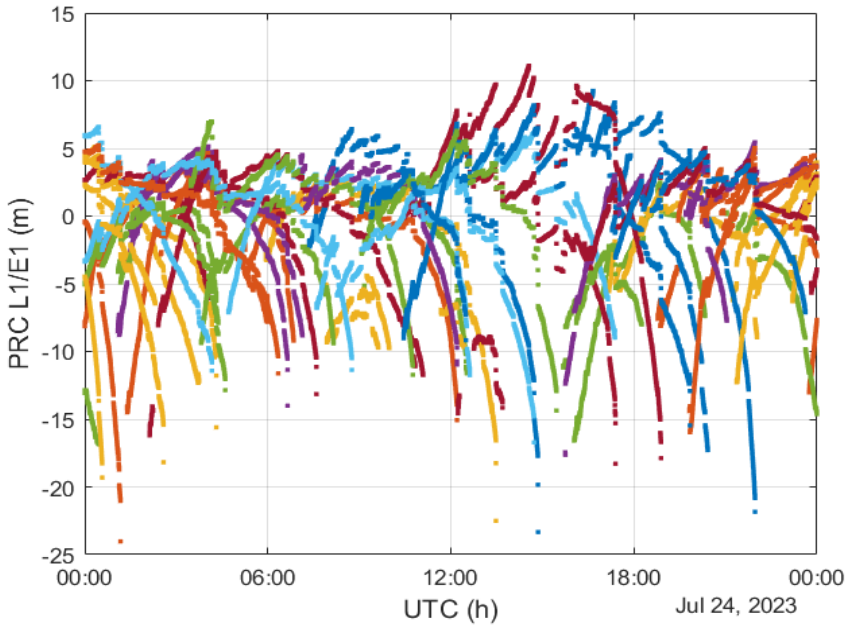
The transmitted pseudorange correction (PRC_{TX}^{i}) to the aircraft (Equation (4)) is determined by averaging the $PRC_{SCA}^{i}(j,t)$ obtained for satellite i by the *M* reference stations with valid corrections for this satellite at time *t*:

$$PRC_{TX}^{i}(t) = \frac{1}{M(t)} \sum_{i=1, j\epsilon s_i}^{M(j)} PRC_{SCA}^{i}(j,t) \quad (4)$$

where: s_i is the set of receivers with valid measurements for satellite *i*.

Figure 3 shows an example of differential corrections, where the different colors represent satellites with valid corrections. Generally, the PRC behaves like a parabola, which values vary accordingly to the elevation angle of the satellites. Typically, the lowest PRC values (in absolute terms) correspond to the highest satellite elevations.

Figure 3 – Pseudorange corrections calculated for 4 reference stations from GBAS Unesp Experimental using single frequency (L1/E1) GPS and Galileo on DOY 205/2024.



In addition to the PRCs, the ground system also determines other parameters, such as the Range Rate Corrections (RRC), σ_{pr_gnd}, and B-Values. RRC (Equation (5)) is applied to the aircraft's corrected pseudorange. The RRC can be calculated by dividing the difference in PRC_{TX} at the current time (t) and the previous time ($t-1$) by the time interval between them, (i.e, Δt):

$$RRC(i,t) = \frac{PRC_{TX}\,(i,t) - PRC_{TX}\,(i,t-1)}{\Delta t} \tag{5}$$

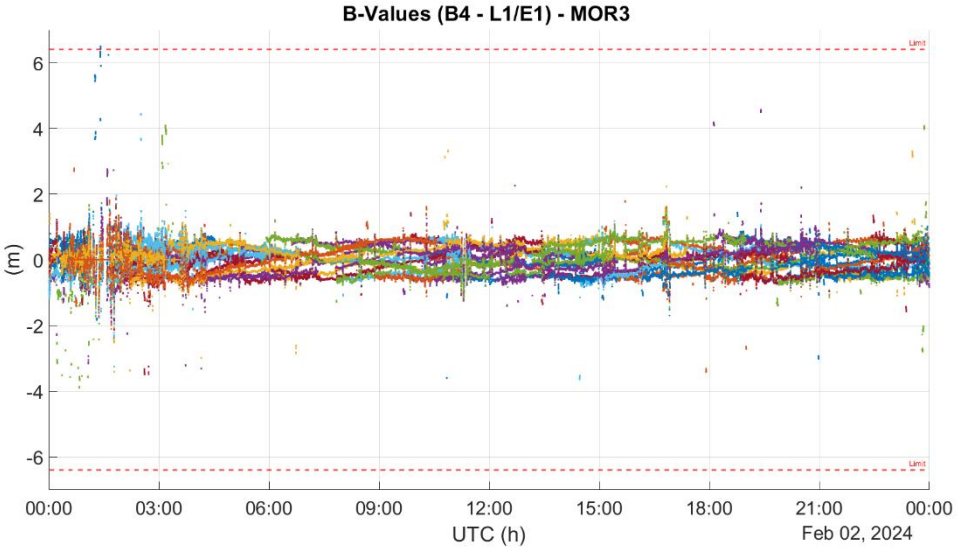
The B-Values are integrity parameters transmitted by the ground system, whose purpose is to check the consistency of the differential corrections provided by each reference station, as well as to detect faults. Considering a GBAS with four reference stations, the B-Values are determined by comparing the differential correction transmitted by one reference station with the average of the other three available (Equation (6)). This procedure is repeated for each reference station.

$$B(i,j) = PRC_{TX}(i) - \frac{1}{M(i)-1} \sum_{k \epsilon S_i, k \neq j}^{n} PRC_{SCA}\,(i,k) \tag{6}$$

The interpretation of the B-Values (Figure 4) indicates the error that would occur in the differential correction of satellite i if the measurement from receiver j were faulty or not available. If receiver j is faulty, the correction is given by the average of the measurements from the other k fault-free receivers tracking satellite i. The closer the B-

Value is of zero, the more consistent the corrections are with the average correction values obtained. According to ED-114A (2013), B-Values can vary from -6.35 m to +6.35 m to be considered valid. Otherwise, the satellite correction will not be used by the aircraft.

Figure 4 – Example of B-Values from a MOR3 station located in Presidente Prudente (São Paulo) on 033/2024.



Source: Silva and Monico (2022).

The σ_{pr_gnd} parameter is generated by the ground system and defines the standard deviation of a normal distribution associated with the residual uncertainty in the differential corrections of the reference stations. In the model adopted by GBAS, some systematic errors, such as multipath and effects related to GNSS receivers, are neglected.

The σ_{pr_gnd} is determined from B-Values using a significant sample of GNSS data to ensure that the condition of normality for systematic errors is met in the values used. Additionally, it considers the intervals of the satellites' elevation angles (e.g., every 5°).

$$\sigma_{pr_gnd}(b,j) = \sigma_B(b,j)\sqrt{(M-1)(\frac{N+1}{N})} \tag{7}$$

where: b represents a satellite elevation interval to be considered; N is the number of B-Values in the satellite elevation interval; $\sigma_B(b,j)$ is the uncertainty calculated for the estimation of errors associated with the B-Values, according to the set of observations from the reference stations:

$$\sigma_B(b,j) = \sqrt{\frac{1}{N(b,j)} \sum_{k=1}^{N(b,j)} (B_k(b,j) - \underline{(B(b,j))})^2} \quad (8)$$

All parameters calculated by GFS, shown in this section, make up the content of Type 1 Messages transmitted by the VDB. In EUROCAE (2013) we can find the set of these parameters to support GAST C approach services.

In the case of a GAST D, the ground subsystem adds Type 11 Messages, which is similar to this MT1 (Message Type 1), but adds parameters related to the smoothing pseudorange using 30s as time constant in the Hatch Filter. On the other hand, GAST F has a Type 42 Message with all parameters related to L5/E5a frequency.

GAST C also transmits other messages via the ground system, which are MT1, MT2 and MT4. Details can be found in EUROCAE (2013). The VDB sends these messages to the aircraft via radio frequency signal. Data transmission is normally carried out in the frequency range from 108 to 117.975 MHz. The VDB antenna must be located so that there is no obstruction to any line of sight at any point within the coverage volume that includes all supported FAS (Final Approach Segment). Nominal GBAS VDB transmission coverage should be omnidirectional with at least 23 nautical miles (about 43 km).

2.1.1 Determining the Aircraft's Position

After receiving the differential corrections and integrity parameters transmitted by the ground subsystem, the aircraft position is computed using the measurements tracked by the aircraft's GNSS receiver. However, before being used, these messages are evaluated by the aircraft subsystem, considering, for example, the received signal strength, the compatibility of the same satellites with the corrections for the valid instants. The accepted measurements are applied to Equation (9) for the aircraft's pseudorange corrected ($PD^i_{cor_air}$) available in RTCA DO-253C (2008):

$$PD^i_{cor_air}(t) = PD^i_{SCA,air}(t) + PRC^i_{TX}(t_{PRC_{TX}}) + RRC^i(t - t_{PRC_{TX}}) - TC^i(t) + c(\Delta t^i_{L1}) \quad (9)$$

where: $PD^i_{SCA,air}(t)$ is the smoothed pseudorange by satellite *i* at the aircraft receiver at time *t*; PRC^i_{TX} is the differential correction transmitted at the time $t_{PRC_{TX}}$; RRC^i is the rate range corrections of satellite *i* multiplied by the difference of the current time *(t)* and the time of transmission of the correction $t_{PRC_{TX}}$; Δt^i_{L1}corresponds to the clock error at

frequency L1 applied to satellite i at time t; TC is the residual tropospheric delay correction determined by Equation (10):

$$TC^i(t) = N_R h_0 \frac{10^{-6}}{\sqrt{(0{,}002+sin^2(\theta_i))}} \left(1 - e^{\frac{-\Delta h}{h_0}}\right) \tag{10}$$

where: N_R is the Refractivity transmitted in Type 2 Messages; h_0 is the height scale in meters, of the troposphere layer, transmitted in Type 2 Messages; θ_i is the satellite's elevation angle; and Δh is the aircraft's height in meters, for the GBAS reference point.

Then, the three-dimensional position (X, Y and Z), in the appropriate reference frame, for example WGS84), and the clock error of the aircraft receiver can be calculated by applying the Least Squares Method:

$$\hat{X} = ((A^T PA)^{-1} A^T P)\Delta PD_{corr_air} \tag{11}$$

For this case, ΔPD_{corr_air} is the vector that represents the difference between the aircraft's corrected pseudorange and the geometric distance ($\Delta PD^i_{cor_air} = PD^i_{cor_air} - R^i_{air}$) for each satellite, at each epoch, considering an approximate position of the aircraft.

The A matrix for the case in question is best given as Local Geodetic System (N, E, Up) with its origin at the aircraft's planned landing point LTP/FTP (Landing Threshold Point/Fictitious Threshold Point). The design matrix A can be computed using the satellites' elevation $(\theta)_i$ and azimuth $(Az)_i$ angles. For Equation (12), the matrix A is composed of GPS (g) and Galileo (e) satellites, with indices ranging from 1 to n.

$$A = \begin{bmatrix} -\cos(\theta g)_1 \cos(Az(g))_1 & -\cos(\theta g)_1 \text{sen}(Az(g))_1 & -\text{sen}(\theta g)_1 & 1 & 0 \\ -\cos(\theta g)_2 \cos(Az(g))_2 & -\cos(\theta g)_2 \text{sen}(Az(g))_2 & -\text{sen}(\theta g)_2 & 1 & 0 \\ -\cos(\theta g)_3 \cos(Az(g))_3 & -\cos(\theta g)_3 \text{sen}(Az(g))_3 & -\text{sen}(\theta g)_3 & 1 & 0 \\ -\cos(\theta g)_4 \cos(Az(g))_4 & -\cos(\theta g)_4 \text{sen}(Az(g))_4 & -\text{sen}(\theta g)_4 & 1 & 0 \\ \vdots & \vdots & \vdots & \vdots & \vdots \\ -\cos(\theta e)_1 \cos(Az(e))_1 & -\cos(\theta e)_1 \text{sen}(Az(e))_1 & -\text{sen}(\theta e)_1 & 0 & 1 \\ -\cos(\theta e)_2 \cos(Az(e))_2 & -\cos(\theta e)_2 \text{sen}(Az(e))_2 & -\text{sen}(\theta e)_2 & 0 & 1 \\ -\cos(\theta e)_3 \cos(Az(e))_3 & -\cos(\theta e)_3 \text{sen}(Az(e))_3 & -\text{sen}(\theta e)_3 & 0 & 1 \\ -\cos(\theta e)_n \cos(Az(e))_n & -\cos(\theta e)_n \text{sen}(Az(e))_n & -\text{sen}(\theta e)_n & 0 & 1 \end{bmatrix} \tag{12}$$

The weight matrix (P) of the measurements from each satellite consists of a diagonal matrix made up of the inverse of the variance free of faults.

$$P = diag\left[\ \sigma^{-2}_{P(1)},\ \sigma^{-2}_{P(2)}, \sigma^{-2}_{P(3)},\ \sigma^{-2}_{P(4)}, \ldots, \sigma^{-2}_{P(N)}\ \right] \tag{13}$$

The term corresponding to the variance (σ^2_P) contains the contribution of all the elements that can lead to errors in the pseudorange measurements:

$$\sigma_P^2(i) = \sigma_{pr_gnd}^2(i) + \sigma_{pr_air}^2(i) + \sigma_{tropo}^2(i) + \sigma_{iono}^2(i) \quad (14)$$

where: σ_{pr_gnd} is the uncertainty associated with errors in the differential correction of the reference stations; the term σ_{pr_air} consists of an error model associated with aircraft pseudorange measurements provided for in RTCA DO253-C (2008); σ_{tropo} is the uncertainty associated with the residual error from tropospheric delay; and σ_{iono} is the uncertainty associated with the residual error from ionospheric delay. Latter it will be presented in more detail due to the difficulties in dealing with the ionosphere in the low latitudes, as well as the effects of the troposphere.

The σ_{pr_gnd} consists of a Ground Subsystem pseudorange error model called the Ground Accuracy Designator (GAD), which is based on the performance of GNSS receivers in mitigating multipath effects. GAD can be expressed as a letter or number indicator in three categories, where:

- **A (0)** – Represents the level of accuracy achievable using commonly available receivers and modest multipath mitigation techniques;
- **B (1)** – Represents the accuracy consistent with the use of modern, higher precision receivers and better multipath mitigation techniques; and
- **C (2)** – Represents the accuracy consistent with the latest generation GNSS receivers and multipath mitigation techniques.

Equation (15) shows the GAD model for the GPS constellation used in GBAS GAST C and D (EUROCAE, 2013).

$$\sigma_{pr_gnd}(\theta_i) = \sqrt{\left(\frac{(a_0 + a_1)e^{\frac{\theta_i}{\theta_0}}}{M}\right)^2 + (a_2)^2} \quad (15)$$

where: *M* is the number of Ground Subsystem reference stations; θ_i is the elevation angle for satellite *i*; a_0, a_1, a_2e θ_0 are parameters defined in Table 3 for each GAD category.

Table 3 – Ground Accuracy Designator or GAD Model for GPS satellites.

GAD category	θ_i (°)	a_0 (m)	a_1 (m)	θ_0 (°)	a_2 (m)
A	≥ 5	0,5	1,65	14,3	0,08
B	≥ 5	0,16	1,07	15,5	0,08
C	> 35	0,15	0,84	1,5	0,04
	5 a 35	0,24	0	-	0,04

Source: Adapted from EUROCAE (2013).

The pseudorange error and uncertainty model arising from the aircraft GNSS receiver is called the Aircraft Accuracy Designator (AAD). Equation (16) defines the estimate of σ_{pr_air}:

$$\sigma_{pr_air}(i) = \sqrt{(\sigma^2_{multipath}(i) + \sigma^2_{noise}(i))} \tag{16}$$

where: $\sigma_{multipath}(i) = 0{,}13 + 0{,}53 * e^{\frac{\theta_i}{10}}$; e $\sigma_{noise}(i) = a_0 + a_1 * e^{\frac{\theta_i}{\theta_0}}$. The σ_{noise} term is calculated according to the performance model defined by AAD for two categories: A and B (Table 4).

Table 4 – AAD Model for GPS satellites.

AAD	θ_i (°)	θ_0 (°)	a_0 (m)	a_1 (m)
A	≥ 5	6,9	0,15	0,43
B	≥ 5	4,0	0,11	0,13

Source: Adapted from EUROCAE (2013).

The residual uncertainty related to the tropospheric delay error is determined using the terms presented above in Equation (17).

$$\sigma_{tropo}(i) = \sigma_N h_0 \frac{10^{-6}}{\sqrt{(0{,}002 + sin^2(\theta_i))}} \left(1 - e^{\frac{-\Delta h}{h_0}}\right) \tag{17}$$

where: σ_N is the refractivity uncertainty, transmitted in Type 2 Messages.

The determination of the uncertainty of the residual error of the ionospheric delay (σ_{iono}), resulting from the spatial and temporal decorrelation for the aircraft can be obtained according to RTCA DO-253C (2008):

$$\sigma_{iono}(i) = F_{pp}(i).\sigma_{vig}.(X_{aircarft} + 2.\tau.V_{aircraft}) \quad (18)$$

where: σ_{vig} is the standard deviation of the vertical ionospheric gradient (meters per meter), transmitted in the Type 2 Message; $X_{aircarft}$ is the distance in meters between the aircraft and the GFS direction; τ is the time constant used in the pseudorange smoothed (100 s); $V_{aircraft}$ aircraft is the horizontal velocity of the aircraft, given in m/s; F_{pp} is the obliquity factor for converting the standard deviation of the ionospheric error from the vertical to the slant direction (satellite-receiver). This factor is dimensionless and can be calculated using Equation (17):

$$F_{pp} = \left[1 - \left(\frac{R_e cos(\theta_i)}{R_e + h_I}\right)^2\right]^{\frac{-1}{2}} \quad (19)$$

where: R_e is the average radius of the Earth; θ_i is the elevation angle of the satellite considered; h_I is the average height in the ionosphere layer (generally 350 km is adopted).

The σ_{vig} parameter in Equation (18) represents the variation in the ionospheric gradient between the reference station and the aircraft, the nominal determination of which comes from observing a few days of ionospheric delay monitoring for the airport region, to obtain a representative value for mitigating residual gradient errors.

Returning to Equation (11), we can define $S = (A^T PA)^{-1} A^T P$ as the term corresponding to the positioning projection matrix. Thus, the standard deviation of the horizontal and vertical components is obtained from Equations (20) and (21):

$$\sigma_{error_horiz.} = \sqrt{\sum_{i=1}^{N} S_{horiz.}^2(i).\sigma_P^2(i)} \quad (20)$$

$$\sigma_{error_vert.} = \sqrt{\sum_{i=1}^{N} S_{vert.}^2(i).\sigma_P^2(i)} \quad (21)$$

where $S_{horiz.}(i)$ and $S_{vert.}(i)$ are, respectively, the components of the projection matrix position, which can be determined by Equations (22) and (23):

$$S_{horiz.}(i) = \sqrt{S_1^2(i) + S_2^2(i)} \quad (22)$$

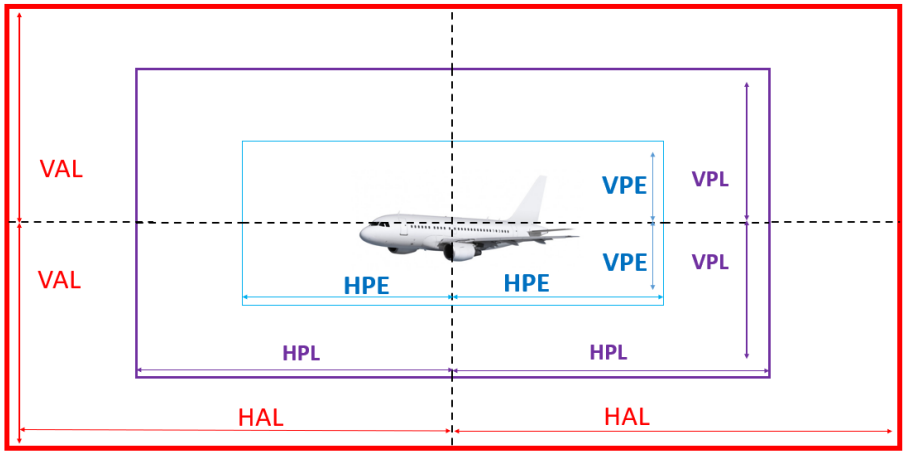
$$S_{vert.}(i) = S_3(i) + S_1(i) * \tan(\theta_{GPA}) \quad (23)$$

where the elements $S_3(i)$, $S_2(i)$ and $S_1(i)$ represent the position occupied, respectively, in the first, second and third columns of row of the projection matrix S. The term θ_{GPA} is the angle of the aircraft's approach path to the runway (a value of 3 degrees is generally adopted).

2.1.2 Integrity Parameters in the Aircraft Position Domain

In the aircraft position domain, integrity can be verified by calculating protection levels. These represent error limits in the horizontal and vertical components of the aircraft's position, which enable or disable the precision approach to be carried out with GBAS. Integrity is maintained when the position errors (PE) are lower than the protection levels (PL) and warning limits (AL), i.e.: PE < PL < AL, in both the horizontal and vertical components (Figure 5).

Figure 5 – Integrity parameters in aircraft position domain.



Source: Adapted from Sabatini et al. (2017).

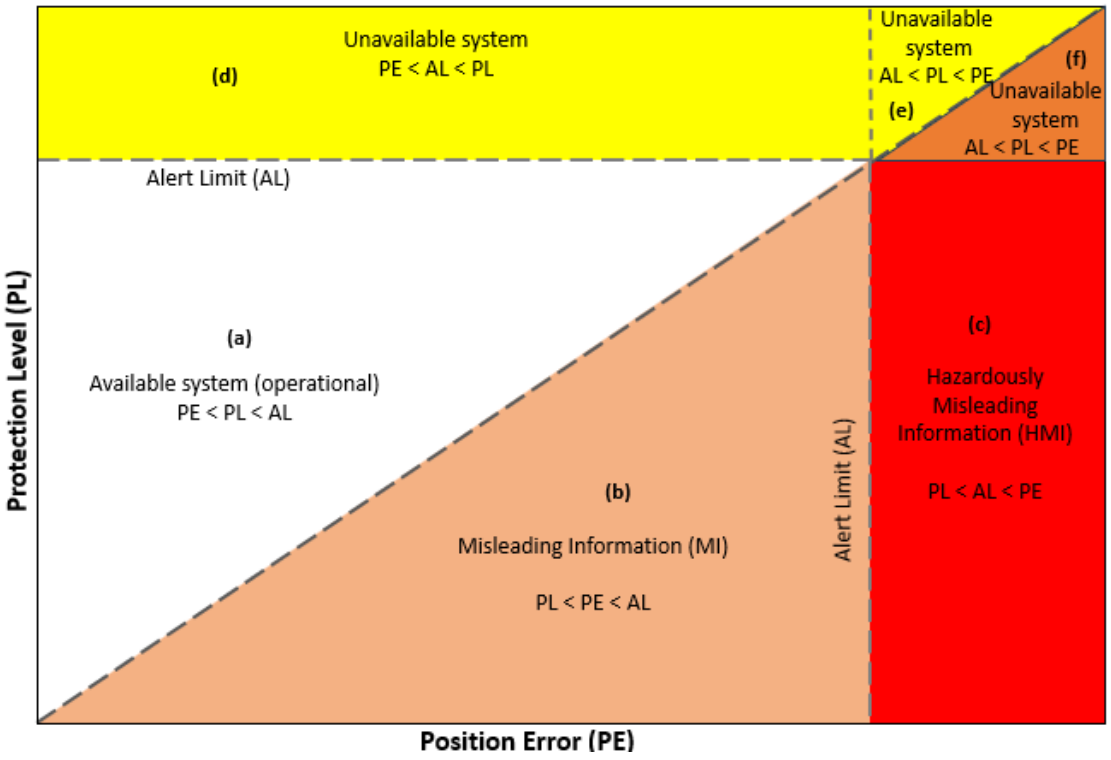
One approach to representing and analyzing GBAS integrity parameters is the Stanford-ESA Integrity Diagram, also known as the "Stanford Plot" (Figure 6). Developed by the Wide Area Augmentation System Laboratory at Stanford University, this method provides a graphical representation of integrity in SBAS and GBAS augmentation systems based on the performance of protection levels and position errors (TOSSAINT et al., 2007; Marini-Pereira, et al., 2021). The diagram plots the position error (PE) against the protection level (PL), allowing the verification of the following conditions:

- System unavailable: Occurs when the protection level exceeds both the position error and the alert limit.

- System available (without restriction): The operational condition in which the protection level is greater than the position error but remains below the alert limit.
- System available with misleading information (MI): Arises when the position error exceeds the protection level but remains below the alert limit.
- Hazardously Misleading Information (HMI) or Hazardously Operation (HO): In this scenario, the system is declared available, yet the position error surpasses both the protection level and the alert limit. This condition may lead users to make erroneous operational decisions.

In Figure 6 case (a), the desired (nominal) condition is achieved, where both PE and PL remain below the AL, ensuring operational integrity. However, cases (b) and (c) illustrate situations in which integrity is not maintained. In case (b), the system issued a warning not to use it, although it could have been used since the alert limit was not exceeded. Statistically, this corresponds to a Type I error, where a usable system was unnecessarily restricted. Conversely, in case (c), the system was deemed usable because the protection level remained below the alert limit; however, the actual position error exceeded the alert threshold. This represents a Type II error, meaning the system was incorrectly allowed when it should have been restricted. In cases (d), (e), and (f), the system must be declared unavailable due to the lack of established integrity (ZABALEGUI et al., 2020).

Figure 6 – Integrity Diagram with the possible events for GBAS.



Source: Adapted of ZABALEGUI et al. (2020).

Protection levels, determined in real time, are derived by extrapolating probability distributions that bound the expected errors for the user (i.e., the aircraft). This conservative approach ensures that operations can be conducted safely while maintaining continuity. The calculation of protection levels is divided into vertical (VPL) and horizontal (HPL) components and is performed under two hypotheses: H_0 and H_1.

- **H_0** represents the nominal, fault-free scenario; and
- **H_1** assumes a single failure in the reference receiver.

For the nominal case (**H_0**), the horizontal and vertical protection levels (HPL and VPL) are obtained using Equations (24) and (25).

$$HPL_{H0} = (K_{ffmd})(\sigma_{error_horiz.}) + D_{horiz.} \quad (24)$$

$$VPL_{H0} = (K_{ffmd})(\sigma_{error_vert.}) + D_{vert.} \quad (25)$$

where K_{ffmd} is a multiplicative factor to ensure that the probability of failure meets the established integrity requirement, whose value is set according to the number of reference stations used to generate pseudorange corrections and the probability distribution adopted: with 2 receivers K_{ffmd}= 5.762 m; 3 receivers K_{ffmd}= 5.810 m; and with 4

receivers K_{ffmd}= 5.847m; $D_{horiz.}$ and $D_{vert.}$ are, respectively, the magnitude of the horizontal and vertical projection, considering the difference between the position solution with pseudorange smoothed at 30s and 100s. However, for the GAST C precision approximation, the values of $D_{horiz.}$ and $D_{vert.}$ are equal to zero, since only the 100s smoothing time constant is used.

In the case of failures in a receiver *j* detected by the B-Value parameter, the HPL and VPL are obtained from equations (26) and (27), according to RTCA DO-253C (2008):

$$HPL_{H1}(j) = \left|\sum_{i=1}^{N}(S_{horiz.}(i))(B(i,j))\right| K_{md}\sqrt{\sum_{i=1}^{N}\sigma_{\text{error_horiz.}}(i)} \quad (26)$$

$$VPL_{H1}(j) = \left|\sum_{i=1}^{N}(S_{vert}(i))(B(i,j))\right| K_{md}\sqrt{\sum_{i=1}^{N}\sigma_{error_vert.}(i)} \quad (27)$$

where K_{md} is the fault detection multiplier, which also depends on the number of reference receivers used: for 2 receivers K_{md} = 2.935 m; for 3 receivers K_{md} = 2.898 m; and using 4 receivers K_{md} = 2.878 m.

2.2. GAST D

GAST-D is the precision approach service that meets the performance requirements for CAT II/III operations (Table 2). To satisfy these requirements, GAST-D introduces a shared responsibility between the Ground and Aircraft Systems for monitoring anomalous ionospheric conditions that may degrade GNSS-based positioning in GBAS (PULLEN et al., 2017).

In contrast, GAST-C relies exclusively on the Ground System for this task. Consequently, if an anomalous ionospheric gradient shifts from the aircraft's location toward the reference stations, it is unlikely to be detected onboard the aircraft.

To mitigate this threat, GAST-D implements multiple integrity monitoring mechanisms, including the Ionospheric Ground Monitor (IGM), the Dual Solution Ionospheric Gradient Monitor Algorithm (DSIGMA), and the Code Carrier Divergence (CCD) monitor (PULLEN et al., 2017). These monitoring techniques will be described in detail in the following subsections.

2.2.1. Monitor DSIGMA

DSIGMA Monitor is the fault protection component installed on the aircraft for GAST D. According to Pullen et al. (2017) and Wang et al. (2020), DSIGMA monitors the impact of anomalous ionospheric gradients through the difference of pseudorange smoothed and their respective corrections, using the smoothing time constants of 100 s and 30 s (Equation (28)):

$$P_{diff}\ (i,t) = (PD_{air,100}(i,t) - PRC_{100}(i,t)) - (PD_{air,30}(i,t) - PRC_{30}(i,t)) \quad (28)$$

where: $PD_{air,100}$ and $PD_{air,30}$ are the pseudorange smoothed on the aircraft for a satellite (i) using the smoothing time constants of 100 s and 30 s, respectively; and PRC_{100} and PRC_{30} are the pseudorange corrections transmitted by the ground system using the 100 s and 30 s smoothing time constants, respectively.

An alert limit (AL_{DSIGMA}) indicating the occurrence of an anomalous ionospheric gradient can be calculated, according to Pullen et al. (2017), by multiplying the standard deviation (σP_{diff}) of the DSIGMA by the fault-free detection factor K_{ffd}:

$$AL_{DSIGMA}\ (i,t) = \sigma P_{diff}(i,t) * K_{ffd} \quad (29)$$

The occurrence of anomalous ionospheric gradients can impact GNSS signals and cause effects on observables. These are identified and monitored by cycle slip and, code carrier divergence (CCD), which will be described below.

2.2.2. Ionospheric Gradient Monitor

The Ionospheric Gradient Monitor (IGM) is designed to detect the arrival of ionospheric fronts that enter the GBAS coverage region and may affect the observations recorded by the reference stations (CIRCIU, 2020). Several methodologies in the literature address different IGM implementations.

Khanafseh et al. (2012) proposed an IGM methodology based on the linear combination of the double-phase difference of the carrier-phase signal between the baselines of the reference stations for the instantaneous detection of ionospheric fronts. This algorithm models the ionospheric front as an inclined gradient and assumes that the baselines between the antennas at the GBAS ground station are aligned with the aircraft track (KHANAFSEH et al., 2012).

Another methodology appears in the SARPs (International Standards and Recommended Practices) update, in which the performance requirements of the reference stations are replaced by a terrestrial ionospheric gradient monitor that has a simpler performance analysis to limit the error caused by an anomalous ionospheric gradient (CIRCIU, 2020). In this monitor, two parameters Y_{EIG} and M_{EIG} must be added to represent the maximum error that the ground system is able to protect against. The first parameter (Y_{EIG}) represents the maximum value of the error ionospheric gradient (E_{IG}) at the GBAS reference point. The second parameter, M_{EIG}, is the maximum slope of the E_{IG} in relation to the distance (*D*) from the GBAS reference point. The maximum error related to the ionospheric gradient, E_{IG}, is calculated according to Equation (30):

$$E_{IG} = Y_{EIG} + M_{EIG}D. \quad (30)$$

2.2.3. Monitor CCD

The use of the smoothed pseudorange in GBAS is intended to minimize some systematic effects of the original observable. However, the linear combination performed by the Hatch Filter, differentiating the code by the carrier-phase (CMC - Code Minus Carrier), results in the duplication of the ionosphere's bias effect (I_f^i) (Equation (31)).

$$PD_f^i(t) - \varphi_{f,t}^i(t) = 2I_f^i(t) - \lambda_f N_i(t) + \varepsilon_{PD,\varphi}^i(t) \quad (31)$$

where: $\varepsilon_{PD,\varphi}^i$ (*t*) corresponds to the unmodeled code and carrier-phase errors at time *t* for satellite *i*, the term related to ambiguity N_i becomes constant after a few minutes and can be disregarded (SUBIRANA et al., 2012).

This divergence between code and carrier-phase, caused by the doubling of the ionospheric delay, becomes more problematic in regions characterized by ionospheric irregularities or the occurrence of anomalous events. In this sense, the CCD monitor makes it possible to analyze the rate of change of this divergence to detect ionospheric gradients that could compromise the integrity of the GBAS. The CCD monitor is based on a low-pass filter that checks the rate of change of the divergence of the CMC (JIANG et al., 2017; PULLEN et al., 2017):

$$dCMC_f^i(t) = \frac{(CMC(t) - CMC(t-1))}{\Delta t} = 2\dot{I}(t) + \dot{\varepsilon}(t)$$

$$F_1(t) = (1-\alpha) * F_1(t-1) + \alpha * dCMC_f^i(t)$$

$$F_2(t) = (1 - \alpha) * F_2(t - 1) + \alpha * F_1(t) \quad (32)$$

where: *F1* is the first smoothing filter for an epoch (*t*); *F2* is the second smoothing filter; and $\alpha = \frac{T}{\tau}$.

A CCD failure is indicated for a satellite whenever the magnitude of the slew rate exceeds 0.0415 m/s or if in more than 30 seconds these CCD slew rates cannot be calculated. The satellite is then excluded from the GAST D solution within two seconds of the onset of all of the following conditions being met simultaneously: a CCD failure condition exists; the time elapsed since take-off is greater than 5 minutes; the calculated ground speed is greater than 55.56 km/h and the calculated position is within the final approach region (PULLEN et al., 2017).

2.3. GAST F

GAST F is a category of precision approach service designed to meet CAT II and III requirements, with performance parameters similar to those of GAST D, as shown in Table 2. This service has not yet been standardized, and most of its definitions and implementations have been developed through research conducted by ICAO working groups and the European Union's SESAR Project (Single European Sky ATM Research) (ROTONDO, 2016).

The primary motivation for developing GAST F is the vulnerability of GAST D in maintaining performance parameters under anomalous ionospheric conditions. Since GAST D relies solely on single-frequency L1 GPS and GLONASS, it is susceptible to ionospheric gradients and scintillation effects. Consequently, one of the key advancements of GAST F is the incorporation of DFDC data, specifically the L1 and L5 signals from GPS and the E1 and E5a signals from Galileo (CAAMANO et al., 2016; FELUX et al., 2019; ROTONDO et al., 2015).

The use of dual-frequency GNSS data offers enhanced capabilities for mitigating systematic effects in GNSS signals, primarily through the application of linear combinations of observables, such as Ion-Free (IFree) and Divergence-Free (DFree) combinations. These techniques help mitigate first-order ionospheric effects (IF) and enable the estimation of multipath and noise by DFree combination (ROTONDO et al., 2015).

This new category of GBAS approach services also incorporates the transmission of GBAS messages via the VDB, accounting for the inclusion of new signals and satellite constellations. Table 5 provides an overview of the messages planned for each GBAS service.

Table 5 – Characterization of the services, messages and signals used in GBAS.

GAST	Signals used	Message Type GBAS
C	L1	1, 2 e 4
D	L1	1, 2, 4 e 11
F – Ifree	L1/L5 and E1/E5a	1, 2, 4, 11, 42 and 50
F - Single Frequency SF L1	L1/L5 and E1/E5a	1, 2, 4, 11, 42 and 50
X and E	L1/L5 and E1/E5a	1, 2, 4 and 11

Source: Adapted EUROCONTROL (2019)

It should be noted that MT42, which has similar parameters to MT1 (as shown in Table 5), was introduced in GAST F to accommodate message content derived from signals on the L5/E5a carrier-phase. Additionally, MT1 itself must be updated with additional blocks to include new parameters from Galileo satellites on the E1 carrier-phase.

Another message type added for GAST F is MT50 (Table 6). According to EUROCONTROL (2019) and Circiu (2020), this message type is being implemented to indicate the usability of differential corrections for the L5/E5a carrier-phase and corrections in the Ion-Free combination. This information will be transmitted in two blocks, each specifying the use of corrections for the GPS and Galileo constellations. Unlike other GBAS messages, MT50 requires less space in message slots and, as noted by Stanisak et al. (2015), is considered relevant for monitoring the integrity of the corrections, as it indicates whether they can be reliably used.

Table 6 – Message content planned for MT50.

Data Content	Definition and number of bits used
Number of supported constellations (=2)	Dual constelation (8 bits)
Content for 36 satellites of 1st constellation	
Usability of L5 correction	Indication for using L5 correction
Usability of IFree correction	Indication for using IFree correction
Content for 36 satellites of 2nd constellation	
Usability of L5 correction	Indication for using L5 correction
Usability of IFree correction	Indication for using IFree correction

Fonte: Adaptado de Stanisak et al. (2015)

According to Rotondo (2016), this introduction of new signals and more satellites will lead to changes in the structure of GBAS message transmission via the VDB antenna, in order to make it compatible with the addition of GBAS DFDC. The current VDB structure contains 8 compartments to house the already regulated GAST C and D approach services, as shown in Table 7.

Table 7 – Distribution of GBAS message transmission compartments by VDB antennas.

Slot	Message Types		GBAS Services
Slot A	MT2	MT4	GAST C
Slot B	MT1		GAST C
Slot C	MT11	MT4	GAST D
Slot D	MT1	MT11	GAST D
Slot E	MT1		GAST C
Slot F	MT11	MT4	GAST D
Slot G	MT1	MT11	GAST D
Slot H			Reserved for GAST MFMC

Source: Adapted from Felux et al. (2016).

Of the VDB's eight compartments (slots A to H), only slot H is completely empty and can be used for GBAS DFDC services which have not yet been regulated. However, as mentioned above, a greater amount of information must be included as a result of the corrections and parameters of MT42, and the updating of MT1 and MT11 which will add signals from other satellite constellations.

Thus, new configurations for transmitting messages are being developed to cover all GBAS DFDC precision approach services. In Stanisak et al. (2015) and Felux et al.

(2018) you can find proposals for transmitting signals that will include GBAS DFDC services in the future.

2.3.1. GAST F Modes

As previously mentioned, in GAST F, the addition of GNSS signals and constellations enables the development of new GBAS mode based on the linear combination of observations. Due to their robustness, these modes can help mitigate ionospheric errors. Among the possible approaches are the GAST F Single Frequency (GAST F SF L1) and GAST F Ion-Free (GAST F IFree) modes, as shown in Table 3.

The GAST F SF L1 mode has been designed to combine Single Frequency L1 (GPS) and E1 (Galileo) observations. Its implementation follows a similar approach to GAST C, incorporating corrections and additional parameters derived from Galileo's E1 carrier-phase into the MT1 parameter set. Conversely, GAST F IFree is a mode intended to utilize dual-frequency (L1/E1 and L5/E5a) signals by combining GPS and Galileo constellations. According to Table 3, this service introduces new GBAS messages, such as MT42, which contains parameters for the L5/E5a signal (analogous to MT1). Another addition is MT50, which indicates the usability of the L5/E5a signals and the Ion-Free combination (Table 6).

The primary objective of using the Ion-Free combination is to mitigate first-order ionospheric errors and the de-correlation of these errors between reference stations and aircraft. This type of service requires modifications in observations and corrections, as described in Equations (33) and (34). At ground level, the generation of IFree corrections ($PRCIF^{i}_{L1,L5}$) is determined by differentiating the corrections in L1 and L5 signals (at ground domain).

$$PRCIF^{i}_{L1,L5}(t) = \frac{(f^2_{L1} PRC_{L1}(i,t) - f^2_{L5} PRC_{L5}(i,t))}{(f^2_{L1} - f^2_{L5})} \tag{33}$$

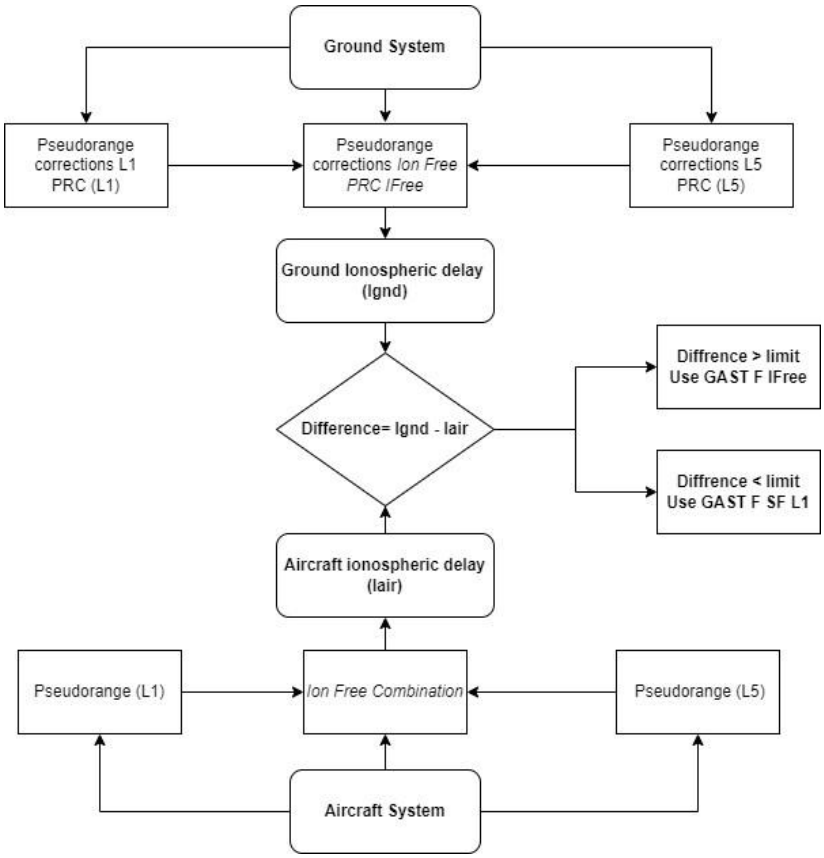
where: PRC_{L1} and PRC_{L5} are pseudorange corrections for L1 and L5 signals, f_{L1} and f_{L5} are respectively frequency used in the combination.

$$\widehat{PD}IF^{i}_{L1,L5}(t) = \frac{(f^2_{L1} \widehat{PD}_{L1}(i,t) - f^2_{L5} \widehat{PD}_{L5}(i,t))}{(f^2_{L1} - f^2_{L5})} \tag{34}$$

where: $\widehat{PD}_{L1}$ and $\widehat{PD}_{L5}$ correspond to the smoothed pseudorange at the respective frequencies (*f*) of the signals (L1 and L5) for each satellite *i*, at time *t*.

It can be seen in Equation (33) and (34), the IFree combination is calculated adding PRC (at ground system) and PD (at aircraft domain). According to EUROCONTROL (2019) this strategy can increase GBAS positions errors due the addition of another signal, caused by the introduction of unmodeled systematic errors from additional observations (in this case, L5 and E5a). Therefore, the choice for one of these two GAST F modes is based on monitoring the ionospheric delay of reference stations and the aircraft (Figure 7). This monitor will indicate the occurrence of ionospheric gradients, where use of the modes will depend on the difference in ionospheric delays. When the monitor threshold is exceeded, the use of IFree can be beneficial to remove the effects of ionospheric gradients at reference stations or on the aircraft. Otherwise, the use of L1 or L5 single-frequency data is more recommended to minimize positioning errors. Ionospheric delay monitoring will be covered in the next subsection.

Figure 7 – Ionospheric delay monitoring for GAST F.



Source: Adapted from EUROCONTROL (2019).

With the introduction of more constellations and signals, uncertainty models at ground and aircraft level have been developed to represent $\sigma_{pr_{gnd}}$ in a similar way to that presented in SubSection 2.1.1, for GAD and AAD. Thus, Gerbeth et al. (2022) present the model based on the elevation angle of GPS satellites L1 and L5, as well as for Galileo E1 and E5a, according to Table 8 for 100 s smoothing time constant.

Table 8 – Uncertainty Models dual-frequency dual constellation ($\sigma_{pr_{gnd}}$) associated with pseudorange from ground system GBAS for GPS and Galileo.

Models	**Equations**
GPS L1	$0{,}1148 * e^{-0{,}0104*\theta}$
Galileo E1	$0{,}1172 * e^{-0{,}01145*\theta}$

Source: Adapted from Gerbeth et al. (2022).

For position estimation using IF observable, a covariance propagation was applied for each constellation, according to Equations (35) and (36) for GPS and Galileo, respectively.

$$\sigma_{pr_{gnd\,IF\,(GPS)}}(i) = \sqrt{(1-\beta)^2 * \left(\sigma^2_{pr_{gnd\ (GPS\,L1)}}(i)\right)^2 + \beta^2 * \left(\sigma^2_{pr_{gnd\,(GPS\,L5)}}(i)\right)^2} \quad (35)$$

$$\sigma_{pr_{gnd\,IF\,(Galileo)}}(i) = \sqrt{(1-\beta)^2 * \left(\sigma^2_{pr_{gnd\ (Galileo\,E1)}}(i)\right)^2 + \beta^2 * \left(\sigma^2_{pr_{gnd\,(Galileo\,E5a)}}(i)\right)^2} \quad (36)$$

where $\beta = \frac{f^2_{L5/E5a}}{(f^2_{L1/E1} - f^2_{L5/E5a})}$.

In the aircraft domain, Gerbeth et al. (2022) shows the $\sigma_{pr_{air}}$ which corresponds to the contribution of PRC error for each satellite, similar to AAD, but including GPS L5, Galileo E1 and E5a, as well as IFree combination for GPS and Galileo.

Table 9 – Uncertainty Models dual-frequency dual constellation ($\sigma_{pr_{air}}$) associated with pseudorange from aircraft system GBAS for GPS and Galileo.

Models	Equations
GPS L1 100 s	$0{,}16 + 0{,}13 * e^{-\theta/30}$
Galileo E1 100 s	$0{,}14 + 0{,}07 * e^{-\theta/14{,}3}$
GPS L5/Galileo E5a 100 s	$0{,}13 + 0{,}06 * e^{-\theta/14{,}3}$
GPS IF 100 s	$0{,}25 + 0{,}35 * e^{-\theta/50}$
Galileo IF 100 s	$0{,}32 + 0{,}2 * e^{-\theta/50}$

Source: Adapted from Gerbeth et al. (2022).

2.3.2. Dual Frequency Ionospheric Delay Monitoring for GAST F

In GAST F, ionospheric gradient monitoring using dual-frequency GNSS data, it is the sole responsibility of the aircraft's system to identify anomalous ionospheric conditions related to the gradient. The method proposed by Felux et al. (2017a) and improved in Felux et al. (2019) named Iono Test, presents a monitoring ionospheric conditions based on a test statistic (I_{test}) that adds the aircraft's ionospheric delay (I_{air}) to the pseudorange corrections delay (I_{PRC}) (Equation (37)).

$$I_{test} = |I_{air} + I_{PRC}| \tag{37}$$

The ionospheric delay is obtained by combining the L1 and L5 frequencies. In the case of I_{air}, at frequency L1, it is calculated by the difference in pseudorange smoothed at each of the frequencies, according to Equation (38).

$$\tilde{I}_{air,i} = \frac{f_{L5}^2}{f_{L1}^2 - f_{L5}^2} \left(\hat{\rho}_{L5,i} - \hat{\rho}_{L1,i}\right). \tag{38}$$

The ionospheric delay referring to the ground subsystem is obtained as a function of the difference in the pseudorange corrections at each frequency, the rate of pseudorange correction (RRC) multiplied by the time difference between the current measurement time and the generation time of the corrections Δt, shown in Equation (39):

$$\tilde{I}_{PRC,i} = \frac{f_{L5}^2}{f_{L1}^2 - f_{L5}^2} \left[\left(PRC_{L5,i} + \Delta t * RRC_{L5,i}\right) - \left(PRC_{L1,i} + \Delta t * RRC_{L1,i}\right)\right]. \tag{39}$$

In the next step, the average of all N ionospheric delay estimated per constellation is removed to obtain a measure of ionospheric delay, as per Equations (40) and (41), which must be for the same set of satellites (FELUX et al., 2017a).

$$I_{air,i} = \tilde{I}_{air,i} - \frac{1}{N}\sum_{i=1}^{N} \tilde{I}_{air,i} \quad (40)$$

$$I_{PRC,i} = \tilde{I}_{PRC,i} - \frac{1}{N}\sum_{i=1}^{N} \tilde{I}_{PRC,i} \quad (41)$$

The strategy for defining tolerance limits for the ionospheric gradient monitoring method proposed by Felux et al. (2017a) is based on the position domain, where the probability is 10^{-9} for the detection of satellite fault by the monitor, if noise and random errors, which have normal distribution, are given by Equation (42):

$$I_{test,i} \leq \frac{E_{v,iono}}{|s_{vert,i}|} - 6.1 * \sigma_{monitor,i}, \quad (42)$$

where $E_{v,iono}$ is the position error in the vertical direction, associated with the ionosphere and consists of the projection of the error along track (E_{atrack}) to the vertical component, given that there is a difference to the point predicted for aircraft landing. This projection is performed by the geometric relationship in Equation (43), using the Glide Path Angle (GPA):

$$E_{atrack} = \frac{E_v}{\tan(GPA)}. \quad (43)$$

The $s_{vert,i}$ (Equation 38) corresponds to the contribution of a satellite in the calculation of the vertical position determined by the projection matrix, presented in subsection 2.1.1, with indices 1 and 3 indicating positions occupied in the first and third row of matrix S.

The $\sigma_{monitor,i}$ is composed of the uncertainties associated with noise arising from the ground (σ_{gnd}) and air (σ_{air}) systems at the respective frequencies L1 and L5, according to Equation (44):

$$\sigma_{monitor,i} = \frac{f_{L5}^2}{f_{L1}^2 + f_{L5}^2}\sqrt{\left(\sigma_{gnd,L1}^2(i) + \sigma_{air,L1}^2(i) + \sigma_{gnd,L5}^2(i) + \sigma_{air,L5}^2(i)\right)}. \quad (44)$$

2.3.3 GNSS Multipath Estimate for GBAS Dual Frequency

In the GAST C and D uncorrelated errors like the receiver noise and multipath are included in the mathematical model by the uncertainty based on the satellite's elevation. These errors are mitigated by the GAD (ground system) e AAD (airborne system) that consider only GPS constellation.

In a GBAS DFDC, one of the possibilities would be to estimate multipath by linearly combining dual-frequency observations. For GAST F, according to Rotondo et al. (2015), the contribution of receiver noise and multipath can be estimated by the CMC differentiation resulting from the DFree combination in Equations (45) and (46).

$$\Phi_{DFree} = \Phi_{L1} - \frac{2}{\alpha}(\varphi_{L1} - \varphi_{L5}), \tag{45}$$

$$PD_{DFree} = PD_{L1}. \tag{46}$$

When performing the CMC_{DFree} (Equation (47)) almost all systematic effects are removed and the result of this operation has mainly the multipath errors and receiver noise for a satellite *i*, visible at station *j* at time *t*.

$$CMC_{DFree} = PD_{L1} - \varphi_{DFree}$$

$$CMC_{DFree}(i,j,t) = PD_{L1} - \Big(-I_{L1}+N_{L1}+\varepsilon_{\varphi,L1} - \frac{2}{\alpha}\big[-(I_{L1} - I_{L5}) + (N_{L1} - N_{L5}) + \big(\varepsilon_{\varphi,L1} - \varepsilon_{\varphi,L5}\big)\big]\Big), \tag{47}$$

where: $\alpha = (1 - \frac{f_{L1}^2}{f_{L5}^2})$, where *f* equals the respective frequencies used; ε corresponds to noise and uncorrelated errors (multipath, for example). The ionospheric delay is eliminated using the following relationship:

$$I_{L1} = \frac{I}{f_{L1}^2} \;;\; I_{L5} = \frac{I}{f_{L5}^2}$$

$$I_{L1} - I_{L5} = \left(1 - \frac{f_{L5}^2}{f_{L5}^2}\right) I_{L1} = \alpha\, I_{L1}$$

$$-\frac{2}{\alpha}\big(-(I_{L1} - I_{L5})\big) = -\frac{2}{\alpha}(-\alpha\, I_{L1}) = 2I_{L1}. \tag{48}$$

Substituting the relationship in Equation (48) into Equation (47) gives an expression for the $CMC_{DFree}$where the effects of the ionosphere are eliminated and, as long as there is no cycle slip, the ambiguity N is constant over time, so that the CMC_{DFree} is reduced to multipath and noise from the pseudorange and carrier-phase.

$$CMC_{DFree}(i,j,t) = PD_{L1} - \Big(-I_{L1}+N_{L1}+\varepsilon_{\varphi,L1} + 2I_{L1} - \frac{2}{\alpha}(N_{L1} - N_{L5}) - \frac{2}{\alpha}(\varepsilon_{\varphi,L1} - \varepsilon_{\varphi,L5})\Big),$$

$$CMC_{DFree} = \big(I_{L1} + \varepsilon_{PD,L1,}\big) - I_{L1} - \varepsilon_{\varphi,L1} + \frac{2}{\alpha}\big(\varepsilon_{\varphi,L1} - \varepsilon_{\varphi,L5}\big),$$

$$CMC_{DFree} = \varepsilon_{PD,L1} - \varepsilon_{\varphi,L1} + \frac{2}{\alpha}\big(\varepsilon_{\varphi,L1} - \varepsilon_{\varphi,L5}\big). \quad (49)$$

The values calculated in Equation (47) represent the raw multipath and noise. The remaining biases, assumed to be constant, are eliminated by applying a moving average over a fixed number of epochs. Thus, multipath and noise for L1 and L5/E5a denoted $CMC_{DFree}(L1)$ and $CMC_{DFree}(L5)$, respectively are obtained:

$$CMC_{DFree}(L1) = \Big[\rho_1 - \varphi_1 + \frac{2}{\alpha}(\varphi_1 - \varphi_5)\Big] - mov_mean(CMC_{DFree}(L1)) \quad (50)$$

$$CMC_{DFree}(L5) = \Big[\rho_5 - \varphi_5 + \frac{2}{\beta}(\varphi_5 - \varphi_1)\Big] - mov_mean(CMC_{DFree}(L5)) \quad (51)$$

where: $\alpha = 1 - \frac{f_1^2}{f_5^2}$, and $\beta = 1 - \frac{f_5^2}{f_1^2}$.

Circiu et al. (2014) and Rotondo et al. (2015) assert that this method of determining multipath and noise can be compared to the traditional method based on pseudorange and carrier-phase measurements (Equations (52 and 53)):

$$MP1_{L1} = \Big[\rho_1 - \Big(1 + \frac{2}{\alpha-1}\Big)\cdot\varphi_1 + \Big(\frac{2}{\alpha-1}\Big)\cdot\varphi_5\Big] - mov_mean(MP1_{L1}) \quad (52)$$

$$MP5_{L5} = \Big[\rho_5 - \Big(1 + \frac{2}{\beta-1}\Big)\cdot\varphi_5 + \Big(\frac{2}{\beta-1}\Big)\cdot\varphi_1\Big] - mov_mean(MP_{L5}) \quad (53)$$

2.3.4 Cycle Slip Monitor for Dual Frequency

Cycle slip can be defined as a discontinuity that occurs in measurements of the carrier-phase. This measurement is the result of the cycle count resulting from the difference between the phase of the carrier received from the satellite and its replica generated in the receiver. At the start of tracking, the fractional part of this counter is known, while the whole number of cycles, called the ambiguity, is unknown. Over time, this counter is incremented by one whole cycle each time the beat phase changes from 2π

to 0. If there are no interruptions in this cycle count, the whole number remains constant from a certain period (SEEBER, 2003; MONICO, 2008).

However, this entire cycle counter is reset when satellite signals are lost or degraded due to obstruction, multipath, low signal strength from satellites with low elevation angles, ionospheric scintillation, sudden antenna variations in kinematic applications such as aviation or ships (SEEBER, 2003). Cycle slip can cause jumps between two epochs or last up to thousands of epochs, which is detrimental to GNSS positioning as this reset can degrade the accuracy of the estimated coordinates.

Signal propagation through the ionosphere is another source that can cause cycle slip. Variations in the number of electrons present in the ionosphere can affect the intensity of GNSS satellite signals and lead to cycle losses. This can occur more frequently in equatorial and low latitude regions, where events such as ionospheric scintillation can lead to greater variability in the ionosphere and be detrimental to GNSS positioning (SEEBER, 2003).

One of the classical methods for detecting cycle slips in GNSS observations was developed by Blewitt (1990) and is known as TurboEdit. This algorithm detects and repairs the occurrence of cycle loss, as well as removing outliers from GNSS measurements. Initially developed for dual-frequency GPS data (L1 and L2), the algorithm does not differentiate and can be adapted for other frequencies as improved by Xu et al. (2020), who adapted it for L1 and L5 frequencies. TurboEdit is based on Melbourne-Wübbena (MW) and Geometry Free linear combinations.

$$\varphi_{MW}(i,t) = \frac{(f_{L1}\varphi_{L1} - f_{L5}\varphi_{L5})}{f_{L1} - f_{L5}} - \frac{(f_{L1}PD_{L1} - f_{L5}PD_{L5})}{f_{L1} - f_{L5}} = \lambda_{WL}N_{WL}, \tag{54}$$

$$\varphi_{GF}(i,t) = \varphi_{L1} - \varphi_{L5} = \lambda_{L1}N_{L1} - \lambda_{L5}N_{L5} + \frac{(f_{L1}^2 - f_{L5}^2)}{f_{L5}^2} I, \tag{55}$$

where: φ_{MW} e φ_{GF} are the linear combinations Melbourne-Wubbena and Geometry Free; φ_{L1} and φ_{L5} are respectively carrier-phase (*f*) L1 and L5; PD_{L1} and PD_{L5} are pseudorange smoothed in L1 and L5; $\lambda_{WL} = c/(f_{L1} - f_{L5})$ corresponds to the wide-lane wavelength; $N_{WL} = N_{L1} - N_{L5}$ is the term that represents wide-lane ambiguity.

The carrier-phase remains stable as long as no cycle slip events occur. To detect them, a moving average filter is used recursively, using the linear combinations Melbourne-Wubbena and Geometry Free and their uncertainty as shown in Equations

(56) and (57). According to Blewitt (1990), the filter's average threshold for indicating a cycle slip is 0.5 cycles.

$$E[N_{WL}(i,t)] = \overline{N_{WL}}(i,t) = \overline{N_{WL}}(i,t-1) + \frac{1}{t}[N_{WL}(i,t) - \overline{N_{WL}}(i,t-1)], \quad (56)$$

$$\sigma^2_{N_{WL}}(i,t) = \sigma^2_{N_{WL}}(i,t-1) + \frac{1}{t}\left[(N_{WL}(i,t) - \overline{N_{WL}}(i,t-1)\right)^2 - \sigma^2_{N_{WL}}(i,t-1)]. \quad (57)$$

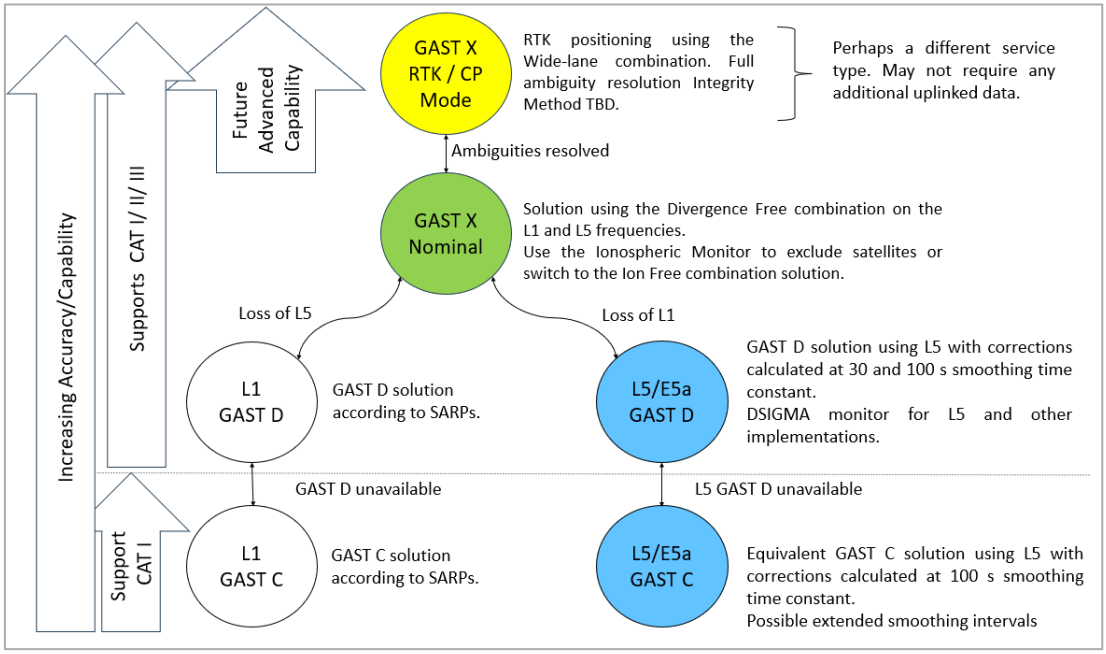
This cycle slip monitor (TurboEdit), described in this section, is one of the classics in the literature, and it is possible to find several works that have made improvements to this algorithm, such as Xu et al. (2020) and Wang and Huang (2023), which show the possibility of not only detecting but also repairing cycle slips. However, as this work will not explore cycle slip correction, this approach will not be demonstrated in depth. More details can be found in the cited references.

2.4 State of the Art: from GAST X to GAST E

A precision approach service proposal, termed GAST X, was developed by Murphy et al. (2021). This GBAS concept is based on the use of GNSS MFMC (Multi Frequency Multi Constellation) data and can be considered an extension of the already regulated GAST C and D services. In its design, GAST X shifts a significant portion of GBAS functionalities to the aircraft subsystem, primarily for monitoring ionospheric effects.

The proposed GAST X model is robust and supports multiple precision approach services, including GAST C, D, and X (Nominal). Figure 8 illustrates the GAST X model developed by Murphy et al. (2021).

Figure 8 – Proposed architecture for GAST X approach service.



Source: Adapted from Murphy et al. (2021).

GAST X has been designed to support CAT II and III precision approaches and can operate in two modes: Nominal and RTK. The GAST X Nominal mode utilizes smoothed pseudoranges obtained through the DFree and Ion-Free linear combinations. According to Murphy et al. (2021), applying the DFree combination to smooth pseudoranges helps minimize systematic effects such as multipath, particularly when a longer smoothing time constant, such as 600 seconds, is used.

Additionally, ionospheric gradient-induced errors can be mitigated by estimating ionospheric delays at both the aircraft and reference stations. If the observed gradient for any satellite exceeds an appropriate ionospheric gradient monitor threshold, the aircraft subsystem can either exclude the satellite from the GBAS differential position solution or switch from using DFree-smoothed pseudorange to Ion-Free smoothed pseudorange for positioning. This approach effectively eliminates the impact of ionospheric gradients, potentially allowing more flexibility in the placement of reference receivers.

Murphy et al. (2021) also introduced the GAST X RTK concept, which employs carrier-phase measurements with the potential for ambiguity resolution. This concept offers centimeter-level positioning accuracy but remains under investigation, primarily due to the challenges associated with real-time ambiguity resolution.

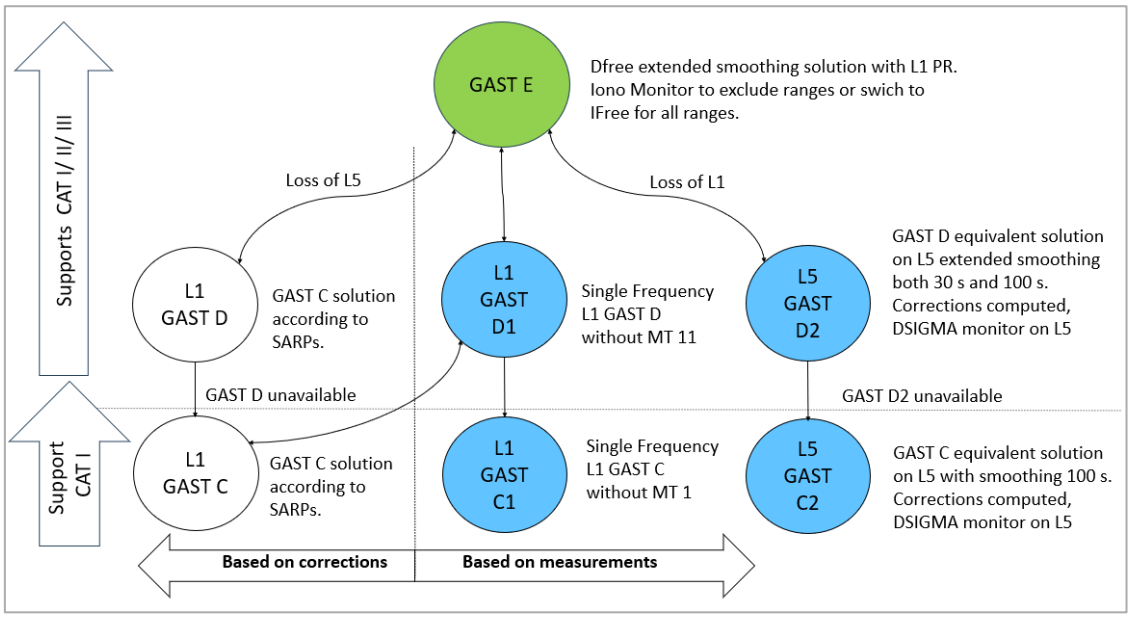
If neither the RTK nor Nominal modes are available, the already regulated GAST C and D services, as specified in SARPs, are activated (as detailed in subsections 2.1 and 2.3). With the inclusion of the L5/E5a carrier-phase, new approach services equivalent to conventional ones have been developed for GAST C and D, utilizing only the L5/E5a carrier-phase while maintaining key configurations. For instance, GAST C continues to apply pseudorange smoothing using the Hatch Filter with a 100-second constant, whereas GAST D performs smoothing with 30- and 100-second constants and includes DSIGMA monitoring. Further details on the implementation of GAST X can be found in Murphy et al. (2021).

It is important to note that, within the scope of the INCT GNSS-NavAer Project, GAST X was also investigated based on the propositions by Murphy et al. (2021) through a postdoctoral study. Some of the findings from this research were presented by Silva et al. (2022) and Silva et al. (2023), indicating that GAST X did not meet the performance requirements for precision approach categories. This conclusion was drawn from an experiment conducted in Presidente Prudente using stations from the INCT GNSS-NavAer Network later referred to as the GBAS UNESP Experimental.

However, in 2023, the proposal for GAST X was revised by the ICAO Navigation Systems Panel (NSP) GBAS Working Group, which has been discussing an operational concept for dual-frequency and multi-constellation (DFMC) GBAS. In this revision, the architecture was modified and renamed as GAST E, incorporating features from both GAST F and GAST X (Murphy et al., 2023). The GAST E architecture proposes the use of GNSS (DFMC) data, raw pseudorange and carrier-phase measurements, eliminating the need for differential corrections present in GAST C and D. Additionally, it preferentially employs the smoothed observable derived from the Divergence-Free linear combination, with a long smoothing time constant ranging f 300 to 600 seconds.

This new DFMC GBAS architecture introduces five new service types: GAST E, the primary (preferred) DFMC mode, and GAST C1, D1, C2, and D2, which are activated as fallback options if GAST E becomes unavailable. It also specifies performance requirements for the L1 and L5 carrier-phases. According to Murphy et al. (2023), the activation of these new services will be facilitated by a new type of GBAS message, MT 23, which will provide interoperability, integrity, and safety information, enabling the appropriate service type to be used for precision approaches.

Figure 9 – Proposed architecture for GAST E approach service.



Source: Adapted from Murphy et al., 2023.

As shown in Figure 9, the legacy GBAS services, GAST C and GAST D, will remain active if the new DFMC services are unavailable. GAST C and D will continue to rely on single-frequency differential corrections, while the new GBAS DFMC services utilize raw GNSS measurements. Further details on this new GBAS DFMC architecture can be found in Murphy et al. (2023).

3. IONOSPHERIC EFFECTS ON GBAS

The ionosphere is the region of the upper atmosphere extending between 50 and 1000 km, characterized by a high concentration of ions and electrons. These charged particles influence the propagation of electromagnetic waves, including signals transmitted by GNSS satellites. The ionospheric effect responsible for signal delay depends on both the frequency of these signals and the Total Electron Content (TEC), which quantifies the number of electrons per square meter. TEC can be measured in the vertical direction (Vertical TEC - VTEC) or along the inclined satellite-receiver path (Slant TEC - STEC) (SAITO and YOSHIHARA, 2017).

Ionospheric delay can introduce errors of up to several ten meters in GNSS-based positioning, particularly in real-time applications. In post-processing methods, the use of

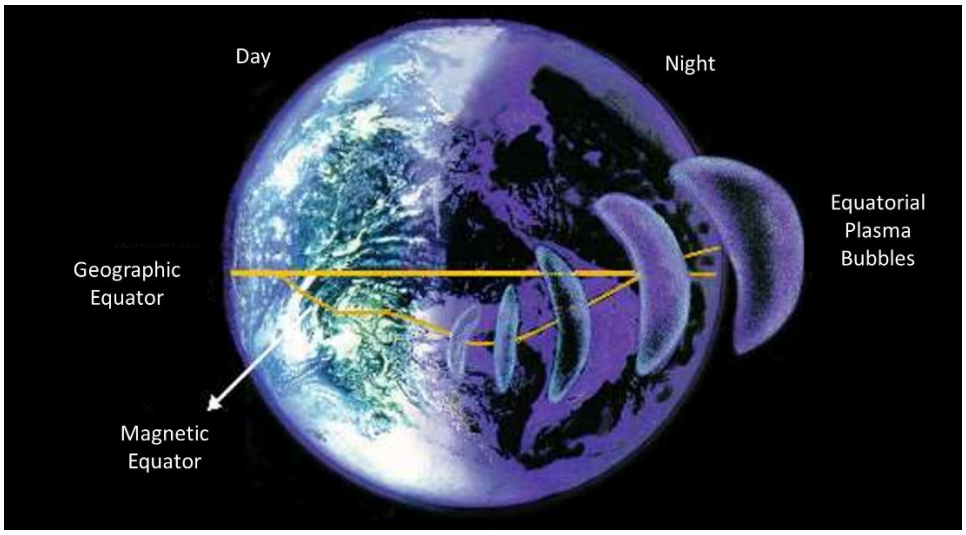
multi-frequency GNSS receivers enables TEC estimation, although an important contribution can be found in Christovam et al. (2023) on the possibility of estimating TEC using single frequency. Furthermore, linear combinations of GNSS signals can mitigate various systematic effects. For instance, the Ionospheric-Free combination, which utilizes dual-frequency GNSS data, can eliminate approximately 99% of first-order ionospheric errors (MONICO, 2008).

In aviation, so far, real-time positioning obtained via GBAS relies solely on single-frequency (L1) GPS or GLONASS signals (ICAO, 2018). This limitation makes positioning more susceptible to ionospheric effects, especially in low-latitude regions, where ionospheric irregularities occur more frequently (PEREIRA and CAMARGO, 2017).

According to Li et al. (2021), ionospheric irregularities are disturbances in plasma density that arise due to various factors, including equatorial plasma drift, peak height and electron density variations in the ionospheric layer, solar cycle fluctuations, neutral winds, seasonal variations, local time, magnetic declination, the equatorial ionization anomaly, and geomagnetic storms.

A significant ionospheric irregularity is due to the Equatorial Plasma Bubble (EPB), which results from a localized reduction in ionospheric plasma density relative to its surroundings (Figure 10). EPBs commonly occur around sunset, initiated by a mechanism known as the Rayleigh-Taylor Instability (LI et al., 2021). During nighttime, electron recombination begins, leading to two plasma diffusion conditions: in the first, plasma moves downward due to cooling, while in the second, it is uplifted by an eastward-directed electric field. As a result, bubble-like structures are formed, where lower-density plasma rises along magnetic field lines (TAKAHASHI et al., 2018; LI et al., 2021).

Figure 10 – Representation of the occurrence of Equatorial Plasma Bubbles.



Source: Adapted from Takahashi et al. (2009).

According to Li et al. (2021), EPBs can cause another phenomenon called ionospheric scintillation, which are rapid fluctuations in the amplitude and phase of satellite signals that cross the ionosphere. According to Moraes et al. (2014) and Moraes et al (2018), scintillation is a phenomenon that usually occurs at night, after sunset. Depending on spatial and temporal distribution, it can represent a problem that impacts on the accuracy and availability of GNSS users, due to various errors such as fading of signal power under scintillation conditions leading to cycle slip and loss of lock.

Ionospheric scintillation can be measured by the S_4 and σ_φ (*Sigma Phi*) indices, which determine the intensity of this phenomenon (MUELLA et al. 2009; PEREIRA and CAMARGO, 2016). S_4 is a dimensionless index used to measure amplitude scintillation. It is calculated as the normalized standard deviation of the signal intensity (SI) in GNSS observations, with trends removed. This signal is generally sampled at a frequency of 50 Hz over an interval of 60 seconds.

The σ_φ consists of the phase scintillation (in radians), measured by the standard deviation of the GNSS signals (σ_e), free trends. Equations (58) and (59) show the S_4 e σ_φ calcs, respectively:

$$S_4 = \sqrt{\frac{\langle SI^2 \rangle - \langle SI \rangle^2}{\langle SI \rangle^2}} \tag{58}$$

$$\sigma_\varphi = \sqrt{\langle \sigma_e^2 \rangle - \langle \sigma_e \rangle^2} \tag{59}$$

Table 10 presents the categories to qualify an ionospheric scintillation based on the S_4 values according to Muella et al. (2009).

Table 10 – Classification of the amplitude scintillation event according to S4 index.

Scintillation	S_4 **(dimensionless)**
Weak	$0,2 < S_4 \leq 0,4$
Moderate	$0,4 < S_4 \leq 0,6$
Strong	$0,6 < S_4 \leq 1,0$
Saturated	$1,0 < S_4 \leq 1,4$

Source: Muella et al. (2009)

The σ_φ scintillation magnitude classification can be expressed in Table 11 according to Hegarty et al. (2001) *apud* Pereira and Camargo (2016).

Table 11 – Ionospheric scintillation classification according to Sigma phi (σ_φ).

Scintillation	σ_φ **(radians)**
Very weak	$0,05 < \sigma_\varphi \leq 0,2$
Weak	$0,2 < \sigma_\varphi \leq 0,3$
Moderate	$0,3 < \sigma_\varphi \leq 0,6$
Strong	$\sigma_\varphi > 0,6$

Source: Pereira and Camargo (2016).

Another effect caused by the ionosphere is the fanding, or variations in GNSS signal strength. Moraes et al. (2018) shows in a study carried out on the crest region of the Equatorial Ionization Anomaly (EIA) that the L2C and L5 signals are more susceptible to the effects of ionospheric irregularities. In this source also showed that the probability of the L1 carrier-phase signal, recorded by receivers in Presidente Prudente – SP (Brazil), being affected by moderate to strong scintillation events was approximately 12 per cent. In the case of the L2C and L5 signals, the probability increases to around 17 per cent.

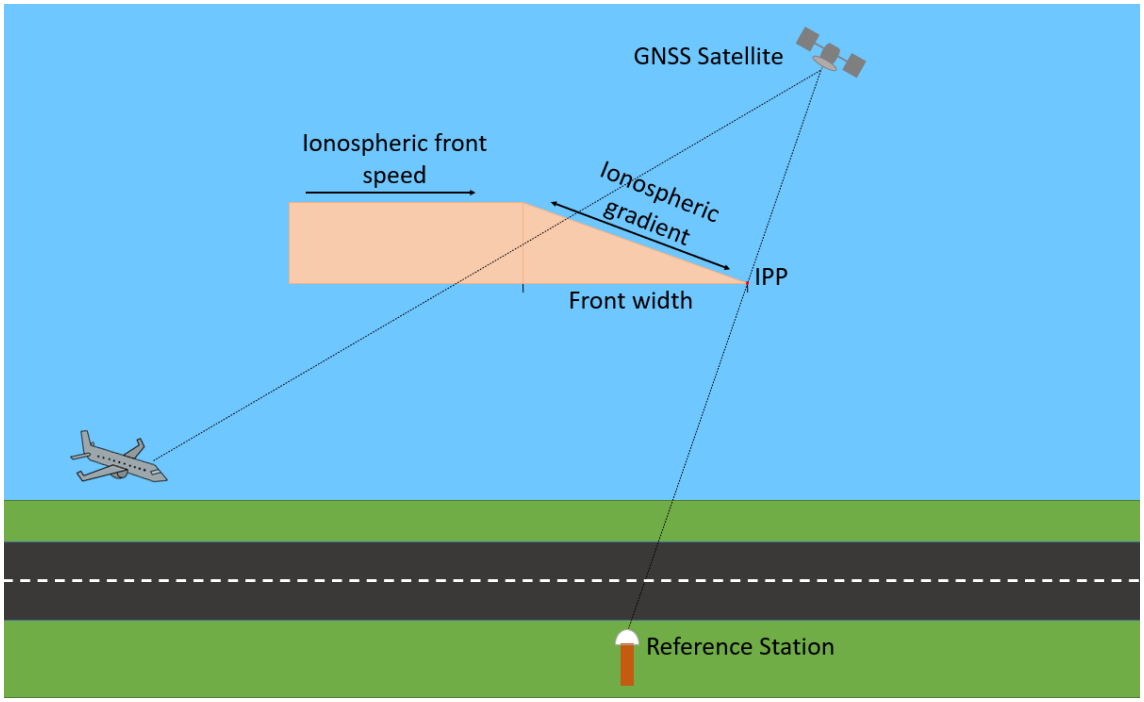
3.1 Ionospheric Gradient

Since GBAS is based on differential positioning, it assumes spatial and temporal correlation of ionospheric delay within its coverage area, which extends approximately 23 nautical miles (NM) or 42 km around the airport. However, this correlation is significantly affected in regions near the geomagnetic equator, as well as high latitudes, where higher electron densities in the ionosphere and frequent occurrences of irregularities, geomagnetic storms, EPBs and scintillation are observed (SAITO and YOSHIHARA, 2018).

In GBAS, when the ionosphere is not homogeneous, the ionospheric delay experienced by the aircraft may differ from that estimated by the reference stations. Consequently, the differential positioning mathematical model may fail to adequately correct for ionospheric delay, leading to positioning errors (SAITO et al., 2017). To mitigate this issue, the correlation between spatial and temporal ionospheric delay gradients must be well understood within the airport region. This requires time-series analysis of GNSS data to characterize ionospheric variability at the location, particularly during periods of high solar activity when major disturbances are more likely to occur. Additionally, if scintillation leads to cycle slips, the pseudorange smoothing process must be restarted, rendering the affected satellite unavailable until the process is completed.

According to Pereira et al. (2017) and Marini-Pereira et al. (2021), determining the ionospheric gradient is an essential part of studying the ionospheric threat model, which analyzes ionospheric variability within the GBAS coverage area. In this model, ionospheric irregularities are represented as a propagating front (Figure 11) characterized by a defined length, width, and velocity, which can cause delay variations even over short distances.

Figure 11 – Representation of an ionospheric front that can generate ionospheric delay decorrelation.

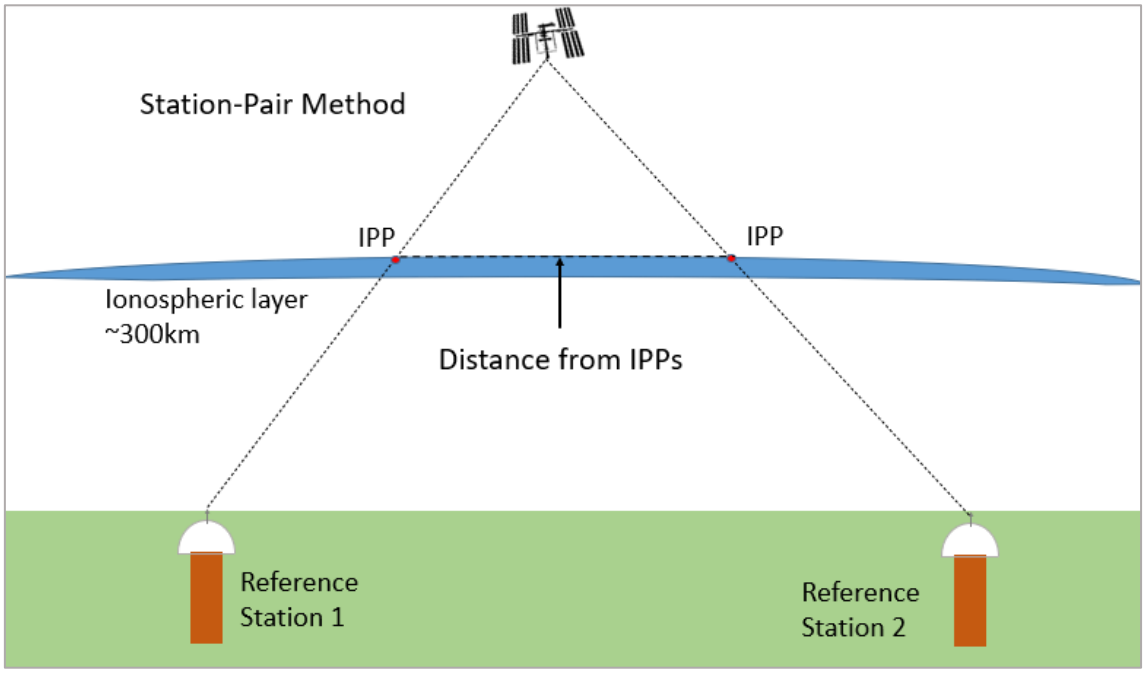


Source: Silva and Monico (2022).

Station Pair and Time-Step methods can be used to determine ionospheric gradients (LEE et al., 2007). The Station Pair method (Figure 12) determines the variation in ionospheric delay (in mm/km) between two reference stations tracking the same satellite at the same time. The ionospheric delays are calculated at the Ionospheric Pierce Point (IPP) for each of the two stations. The IPP is the point where GNSS signals intercept the ionosphere layer at an altitude of approximately 300 kilometers. The ionospheric gradient ($\nabla_{sp}(i)$) is estimated by dividing the difference in ionospheric delay at each station ($I_{r1}(i), I_{r2}(i)$), by the distance between the IPPs ($D_{IPP(r1r2)}$), as shown in Equation (60).

$$\nabla_{sp}(i) = \frac{I_{r1}(i) - I_{r2}(i)}{D_{IPP(r1r2)}} \tag{60}$$

Figure 12 – Representation of the Station Pair Method for determining the ionospheric gradient.

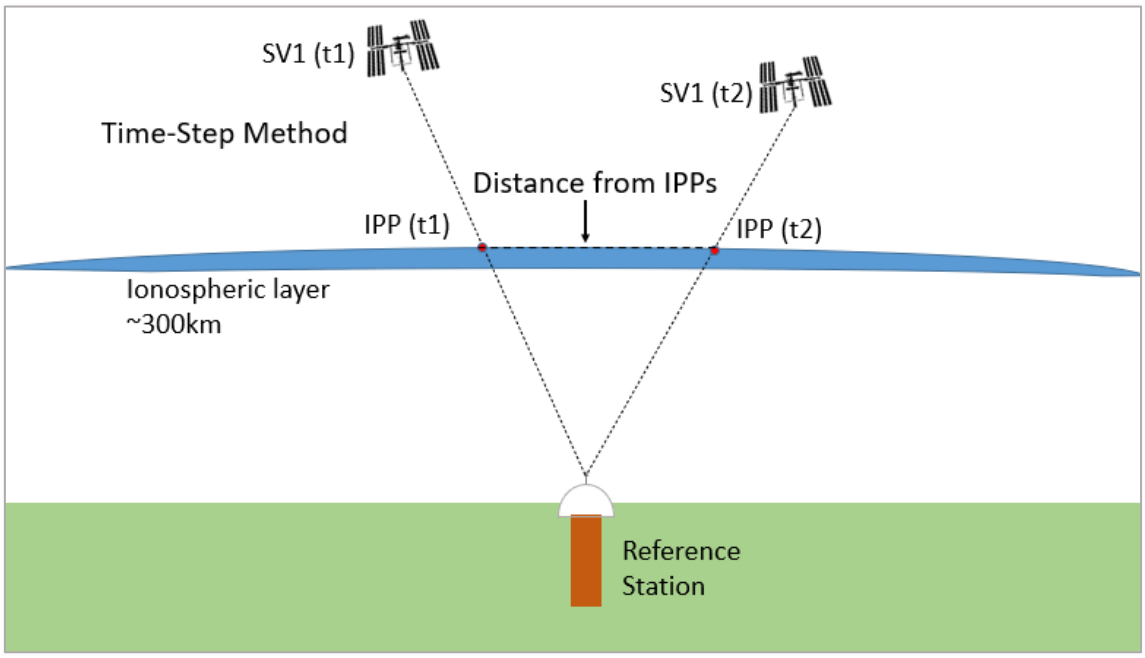


Source: Adapted from Pereira et al. (2017).

The Time-Step method (Figure 13) determines the ionospheric gradient ($\nabla_{ts}(i)$) with just one reference station, by dividing the difference in ionospheric delay at times *t1* e *t2* ($I_{t1}(i)$, $I_{t2}(i)$) by the distance between the IPPs at each time ($D_{IPP(t1t2)}$). Lee et al. (2007) states that a time difference (*t1* - *t2*) of 30 s can result in a distance between IPPs of approximately 10 km, depending on the elevation angle. This distance is less than the radius of the GBAS coverage area.

$$\nabla_{ts}(i) = \frac{I_{t1}(i) - I_{t2}(i)}{D_{IPP(t1t2)}} \quad (61)$$

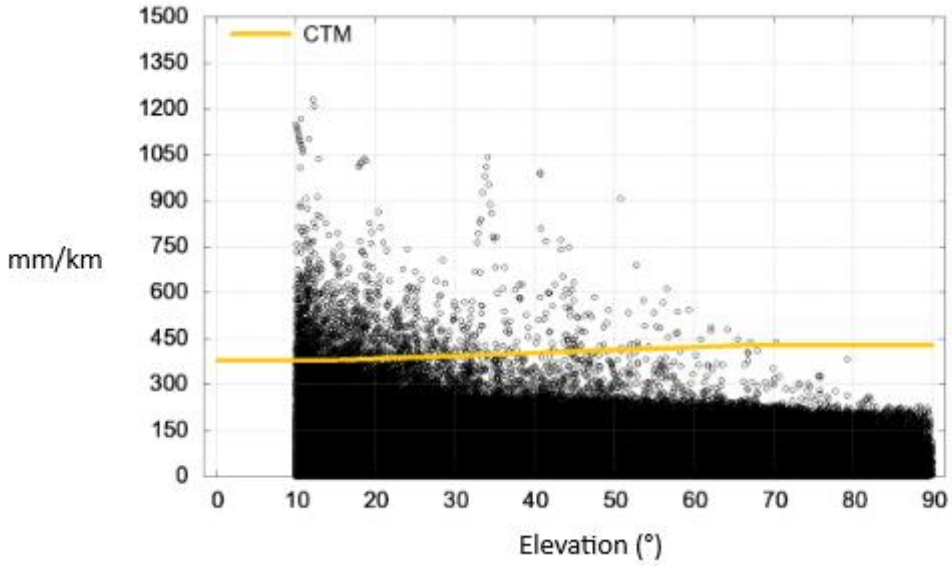
Figure 13 – Representation of the Time-Step Method for determining the ionospheric gradient.



Source: Adapted from Pereira et al. (2017).

These methodologies for determining ionospheric gradients can be found in the literature that contextualizes the reality of low latitudes in Brazil. Pereira (2018) presents a study for an ionospheric threat model for Brazil, comparing the ionospheric gradient values from this study with the CONteminous United States (CONUS) (Figura 14). It is noted that the ionospheric gradient values reach 1200 mm/km, exceeding the CONUS model (which has a limit of 375 to 425 mm/km).These large ionospheric gradients were also observed in other works such as Yoon et al. (2017); Marini-Pereira et al. (2021); and Marini-Pereira et al. (2023) indicating the susceptibility of the Brazilian territory to the effects of the ionosphere.

Figure 14 – Estimated ionospheric gradients for Brazil in the ionospheric threat model study.



Source: Adapted from Pereira (2018).

It is important to note that, as discussed above, more recent GBAS architectures have adopted alternative metrics to assess the impact of ionospheric gradients, such as the Test statistic presented in Section 2.4, as well as the CCD Monitor.

4. GBAS UNESP EXPERIMENTAL

The GBAS UNESP Experimental project comprises a network of GNSS stations from the INCT GNSS-NavAer Network, designed to evaluate and simulate various implementations of GBAS DFDC. Although it is not deployed as normally a GBAS system looks like, it is expected to provide opportunities for a variety of studies, not only for the INCT researchers, but also for the community involved in studies similar to this one.

The experiment was designed based on the concept that stations representing both ground and aircraft systems (in static mode) can be utilized to monitor GBAS performance. A monitoring system of this nature has the capability to detect unfavorable conditions before an aircraft approaches the airport, suggest routes that are less affected by ionospheric gradients, identify satellites most impacted by systematic effects, and select the most appropriate GAST category for precision approach operations.

The architecture deployed at Presidente Prudente consists of four stations representing the ground system: PRU2, PRU4, DMC1, and MOR3. Additionally, two other stations, STPZ and STAV, are used to simulate aircraft in static mode or as monitoring stations. Figure 15 illustrates the locations of these stations in Presidente Prudente (Sao Paulo, Brazil), while Table 12 provides the coordinates of each station, in SIRGAS2000 (from October 10, 2024). The STPZ and STAV stations are positioned 13 km and 9.8 km, respectively, from the designated landing point, representing two approach routes in this experiment.

Figure 15 – GNSS stations comprising the GBAS UNESP Experimental project.

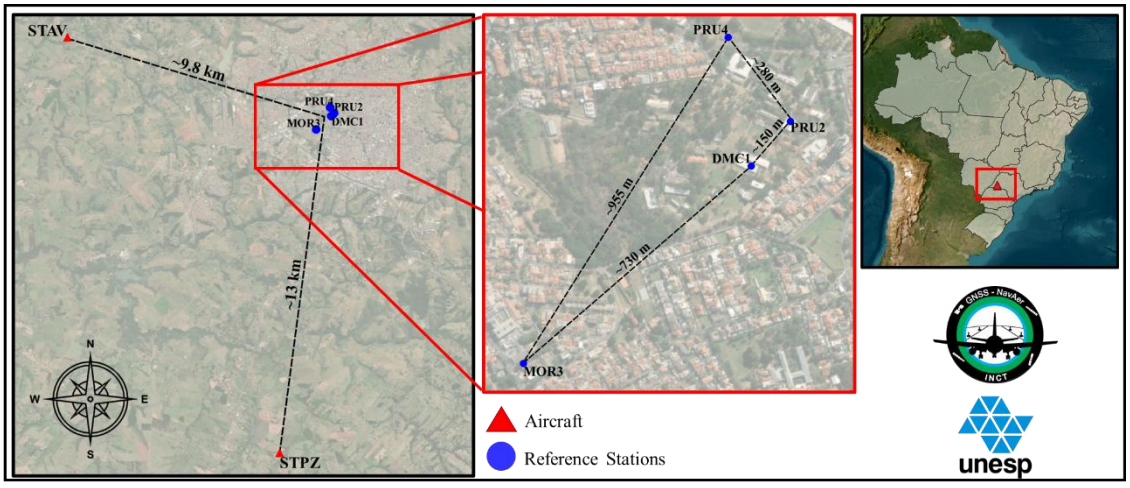


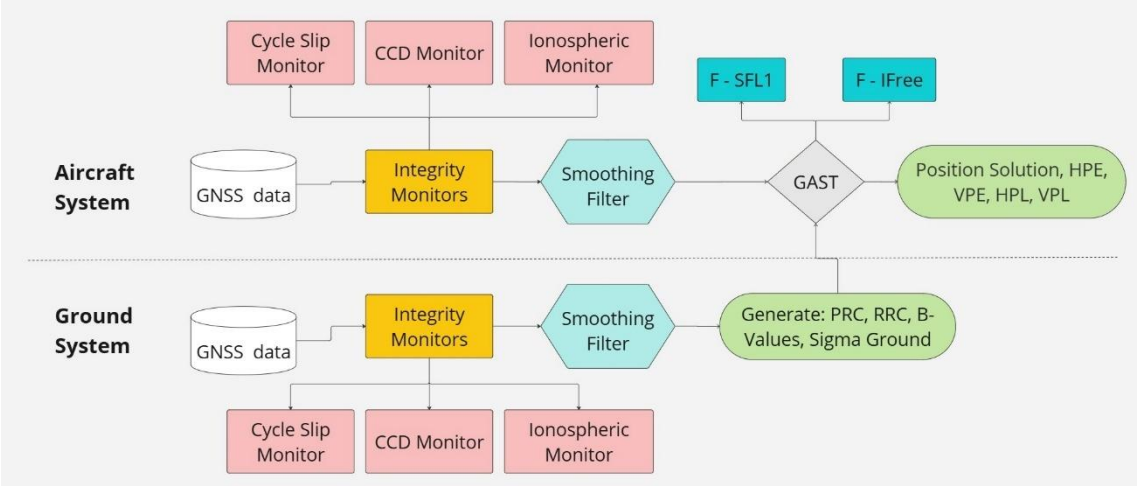
Table 12 – Coordinate of the stations that compose the GBAS UNESP Experimental.

Station	Latitude (°)	Longitude (°)	Altitude (m)
PRU2	-22° 07’ 19,3323”	-51° 24’ 25,4861”	441.820
PRU4	-22° 07’ 12,2912”	-51° 24’ 30,6952”	433.080
DMC1	-22° 07’ 23,0703”	-51° 24’ 28,7699”	444.560
MOR3	-22° 07’ 39,6630”	-51° 24’ 47,8739”	454.140
STPZ	-22° 07’ 27,2076”	-51° 24’ 33,5570”	427.530
STAV	-22° 07’ 47,2843”	-51° 24’ 59,5347”	430.430

All GNSS stations are equipped with a Septentrio Polar RX5s GNSS receiver, which supports multi-frequency and multi-constellation data tracking. Additionally, a Choke Ring antenna is used to minimize multipath effects from the surrounding environment. The GBAS UNESP project uses a dual constellation (GPS and Galileo) and dual frequency signals (L1/L5 and E1/E5a). An elevation mask of 10° was applied for data processing, both at the reference stations and on the simulated aircraft.

The data processing was carried out by an in-house implementation in MATLAB, only for post-processing mode. As it can be seen, Figure 16 provides an overview of the main activities and functionalities of the Ground and Aircraft Systems within the GBAS Monitoring Station. Notably, the cycle slip, Code-Carrier Divergence, ionospheric gradient, and smoothed pseudorange monitors operate similarly at both the reference stations and on the aircraft. All these functionalities were jointly coded and implemented by the GBAS Research Group of the INCT GNSS-NavAer Project and some results were published in De Souza et al. (2025).

Figure 16 – Main activities proposed for the GBAS Monitoring Station.



The details of these ground and aircraft functions will be described in the following sections.

4.1 Main Task of Ground System

The purpose of the ground system is to generate pseudorange corrections and integrity parameters from the reference stations and transmit them to the aircraft to enhance positioning accuracy.

At the ground level, GNSS data in RINEX (Receiver INdependent EXchange format) from each reference station is initially processed taking into consideration dual-frequency and dual-constellation observations (GPS and Galileo, L1/E1, and L5/E5a). Subsequently, three primary monitors are applied: cycle slip detection, code-carrier divergence, and ionospheric gradient monitoring:

- **Cycle Slip Monitor**: Due to the reliance on carrier-phase measurements for pseudorange smoothing, the occurrence of cycle slips must be monitored, as any discontinuity in the measurements necessitates the restart the pseudorange smoothing. The TurboEdit method, described in subsection 2.3.4, is employed for this task. A deviation exceeding half a cycle indicates a cycle slip, requiring the reset of pseudorange smoothing for the affected satellite at the detected time instant;
- **CCD Monitoring**: Code-carrier divergence is another critical parameter monitored in GBAS, as it may result from anomalous ionospheric gradients. CCD monitoring is performed by evaluating the rate of change of the Code-Minus-Carrier (CMC) combination using a two-stage (or cascade) low-pass filter, as discussed in subsection 2.2.3. The threshold for indicating CCD failure is set at 0.0415 m/s, as established by Pullen et al. (2017); and
- **Ionospheric Gradient Monitor**: The ionospheric gradient is assessed using two methods. The first is the Time-Step Method, applied to each reference station, as outlined in Section 2.3. In this method the ionospheric delay is calculated using the dual-frequency combination of L1/E1 and L5/E5a. The second method involves a test statistic that compares the ionospheric delay observed by the aircraft with the corrections provided by the reference stations (Section 2.3.1). This test statistic also utilizes L1/E1 and L5/E5a multi-frequency data. Based on

the difference in ionospheric delay between the reference stations and the aircraft, the appropriate approach level (GAST F SF L1 or GAST F IFree) can be selected.

The subsequent stage of the ground system's operation involves generating the content of the messages transmitted to the aircraft. After excluding observations and satellites flagged by the ground integrity monitors, pseudorange smoothing is performed for both L1 and L5 frequencies using a Hatch Filter with a time constant of 100 seconds, in addition to the Ion-Free linear combination, as detailed in Section 2.3.1. In the event of cycle slip, CCD, or ionospheric gradient failures, measurements from the affected satellites are excluded for 100 seconds after the monitors are triggered.

The smoothed pseudorange are used to calculate the MT1 message content, which includes pseudorange corrections, range rate corrections, B-values, and ground sigma values for L1, L5, and IFree combinations. The application of these parameters adheres to the Minimum Operational Performance Standards (MOPS) recommendations, as outlined in Table 13. The exceeding of these values presented in Table 13 implies that excluding satellites

Table 13 – Range of values calculated by Ground System to be transmitted to aircraft.

Parameters	Range of values
PRC	+/-327.67 m
RRC	+/-32.767 m/s
Sigma ground	0 to 5.08 m
B-Values	+/-6.35 m

Source: EUROCAE (2013).

4.2 Aircraft System

Similar to the ground system, GNSS data is also monitored in the aircraft domain to detect cycle slips, CCD failures, and anomalous ionospheric gradients. If the predefined thresholds for these monitors are exceeded, the affected satellites are excluded to ensure that the positioning solution is less influenced by systematic errors, in compliance with performance requirements.

The smoothing process is then started, depending on the operating conditions and the type of service to be used. There are two possible service types: GAST F SF L1 and GAST F IFree. In both services, the Hatch Filter is applied with a smoothing time constant

of 100 seconds, as well as the cycle slip monitor as in the ground system. It is important to highlight that the adopted GBAS architecture designates the airborne system as responsible for determining which service to execute, based on signal integrity monitors, particularly the ionospheric gradient monitor. As discussed in Section 3.1, in the event of ionospheric decorrelation detection (indicative of anomalous ionospheric gradients), the GAST F IFree service should be selected for use.

Across all GBAS categories, the Aircraft System utilizes the information provided by the Ground System — including pseudorange corrections (PRC), range rate corrections (RRC), B-values, ground sigma values, and other parameters from the MT1 message — to compute the 3D position (X, Y, and Z in the WGS84 reference system, as well as North, East, and Up coordinates in the local geodetic system). Additionally, the system calculates the standard deviation for all components, determines the horizontal and vertical protection levels, and evaluates accuracy, integrity, and operational availability on an epoch-by-epoch basis.

5. MULTIPATH AND NOISE FROM GBAS STATIONS

The first operational step carried in this work was to analyze the nominal conditions regarding the effects of multipath and noise for each station. As previously mentioned, these errors are not accounted for in the GBAS mathematical model. Multipath was estimated using two methods: the Code-Minus-Carrier (CMC) of the DFree linear combination and the Multipath index (MP), as described in Section 2.3.3. Both methodologies utilize dual-frequency observations (L1/E1 and L5/E5a) from GPS and Galileo, respectively.

The nominal conditions for multipath and noise were evaluated during periods of low ionospheric scintillation. In Presidente Prudente, this period typically occurs between May and August (MUELLA et al., 2009). The remaining months of the year are characterized by the presence of scintillation, which can distort GNSS signals and potentially confound multipath results with scintillation effects, particularly at elevation angles below 30°.

The results of this analysis, including multipath estimates and associated statistics such as the average, standard deviation, maximum values, and percentiles, will be presented for each station in the following sections. The study considered data from eleven days during the low scintillation period to calculate multipath and derive the relevant statistical metrics. In Appendices A to F there is a set of photos characterizing the surroundings of each GBAS Unesp Experimental station.

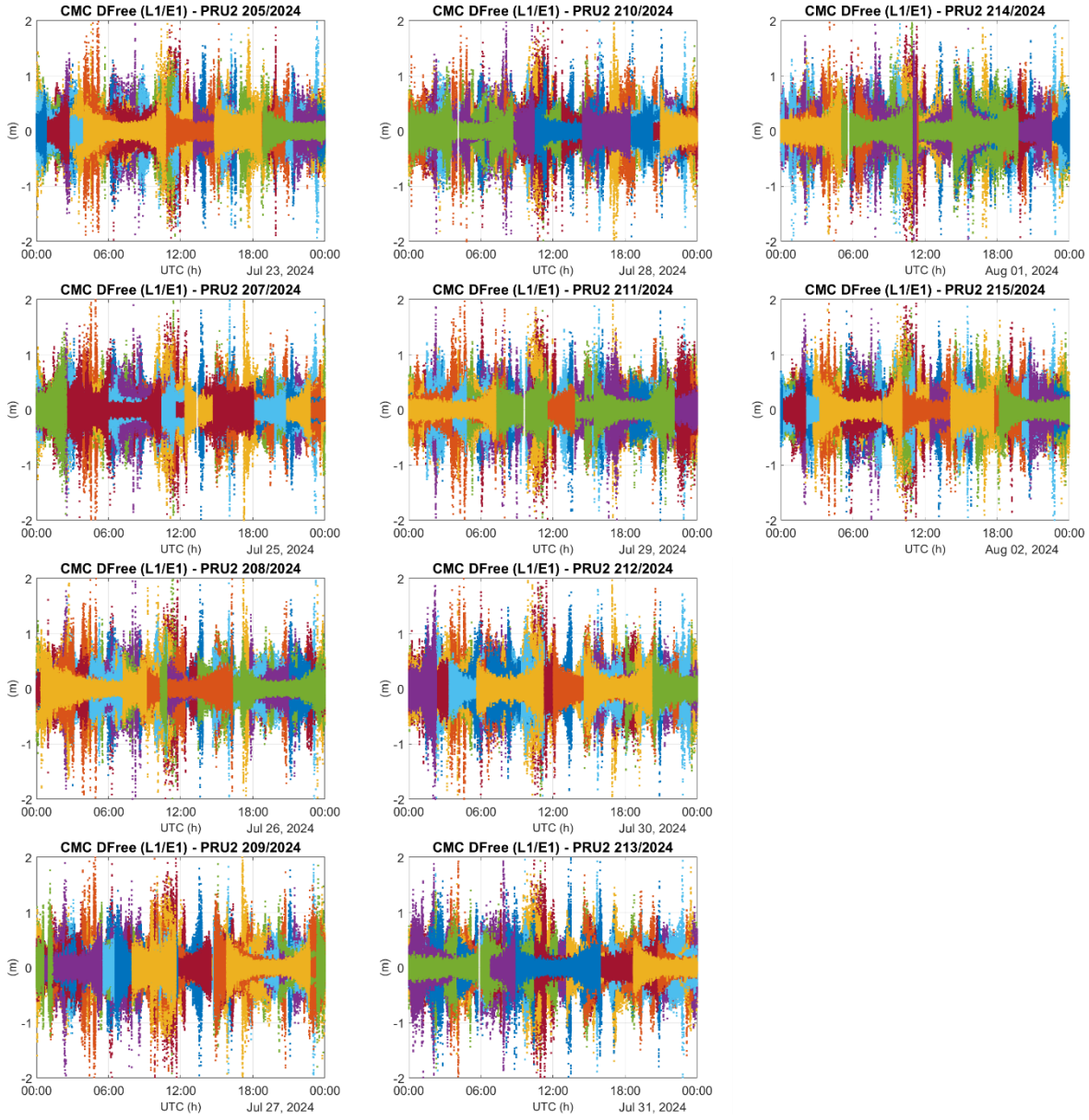
5.1. PRU2 Station

PRU2 station composes of UNESP's legacy in ionospheric scintillation monitoring and has been operational since 2011. The PRU2 station is distinguished by its location adjacent to trees that have grown around it. Due to its surroundings, Figure 17 indicates high multipath values for L1/E1 signals exceeding 2 meters, particularly at lower elevation angles. Data from this station was not included in the analysis for DOY (Day Of Year) 206/2023 due to data unavailability.

In environments with minimal variations around the GNSS antenna, multipath effects for GPS satellites exhibit good repeatability. This is attributed to the orbital period of GPS satellites, which is approximately 12 sideral hours (approximately). As a result, GPS satellites pass through the same positions daily, recording similar multipath effects

in successive days, assuming the surrounding environment remains unchanged and no phenomena such as ionospheric scintillation occur. For Galileo satellites, this repeatability can only be observed every 10 days, as their orbital period is approximately 14 sideral hours. Figure 17 illustrates this characteristic of multipath repeatability, particularly for GPS satellites over the succession of days analyzed. The largest multipath peaks occur at approximately the same times (notably around 06:00 and 12:00 UTC).

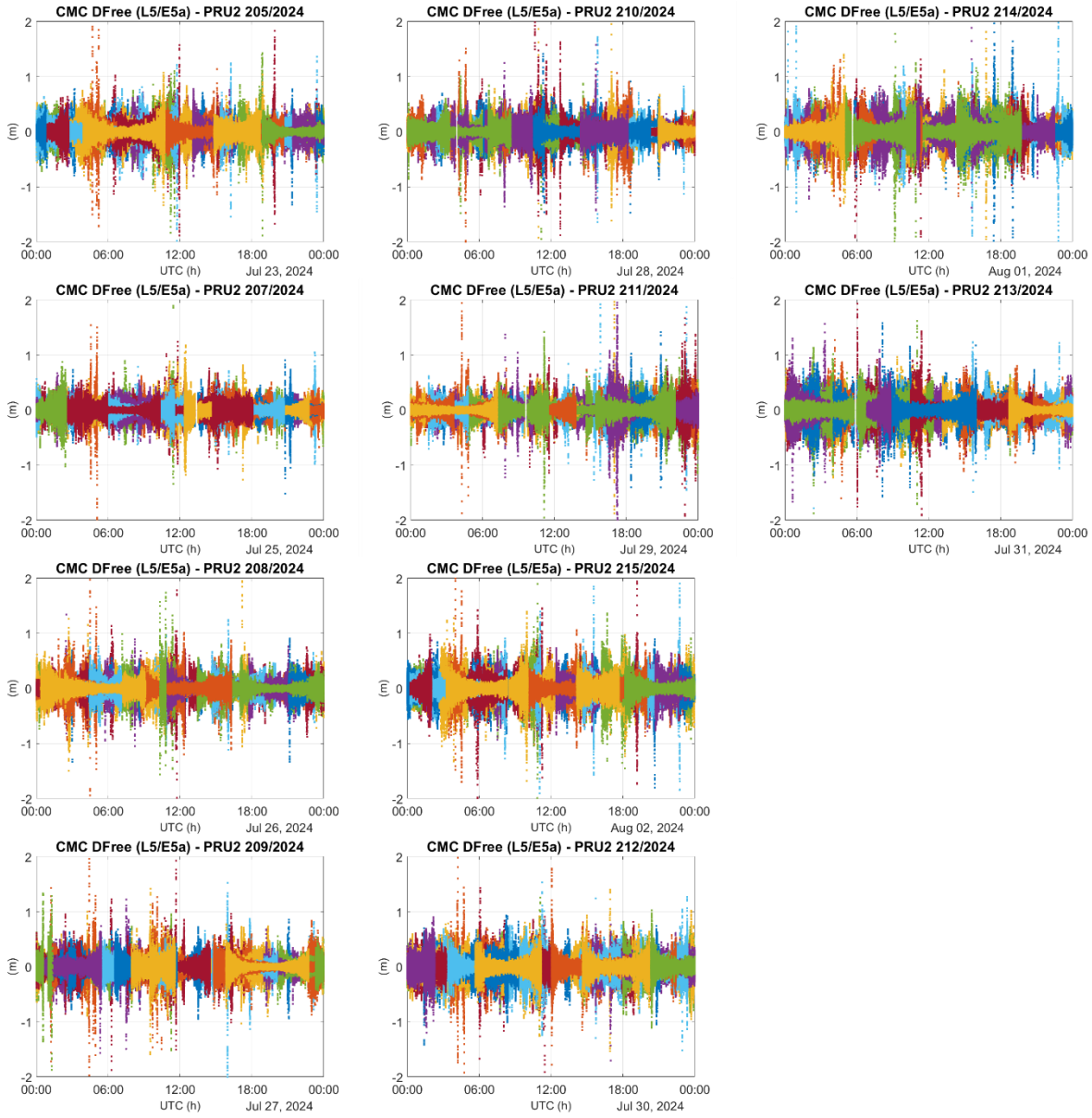
Figure 17 – Multipath (L1/E1) values estimated for the PRU2 station by CMC DFree method.



The multipath and noise results estimated for the L5/E5a frequency (Figure 18) also exhibit similar patterns and behavior over the analyzed days. However, it is visually

evident that the multipath values for the L5/E5a carrier-phase are lower than those for the L1/E1 carrier-phase. These findings align with studies published by Circiu et al. (2014) and Rotondo et al. (2015), which demonstrate that the L5/E5a carrier-phase is more resistant to multipath effects compared to the L1/E1 carrier-phase.

Figure 18 – Multipath (L5/E5a) values estimated for the PRU2 station using the CMC DFree method.



Two additional characteristics related to the repeatability of multipath can be observed in Figures 19 and 20, where the time axis (X-axis) is replaced by the azimuth and elevation of the satellites, respectively. These analyses allow for the identification of regions most and least affected by multipath. Specifically, the region between azimuths

of 140° and 220° is the least affected by multipath, while other regions around the antenna exhibit higher multipath peaks. Furthermore, the analysis based on satellite elevation reveals that the highest multipath peaks occur within the 10° to 20° elevation range.

Figure 19 – Multipath (L1/E1) values estimated for azimuth using the CMC DFree method at the PRU2 station.

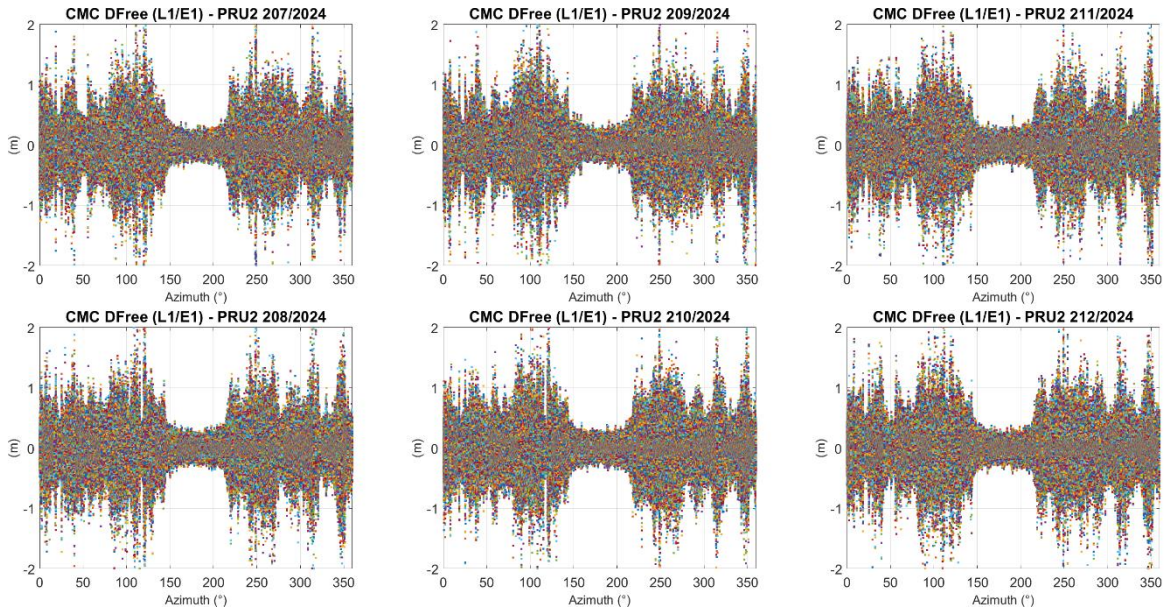
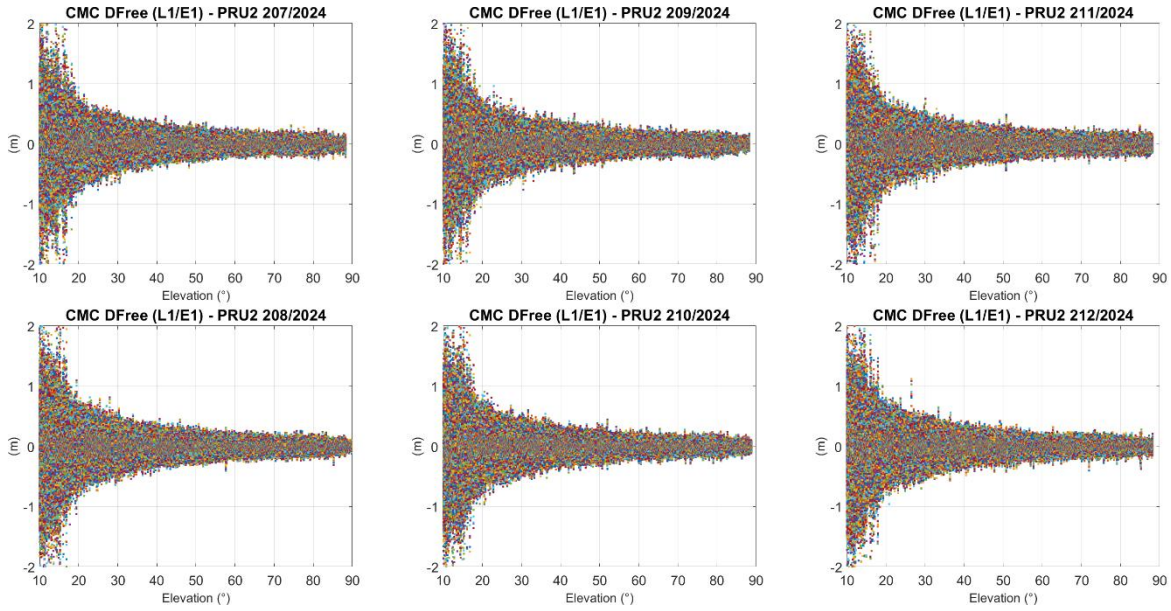


Figure 20 – Multipath (L1/E1) values estimated for elevation using the CMC DFree method at the PRU2 station.

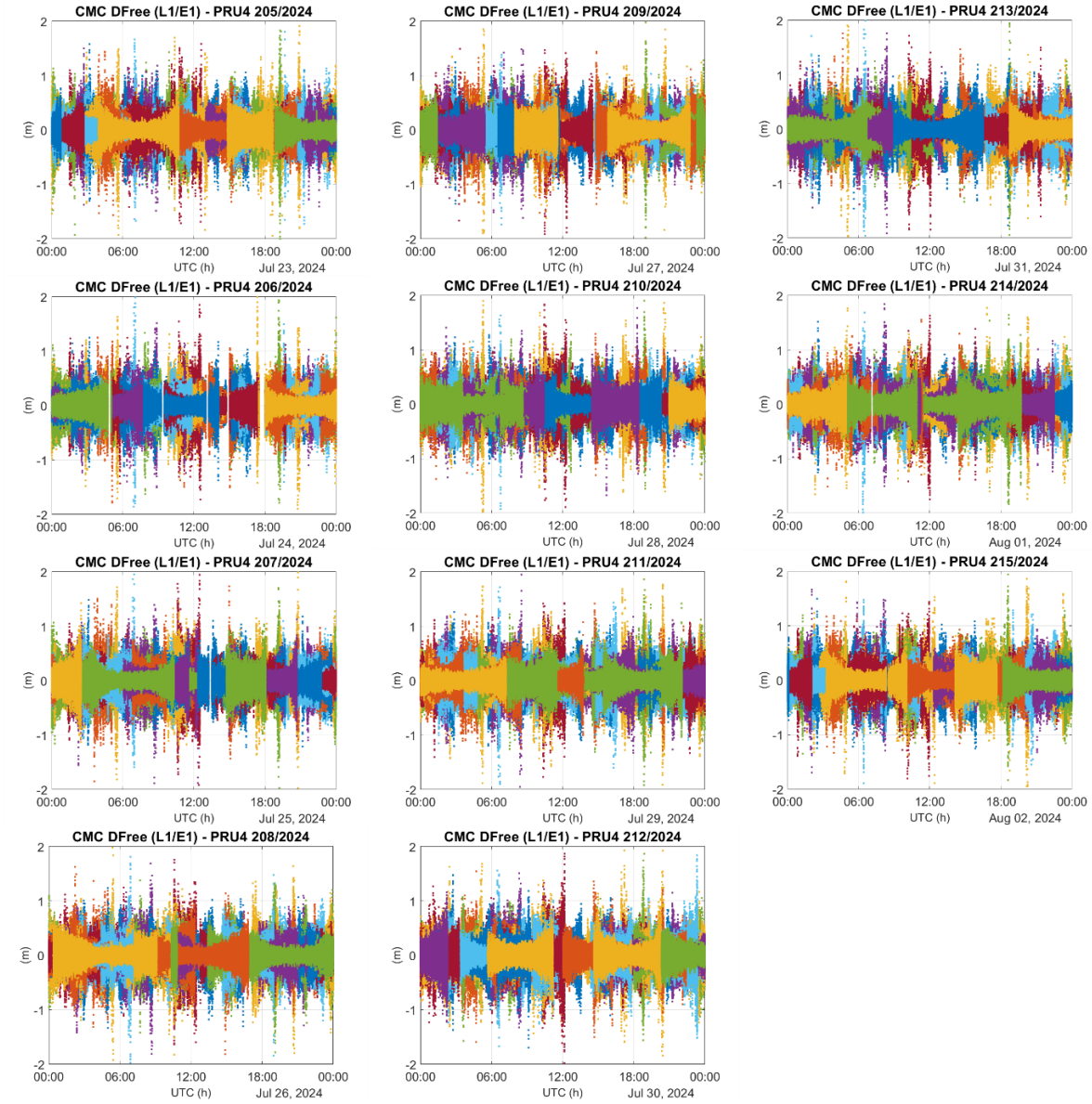


5.2. PRU4 Station

The PRU4 station is also part of the legacy set of the INCT GNSS-NavAer Network for monitoring ionospheric scintillation. It has been in operation since 2017 and is located in the Space Geodesy Laboratory building on the UNESP Campus in Presidente Prudente.

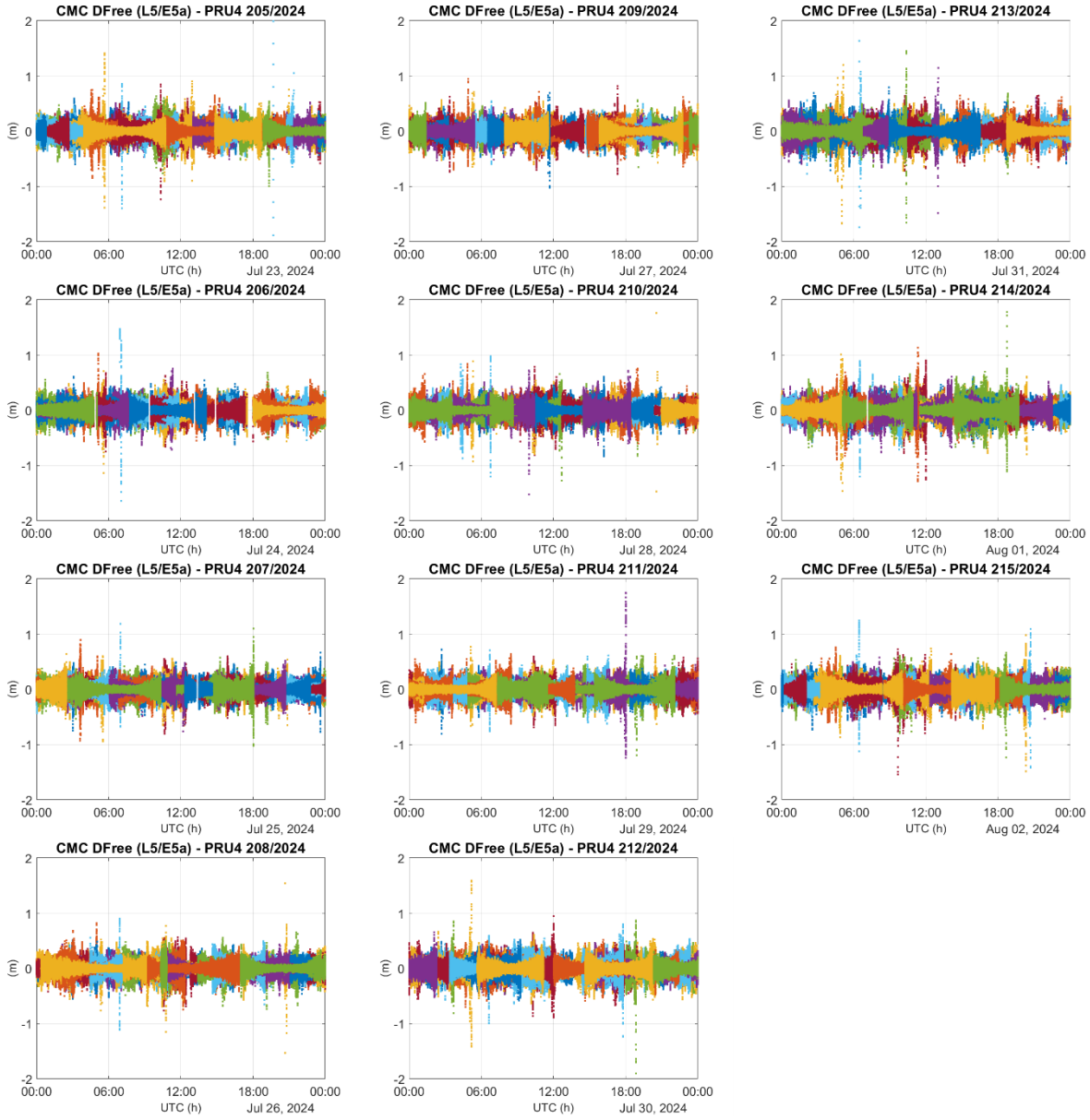
The multipath and noise estimated by CMC DFree maintain their signature characteristics over the succession of days analyzed, with peaks exceeding 2 m. However, Figure 21 shows that most of the time the multipath is in the -1 to 1 m range. It can also be seen that almost all of the highest multipath peaks occur around noon UTC (Universal Time Coordinated).

Figure 21 – Multipath (L1/E1) values estimated for PRU4 station by CMC DFree.



For the L5/E5a carrier-phase (Figure 22) multipath values are lower than for the L1/E1, remaining in the -0.5 to 0.5m range on almost all days. Compared to the PRU2 station, at the PRU4 station the estimated multipath for the L5/E5a carrier-phase had fewer peaks, which did not characterize repeatability on the days analyzed.

Figure 22 – Multipath (L1/E1) values estimated for PRU4 station by CMC DFree.



On the L1/E1 carrier-phase, which has the characteristic of multipath repeatability, the plot of multipath by azimuth shows that most of the peaks are concentrated in the 150° azimuth region (Figure 23). On the other hand, these multipath peaks are associated with the elevation of the satellites, especially in the 10 to 20° range, as shown in Figure 24. And similarly to PRU2, there is also a region less affected by multipath which lies between 150 and 220°, approximately. In other regions the multipath estimated maintains between in the -1 to 1m range.

Figure 23 – Multipath (L1/E1) values estimated for azimuth using CMC DFree from PRU4 station.

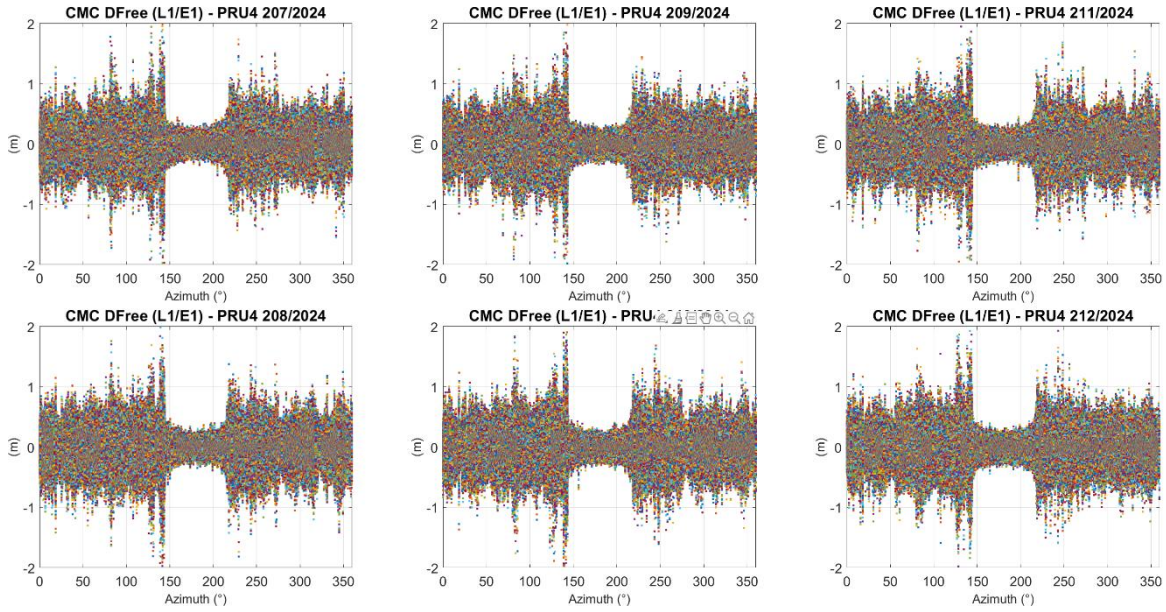
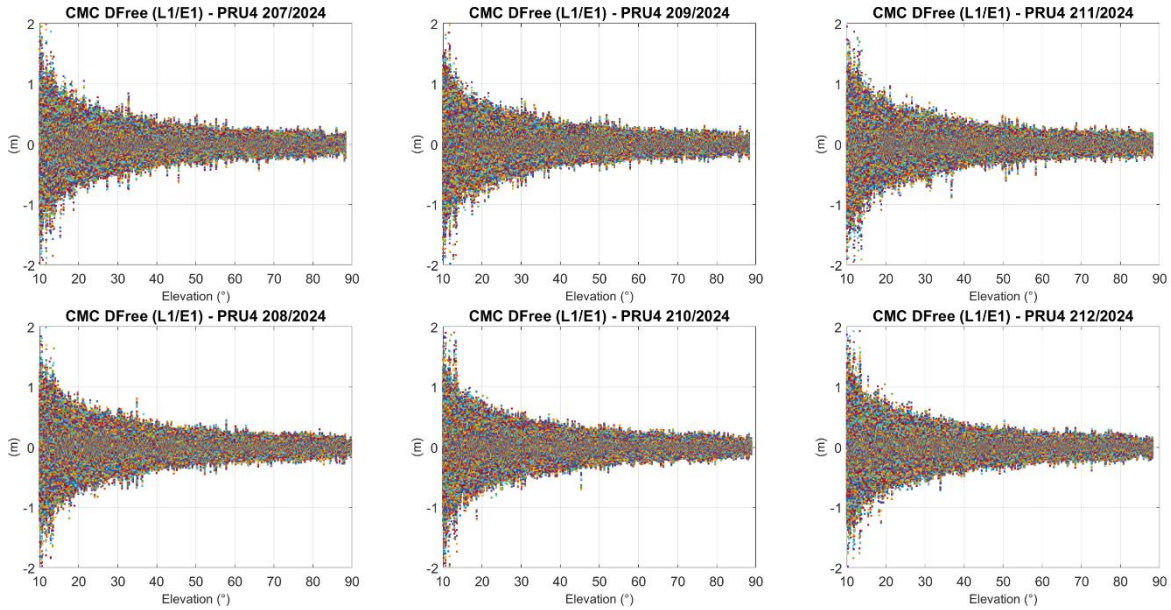


Figure 24 – Multipath (L1/E1) values estimated for elevation using CMC DFree from PRU4 station.



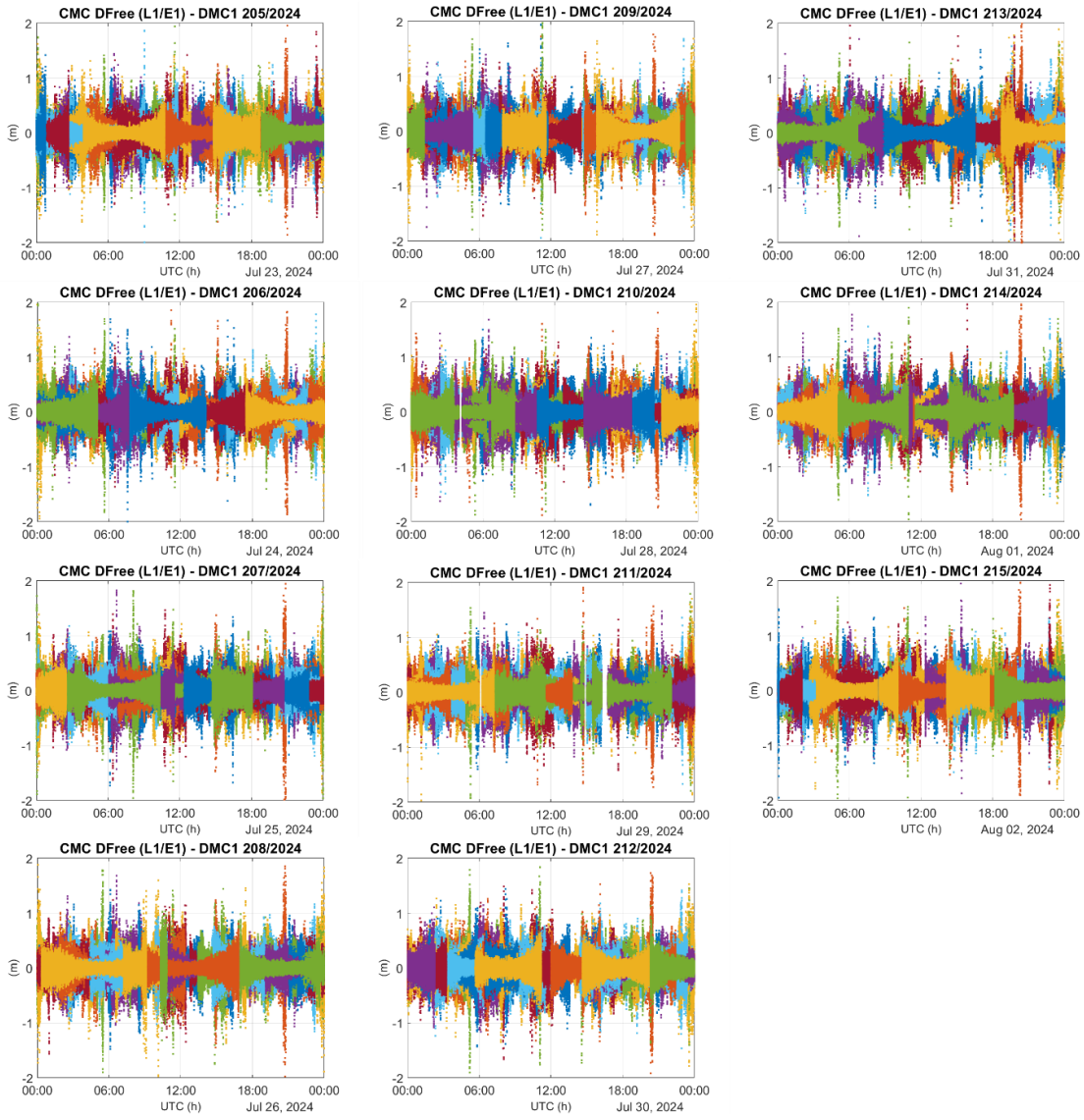
5.3. DMC1 Station

The DMC1 station is located in the Mathematics Department building on the UNESP Campus in Presidente Prudente-SP (Brazil). This station started operation in

2019 when the INCT GNSS-NavAer Project started with the aim of deploying a kind of GBAS prototype. In September 2024, the DMC1 station was deactivated, and the receiver was moved to another location at UNESP.

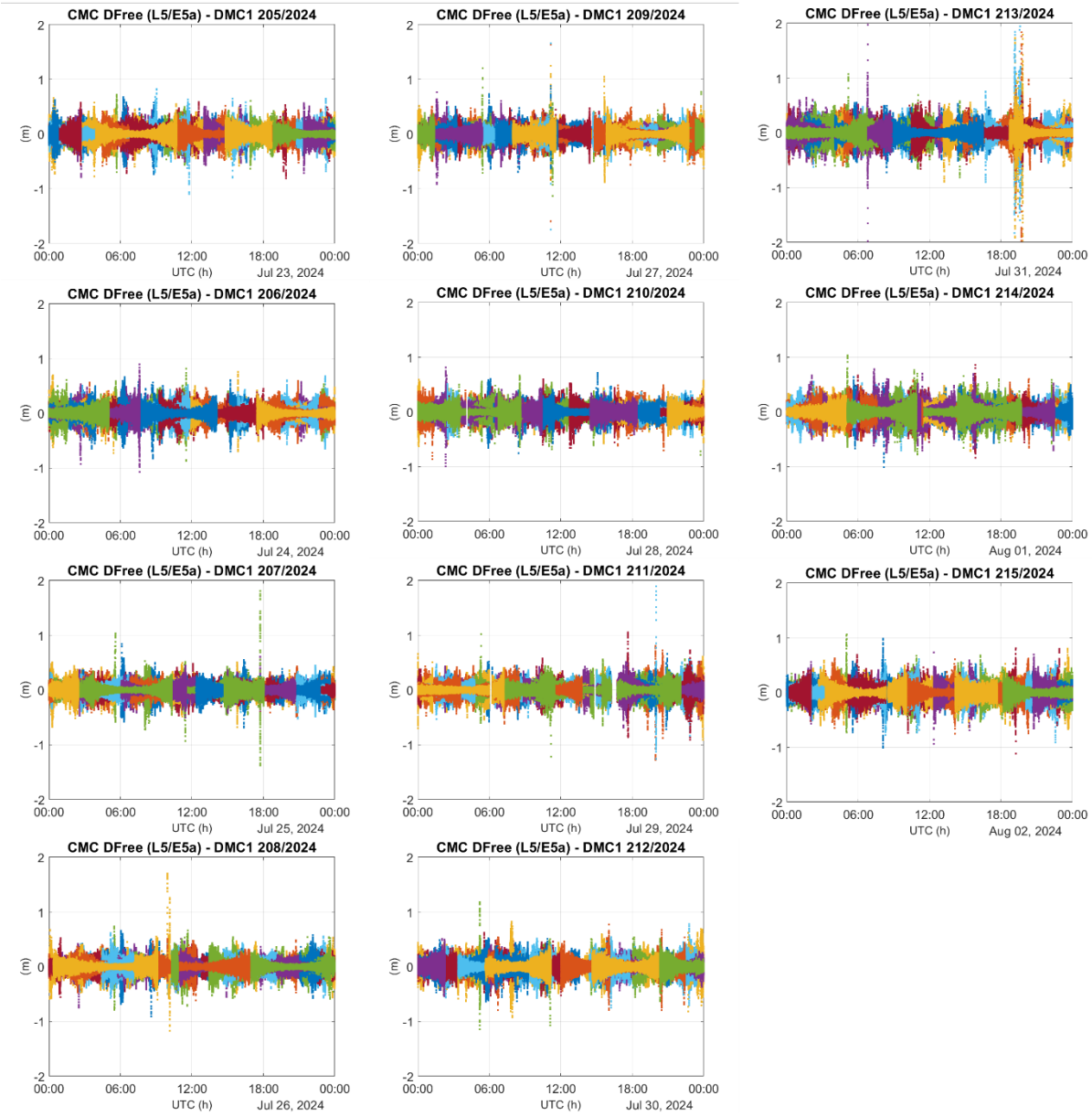
The nominal multipath conditions for the L1/E1 frequency of this station can be seen in Figure 25. There are multipath peaks at specific times such as 0:00, 6:00, 12:00 and 20:00 (approximately) for the days analyzed. It can be seen that most of the estimated multipath values are in the -1 to 1 m range.

Figure 25 – Multipath (L1/E1) values estimated for DMC1 station by CMC DFree.



The estimated multipath values for the L5/E5a carrier-phase are characterized by a reduction in the estimated values, being in the -0.5 to 0.5 m range, meaning a lower occurrence of multipath peaks.

Figure 26 – Multipath (L5/E5a) values estimated for DMC1 station by CMC DFree.



The spatial distribution of the occurrence of multipath (Figure 27) shows that the peaks occur in the azimuth regions from 0 to 50° and other areas close to the azimuths of 220° and 315°. This station also shows an area less affected by multipath, which is the 150 to 220° azimuth direction. Station DMC1 also maintains the characteristic of having the highest multipath values associated with the low elevation of the satellites, especially in the 10 to 20° range (Figure 28).

Figure 27 – Multipath (L1/E1) values estimated for azimuth using CMC DFree from DMC1 station.

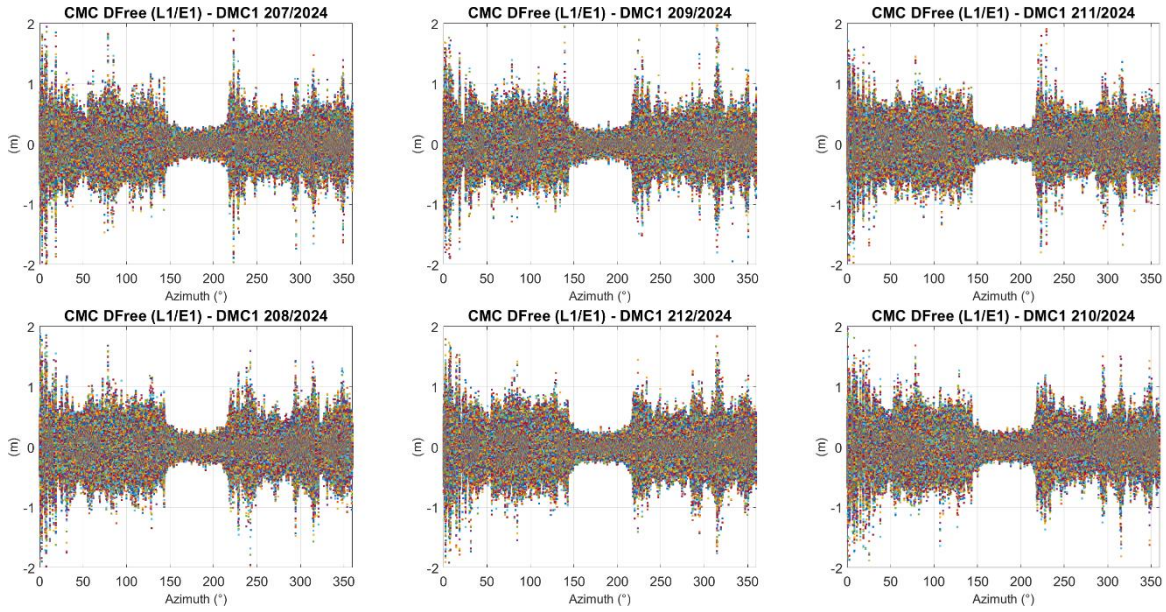
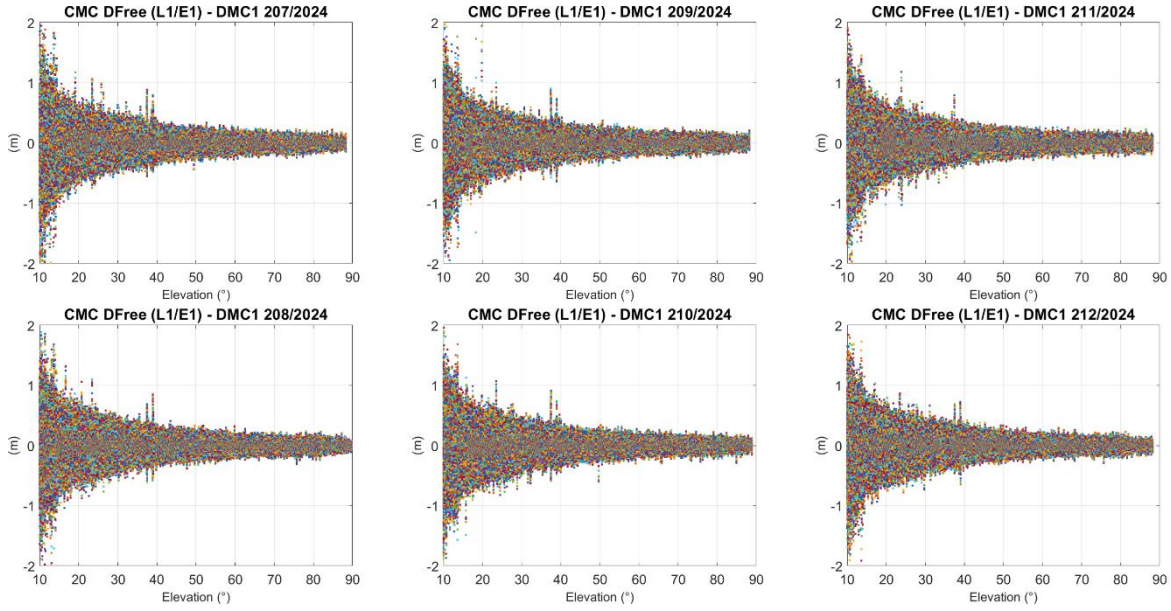


Figure 28 – Multipath (L1/E1) values estimated for elevation using CMC DFree from DMC1 station.



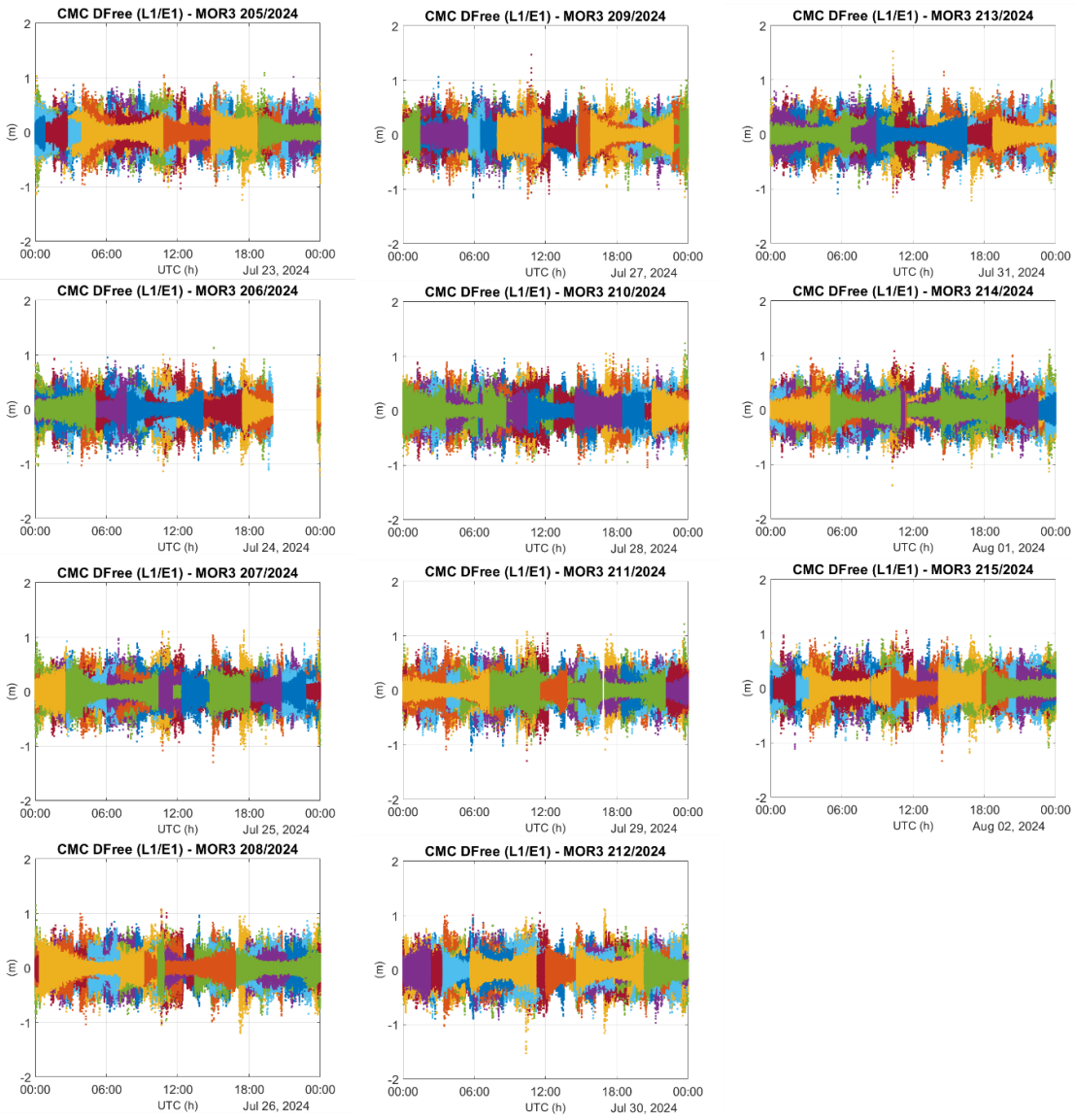
5.4. MOR3 Station

The MOR3 station corresponds to the fourth receiver in the ground system of the GBAS UNESP Experimental Prototype discussed in this work. It is located at the UNESP

facility in the Morumbi neighborhood in Presidente Prudente - SP (Brazil) and has been in operation since 2021.

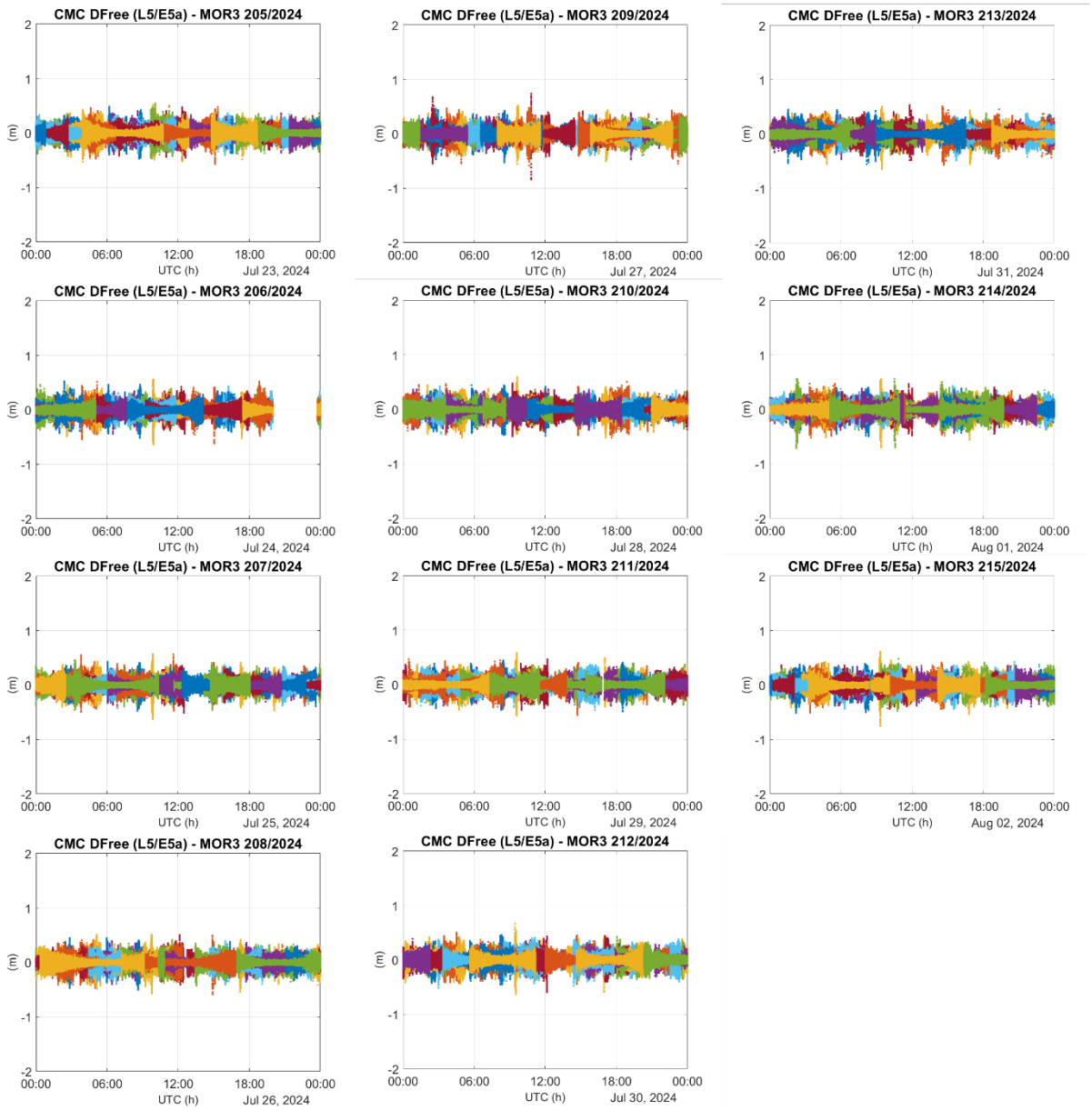
In the multipath analysis for the days considered and compared to the other ground stations, MOR3 has the lowest occurrence of multipath peaks (Figure 29). Most of the time, the values for L1/E1 frequency are below the -1 to 1m range and show the characteristic of symmetry of the values within this range.

Figure 29 – Multipath (L1/E1) values estimated for MOR3 station by CMC DFree.



For the L5/E5a carrier-phase, the estimated multipath is characterized by the low occurrence of peaks and by being below -0.5 to 0.5 m for most of the days analyzed. These results once again reaffirm the potential of the L5/E5a carrier-phase to be resilient to the effect of multipath.

Figure 30 – Multipath (L5/E5a) values estimated for MOR3 station by CMC DFree.



The plot of the spatial distribution of multipath at station MOR3 stands out because it only shows the direction least affected by multipath, which is between 150 and 220° (approximately). In the other directions, there are no major variations in the values, which are in the -1 m to 1 m range. In terms of satellite elevation, multipath values decrease with increasing elevation.

Figure 31 – Multipath (L1/E1) values estimated for azimuth using CMC DFree from MOR3 station.

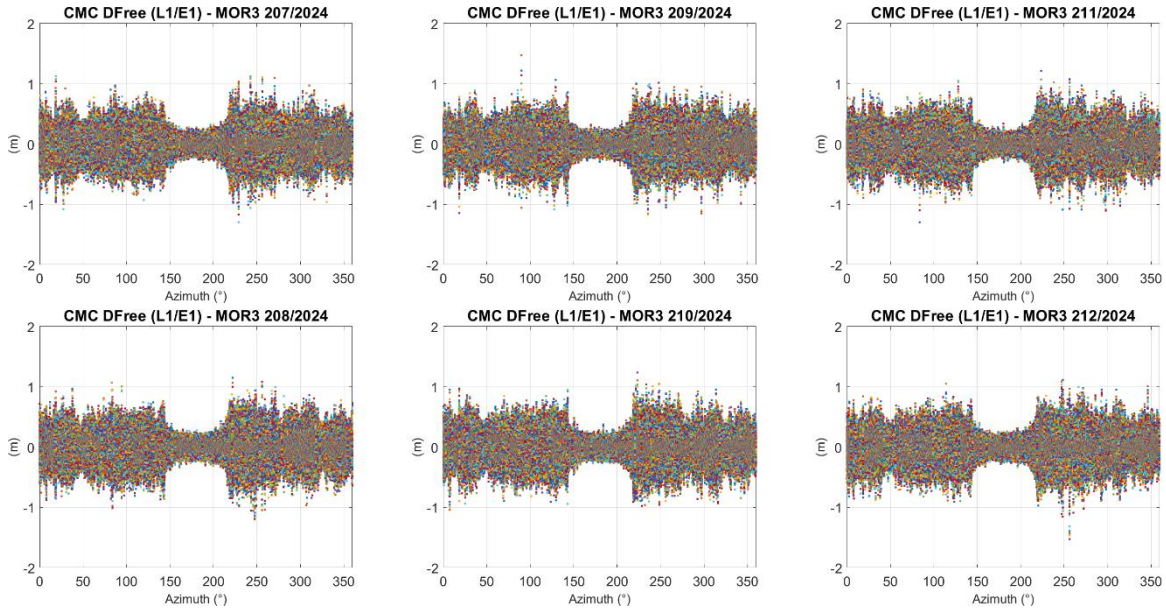
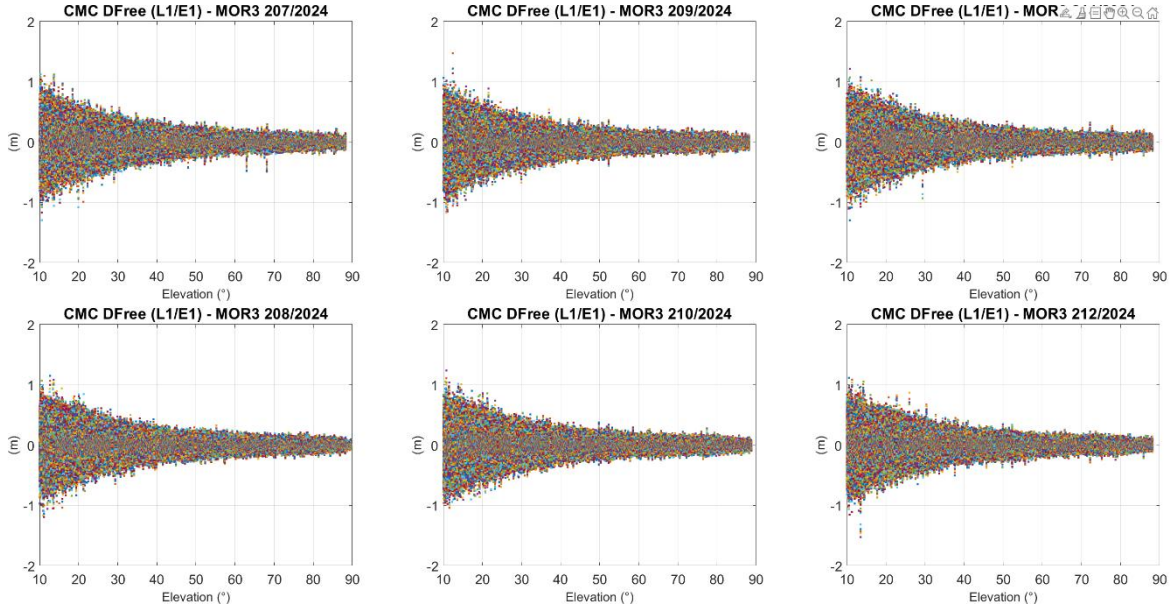


Figure 32 – Multipath (L1/E1) values estimated for elevation using CMC DFree from MOR3 station.



5.5. STPZ Station

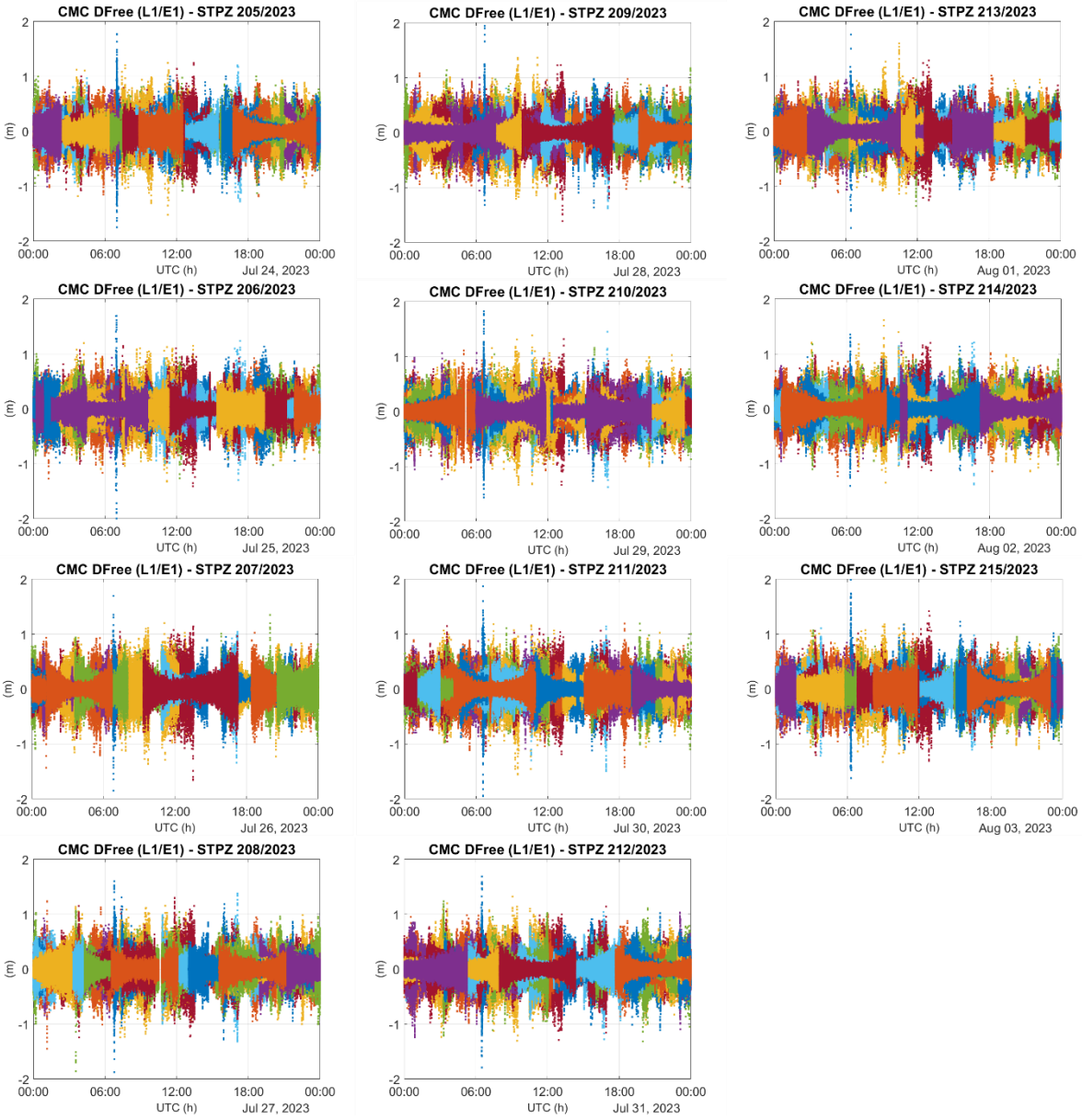
The STPZ station, installed in March 2023, was configured as an aircraft (in static mode) within the UNESP Experimental GBAS Prototype. It is located in the rural area of

the municipality of Pirapozinho-SP and is about 13 km away from the reference stations (PRU2, PRU4, DMC1 and MOR3).

The analysis of the nominal multipath conditions for this station was carried out for the year 2023, but on the same dates as the other stations. During the 2024 dates, the STPZ GNSS receiver had problems recording the observations.

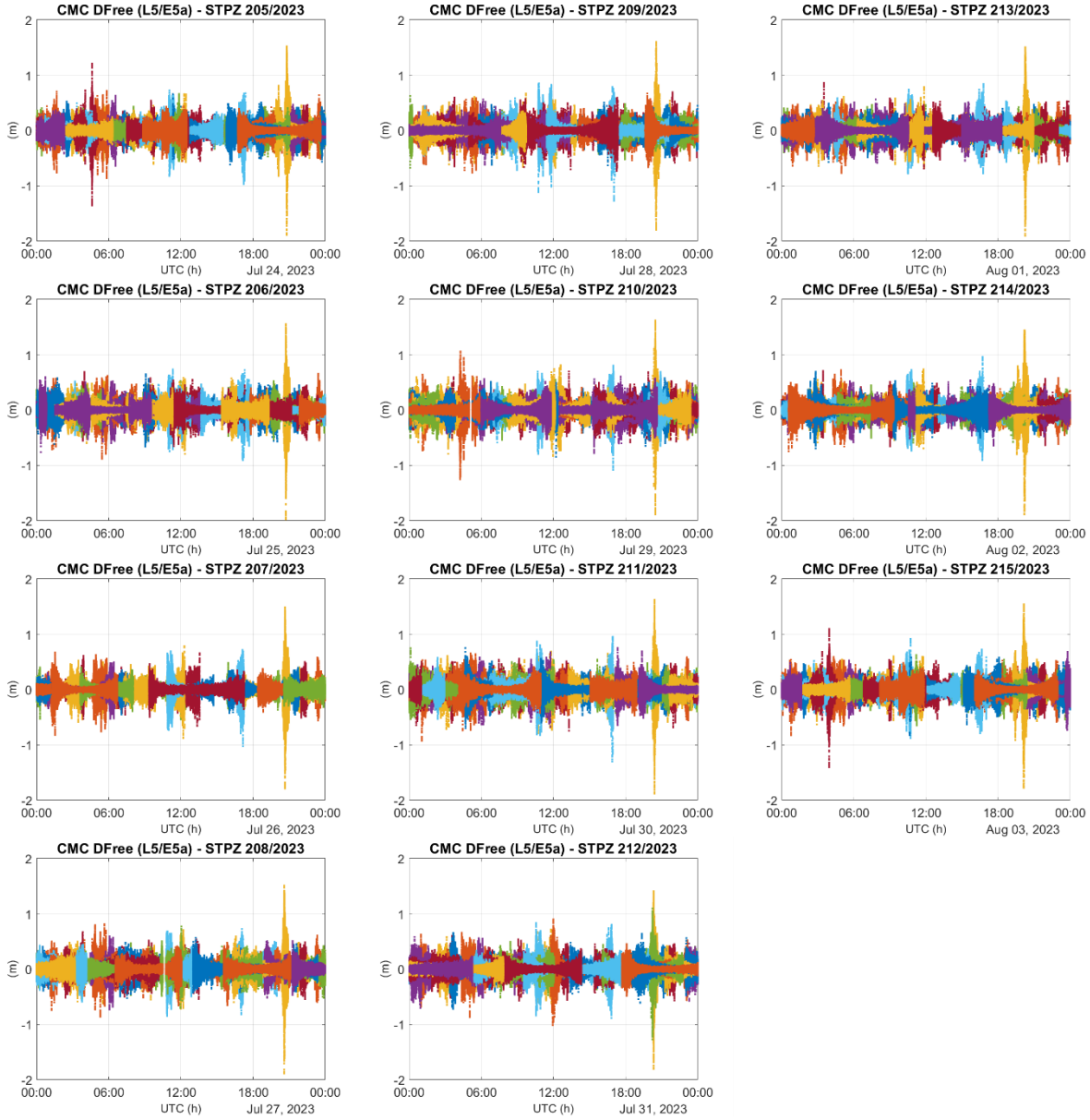
The temporal analysis of multipath for the L1/E1 carrier-phase is marked by the occurrence of multipath peaks at two times: around 6 am and 12 pm. It also maintains the characteristic symmetry of values varying from -1 m to 1 m, also observed at the ground stations.

Figure 33 – Multipath (L1/E1) values estimated for STPZ station by CMC DFree.



Multipath for the L5/E5a carrier-phase at the STPZ station maintains the characteristic of reduced effect compared to the L1/E1 frequency. However, at this station there was a peak in high levels of multipath every day around 8 pm. This pattern of local occurrence did not appear repeatedly at the other stations analyzed for the L5/E5a carrier-phase. Despite this peak of higher multipath elevation, it can be seen that for the longest time the variation was in the -0.5 m to 0.5 m range.

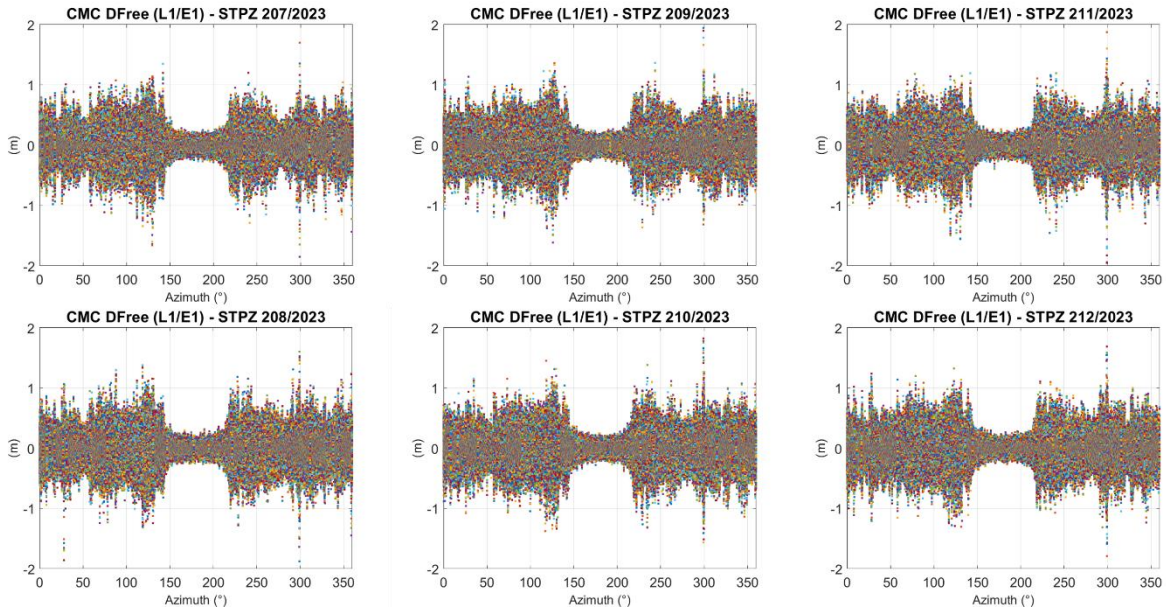
Figure 34 – Multipath (L5/Ea) values estimated for STPZ station by CMC DFree.



From a spatial point of view (Figure 35), the highest multipath peaks at the STPZ station occur in the 130° azimuth direction (approximately) and near the 330° azimuth,

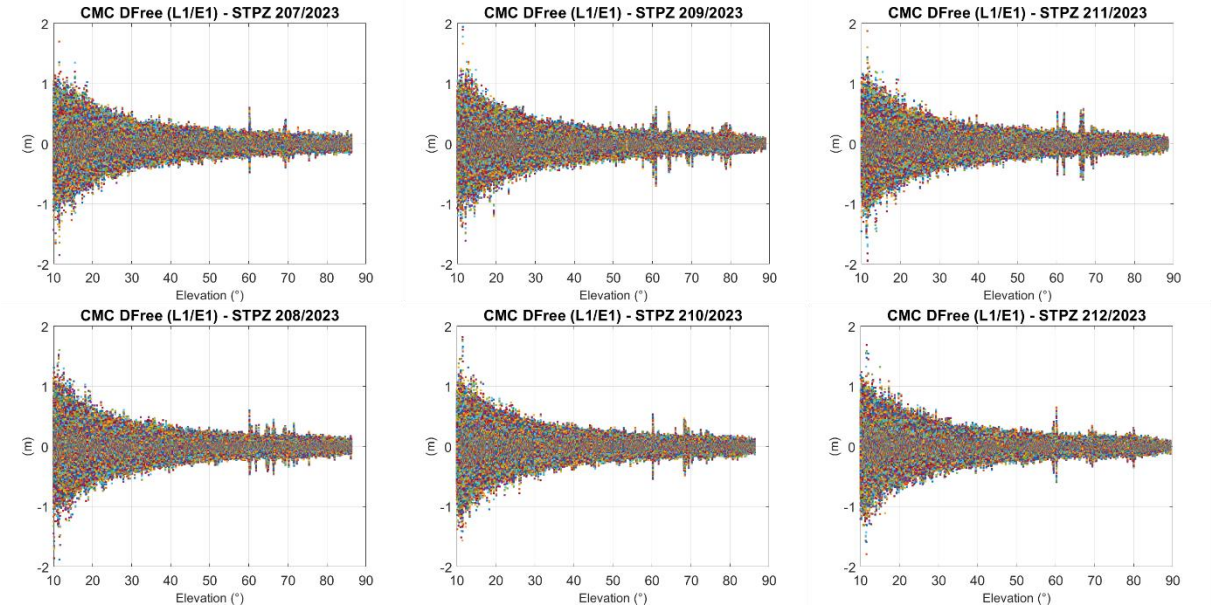
where the highest value peaks are located. As with the other stations, the region between 150 and 220° azimuth is the area least affected by multipath.

Figure 35 – Multipath (L1/E1) values estimated for azimuth using CMC DFree from STPZ station.



Considering the elevation of the satellites, the station retains the characteristic of having the highest multipath values for satellites with elevations between 10 and 20°. It is important to note that anomalous conditions occur at this station, between the elevations of 60 and 70°. Some multipath peaks exceed 0.5 m (in absolute value), when the normal trend is towards low values, as seen at this station and the others when multipath is analyzed as a function of elevation. This is a particular condition of the station, and the cause of this systematic error has not yet been investigated.

Figure 36 – Multipath (L1/E1) values estimated for elevation using CMC DFree from STPZ station.

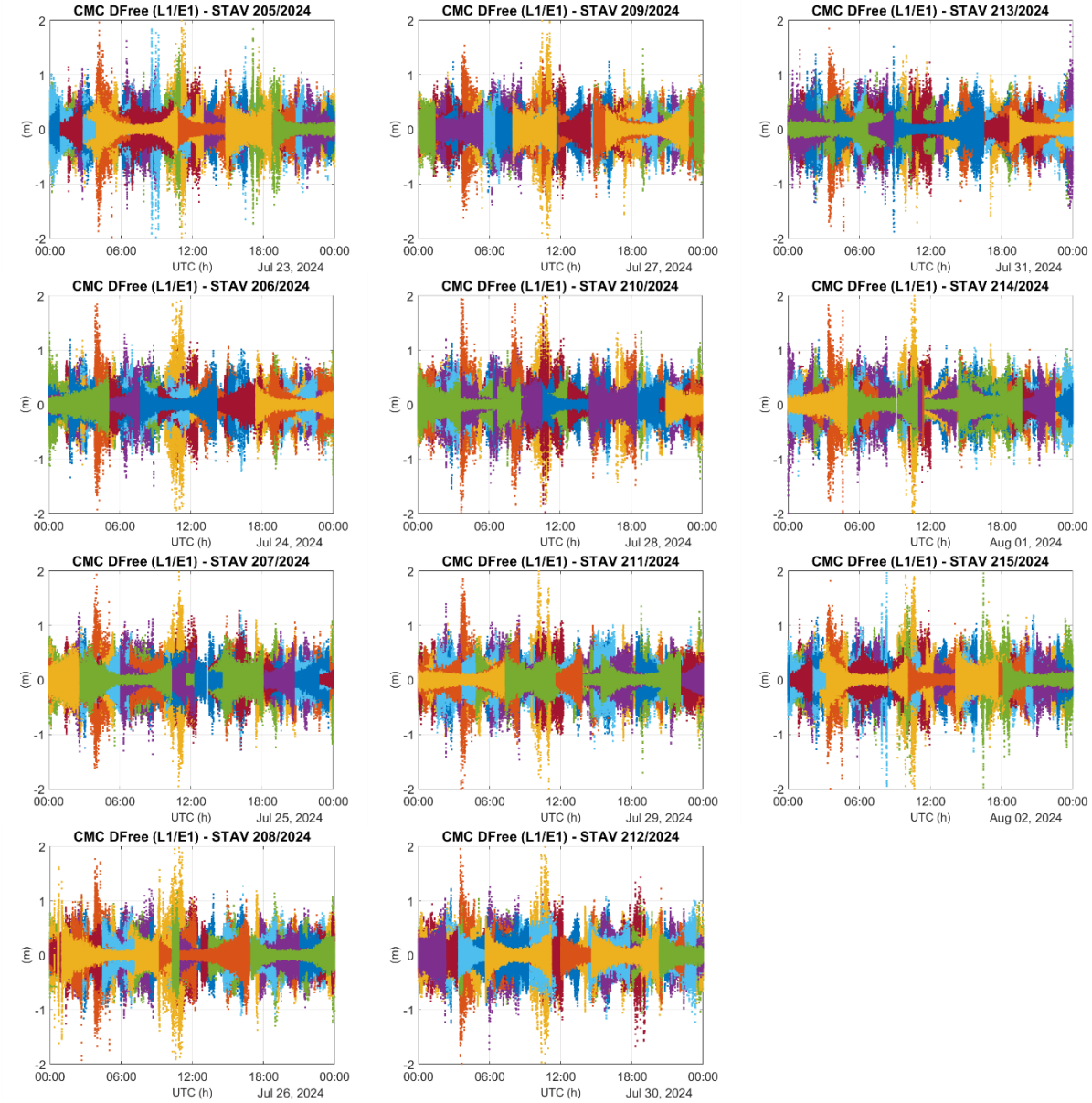


5.6. STAV Station

The STAV station is the second GNSS receiver installed as an aircraft in the GBAS UNESP Experimental Prototype configuration. The station is in the rural area of the city of Alvares Machado and is approximately 9.8 km from the stations the ground system.

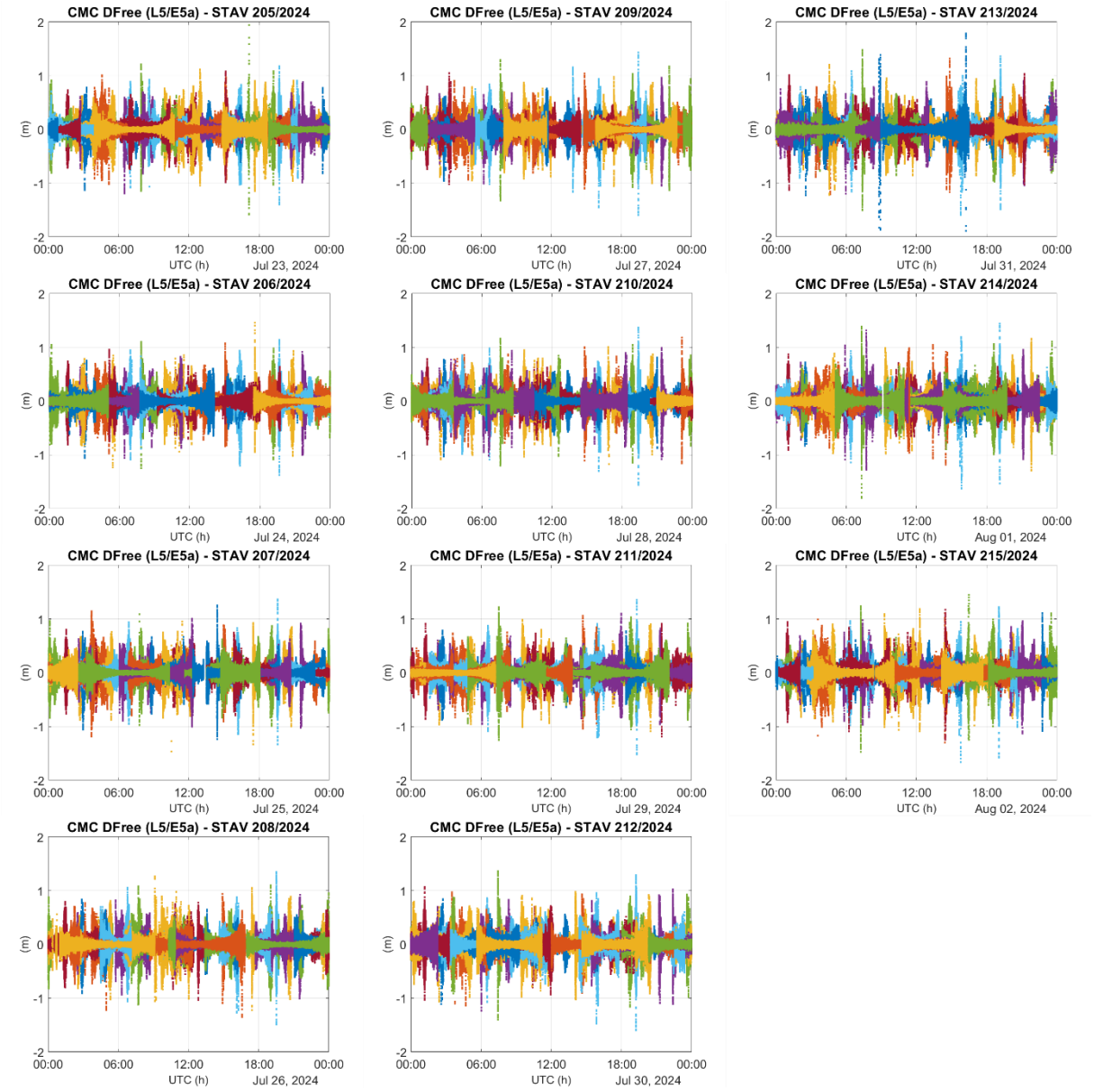
Figure 37 shows the nominal multipath condition for the L1/E1 carrier-phase, which from a temporal point of view is marked by the occurrence of multipath peaks at the following approximate times: 4 am, 12 pm and 6 pm. These peaks exceed the -1m to 1m range that characterizes the station on the days analyzed, maintaining the random nature of the effect that was seen at all stations.

Figure 37 – Multipath (L1/E1) values estimated for STAV station by CMC DFree.



Compared to the other stations, the L5/E5a multipath at STAV has the highest temporal occurrence of multipath peaks, so visually it remains at the regular values seen at the other stations. The values exceed the -1 m to 1 m range and in some cases approach 2 m.

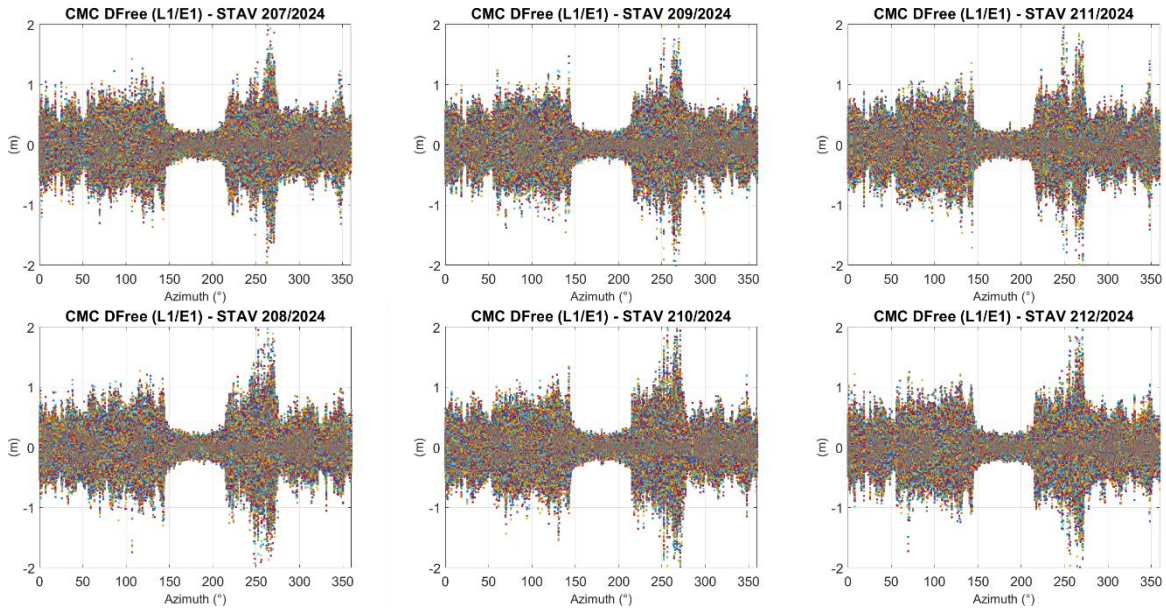
Figure 38 – Multipath (L5/Ea) values estimated for STAV station by CMC DFree.



The spatial distribution of multipath (L1/E1) shows that the region most affected by this effect is around 250° azimuth (Figure 39). As with the other five UNESP Experimental GBAS stations, the region between 150° and 220° azimuth is the least affected by multipath. In this case, it is noteworthy that all stations exhibit a characteristic satellite geometry, predominantly toward the southern direction, where satellites are typically observed at elevations above 40°, and are therefore less susceptible to multipath effects. This geometric arrangement of satellites above 40° is related to the location of the stations closer to the region where the South Atlantic Magnetic Anomaly phenomenon occurs. This region is characterized by a weaker magnetic field and lower satellite

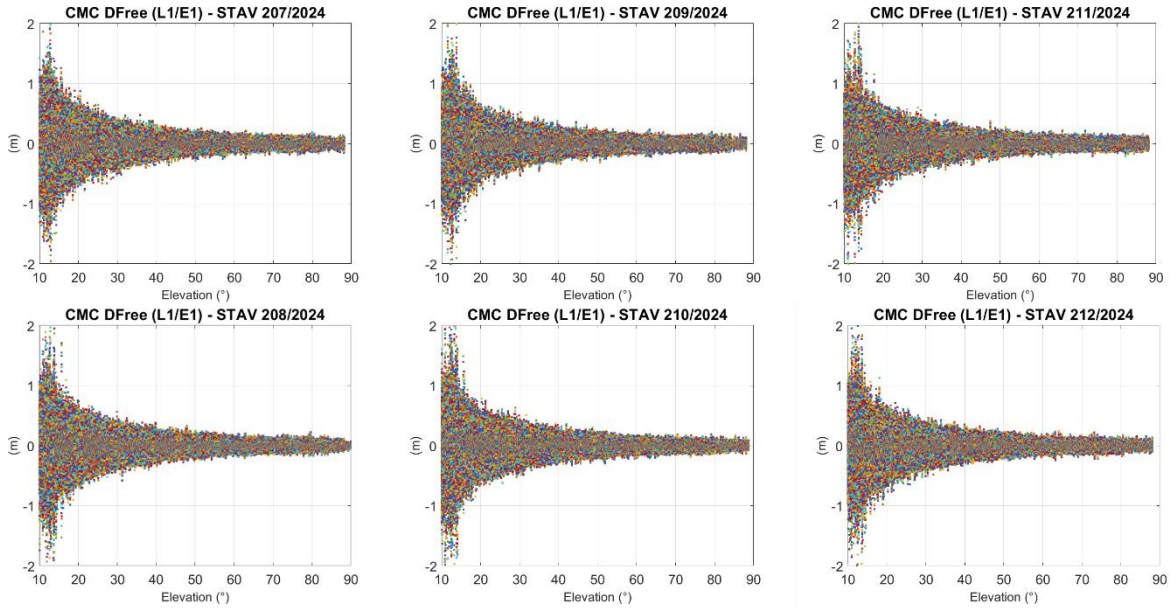
availability due to vulnerability to the effects of ionizing radiation on satellite components.

Figure 39 – Multipath (L1/E1) values estimated for azimuth using CMC DFree from STAV station.



From the point of view of satellite elevation, STAV maintains the characteristic seen in all the stations, being most affected by multipath in satellites with elevations between 10 and 20°.

Figure 40 – Multipath (L1/E1) values estimated for elevation using CMC DFree from STAV station.



5.7 Statistical Characterization of Estimated Multipath

The multipath values presented in this section were analyzed using the mean, standard deviation, and 95th percentile. These statistical indicators were organized into tables grouping station pairs solely for page layout management; thus, there is no analytical relationship between the paired stations and the reported values. Table 14 presents the average estimated multipath for MP and CMCDF values for six GNSS stations over 11 days, comparing the L1 and L5 frequencies across two elevation ranges (10°–30° and 30°–90°).

Table 14 – Average of the estimated multipath over the 11 days.

Station	MP1 (m) 10 to 30°	MP1 (m) 30 to 90°	MP5 (m) 10 to 30°	MP5 (m) 30 to 90°	CMCDFL 1 (m) 10 to 30°	CMCDFL 1 (m) 30 to 90°	CMCDFL 5 (m) 10 to 30°	CMCDFL 5 (m) 30 to 90°
PRU2	-8.52E-05	-5.79E-05	-8.52E-05	-5.79E-05	-3.04E-05	-6.03E-07	-1.51E-06	-1.69E-06
PRU4	-3.78E-05	-5.73E-05	-3.78E-05	-5.73E-05	-1.50E-05	6.92E-06	8.03E-06	2.06E-06
DMC1	-6.76E-05	-4.87E-05	-6.76E-05	-4.87E-05	-2.87E-05	8.73E-06	1.81E-06	2.29E-06
MOR3	1.26E-04	-1.81E-04	1.26E-04	-1.81E-04	-1.08E-06	-3.75E-06	-8.26E-06	8.06E-07
STAV	-2.72E-05	-5.15E-05	-2.72E-05	-5.15E-05	2.02E-05	4.77E-06	4.53E-07	-1.05E-06
STPZ	-5.29E-05	-3.49E-05	-5.29E-05	-3.49E-05	-6.35E-06	2.79E-06	-2.05E-06	1.33E-06

The results show that multipath effects are more pronounced at lower elevations (10°–30°), particularly for the L1 band, with PRU2 exhibiting the negative bias (−8.52E-05 m) and MOR3 displaying a positive bias (1.26E-04 m). The L5 band generally performs better, with smaller MP values, confirming its enhanced resistance to multipath. The CMCDF method effectively reduces multipath errors, particularly for L5, where residuals are very close to zero. However, some stations, such as STAV and PRU4, show slight positive biases in CMCDFL1 and CMCDFL5, possibly due to residual noise.

Table 15 summarizes the standard deviation of estimated multipath (MP) and CMCDF errors across six GNSS stations over 11 days, comparing L1 and L5 frequencies at low (10°–30°) and high (30°–90°) elevation angles.

Table 15– Average of standard deviation of the multipath estimated for each station on the days analyzed.

Station	MP1 (m) 10 to 30°	MP1 (m) 30 to 90°	MP5 (m) 10 to 30°	MP5 (m) 30 to 90°	CMCDFL 1 (m) 10 to 30°	CMCDFL 1 (m) 30 to 90°	CMCDFL 5 (m) 10 to 30°	CMCDFL 5 (m) 30 to 90°
PRU2	0.229	0.079	0.229	0.079	0.239	0.079	0.155	0.045
PRU4	0.202	0.086	0.202	0.086	0.200	0.085	0.098	0.036
DMC1	0.182	0.072	0.182	0.072	0.183	0.072	0.092	0.033
MOR3	0.164	0.079	0.164	0.079	0.155	0.068	0.072	0.026
STAV	0.182	0.058	0.182	0.058	0.182	0.058	0.114	0.025
STPZ	0.176	0.071	0.176	0.071	0.176	0.071	0.104	0.029

The data reveals clear trends in multipath variability, emphasizing the impact of elevation angles, signal frequency (L1 vs. L5), and processing methodology (MP vs. CMCDF). At low elevations (10°–30°), the standard deviation is consistently higher across all stations, with PRU2 showing the worst performance (0.229 m for MP1), likely due to signal obstruction or reflective surfaces near the antenna. In contrast, MOR3 exhibits the lowest noise levels (0.164 m for MP1), suggesting an optimized site with minimal interference. The CMCDF method significantly reduces multipath errors, particularly for L5, where deviations drop below 0.05 m at high elevations—confirming its effectiveness in GNSS error mitigation.

The L5 signal demonstrates superior robustness compared to L1, with marginally lower standard deviations in MP and drastically improved results after CMCDF processing. For instance, STPZ records a reduction from 0.176 m (MP1, 10°–30°) to 0.104 m (CMCDFL1) and further down to 0.029 m (CMCDFL5, 30°–90°). This trend

highlights L5's inherent resistance to multipath, making it preferable for high-precision applications. However, L1 still shows utility in scenarios where legacy systems dominate, though its performance is more susceptible to environmental noise.

Table 16 shows the average of the 95% percentile of the estimated multipath at each station over the 11 days of the campaign analyzed. The results demonstrate a consistent pattern where multipath errors are significantly larger at lower elevation angles (10°-30°) compared to higher elevations (30°-90°).

Table 16– Average of the 95% percentile of the multipath estimated for each station on the days analyzed.

Station	MP1 (m) 10 to 30°	MP1 (m) 30 to 90°	MP5 (m) 10 to 30°	MP5 (m) 30 to 90°	CMCDFL1 (m) 10 to 30°	CMCDFL1 (m) 30 to 90°	CMCDFL5 (m) 10 to 30°	CMCDFL5 (m) 30 to 90°
PRU2	0.343	0.128	0.343	0.128	0.343	0.128	0.195	0.128
PRU4	0.314	0.138	0.314	0.138	0.314	0.138	0.144	0.138
DMC1	0.283	0.115	0.283	0.115	0.283	0.115	0.138	0.115
MOR3	0.251	0.110	0.251	0.110	0.252	0.110	0.116	0.110
STAV	0.284	0.093	0.284	0.093	0.284	0.093	0.159	0.093
STPZ	0.281	0.115	0.281	0.115	0.281	0.115	0.156	0.115

For instance, PRU2 shows 0.343m errors for MP1 at low elevations versus 0.128m at high elevations. This pattern holds true across all stations and processing methods, confirming that signal paths near the horizon are more susceptible to multipath interference. The CMCDF method proves particularly effective in reducing extreme errors, with PRU4's L1 errors decreasing from 0.314m (MP) to 0.144m (CMCDF) at low elevations.

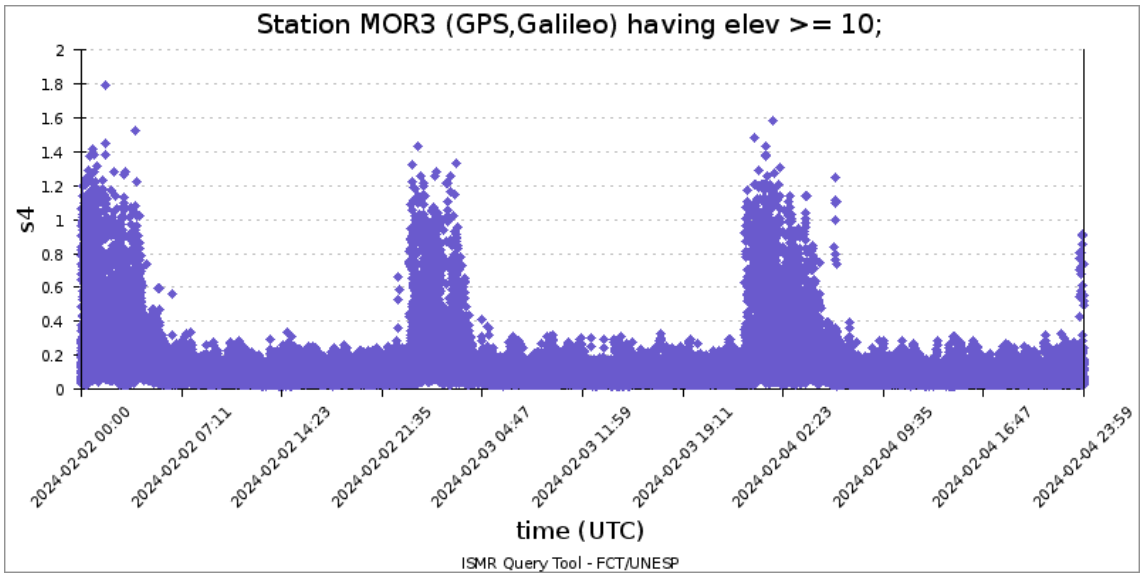
While the MP values show identical results for L1 and L5 frequencies, the CMCDF-processed data reveals L5's superior performance. At MOR3 station, CMCDFL5 errors (0.110m) are slightly lower than CMCDFL1 (0.116m) at low elevations, suggesting better multipath resistance in the modern L5 signal. This advantage becomes more pronounced when comparing the reduction ratios from MP to CMCDF values across frequencies.

6. GBAS EXPERIMENTS AND RESULTS

In this work, the GBAS DFDC was conducted for two categories: CAT I SF L1 and CAT I IFree. The study was based on the GBAS UNESP Experimental architecture described in Chapter 4, which includes four reference stations and two stations configured as aircraft in static mode, but with the data processed as kinematic.

The performance was analyzed on days characterized by high ionospheric scintillation (DOY 33 to 35, 2024, or February 2 to February 4, 2024). As shown in Figure 41, these days experienced scintillation with S4 values exceeding 0.6, which, according to Muella et al. (2009), is classified as strong. Scintillation events occurred both before and after midnight. Since Figure 41 is in UTC time, the corresponding local time is approximately after sunset, considering the -3 hour conversion.

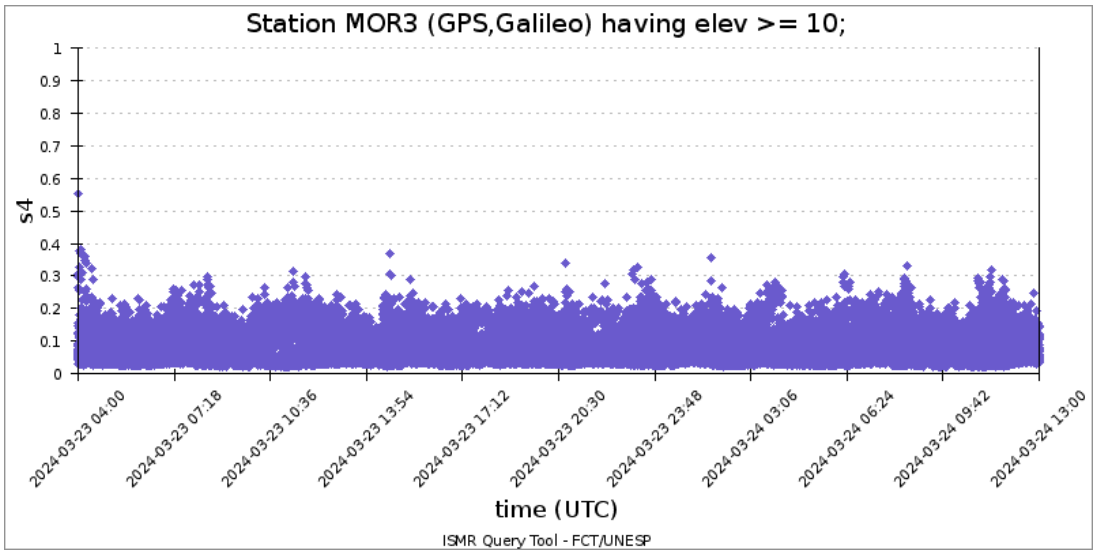
Figure 41 – S4 index in the high ionospheric scintillation scenario.



Additionally, the analysis was conducted over three days with low scintillation (DOY 83 to 85, 2024, or March 23 to March 26, 2024). However, this period encompassed only 66 hours rather than the full 72 hours corresponding to three complete days. This discrepancy resulted from scintillation occurring at the beginning of DOY 83 and at the end of DOY 85. Moreover, it was challenging to identify days with complete

datasets and consistent receiver configurations aligned with the implementation.

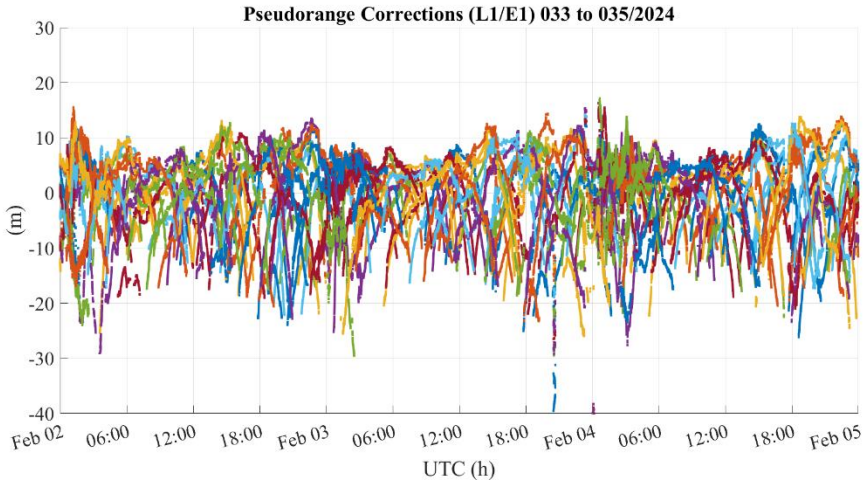
Figure 42 – S4 index in the low ionospheric scintillation scenario.



6.1. GBAS CAT I SF L1: High Ionospheric Scintillation Scenario

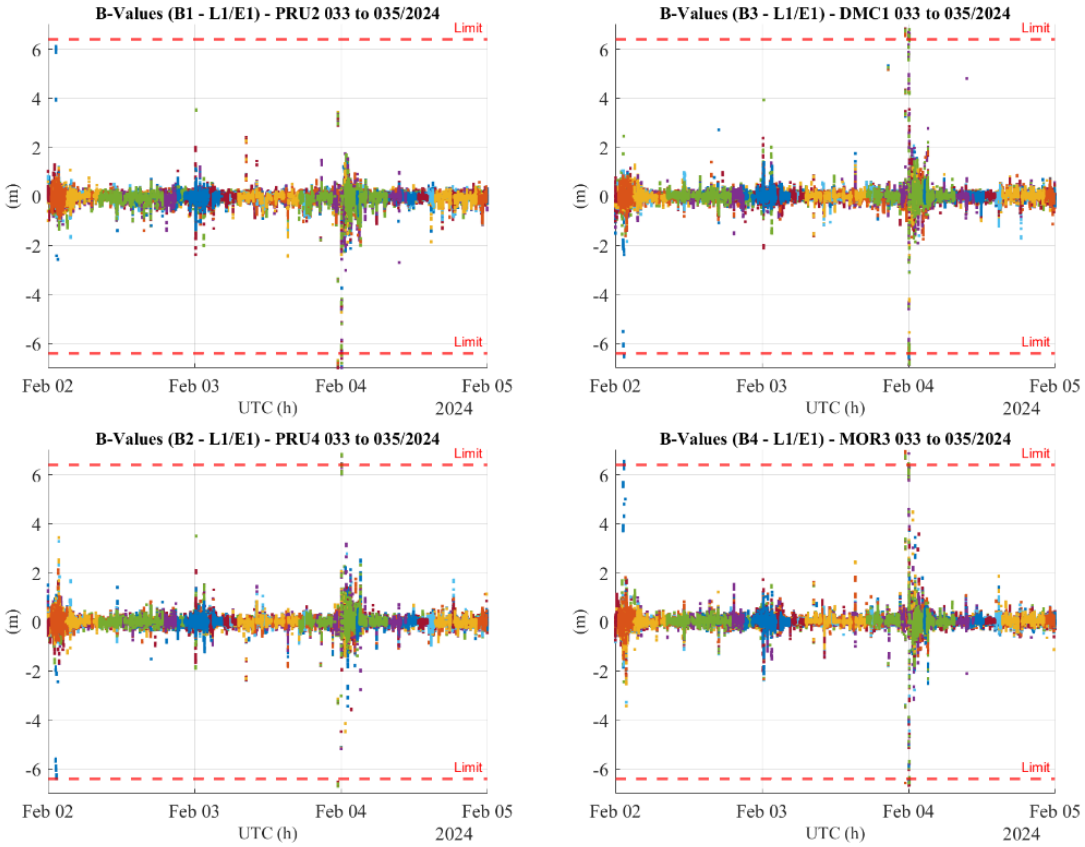
As previously mentioned, the ground system configuration and receiver are the same for both the STAV and STPZ stations, which were used as the aircraft in this experiment. Consequently, the results were applicable to both stations. The differential corrections generated by the Ground System for all GPS and Galileo satellites (on L1 and E1) are shown in Figure 43. The parabolic pattern predicted in the literature (SILVA and MONICO, 2022) is evident. For most of the time, the corrections range between approximately 20 m and -30 m. However, around midnight on DOY 035/2025, the corrections reach values of -40 m and 20 m, likely related to the scintillation activity at that moment.

Figure 43 – Pseudorange Corrections for L1/E1 for the period from 033 to 035/2025.



These corrections represent the average of the four reference stations. The consistency of each station's contribution to this correction can be assessed through the B-Value integrity parameter, shown in Figure 44. This indicator is calculated for each station, and the closer its value is to zero, the more consistent the station's corrections are. As observed, most B-Values fall within the -1 m to 1 m range, with some peaks exceeding -2 m and 2 m during periods of ionospheric scintillation. Additionally, the peaks of the highest PRC values (shown in Figure 43) align with the highest B-Values across all stations. It is important to note that the B-Value serves as a quality control parameter; if it exceeds an absolute value of 6.4 m, the satellite's differential correction is not utilized.

Figure 44 – Ground integrity parameter B-Values calculated by the ground system for the period from 033 to 035/2025.



Statistically, the performance of the B-Values can be evaluated using indicators such as the mean, standard deviation, and the 95th percentile of the values obtained from each station (Table 17). It becomes evident that the PRU2 station exhibited more discrepant corrections compared to the average of the other stations. Notably, the 95th percentile of the B-values for PRU2 were higher than those observed at the other stations. This noisier pattern of PRU2 was further corroborated by the multipath analysis presented in Chapter 5.

Table 17– Statistical indicators of the B-Values for the reference stations during periods of high ionospheric scintillation.

B-Values/ Station	Mean (m)	Standard deviation (m)	Percentile 95% (m)
B1 - PRU2	-0.051	0.246	0.347
B2 - PRU4	0.009	0.312	0.237
B3 - DMC1	0.016	0.213	0.221
B4 - MOR3	0.026	0.237	0.217

Another function performed on the ground system is the detection of anomalous ionospheric gradients. Figure 45 shows the ionospheric gradient values calculated by the Time-Step Method for the MOR3 station representing the ground system every 1 min using observations at L1 and L5. It can be seen that the gradient values are high during the occurrence of ionospheric scintillation. It is important to note that in the context of this work this monitor did not exclude satellite measurements, this function was performed by the cycle slip and CCD monitors.

Figure 45 – Ionospheric Gradient Monitoring for Ground System and Aircraft System for the period 033 to 035/2024.

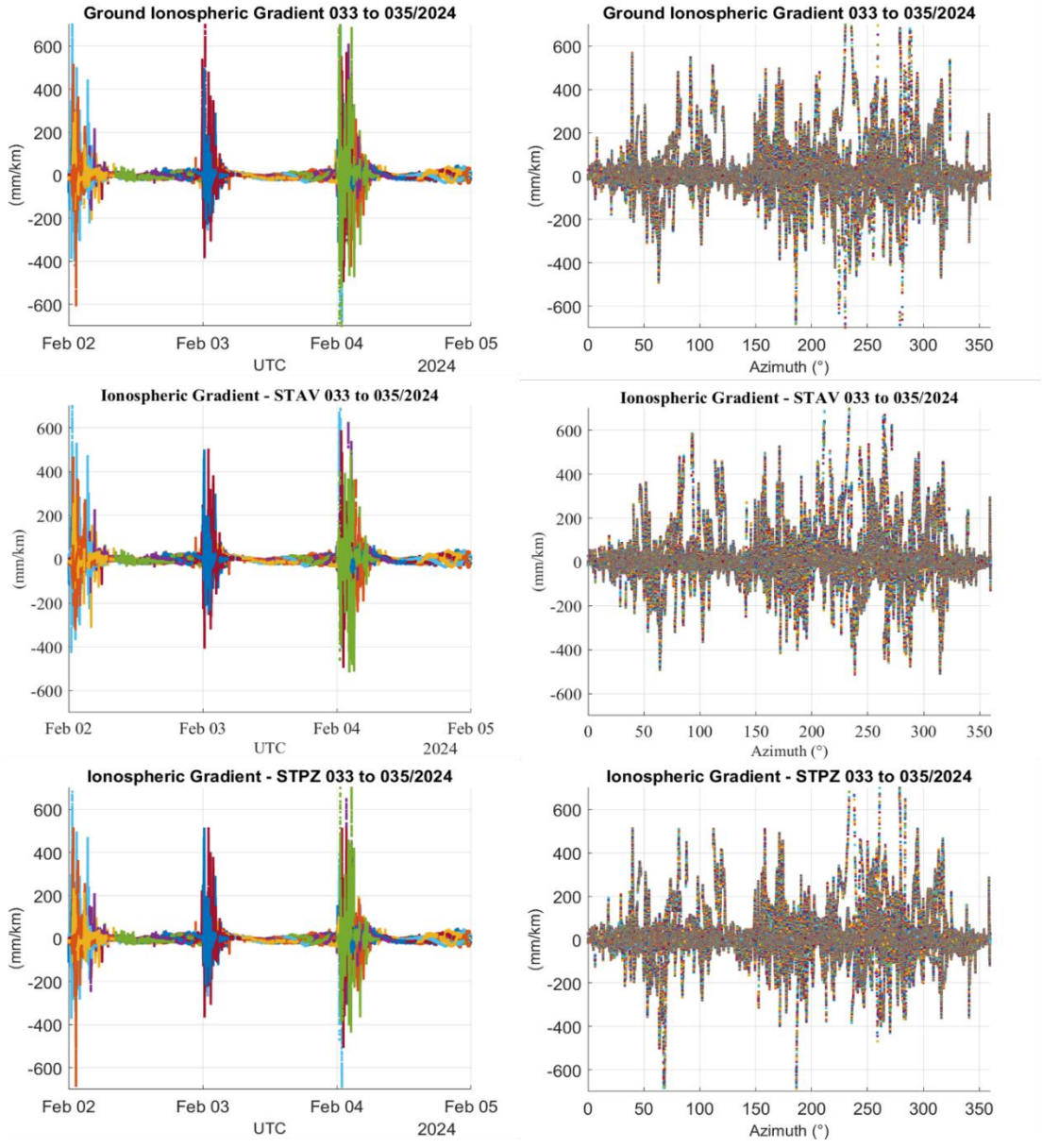
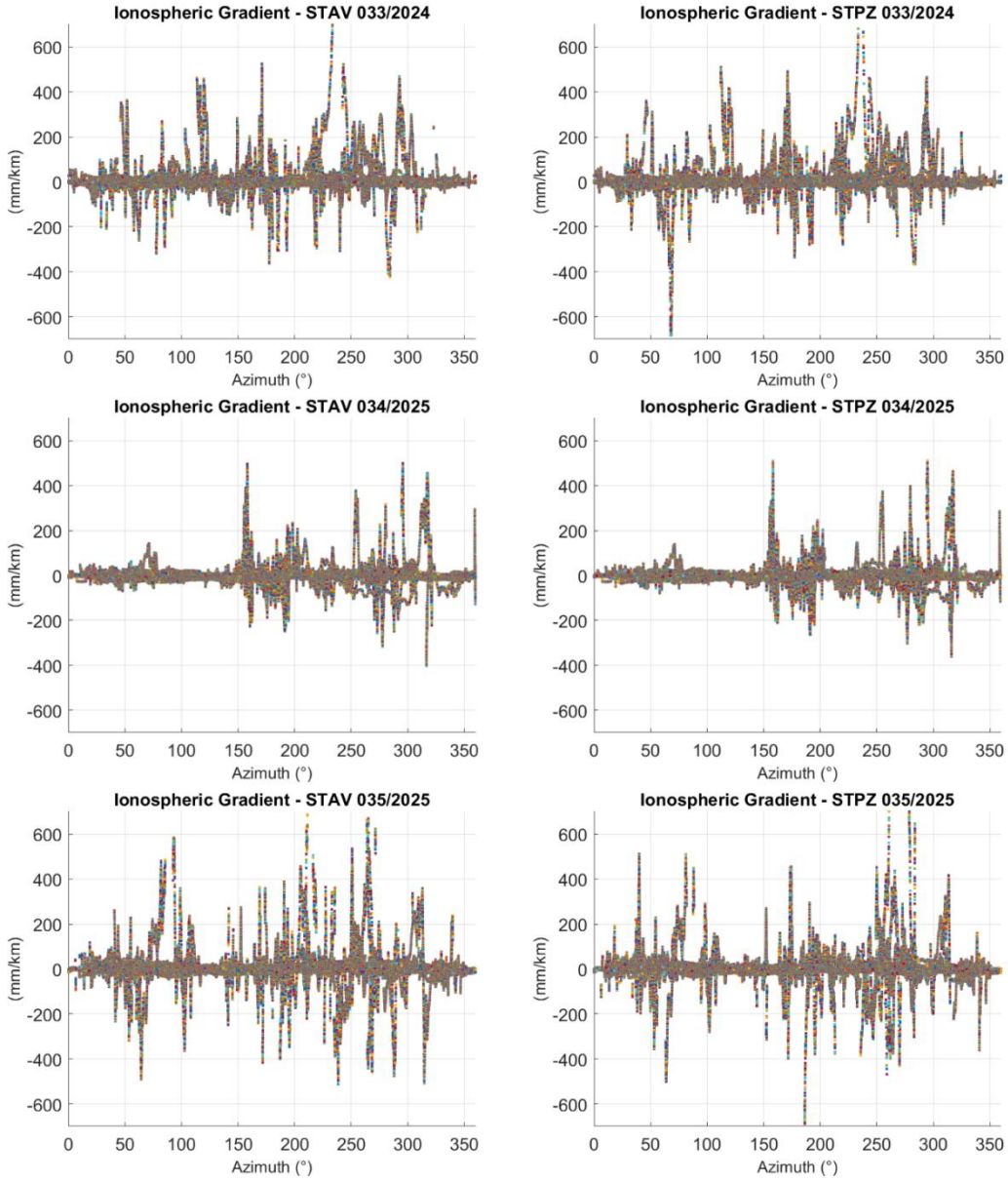


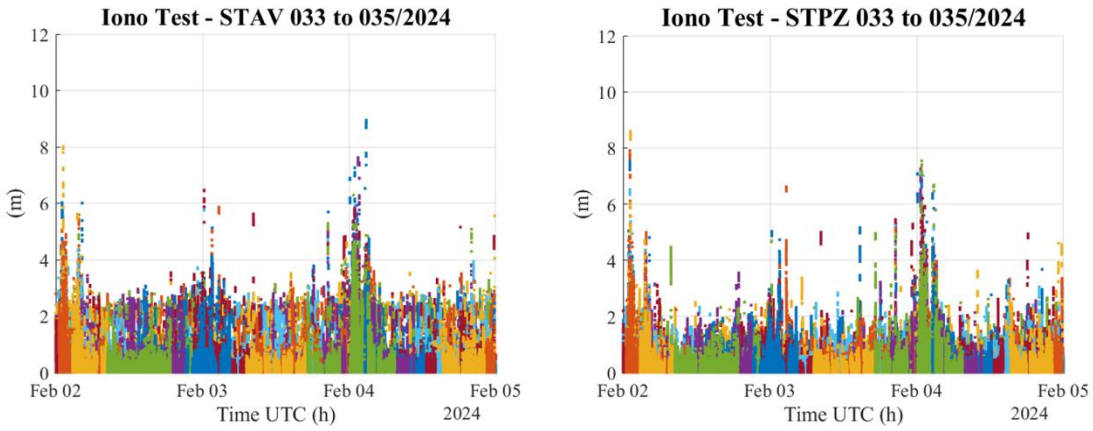
Figure 46 also shows that, during the analyzed days, the highest ionospheric gradient peaks are observed in the azimuth direction of approximately 200°, ranging from southwest to northwest. However, a detailed daily analysis reveals some peculiarities in the behavior of ionospheric gradients at the stations used as aircraft. On DOY 034/2024, ionospheric gradients exceeding 200 mm/km were observed for satellites located between azimuths of 150° and 360° (from south to north) at both the STAV and STPZ stations. Additionally, on DOY 033/2024, at the STPZ station around an azimuth of 70°, ionospheric gradient values reached approximately -700 mm/km, indicating significant localized variations.

Figure 46 – Spatial distribution of ionospheric gradients at STAV and STPZ stations for DOYs 033, 034 and 035/2024.



In addition to analyzing the gradients, the statistical Iono Test was conducted at the aircraft level to evaluate the ionospheric delay between ground and aircraft stations, as described in Subsection 2.3.2. Figure 47 presents the Iono Test values for the STAV and STPZ stations. It is evident that during periods of ionospheric scintillation, there are peaks indicating greater discrepancies in the ionospheric delay. In the Iono Test, the closer the ionospheric delays of the aircraft and ground stations are to zero, the higher the correlation between them

Figure 47 – Iono Test estimates for STAV and STPZ aircraft in DOYs 033 to 035/2024.



Visually, as shown in Figure 47, the Iono Test values for the two stations were very similar and exhibited comparable patterns during the analyzed period. Statistically, it can be concluded that the STPZ station had a higher correlation of ionospheric delay with the ground stations. Table 18 indicates that the mean, standard deviation, and 95th percentile values for STPZ were lower than those for STAV. A possible explanation for this difference relates to the stations' locations and the movement of the ionospheric front. Specifically, the STPZ station is aligned along a north-south direction, while the STAV station is oriented east-west relative to the base stations. Since the ionospheric front moves from east to west, the ionospheric gradients observed at the reference stations differ slightly from those at STAV. It is important to emphasize that, for this work, the Iono Test was used solely for monitoring ionospheric conditions on the ground and aircraft; it was not employed to exclude any data.

Table 18 – Statistical indicators of the Iono Test estimate for the STAV and STPZ stations in the period 033 to 035/2024.

Iono Test statistical	STAV	STPZ
Mean	0.379 m	0.312 m
Standard deviation	0.536 m	0.397 m
Percentile 95%	1.603 m	0.952 m

In the aircraft system, the coordinates of the STAV station were calculated, as well as the position errors and protection levels. Figures 48 and 49 show the performance of the horizontal and vertical components respectively. A pattern of peaks in position errors and protection levels is observed during periods of ionospheric scintillation, particularly on DOY 033/2024 (February 2, 2024), when the HPL exceeds the HAL

Figure 48 – GBAS performance CAT I SFL1 for the horizontal position at the STAV station during the period of high ionospheric scintillation.

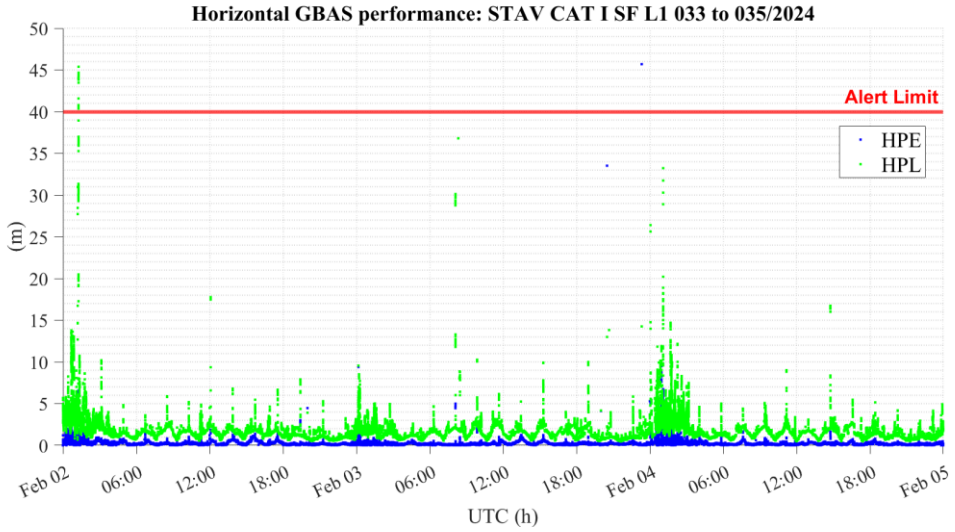
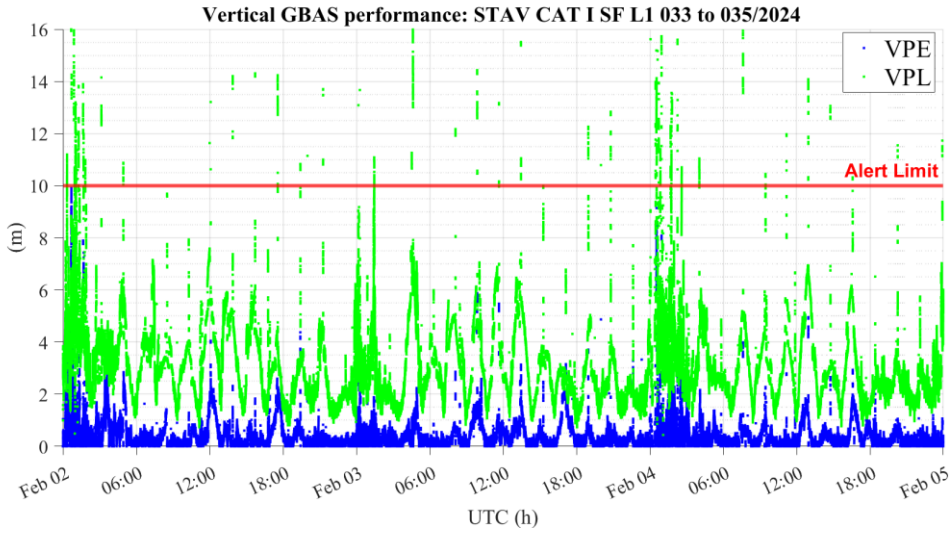


Figure 49 – GBAS performance CAT I SFL1 for the vertical position at the STAV station during the period of high ionospheric scintillation.

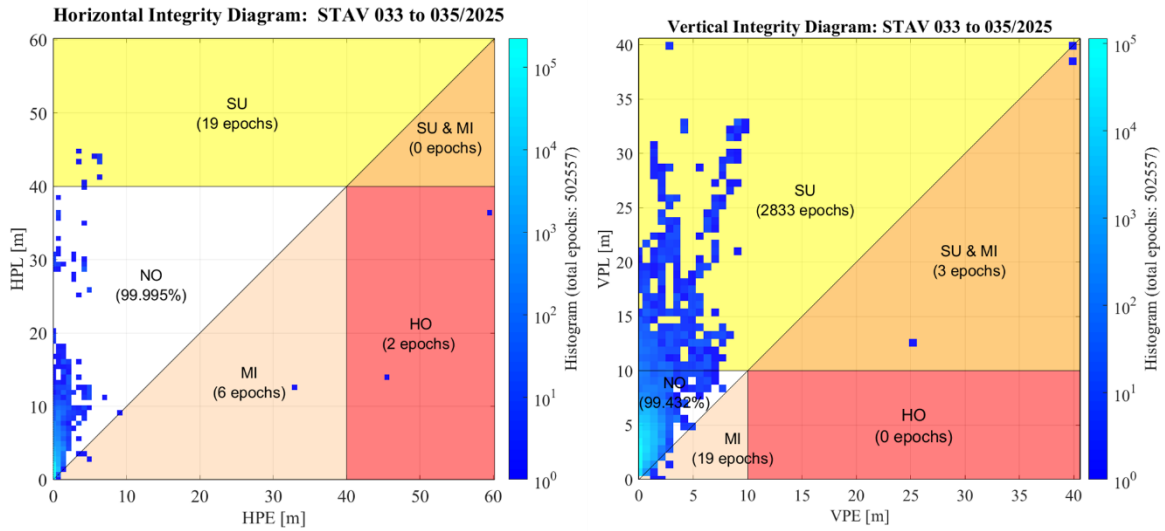


It is important to note that the different scales used in Figures 48 and 49 are due to the higher alert limit for the horizontal component compared to the vertical one. The vertical alert limit is 10 m, and it is visually evident that the vertical component exhibits more periods with higher VPL than VPE, especially during ionospheric scintillation events on DOY 033 and 035/2024 (February 2 to 4, 2024).

In this study adopted horizontal and vertical alert limits (40 m and 10 m, respectively) correspond to the decision distance for CAT I, defined as 1,163 m from the reference stations. In contrast, the distances from STAV and STPZ to the reference stations are 9,800 m and 13,000 m, respectively. If HAL and VAL were computed for these greater baselines, the resulting values would be higher, potentially leading to fewer integrity loss events due to overlapping alert limits.

The GBAS performance, as indicated by the time series of position errors and protection levels, can also be assessed in Figure 50. This figure shows the percentages of GBAS CAT I operational conditions (NO) for both the horizontal and vertical components, along with the number of epochs with integrity events: system unavailable (SU), misleading information (MI), and hazardously misleading information (HMI). Out of 518,400 epochs of GNSS data recorded over the three days, 502,557 contained a GBAS positioning solution. For the remaining 15,843 epochs, about 2.2 hours, there was no solution due to data quality monitoring, including cycle slip detection, restart smoothing filter, CCD, and position adjustment.

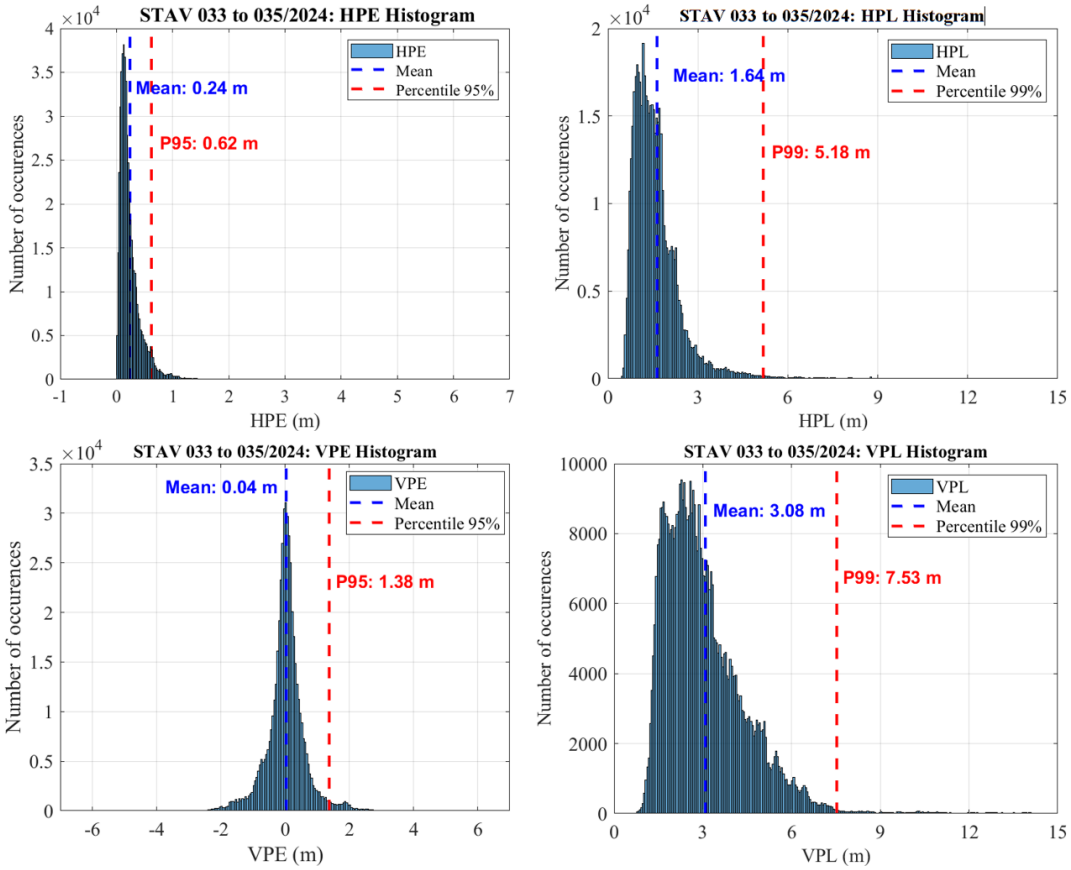
Figure 50 – Integrity diagram for the horizontal and vertical components of GBAS CAT I SFL1 for the STAV station during the period of high ionospheric scintillation.



Considering the epochs processed, GBAS achieved more than 99 per cent operational conditions in both components (99.995 per cent at horizontal and 99.432 per cent at vertical), i.e. with position errors lower than the protection levels, and both lower than the horizontal and vertical alert limits. In the vertical component there were 2207 epochs (around 18 minutes) of system unavailable (SU) compared to 54 epochs in horizontal position.

Another analysis of position errors and protection levels is presented in Figure 51, along with their respective histograms. For the horizontal component, the mean HPE was 0.24 m, while the mean VPE was 0.04 m. In the vertical component, both positive and negative errors were considered; the HPE is calculated from the resulting errors in the North and East components, which explains why its histogram contains only positive values. According to GBAS accuracy requirements, 95% of the HPE values are at or below 0.64 m, and the 95th percentile of the VPE was 1.64 m. These values satisfy the accuracy performance criteria established for CAT I, as outlined in Table 2.

Figure 51 – Histograms of positioning errors and protection levels for GBAS CAT I SFL1 at the STAV station during a period of high ionospheric scintillation.



In terms of protection levels, the values for the horizontal component were also better than those for the vertical component. The HPL had an average of 1.64 m and a 99th percentile of 5.18 m, whereas for the VPL, the respective values were 3.08 m and 7.53 m. Regarding the protection levels, the performance requirement is more stringent and should be represented by the 99th percentile to ensure greater safety, continuity, and availability, as the protection levels reflect uncertainty regarding positioning errors. Although the 99th percentile of the VPL is below 10 m (alert limit), the time series plots and the histogram itself indicate that, particularly under ionospheric scintillation conditions, the VPL exceeds this alert limit.

The performance of the STPZ station was similar to that of the STAV station. As observed in the time series of position errors and protection levels (Figures 52 and 53), the most critical periods occurred during the ionospheric scintillation events in the early hours and at the end of each day. During these periods, the protection levels exceeded the alert thresholds, particularly on DOYs 33 and 35 for the vertical component.

Figure 52 – GBAS performance CAT I SFL1 for the horizontal position at the STPZ station during the period of high ionospheric scintillation.

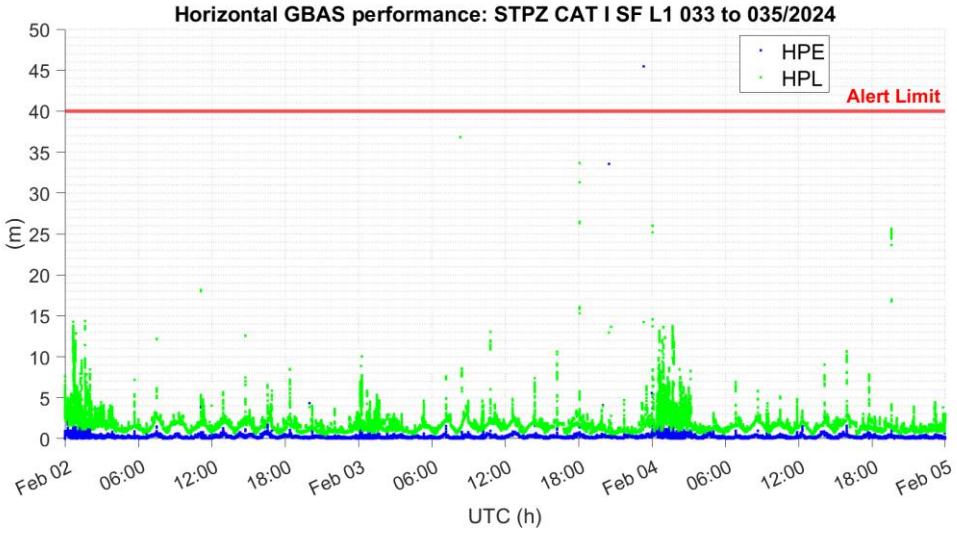
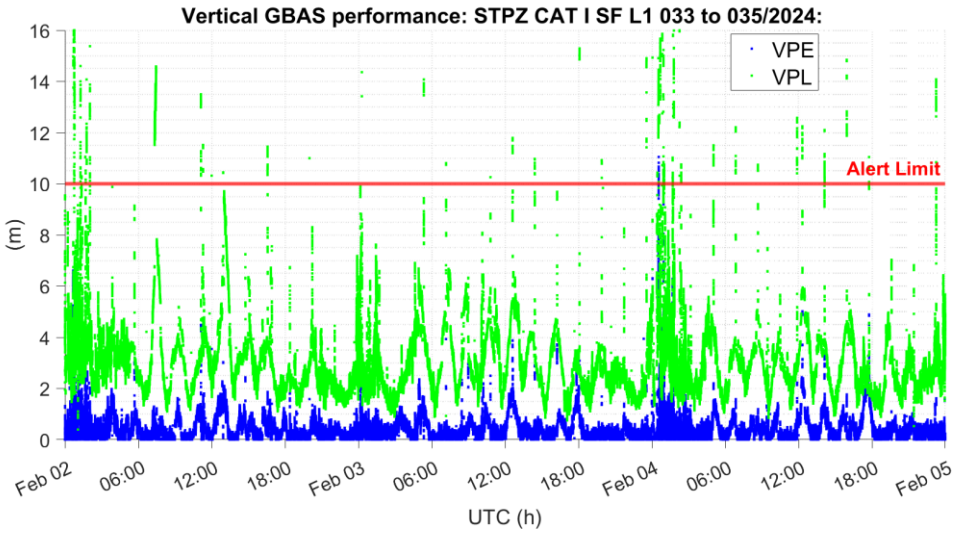
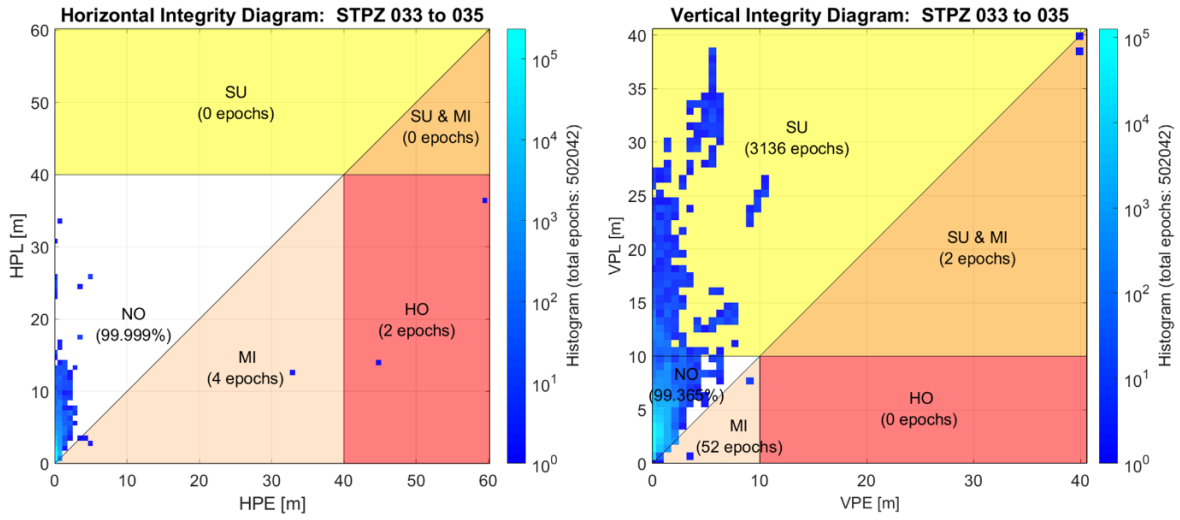


Figure 53 – GBAS performance CAT I SFL1 for the vertical component at the STPZ station during the period of high ionospheric scintillation.



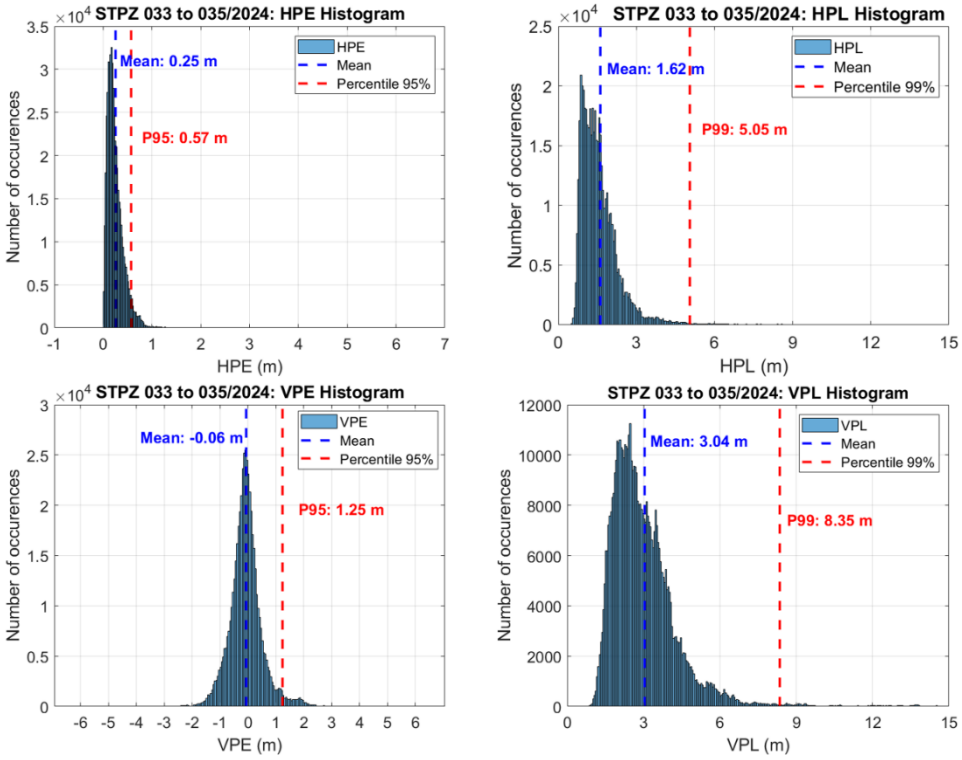
These values of position errors and protection levels ensured 99.999% availability of CAT I operational conditions for the horizontal position and 99.432% for the vertical component. Beyond these values, the Integrity Diagram reveals that during 3,136 epochs (approximately 26 minutes), the GBAS was unavailable due to non-compliance with vertical component requirements. Additionally, there were 52 epochs of misleading information, where the VPE exceeded the VPL but remained below the alert limit.

Figure 54 – Integrity diagram for the horizontal and vertical component of GBAS CAT I SFL1 for the STPZ station during the period of high ionospheric scintillation.



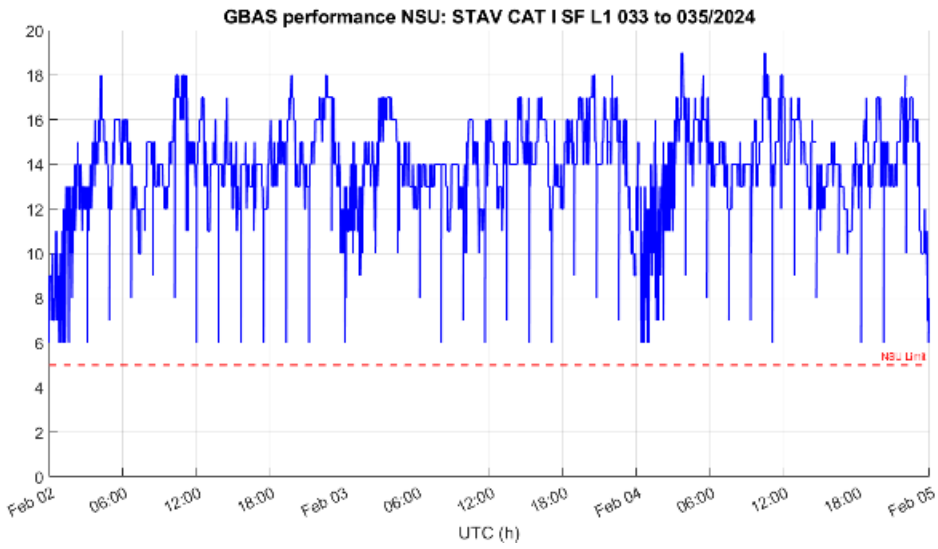
Similar to the performance of STAV, the histograms of position errors and protection levels for the STPZ station reinforce compliance with CAT I requirements, maintaining the 95th percentile of vertical errors below 4 m and the 99th percentile of the VPL below 10 m. However, it is important to highlight that there were 3,136 epochs of GBAS unavailability. If these epochs occur continuously, they could compromise precision approaches using GBAS.

Figure 55 – Histograms of positioning errors and protection levels for GBAS CAT I SFL1 at the STPZ station during a period of high ionospheric scintillation.



The GBAS performance shown for both STAV and STPZ that the aircraft is affected by varying satellite geometry, as expected. In this work it has been configured in a such way that the ground system and the aircraft use the same satellites. Thus, Figure 56 shows the number of satellites for the STAV station, which are the same for STPZ. In the period analyzed the number of satellites varies from 19 to 6 satellites (6 satellites are the minimum for redundancy in the dual constellation position adjustment). The periods with number of satellites used (NSU) of 6 satellites correspond to the periods when protection levels are the highest. According to Silva and Monico (2022), VPL is very susceptible to variation in the satellite geometry. Such low number of satellites is a consequence of using CCD cycle slip monitors that excluded satellites for at least 100 seconds once a slip is flagged.

Figure 56 – Number of satellites used in GBAS STAV (CAT I SF L1) in DOY 033 to 035/2024.



The consequence of the application of the monitors is illustrated in Figures 57 and 58, which shows the status of each satellite during the period analyzed. Satellites marked in green indicate available with usable data, while red denotes cycle slip occurrences and blue represents CCD failures. Satellites numbered 1 to 32 correspond to GPS, and 71 to 106 refer to Galileo.

The inclusion of the Galileo constellation proves be beneficial, as GPS satellites exhibit higher occurrence of cycle slips and CCD failures at both STAV and STPZ stations. These occurrences are aligned with periods of elevated protection levels observed in Figure 53, leading to a temporary reduction of usable satellites.

Figure 57 – Status of GNSS signals on the L1/E1 carrier-phase at the STAV station from days 033 to 035 of 2024.

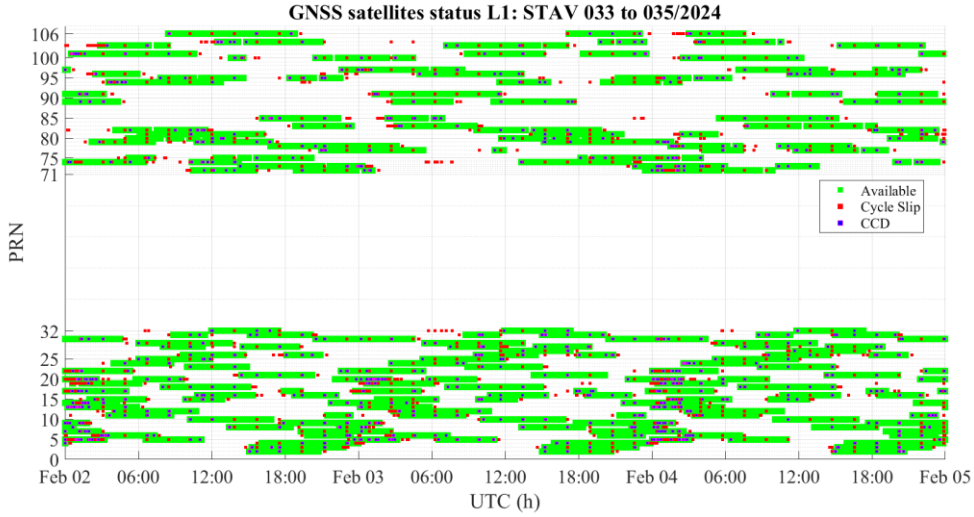
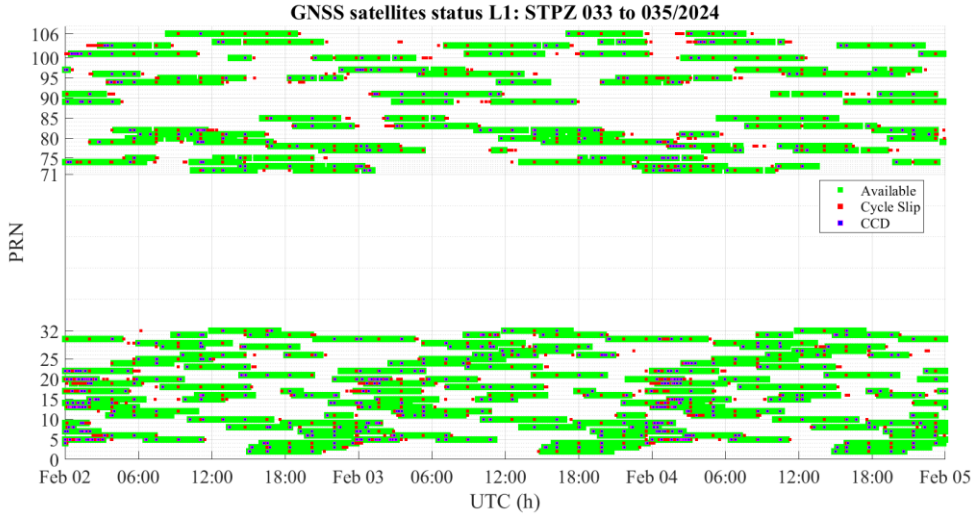


Figure 58– Status of GNSS signals on the L1/E1 carrier-phase at the STPZ station from days 033 to 035 of 2024.

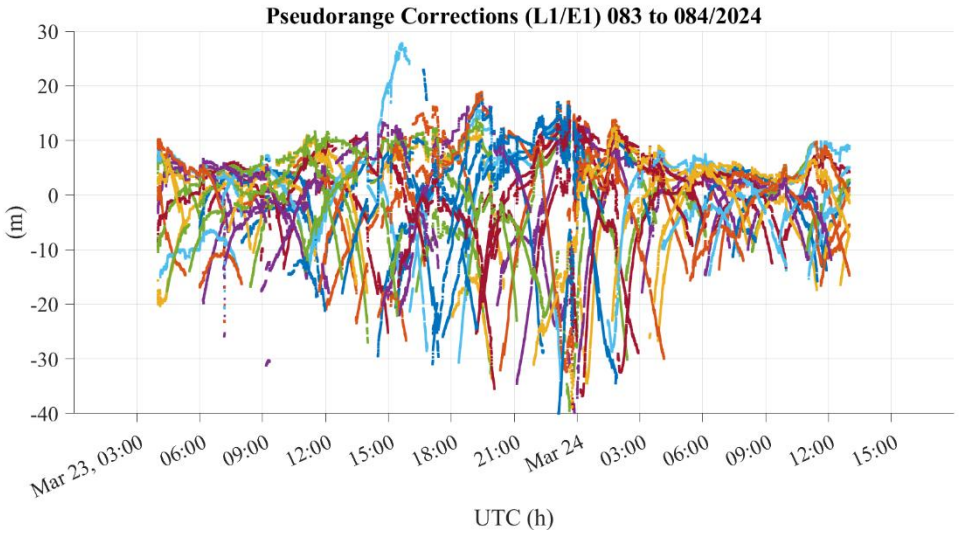


6.2. GBAS CAT I SF L1: Low Ionospheric Scintillation Scenario

The performance analysis scenario under low ionospheric scintillation corresponds to 34 hours of data, from 04:00 on March 23, 2024, to 13:00 on March 24, 2024 (DOY 83 and 84) as stated earlier. This period comprises a total of 237,600 data epochs. Figure 59 shows the differential corrections calculated by the ground-based system. Even in the absence of ionospheric scintillation, a correction peak exceeding 30 m was observed during the transition between DOY 83 and 84. The underlying cause of

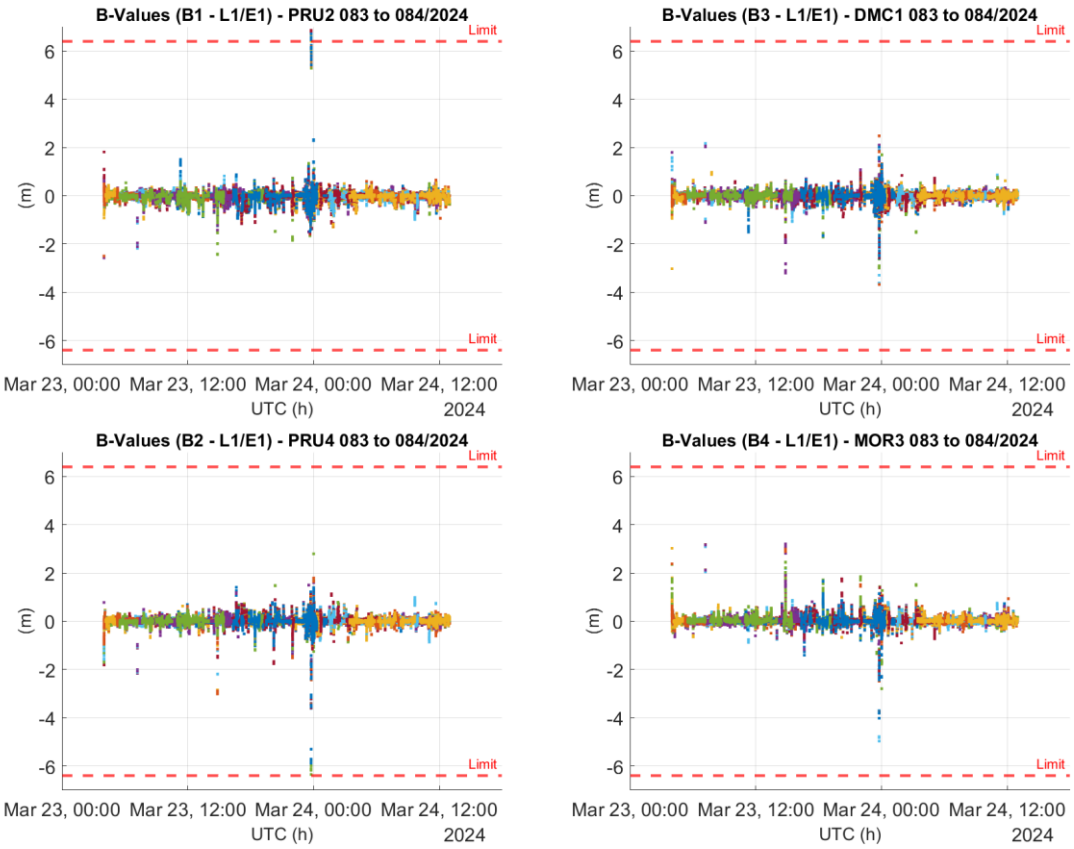
this event was not identified in this study. A possible explanation could be its association with satellites at low elevation angles, near 10°. However, such a characteristic would be expected across all satellites, which was not the case. Additionally, one can observe that the parabolic behavior of differential corrections is predominant.

Figure 59 – Pseudorange Corrections for L1/E1 for the low ionospheric scintillation scenario.



The analysis of the consistency of differential corrections from each reference station, conducted using the B-Values, indicates that the variation was generally low, predominantly ranging between -0.5 m and 0.5 m. Figure 60 presents the ground integrity parameter B-Values calculated by the ground system for the period from 083 to 084/2024. Notably, only the PRU2 reference station exhibited B-Values exceeding 6.4 m, suggesting potential anomalies in its differential corrections during this interval.

Figure 60 – Ground integrity parameter B-Values calculated by the ground system for the period from 083 to 084/2025.



Under low scintillation conditions, the PRU2 reference station exhibited the highest B-Values, particularly in terms of standard deviation (0.233 m) and the 95th percentile (0.379 m) (Table 19). In contrast, the other three stations demonstrated significantly lower values for these metrics compared to PRU2, indicating that PRU2 was the noisiest ground station within the system. It was already observed previously with the other data set.

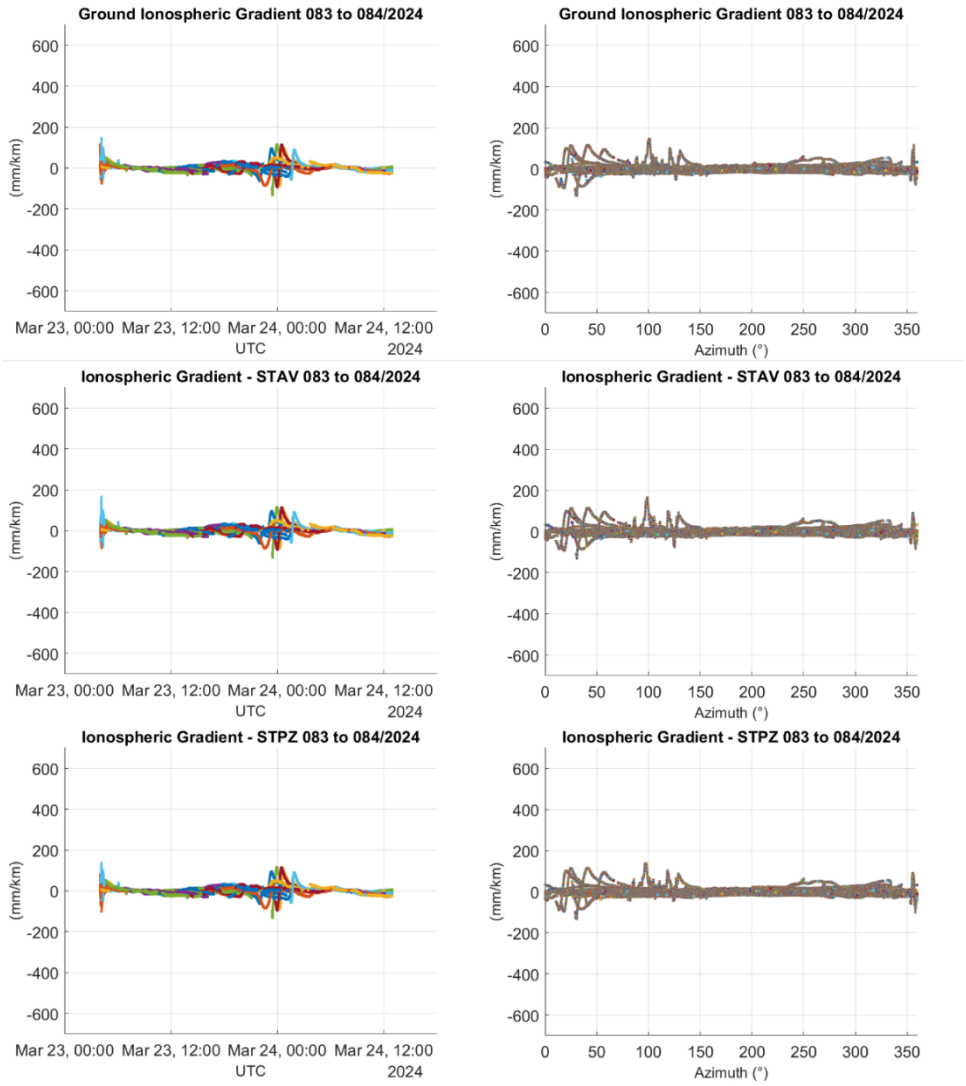
Table 19 – Statistical indicators of the B-Values for the reference stations during periods of low ionospheric scintillation.

B-Values/ Station	Mean (m)	Standard deviation (m)	Percentile 95% (m)
B1 - PRU2	-0.043	0.233	0.379
B2 - PRU4	0.007	0.140	0.219
B3 - DMC1	0.005	0.120	0.240
B4 - MOR3	0.031	0.124	0.230

The monitoring of ionospheric gradients during periods of low scintillation

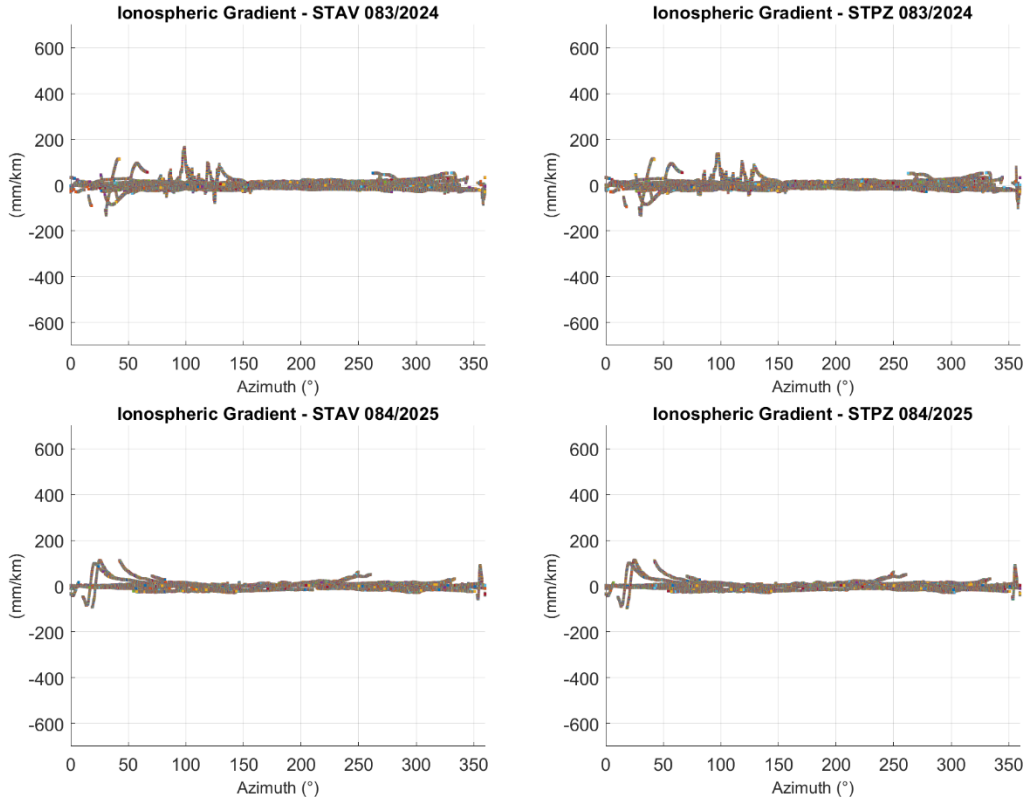
consistently revealed low magnitudes (below 200 mm/km in absolute values) across both the ground-based system and the two aircraft. The highest gradient values were observed during the transition to DOY 84, predominantly occurring within the 0° to 100° azimuth range, corresponding approximately to the north-to-east sector.

Figure 61 – Ionospheric Gradient Monitoring for Ground System and Aircraft System for the period 083 to 084/2024.



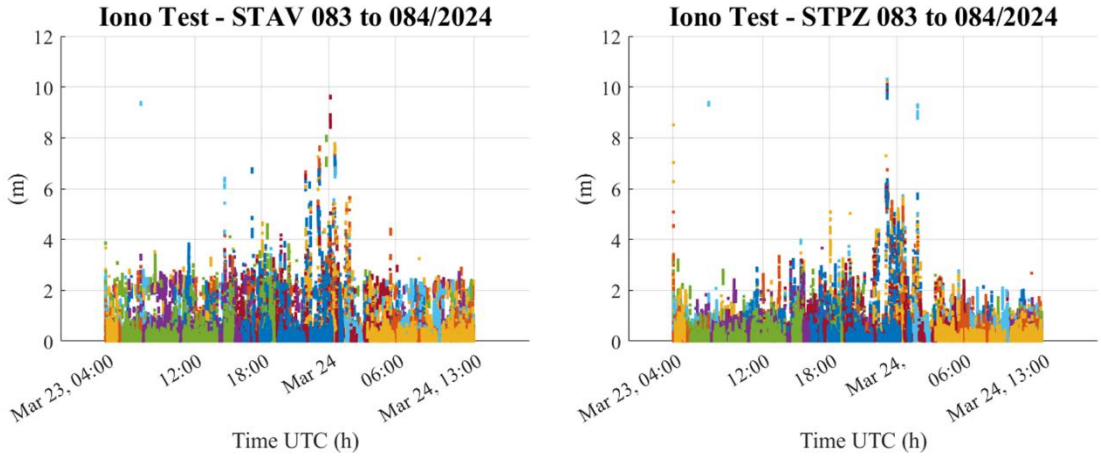
The daily analysis of ionospheric gradients for the STAV and STPZ reference stations (Figure 62) revealed similar gradient magnitudes at both locations. Distinct spatial variations were observed, particularly in the north-to-east azimuth sector (0° to 100°) during DOY 083. These variations became more concentrated (azimuth from 0° to 50°) during DOY 084.

Figure 62 – Spatial distribution of ionospheric gradients at STAV and STPZ stations for DOYs 083 and 084/2024.



The same small variation in the ionospheric gradient observed in the transition to DOY 084 can also be seen in the Iono Test. At both stations STAV and STPZ there was a peak in the estimated values at the beginning of DOY 084, although no ionospheric scintillation occurred.

Figure 63 – Iono Test estimates for STAV and STPZ aircraft in DOYs 083 to 084/2024.



It is interesting to note in Table 20 that the meaning, deviation and 95% percentile values for DOY 083 to 084/2024 are similar to the values obtained for the period with ionospheric scintillation. Again, the STPZ station presented lower Iono Test values than the STAV, indicating that there is a stronger correlation between the ionospheric delay and the ground stations.

Table 20 – Statistical indicators of the Iono Test estimate for the STAV and STPZ stations in the period 083 to 084/2024.

Iono Test statistical	STAV	STPZ
Mean	0.358 m	0.313 m
Standard deviation	0.557 m	0.487 m
Percentile 95%	1.601 m	0.974 m

Results from the aircraft system for the STAV station (Figures 64 and 65) showed that horizontal position errors and protection levels stayed below the alert threshold throughout the observation period. Although the HPL consistently remained below the alert limit, the HPE occasionally exceeded the HPL. In the vertical domain, both the VPL and VPE surpassed the vertical alert limit during certain intervals.

The protection level variations correlate strongly with the number of satellites available for positioning. The GBAS UNESP Experimental system's monitoring algorithms resulted in periodic satellite exclusions, which directly impacted the protection level. The identified characteristic, also observed during scintillation periods, suggests potential integrity-threatening events that could impact system continuity. These phenomena may lead to service interruptions, ultimately affecting the availability of GBAS-enabled precision approaches.

Figure 64 – GBAS performance CAT I SFL1 for the horizontal position at the STAV station during the period of low ionospheric scintillation.

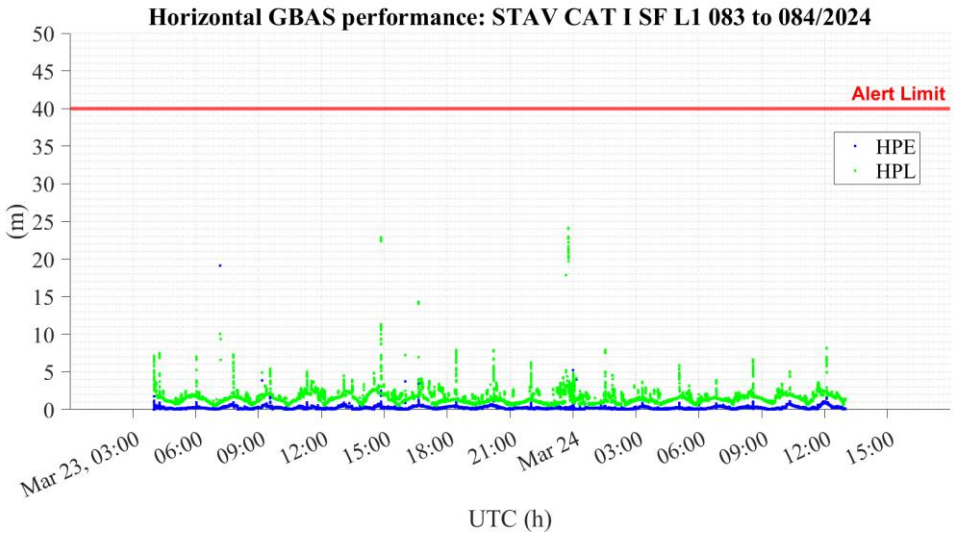
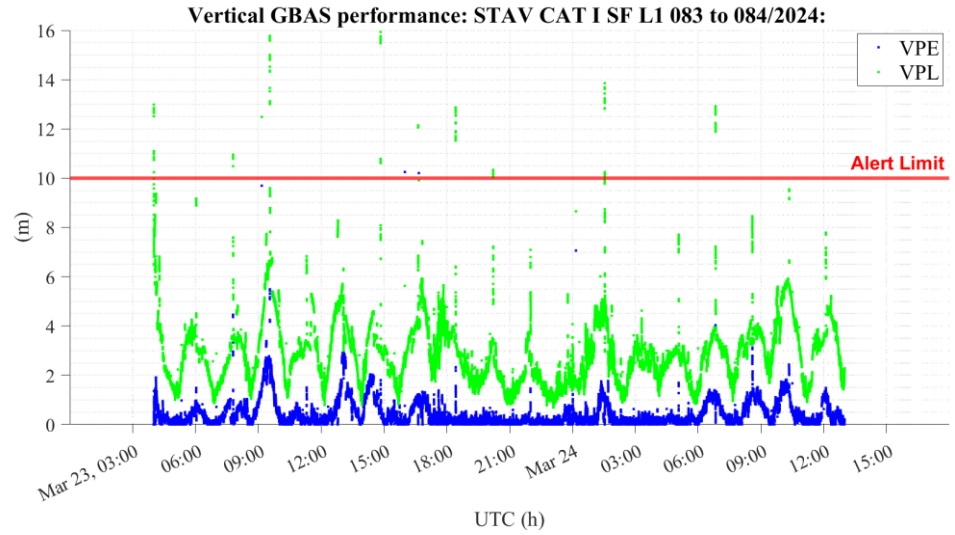


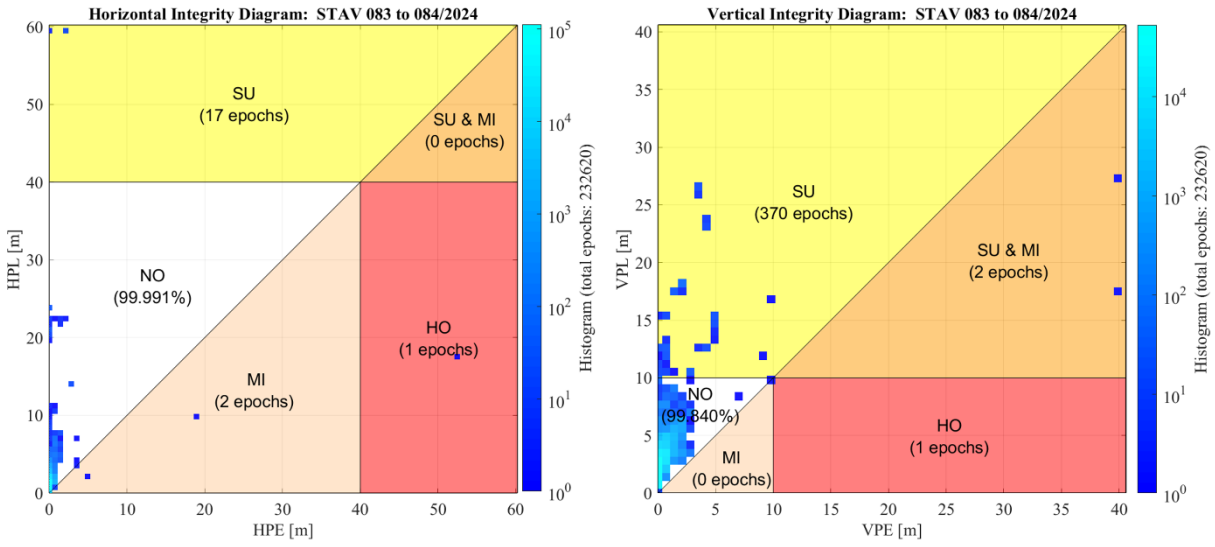
Figure 65 – GBAS performance CAT I SFL1 for the vertical component at the STAV station during the period of low ionospheric scintillation.



Analyzing the Integrity Diagram (Figure 66), for the vertical component, GBAS had 99.840% of the epochs with solutions under operational conditions for CAT I. In the horizontal position, this performance was 99.991%. A total of 232,620 epochs were processed as GBAS. Of these amounts, 17 was unavailable (with HPL greater than the alert limit) for the horizontal position, 2 with misleading information (HPE greater than HPL) and 1 with HPE greater than the alert limit (HO). In terms of the vertical component, there were more loss-of-integrity events with 370 unavailability (SU) epochs, 1 epoch with VPE greater than the alert limit, and 2 epochs in which both VPE and VPL were

greater than the vertical alert limit. On the other hand, for 4980 epochs there were no solutions as consequence and excluded because of the monitors applied by both ground and aircraft systems, taking into account cycle slip, high B-Values and CCD and quality control in positioning adjustment.

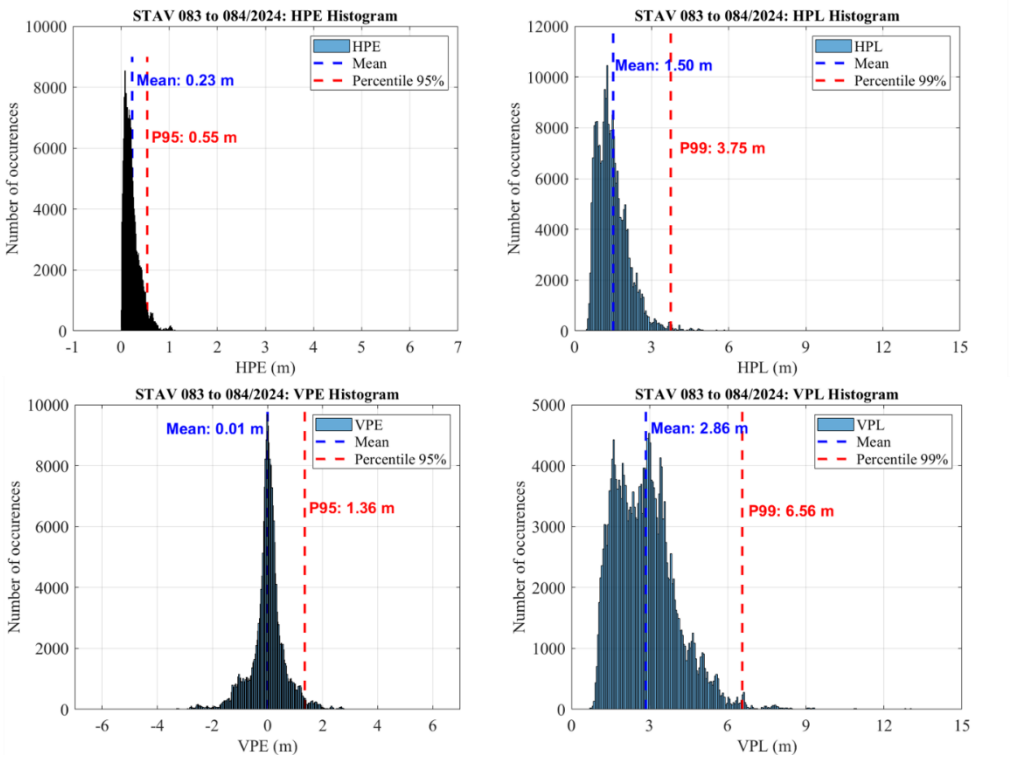
Figure 66 – Integrity diagram for the horizontal and vertical component of GBAS CAT I SFL1 for the STAV station during the period of low ionospheric scintillation.



Detailed analysis of GBAS CAT I performance during low ionospheric scintillation conditions is presented in the position error and protection level histograms (Figure 67). The system met all accuracy performance requirements, with 95th percentile values of 0.55 m (HPE) and 1.36 m (VPE) for horizontal and vertical position errors, respectively. Notably, the vertical component, which is more critically affected by systematic errors, was errors below the 4 m threshold required for CAT I precision approaches.

Protection level performance similarly complied with requirements, as demonstrated by 99th percentile values remaining below the alert limits. However, the epochs where the VPL exceeded 10 m may indicate potential challenges to the GBAS continuity requirement. The current analysis focuses primarily on accuracy and integrity metrics, with continuity performance reserved for future detailed examination

Figure 67 – Histograms of position errors and protection levels for GBAS CAT I SFL1 at the STAV station during a period of low ionospheric scintillation.



The results obtained for STPZ aircraft were similar to those of STAV. The time series of position errors and protection levels (Figures 68 and 69) were below the limits most of the time. In the vertical component, there were more occurrences of VPL exceeding the warning limit.

Figure 68 – GBAS performance CAT I SFL1 for the vertical component at the STPZ station during the period of low ionospheric scintillation.

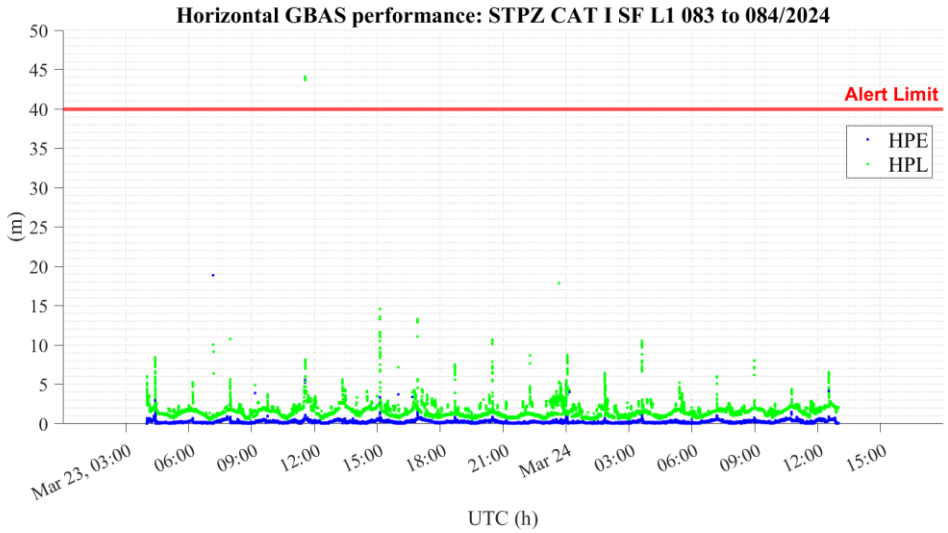
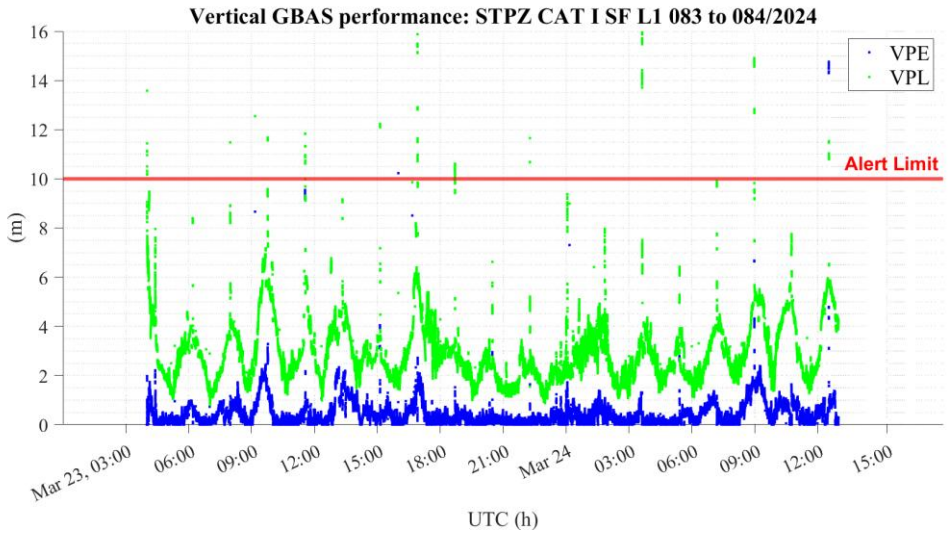


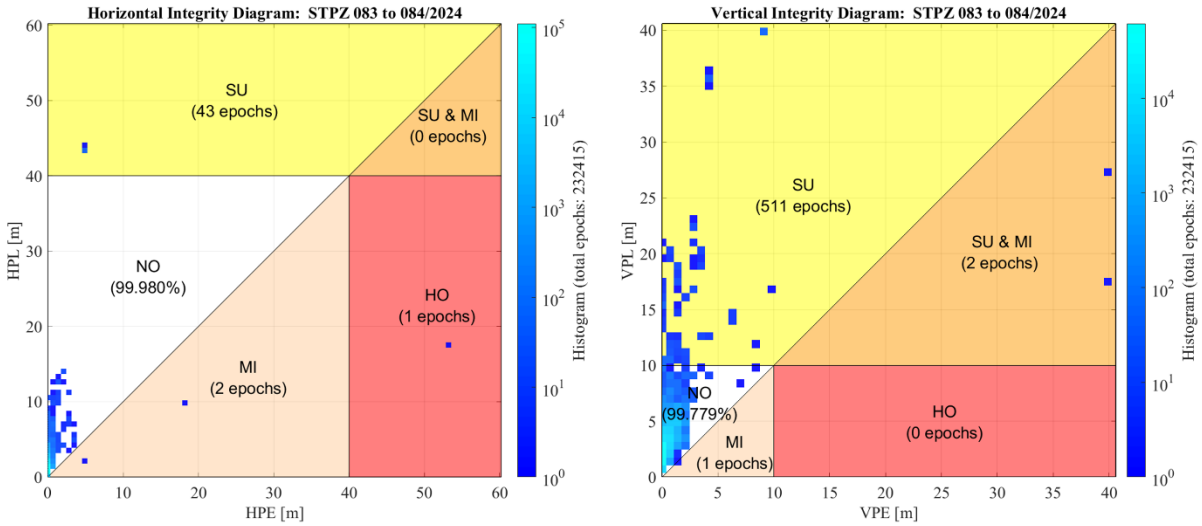
Figure 69 – GBAS performance CAT I SFL1 for the vertical component at the STPZ station during the period of low ionospheric scintillation.



Of the 237600 GNSS data epochs from this period, 232415 provide GBAS positioning solution. The remaining 5185 epochs without solution were due to the application of cycle slip monitors, resetting pseudorange smoothing, high CCD values and quality control in position adjustment.

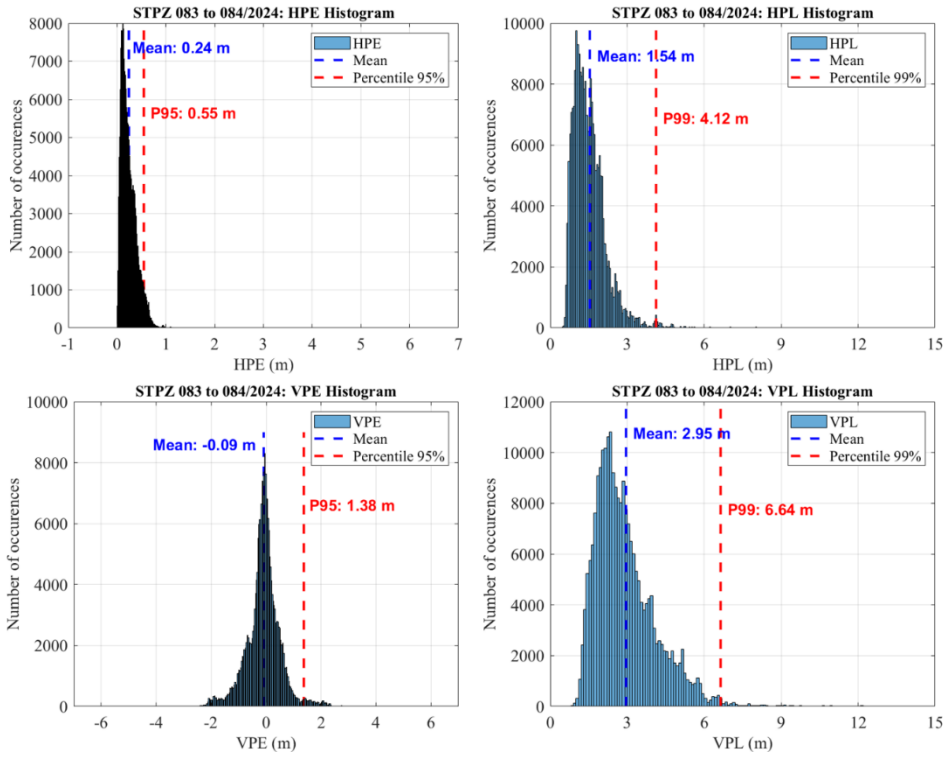
The Integrity Diagram shows that the STPZ station had 99.80% CAT I operability for the horizontal position and 99.779% for the vertical component. This almost identical performance differs when analyzing the loss of integrity events, because in the vertical component, there were 511 epochs of unavailable system, when VPL was higher than the alert limit, as well as 1 epoch of misleading information, and 2 epochs in which the VPL and VPE were higher than the alert limit. In the horizontal component, there were 43 epochs when the system was unavailable, 1 epoch of misleading information, and 2 epochs when the HPE was higher than the alert limit.

Figure 70 – Integrity diagram for the horizontal and vertical component of GBAS CAT I SFL1 for the STPZ station during the period of low ionospheric scintillation.



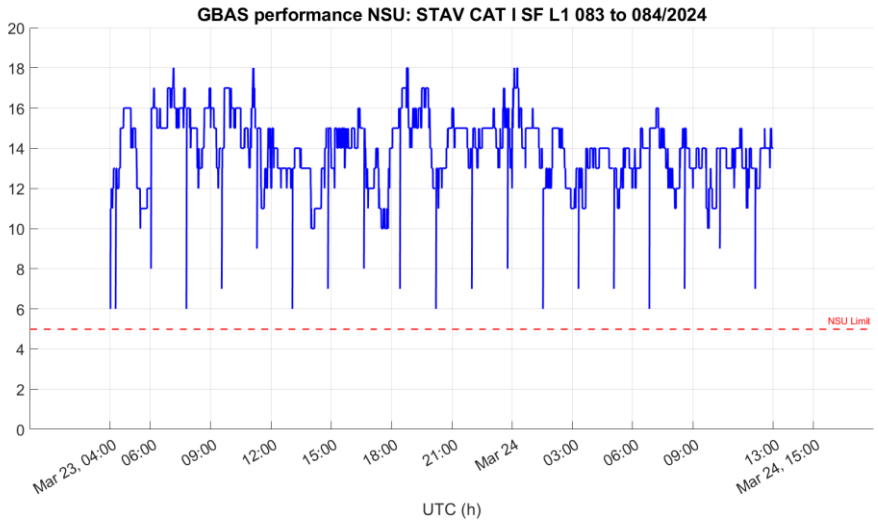
Analyzing the histograms of position errors and protection levels (Figure 71), one can again see that the accuracy performance requirements for CAT I were reached. The 95% percentile for HPE was 0.55 m and for VPE 1.38 m in absolute values. The performance requirement for protection levels is also met, with 99% percentile values of 4.12 m (HPL) and 6.64 m for VPL. Therefore, one concern with this performance is the fact that the VPL in some epochs exceeds the alert limit, which can have an impact on continuity.

Figure 71 – Histograms of position errors and protection levels for GBAS CAT I SFL1 at the STPZ station during a period of low ionospheric scintillation.



In the low ionospheric scintillation scenario, the geometry also affected GBAS performance in periods with NSU equal to 6. According to Figure 72, one can observe that NSU varied from 18 to 6 satellites, and this minimum number influenced the VPL values above the vertical alert limit shown in Figure 69.

Figure 72 – Number of satellites used in GBAS STAV (CAT I SF L1) in DOY 083 to 084/2024.



The observed variation in the number of satellite stems from cycle slip and CCD failures, as demonstrated in Figures 73 and 74. These figures depict the GNSS data series, highlighting periods of satellite availability and temporary exclusions. Following a cycle slip or CCD event, satellites underwent for a restart period of 100 seconds before returning to operational status.

Figure 73 – Status of GNSS signals on the L1/E1 carrier at the STAV station from days 083 to 084 of 2024.

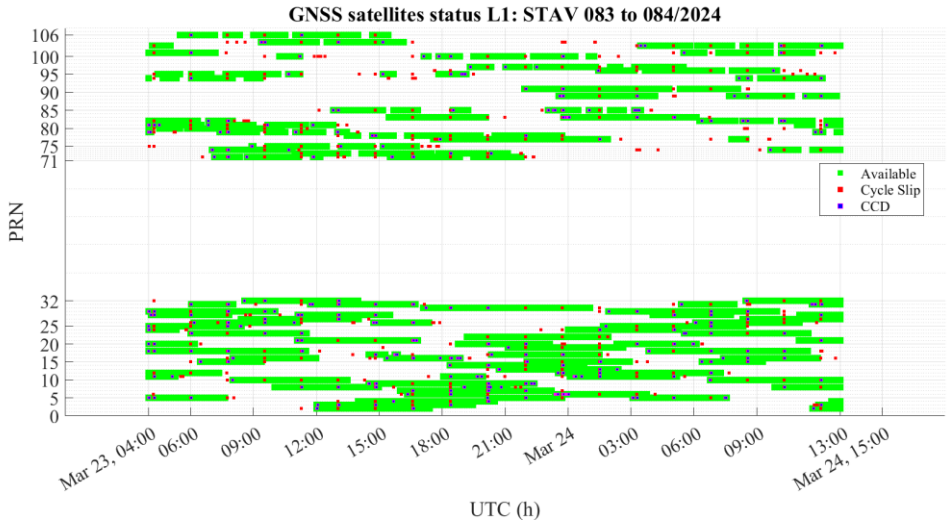
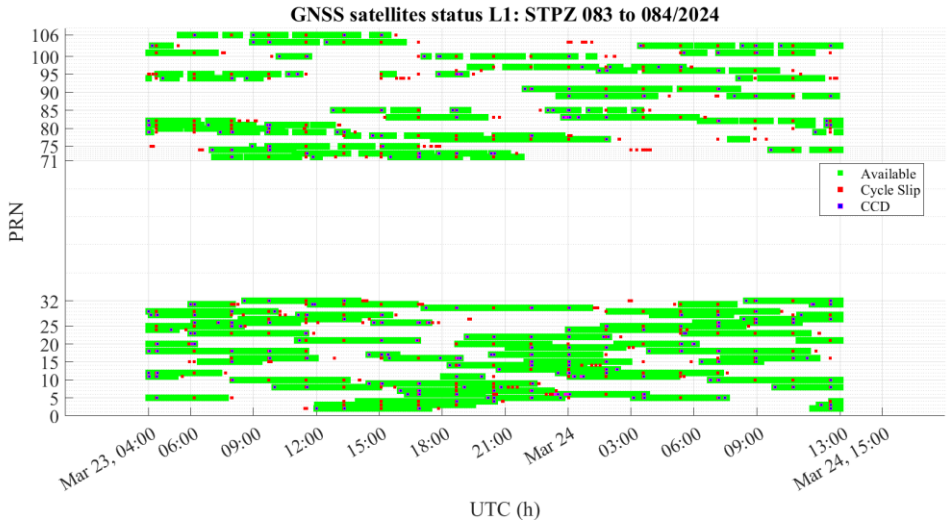


Figure 74– Status of GNSS signals on the L1/E1 carrier-phase at the STPZ station from days 083 to 084 of 2024.

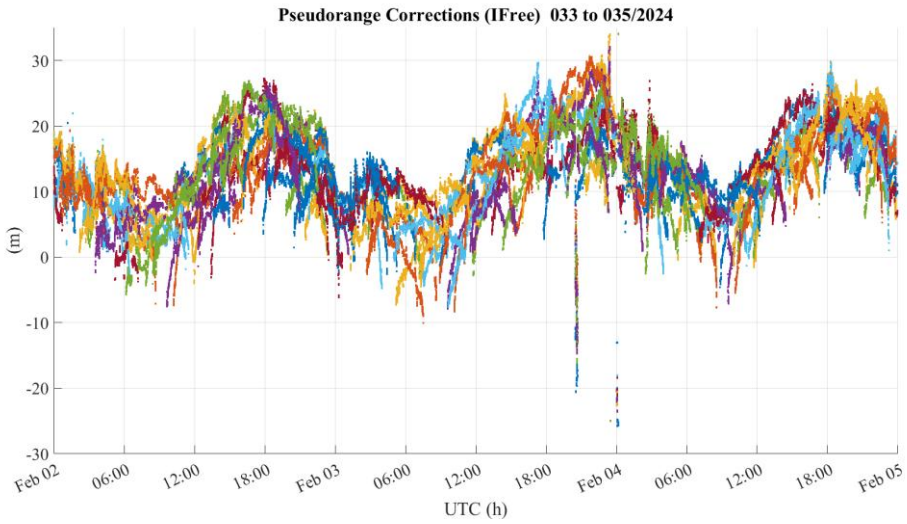


6.3. GBAS CAT I IFree: High Ionospheric Scintillation Scenario

The GBAS CAT I IFree scenario was implemented during the period of ionospheric scintillation while maintaining the ground system and aircraft processing architecture used for the SF L1 scenario. The ground system generated L1/E1 and L5/E1 differential corrections from each of the four reference stations, which were then used to compute the IFree correction (Figure 75), as described in Equation (31).

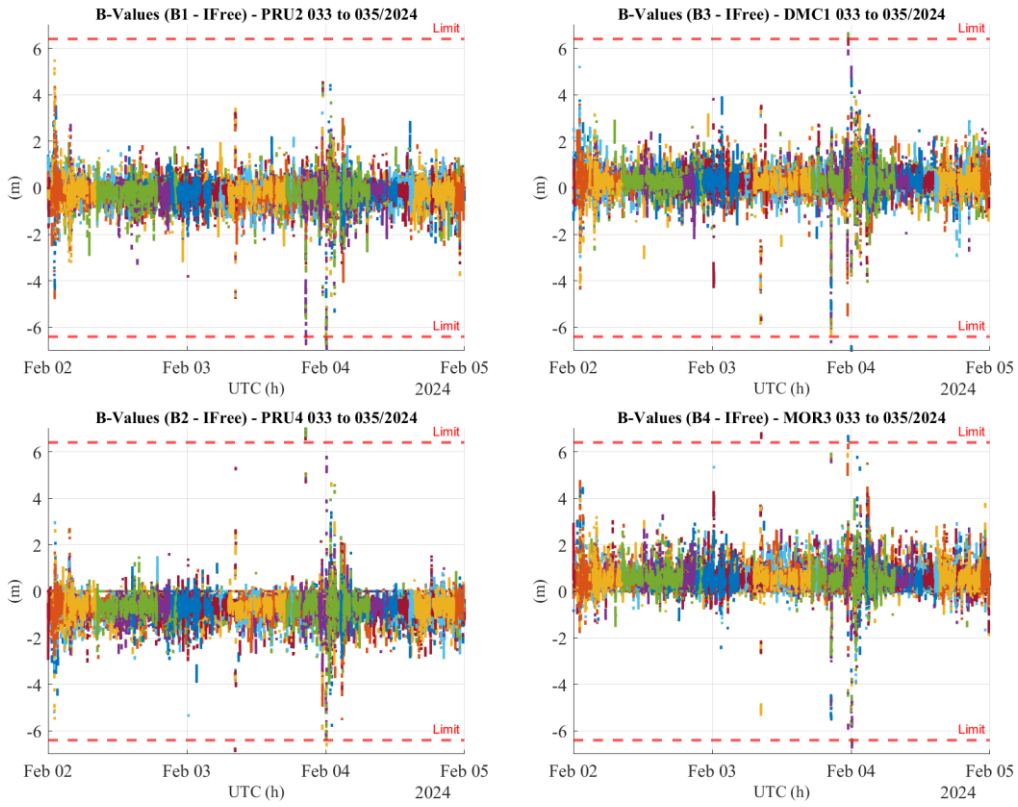
During the processed period, the corrections mostly ranged between -10 m and 30 m, generally exhibiting the expected parabolic pattern. However, some anomalous peaks were observed on DOY 034 between 18:00 and 00:00 (DOY 035). The cause remains unidentified as they were unrelated to ionospheric scintillation.

Figure 75 – Pseudorange Corrections IFree estimated for the period from 033 to 035/2025.



The estimated B-values for the IFree mode indicate that the differential corrections exhibited greater noise compared to the SF L1 scenario (Figure 76). The analysis reveals that stations PRU2 and DMC1 displayed B-value variations ranging from -2 m to 2 m, whereas stations PRU4 and MOR3 showed dispersions of 0 to -2 m and 0 to 2 m, respectively.

Figure 76 – Ground integrity parameter B-Values calculated by the ground system for IFree modo to the period from 033 to 035/2025.



Although Figure 76 shows that most B-values remained below the threshold of ±6.40 m, all stations exhibited increased B-values, with some instances exceeding this limit. Table 21 highlights the noisier IFree B-values, demonstrating elevated statistical indicators across all stations compared to those presented in Table 17. For instance, the standard deviation, reflecting estimation uncertainty, reached 1.278 m at station PRU2, a fivefold increase over the SF L1 mode at the same station. This observation aligns with literature, such as Circiu et al. (2014) and Felux et al. (2017b), which anticipate degraded noise performance in IFree mode due to its inherent processing characteristics.

Table 21 – Statistical indicators of the B-Values IFree for the reference stations during periods from 033 to 035/2024.

B-Values/ Station	Mean (m)	Standard deviation (m)	Percentile 95% (m)
B1 – PRU2	-0.131	1.278	0.750
B2 – PRU4	-0.587	0.783	1.118
B3 – DMC1	0.249	0.943	0.744
B4 – MOR3	0.471	0.940	0.993

In the aircraft system, protection levels and position errors were computed for the IFree mode (Figures 77 and 78), initially for the STAV station. Out of the total 518,400 possible epochs (corresponding to 3 days of data), 447,640 epochs were successfully resolved as GBAS IFree solutions. Both horizontal and vertical components exhibited brief gaps in HPE, HPL, VPE, and VPL values due to data exclusion triggered by the GNSS data quality monitors.

Figure 77 – GBAS performance CAT I IFree for the vertical component at the STAV station during the period of high ionospheric scintillation.

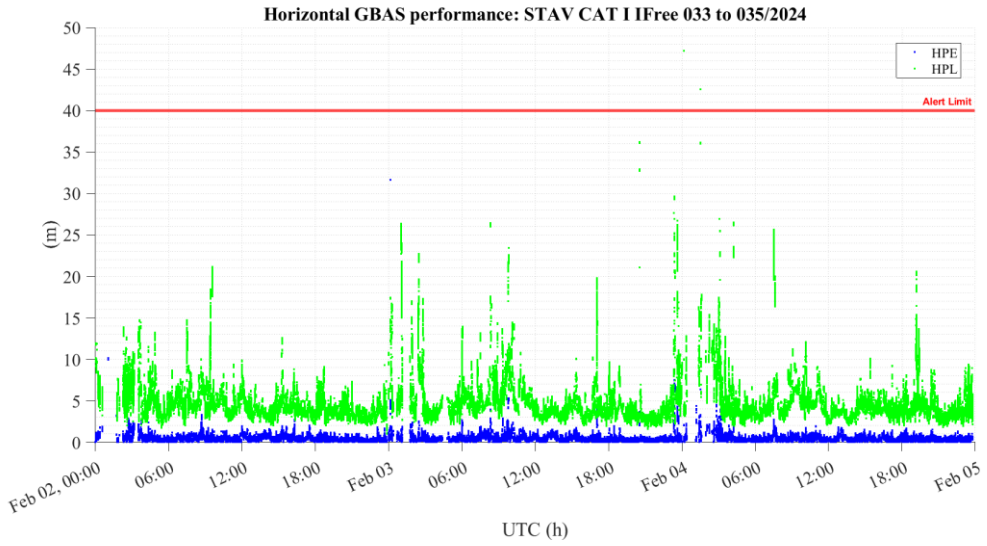
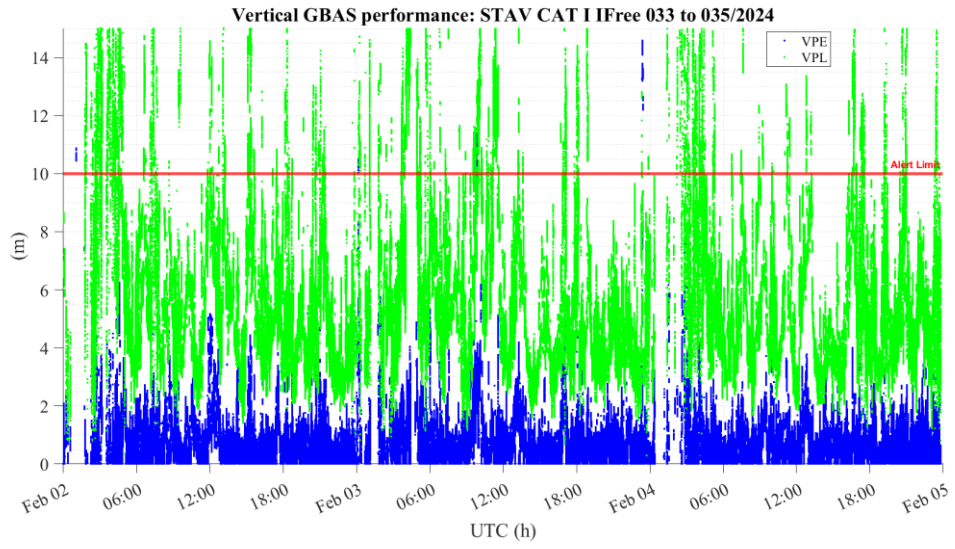
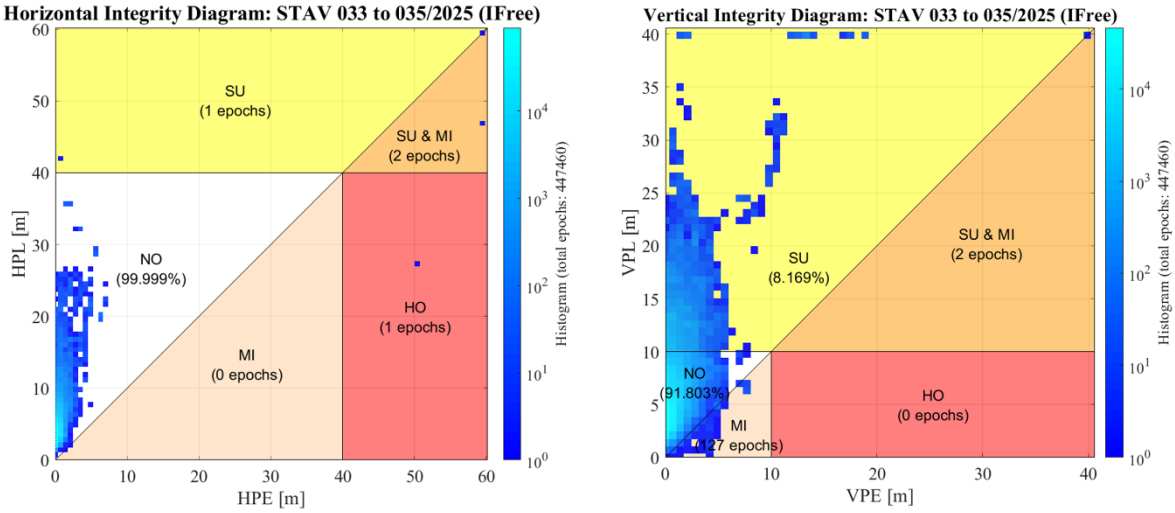


Figure 78 – GBAS performance CAT I IFree for the vertical component at the STAV station during the period of high ionospheric scintillation.



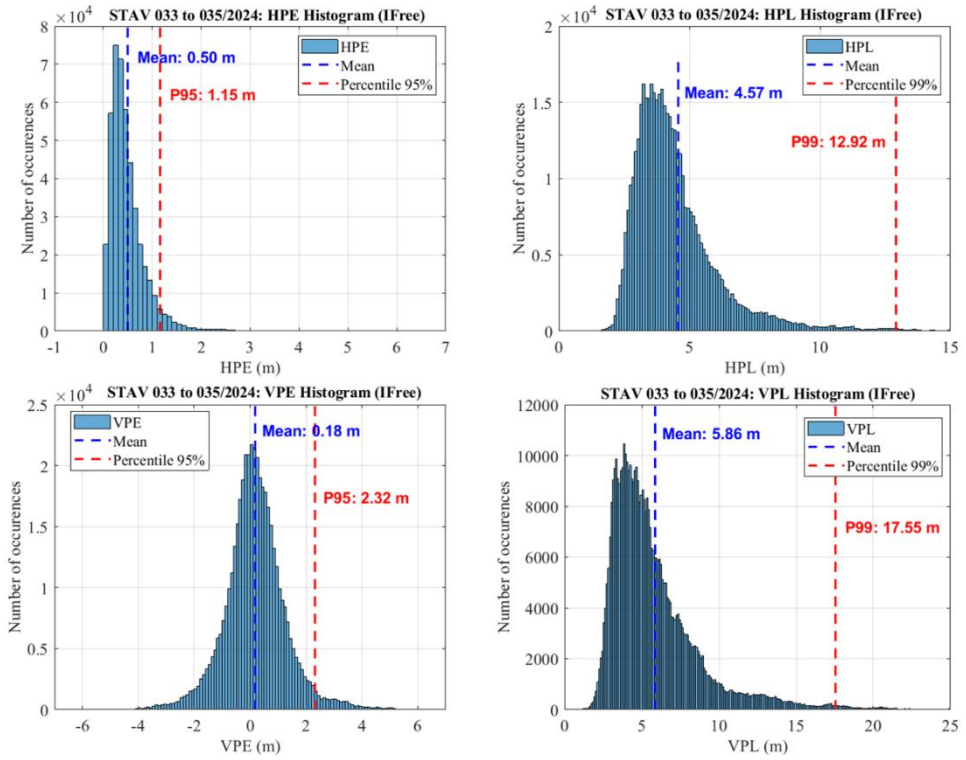
The analysis revealed not only periods without positioning solutions but also a notably degraded performance in the vertical component, characterized by elevated VPL values and more frequent exceeding the VAL. As shown in Figure 79, while 99.999% of epochs comport CAT I operational requirements for the horizontal component, only 91.803% satisfied the vertical criteria. The system becomes unavailable during 8.169% of epochs due to VPL exceeding VAL. Additionally, 127 epochs exhibited misleading information, where the VPE was higher than VPL but remained below the VAL.

Figure 79 – Integrity diagram for the horizontal and vertical component of GBAS CAT I IFree for the STAV station during the period of high ionospheric scintillation.



The histograms of HPE and VPE (Figure 80) demonstrate that the 95% accuracy requirement was met for the GBAS IFree solution at station STAV, with 95th percentiles of 1.15 m and 2.32 m for horizontal and vertical components, respectively. However, the performance requirement for protection levels was not satisfied in the vertical dimension, as the 99th percentile VPL reached 17.55 m - significantly exceeding the 10 m alert limit. This condition, observed during 8.169% of the analyzed period (Figure 79), poses a threat to GBAS continuity requirements.

Figure 80 – Histograms of position errors and protection levels for GBAS CAT I IFree at the STAV station during a period of high ionospheric scintillation.



The results for the aircraft at the STPZ station were similar to those presented for STAV. There were 444,278 epochs with the GBAS IFree solution and it is also possible to observe these epochs not processed by the application of GNSS data quality monitors and position adjustment. The HPE and HPL remain almost the entire period below the horizontal alert limit. While the VPL performance was also degraded with several epochs overlapping the alert limit.

Figure 81 – GBAS performance CAT I IFree for the horizontal position at the STPZ station during the period of high ionospheric scintillation.

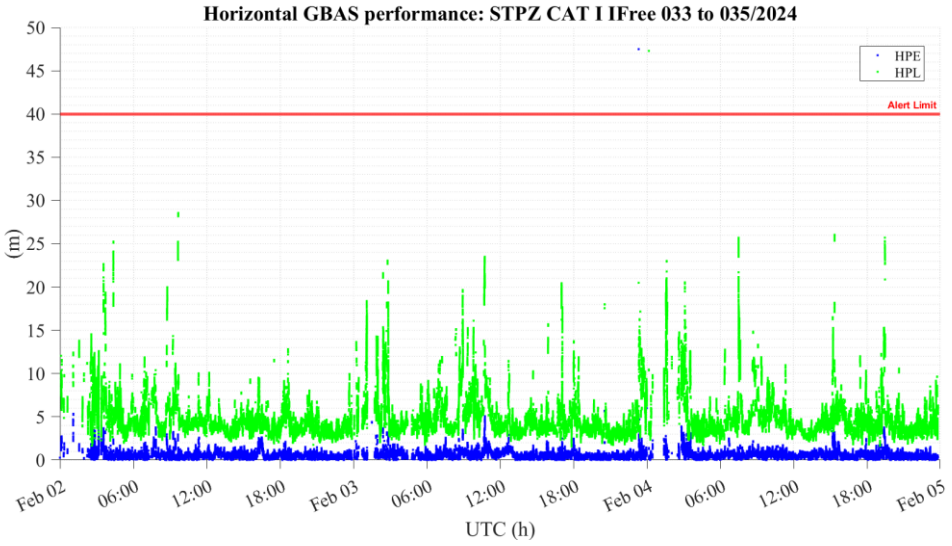
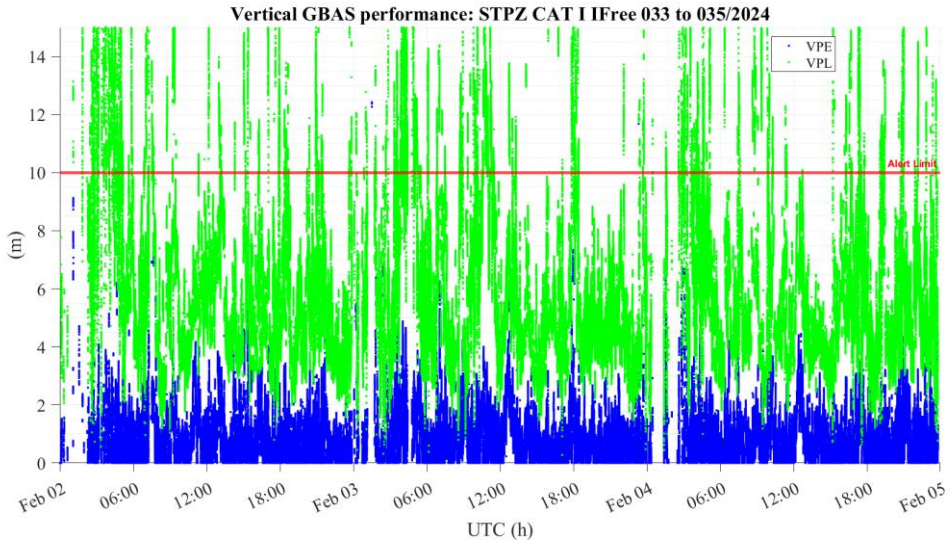
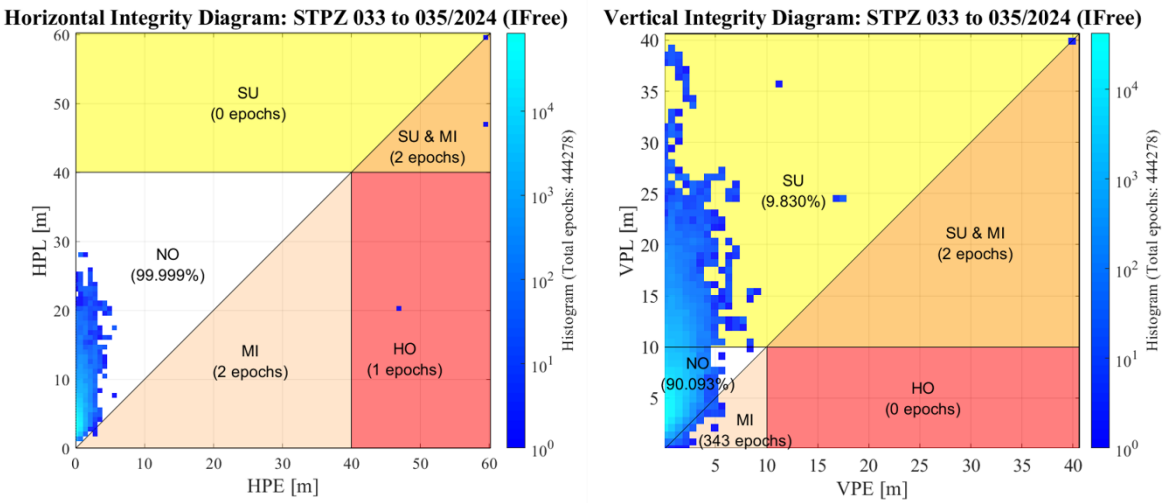


Figure 82 – GBAS performance CAT I IFree for the vertical component at the STPZ station during the period of high ionospheric scintillation.



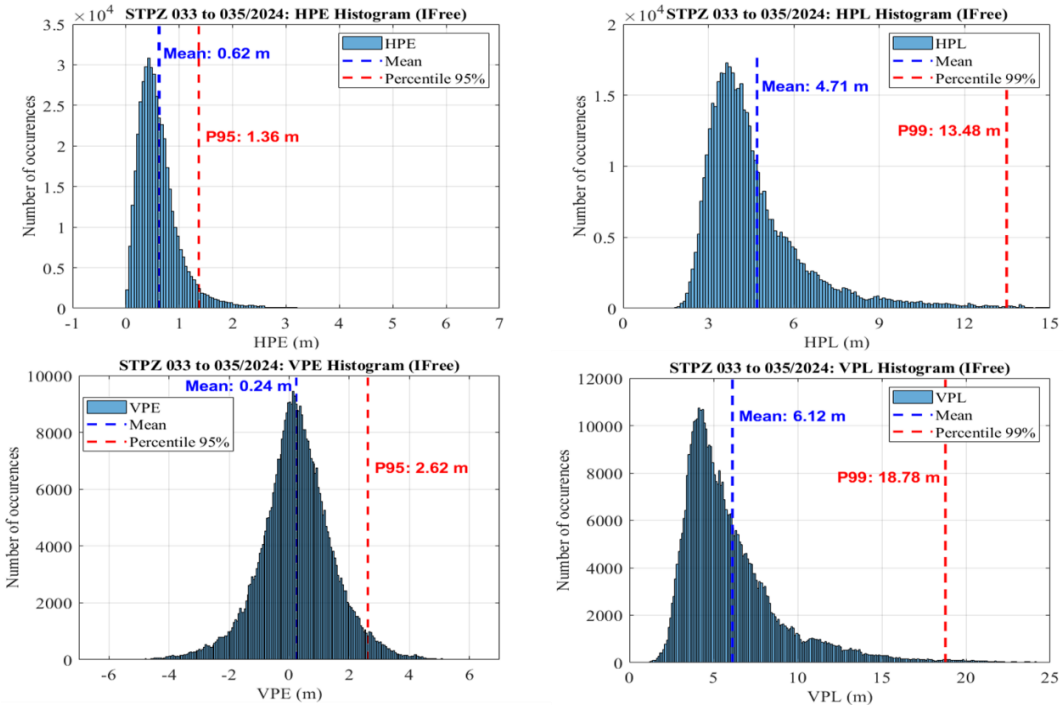
GBAS IFree provide the operational conditions for CAT I in 99.999% of the epochs in the horizontal position and 90.093% for the vertical, lower performance than STAV (Figure 101). In addition, STPZ presented more integrity loss events in the vertical component, with 9.830% of the epochs of system unavailable and 343 epochs of misleading information epochs.

Figure 83 – Integrity diagram for the horizontal and vertical component of GBAS CAT I IFree for the STPZ station during the period of high ionospheric scintillation.



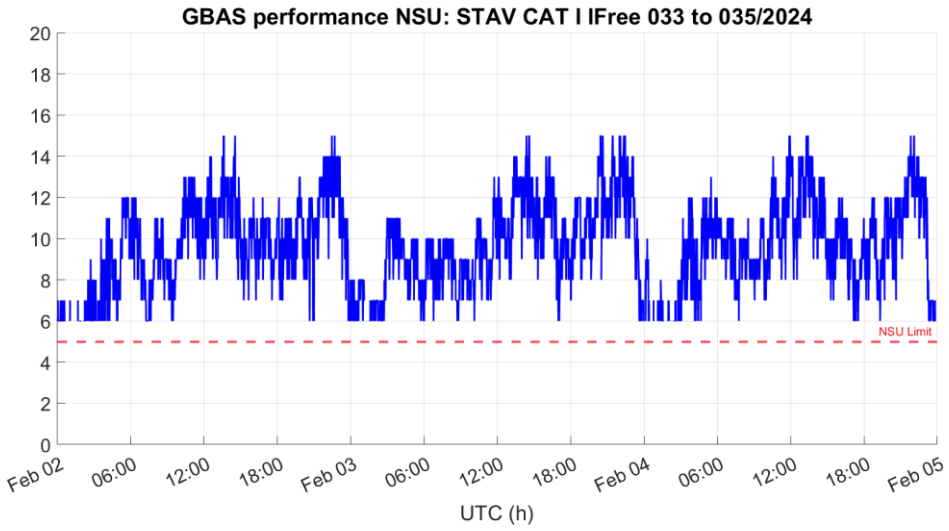
At the STPZ station, the protection levels also failed to meet the performance requirement for the vertical component, as the 99% percentile was 18.78m. This occurred in 9.830% of the epochs, which means a threat to the continuity and availability of GBAS. Although higher than the values for SF L1 mode, the HPE and VPE for IFree mode met the accuracy requirement 95% of the time, with values of 1.36 m and 2.62 m, respectively, for the CAT I accuracy approach.

Figure 84 – Histograms of position errors and protection levels for GBAS CAT I IFree at the STPZ station during a period of l ow ionospheric scintillation.



An analysis of the NSU in GBAS operating in IFree mode (Figure 85) reveals that the maximum number of satellites used was 15. This limitation occurs because not all GPS satellites transmit L5 carrier-phase data. Additionally, it is evident that during several intervals, the minimum number of satellites used drops to six for brief periods. This reduction leads to a degradation of the VPL, as observed in Figure 96, compromising the integrity of GBAS in this scenario.

Figure 85 – Number of satellites used in GBAS STAV (CAT I IFree) in DOY 033 to 035/2024.



The monitoring results for cycle slips, CCD failures, and GNSS data availability status on L1/E1 and L5/E5a carrier-phase at the STAV and STPZ stations are presented in the Appendices section.

These results, discussed in Sections 6.1, 6.2, and 6.3 and obtained using the GBAS UNESP Experimental prototype, are summarized in Table XX, which presents the vertical component results for the number of epochs processed in GBAS SF L1 mode (under both high and low ionospheric scintillation conditions) and in the IFree mode, at the STAV and STPZ stations.

Table 22 - Summary of the perfomance of experiments conducted using the GBAS UNESP Experimental prototype.

Vertical performance at STAV station					
Approach service and period	Available epochs (processed)	MI – Vertical (epochs)	HO – Vertical (epochs)	Unavailable – Vertical (epochs)	Operational Vertical %
SF L1 high scintillation	502557	19	0	2836	99.84
SF L1 low scintillation	232620	0	1	372	99.84
Iono Free high scintillation	447460	127	0	8.17%	91.803
Vertical performance at STPZ station					
Approach service and period	Available epochs (processed)	MI - Vertical (epochs)	HO - Vertical (epochs)	Unavailable – Vertical (epochs)	Operational Vertical %
SF L1 high scintillation	502042	52	0	3138	99.84
SF L1 low scintillation	232415	1	0	513	99.779
Iono Free high scintillation	447278	343	0	9.83%	90.093

At the STAV station, the GBAS SF L1 mode exhibited consistently high vertical operational availability under both ionospheric conditions. During periods of high scintillation, a vertical availability of 99.84% was achieved, with 19 epochs classified as Misleading Information (MI), no occurrences of Hazardously Misleading Information (HO), and 2,836 unavailable epochs. Under low scintillation, performance further improved, maintaining the same availability of 99.84%, with no MI events, only a single HO epoch, and a substantially reduced number of unavailable epochs (372), reflecting a more stable ionospheric environment. In contrast, the IFree combination under high scintillation led to a noticeable degradation in vertical performance, with availability decreasing to 91.803%, accompanied by 127 MI epochs and a higher proportion of unavailable epochs. These results indicate that, despite its capability to mitigate first-order ionospheric effects, the IFree combination introduces increased measurement noise

and variance, which adversely affect protection levels and, consequently, vertical service availability.

A similar performance pattern was observed at the STPZ station. For the SF L1 mode under high scintillation, vertical operational availability reached 99.84%, with 52 MI epochs, no HO events, and 3,138 unavailable epochs. Under low scintillation, availability remained very high at 99.779%, with only 1 MI epoch, no HO, and 513 unavailable epochs, confirming the beneficial impact of quieter ionospheric conditions. Conversely, the Iono-free combination under high scintillation resulted in a significant reduction in vertical availability to 90.093%, together with 343 MI epochs and a larger number of unavailable epochs. Overall, the results at STPZ corroborate those obtained at STAV, demonstrating that the SF L1 mode provides superior robustness in terms of vertical availability, whereas the Iono-free strategy suffers from reduced availability in environments affected by strong ionospheric scintillation.

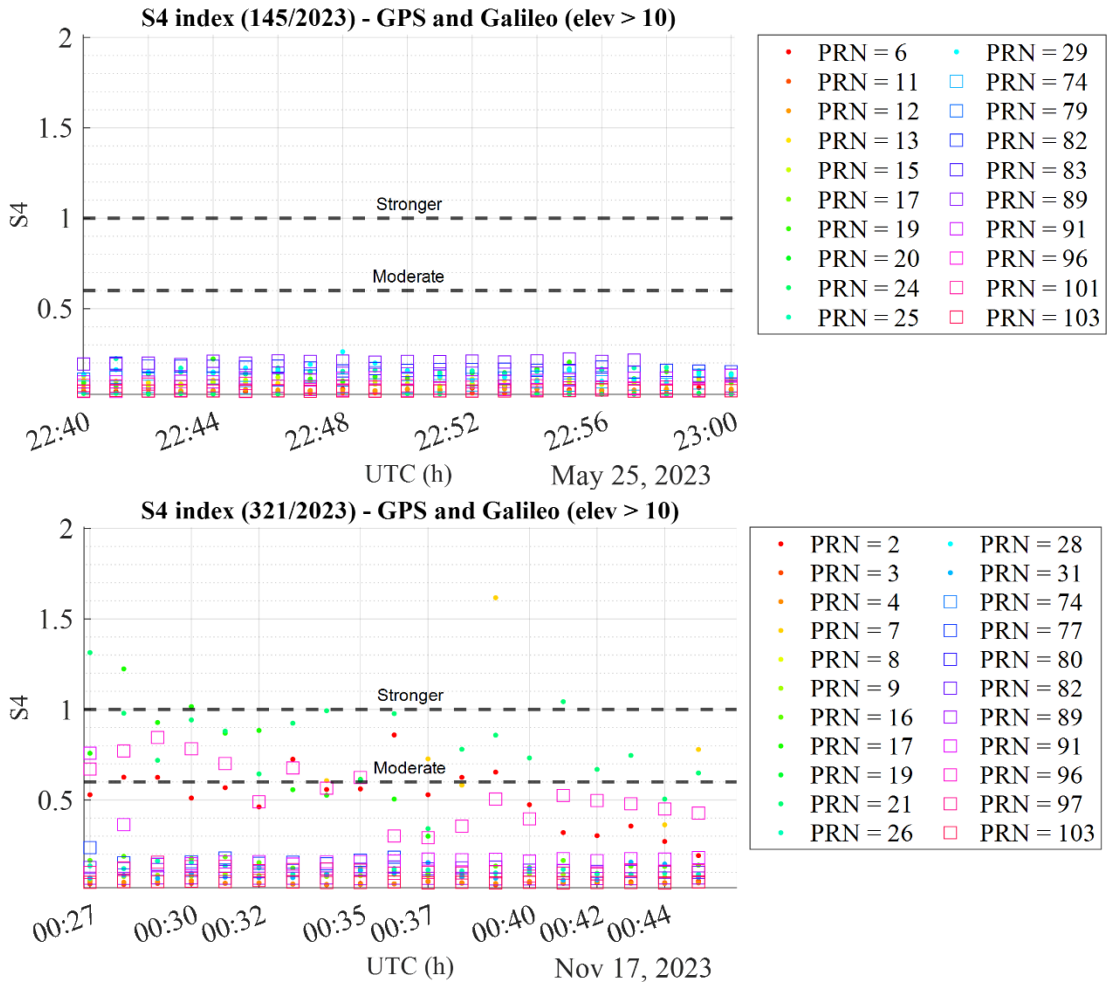
6.4. GBAS CAT I SF L1: Kinematic Mode for UAV test

The experiments presented in the previous sections were based on analyzing the GBAS performance with the aircraft simulated in static mode, but the data was processed as it was in kinematic. The experiment in this section, on the other hand, will present performance in kinematic mode using Unmanned Aerial Vehicle (UAV) test.

UAV has been explored in aviation research, as they allow GBAS issues to be developed and analyzed at a lower cost than conventional manned aircraft. The flexible structure of UAV allows them to be adapted to carry a GNSS receiver and antenna suitable for aviation experiments. Therefore, it makes it possible to collect data, test and improve algorithms and equipment related to GBAS, verifying their effectiveness in real flight situations. In equatorial and low latitude regions, for example, the flexibility of using UAV can enable studies into the effects of ionospheric scintillation on GNSS positioning.

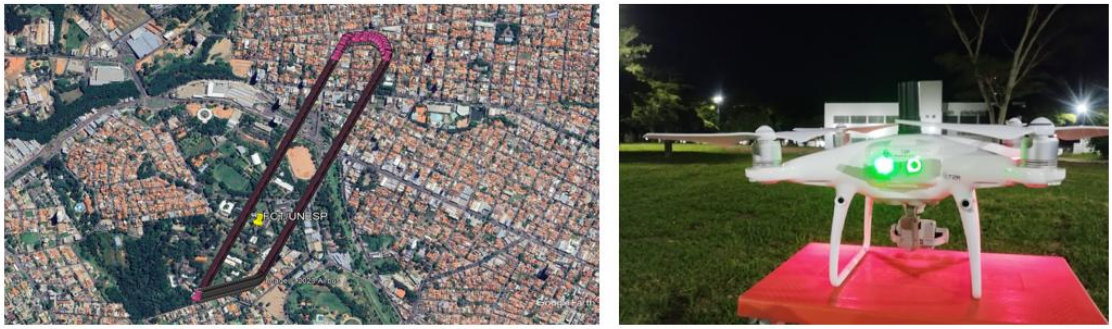
The aim of this study is to analyze the performance of UAV flights carried out in Presidente Prudente/SP during periods of low and high ionospheric scintillation. The flights were carried out on 05/25/2023 (145/2023) and 11/16/2023 (321/2023), which represent days with low and high ionospheric scintillation, as show Figure 86. GPS satellites are numbered from 1 to 32, while Galileo are numbered from 71 to 106.

Figure 86 – S4 index for ionospheric scintillation scenario on DOYs 145/2023 and 321/2023.



The flight planning trajectory for the experiment was 2.8 km (Figure 87 a). The approximate average flight speed was 30 m/s. The UAV used was the Phantom 4 Pro model, with an on-board Ublox F9P GNSS receiver, tracking multi-constellation data using a BT-560 GNSS antenna (Figure 87 b). However, only GPS and Galileo data was used for GBAS processing, with a sample interval of 0.2 s and an elevation mask of 10°.

Figure 87 a) General view of the trajectory of the flight carried out in Presidente Prudente - SP. b) UAV Phantom 4 Pro model used in the GBAS kinematic experiment.



The data collected during this trajectory, illustrated in Figure 87 a), was processed as GBAS GAST C (i.e. CAT I precision approximation category), using 4 stations from the INCT GNSS-NavAer Network: PRU2, PRU4, DMC1 and MOR3, as GBAS reference stations.

6.4.1. Kinematic GBAS processing

GBAS processing was carried out using PEGASUS software, developed by EUROCONTROL. The choice of PEGASUS software for processing the kinematic mode was due to the incompatibility of our implementation in synchronizing differential corrections and UAV observations with different samples.

PEGASUS is an acronym of Prototype EGNOS GBAS Analysis System Using SAPPHIRE, a software developed by the European Organization for the Safety of Air Navigation (EUROCONTROL). This software processes data to analyze air navigation performance in terms of GNSS accuracy, integrity, continuity, and availability, based on EGNOS and GBAS augmentation systems, while considering the requirements defined in ICAO standards (EUROCONTROL, 2019).

PEGASUS enables the operational validation of aviation-oriented GNSS augmentation systems (such as SBAS and GBAS), the prediction of future or experimental system capabilities, and the selection of future sites for ground station subsystem placement. The tool was developed as a set of modular components, each designed to perform specific tasks flexibly.

For the kinematic GBAS experiment, the GBASMessenger and GNSS Solution Modules were used. The former corresponds to the ground system functionalities, including the generation of differential corrections for the four reference stations and the computation of integrity parameters. The GNSS Solution Module was applied in the aircraft system, using ground data to determine the position of UAV during flight and to calculate protection levels.

At ground system for GAST C, conventional settings were used such as 0.5 s sampling, 100 s pseudorange smoothing time constant, GAD B, 14 mm/km of sigma VIG, 12700 m height scale, 320 refractivity index, 20 refractivity uncertainty. On the aircraft system, the AAD was A, the smoothing time constant was also 100 s, the monitor signal SNR was 33 dbHz, and the minimum S (vertical and lateral) was 3.5, in accordance with SARPs standards for GAST C.

To evaluate quality of the results of the GBAS, the flight data was also processed as kinematic relative positioning, in the post-processing mode using the RTKLib software (demo5 b34c version). This processing used the MOR3 station as a base (reference station). In addition, maintaining the 10° elevation mask, it used GPS and Galileo satellites (L1, L2 and E5b), broadcast ephemerides, the IFree linear combination to remove ionospheric delay, the Saastamoinen model for tropospheric correction, and the combined (forward + backward) positioning solution filter.

This solution was used to generate the (reference) coordinates of the flight and compare them with those obtained by GBAS mode, making it possible to obtain horizontal and vertical position errors by transforming the coordinates to the Local Geodetic System (LGS). The results for the low and high scintillation scenarios will be analyzed in the next subsection.

6.4.2. GBAS Kinematic: low Scintillation Scenario

Data flight processing in the PEGASUS software took around 5 minutes of data to initialize. Therefore, data of 4,530 epochs (approximately 16 minutes) were processed. On the other hand, processing in Relative Kinematic mode had an initialization period of 35 seconds and processed a total of 6,477 epochs (approximately 21 minutes). Therefore, only the epochs with GBAS and Relative Kinematic results will be analyzed for the quality purpose.

Figure 88 shows the standard deviation of Relative Kinematic results for E, N and Up components. It can seen that most of the time, E and N were lower than 0.02 m of

precision while Up or vertical component maintained between 0.03 and 0.04 m. These results indicate that even with a float positioning solution, the precision was quite satisfactory.

Figure 88 – Standard Deviation of Relative Kinematic Positioning during flight in low ionospheric scintillation.

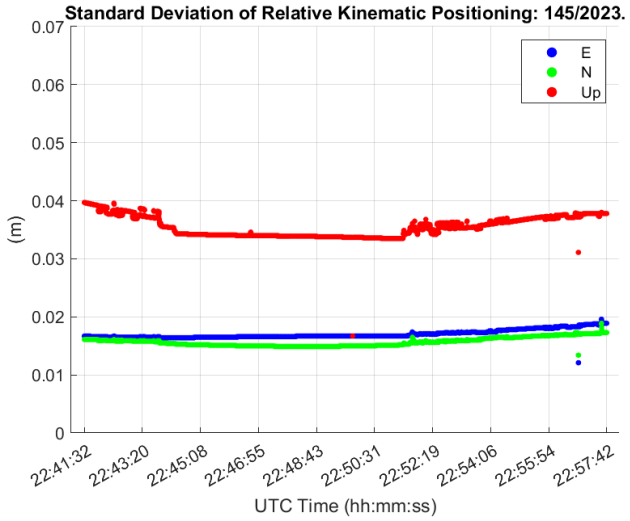
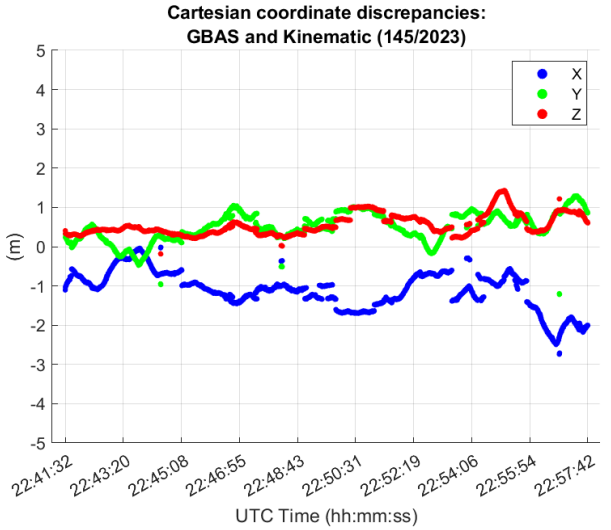


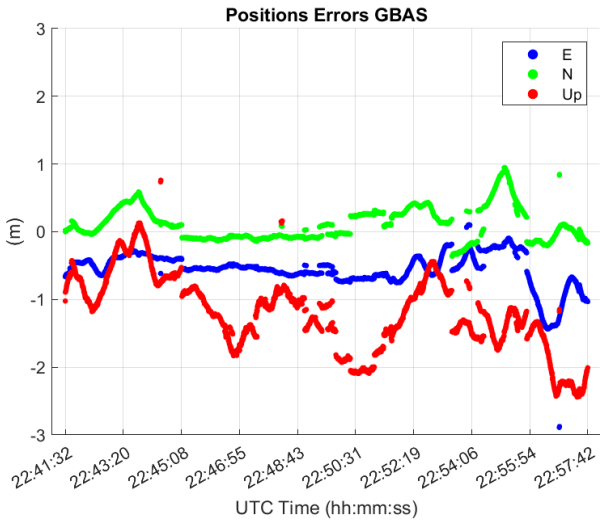
Figure 89 shows the discrepancies in geocentric Cartesian coordinates estimated by GBAS and the Kinematic Relative. The largest discrepancy was for the X component, reaching -2.741 m, while the Y and Z components showed similar behavior for most of the flight, ranging from 0 to 2 m.

Figure 89 – Discrepancies of the geocentric Cartesian coordinates estimated for flight by the GBAS and Kinematic Relative positioning during low scintillation.



Using the coordinates estimated by the two methods and taking the Kinematic Relative as a reference, it was possible to obtain the coordinates discrepancies in the Local Geodesic System, which for this work represents the position errors for the horizontal (E and N) and vertical (Up) components. Figure 90 shows that the vertical error is the one that reaches the highest values (absolute) during almost the entire flight, from 0 to - 2 m approximately, while horizontally E and N vary from 1 to -1 m in the part of the solutions processed.

Figure 90 – Position errors in the Local Geodetic System applied to flight in the low ionospheric scintillation scenario.



The resultant of the E and N components gives horizontal position errors which, when compared with the horizontal protection levels, indicate the GBAS availability condition (Figure 91). Alternatively, the Up component should be compared with the VPL to assess availability in the vertical component (Figure 92).

Figure 91 – GBAS performance for the horizontal component on DOY 145/2023.

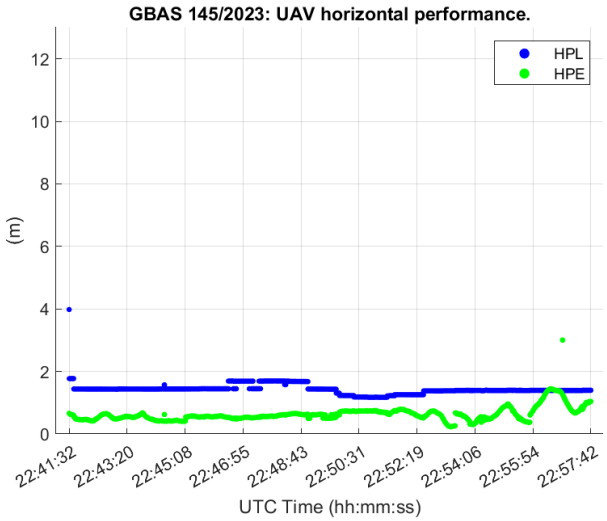
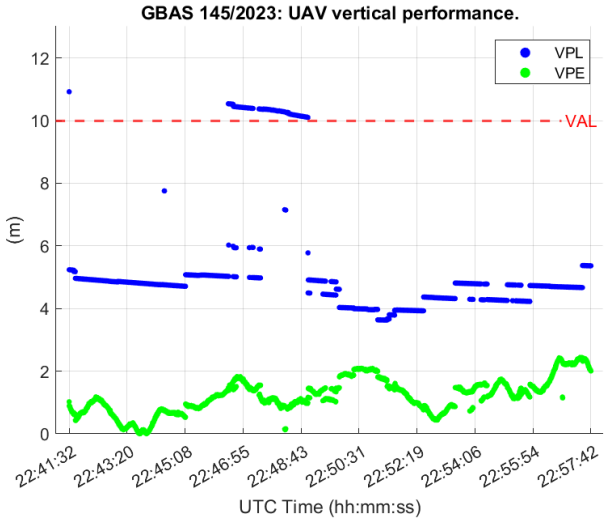


Figure 92 – GBAS performance for the vertical component on DOY 145/2023.



Once again, it should be noted that, for this work, conservative alert limit values at the aircraft decision height were adopted. Thus, HAL and VAL values of 40 m and 10 m, respectively, were considered. If alert limits as a function of distance had been adopted, the results would have differed from those presented in Figures 91 and 92.

The performance based on position errors and protection levels during low scintillation day can also be summarized in Table 22 with the average, maximum and percentile values. The vertical component is usually the most affected in GNSS positioning and showed the highest values of the 3 indicators analyzed, except for the maximum value of HPE which exceeded that of VPE.

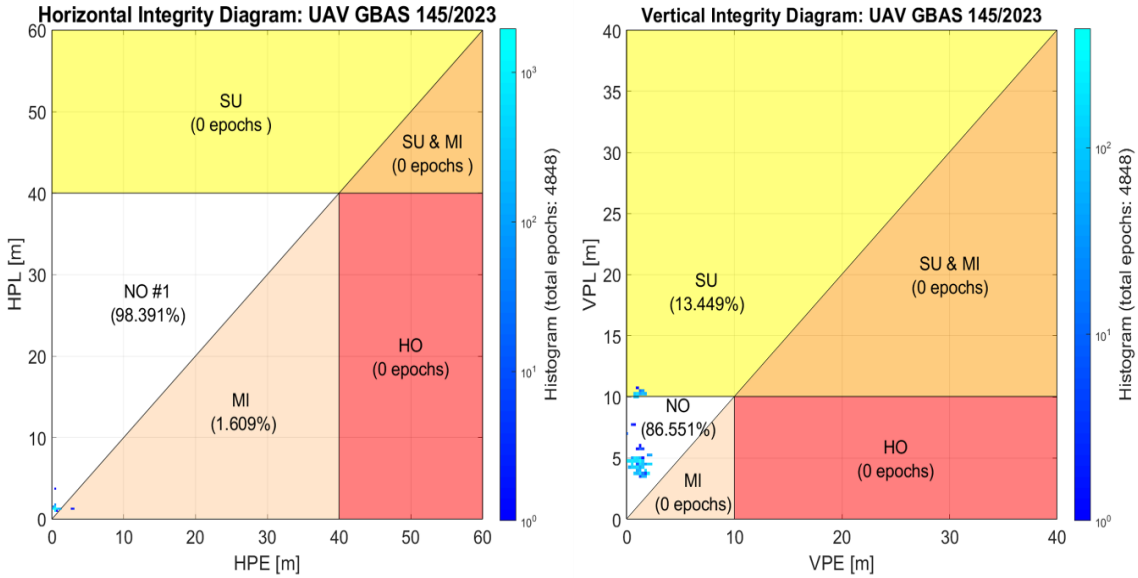
Table 23 – HPE and VPE performance during flight in the low scintillation scenario.

Parameters	Mean (m)	Maximum (m)	Percentile (95%) HPE and VPE	Percentile (99%) HPL and VPL (m)
HPE	0.629	3.007	1.036	-
HPL	1.420	3.982	-	1.696
VPE	1.212	2.440	2.226	-
VPL	5.373	10.921	-	10.450

The horizontal component had 98.391% of solutions in operational conditions with position errors lower than the protection levels. There were 78 epochs with data processed as GBAS where the HPE exceeded the HPL, but they were lower than the alert limit, which for CAT I is 40 m. This corresponds to 1.609% of the epochs. In Figure 93 such condition is classified as Misleaning Information, which is statistically classified as a Type 1 Error, since in this case the HPE is much lower than the alert limit.

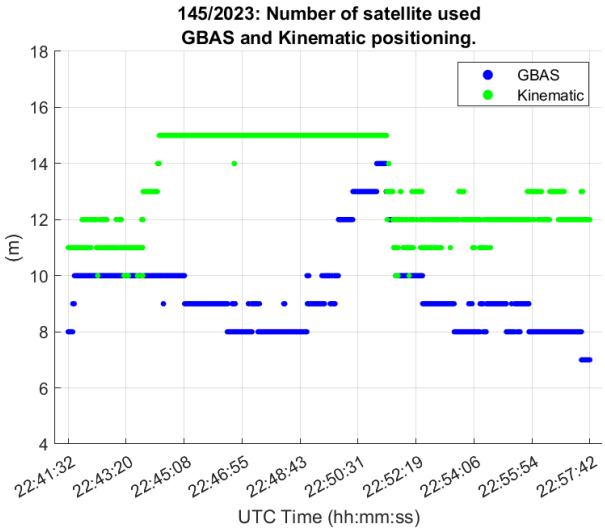
The performance of the vertical component, as expected, was lower than the horizontal component, with 88.551% of solutions being in operational conditions. However, this loss of availability was due to 13.449% of the epochs having a VPL greater than the alert limit, indicating loss of integrity and unavailability status for GBAS use in these conditions. Although the VPE was lower than the VPL throughout the flight, performance requirements also dictate that the VPL be lower than the VAL, which for CAT I is 10 m. Such a situation shows us that the stochastic model of the observation could be better, a detail that may be investigated in the future.

Figure 93 – Integrity diagram on the 145/2023 flight.



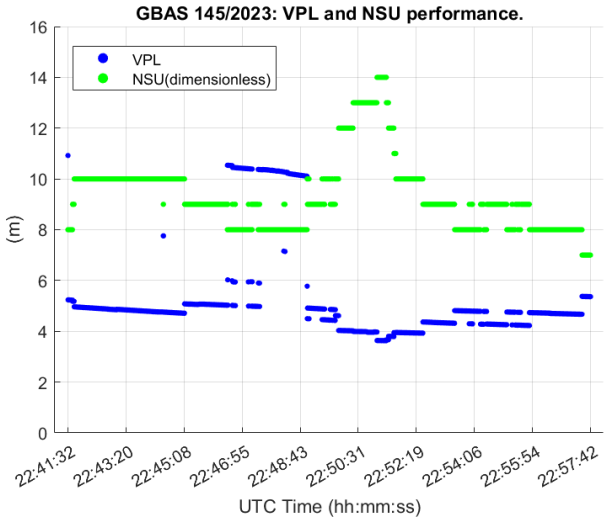
This reduction in performance of the vertical component is related to the number of satellites used in positioning. Figure 94 shows a comparison of the number of satellites used in GBAS and in the Kinematic Relative data processing. As the processing involved two different software packages and positioning methods, the number of satellites used does not match. Regarding GBAS, which has stricter quality control and performance requirements, it excluded more satellites than the Kinematic Relative, due to decorrelation problems, missing ephemerides and resetting of the smoothing filter. In GBAS mode, the NSU ranged from 7 to 14 satellites, while in Relative Kinematic it was from 10 to 15 satellites.

Figure 94 – Number of satellites used in GBAS and Kinematic Relative positioning for the 145/2023 flight.



It's interesting to note that the period between 22:46:55 and 22:48:43 corresponds in Figure 94 to the period when GBAS is unavailable, due to the VPL exceeding VAL. During this period the NSU decreases to 8 in GBAS, while in Kinematic Relative it reaches a maximum of 15. This exclusion degrades the satellite geometry in GBAS mode, impacting the VPL values, as already pointed out by Silva and Monico (2022). Figure 95 shows the relationship between VPL and NSU. Reducing the NSU to 8 satellites affects the geometry, increasing the VPL up to 10.921 m.

Figure 95 – Performance of VPL and NSU in GBAS positioning for day 145/2023.

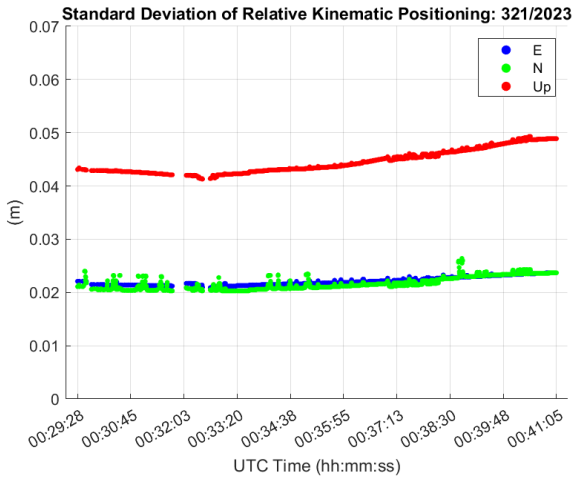


6.4.3. GBAS Kinematic: high scintillation scenario

The flight carried out during the period with occurrence of ionospheric scintillation had fewer positioning solutions in GBAS mode compared to the day without scintillation. A total of 2,936 epochs had GBAS solutions, which took around 11 minutes. On the other hand, in Relative Kinematic mode there were 5288 epochs as float solutions from the start of the flight of approximately 17 min. However, for the following analyses, only the 2,936 epochs coinciding with the GBAS solution were considered.

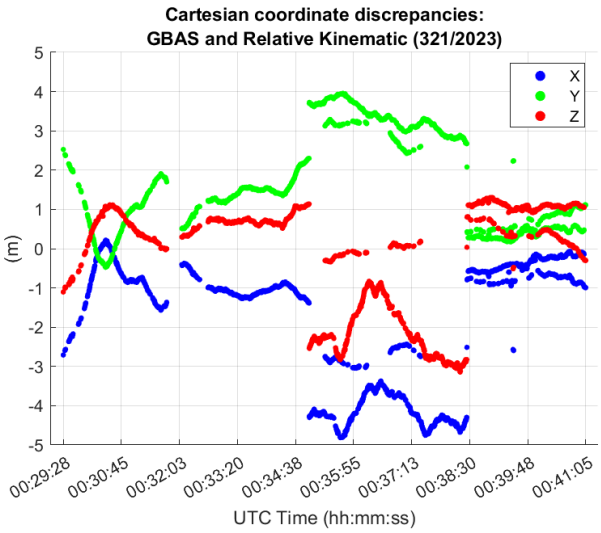
The accuracy of the coordinates (local geodetic system – LGS) estimated by Relative Kinematic Positioning can be seen in Figure 96. The E and N components had a standard deviation of between 0.02 and 0.03 metres, while the Up component remained between 0.04 and 0.05 metres. Some empty spaces can be seen in the graph and correspond to epochs without a positioning solution.

Figure 96 – Standard Deviation of Relative Kinematic Positioning during flight in high ionospheric scintillation.



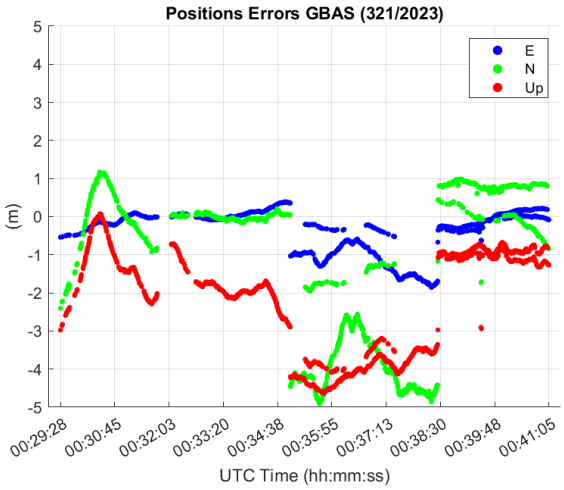
In terms of estimated coordinates, Figure 97 shows the difference between the positions obtained by the two positioning methods during high ionospheric scintillation scenario. It can be seen high discrepancies in coordinates ranging from -5 to 4 metress, especially in the time interval from 00:34 to 00:38. The largests discrepancies occurred during this period, such as in the X coordinate, reaching -4.813 metres. This larger variability in the coordinate discrepancies may be related more to the performance of GBAS, as it can be seen that there was no significant variation in the standard deviation of the Relative Kinematics, and it is important to remember that it was carried out in post-processing with forward and backward mode.

Figure 97 – Discrepancies of the geocentric Cartesian coordinates estimated applied to flight by the GBAS and Kinematic Relative positioning during high scintillation.



When converting these errors to the LGS, it can be seen that, in general, the largest errors occur in the Up vertical component, however, in the period from 00:34 to 00:38, the N component reaches -4,909 meters, associated with the greater variation reported earlier in the comparison of coordinate discrepancies.

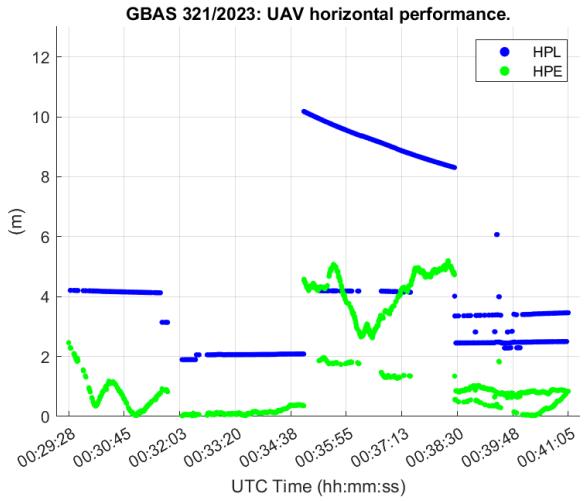
Figure 98 – Position errors in the LGS for flight in the high ionospheric scintillation scenario.



Figures 99 and 100 allow us to analyse the performance of GBAS by comparing the position errors with the protection levels. In the horizontal component, visual analysis indicates that HPE may outperform HPL at certain times. However, the implementation of a counter for the number of occurrences in which position errors exceeded the

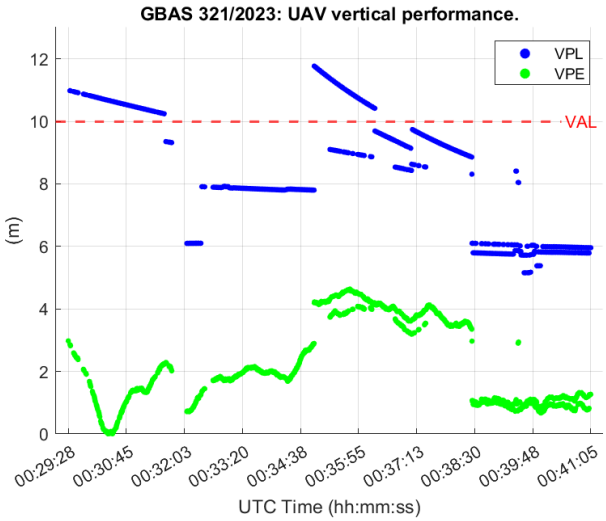
protection levels showed that this was not the case, but rather a misinterpretation caused by the plot's scale.

Figure 99 – GBAS performance for the horizontal component on DOY 321/2023.



In the vertical component, the VPE also does not exceed the VPL in any of the 2936 epochs with solution. However, the VPL exceeds the VAL at the beginning of the flight (approximately 00:28 to 00:32) and in the period already reported (00:34 to 00:36). In total, there were 660 epochs with VPL greater than the alert limit, making GBAS unavailable for precision approaches in these conditions.

Figure 100 – GBAS performance for the vertical component on DOY 321/2023.



The Integrity Diagram of the horizontal component corroborates this performance statement, showing that 100% of the epochs are in a state of GBAS availability. With

these VPE and VPL results, the vertical component obtained 77.52% of the epochs processed with CAT I availability. The rest of the epochs (22.48%) were unavailable due to protection levels exceeding the alert limit.

Figure 101 – Integrity diagram on the 321/2023 flight.

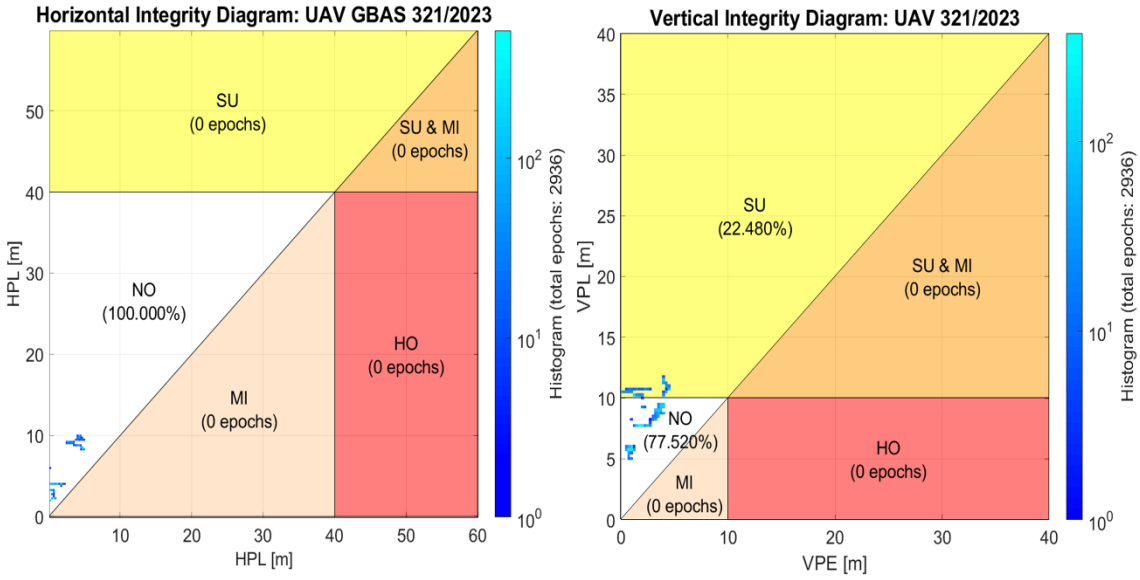


Table 23 summarizes the GBAS performance by mean, maximum and 95% percentile position errors and protection levels. The horizontal component met the performance requirements for CAT I, although it had the highest estimated error of 5,200 m. The vertical component, however, had a problem with VPLs above the 10 m limit.

Table 24 – HPE and VPE performance during flight in the high scintillation scenario.

Parameters	Mean (m)	Maximum (m)	Percentile HPE and VPE (95%) (m)	Percentile HPL and VPL (99%) (m)
HPE	1.609	5.200	4.874	-
HPL	4.666	10.181	-	10.114
VPE	2.291	4.636	4.292	-
VPL	8.287	11.768	-	11.657

As shown in the low scintillation scenario, GBAS performance at high scintillation is also affected by the reduction in satellites (Figure 102). Data of some epochs were processed using only the minimum number of 5 satellites, i.e. with no

degrees of freedom for position quality estimation. Hence it increases the position errors and protection levels in the high scintillation scenario. The relationship between NSU and VPL (Figure 103) is also observed and the times when GBAS was unavailable were usually with NSU equal to 5 and 6. It is important to note that even in Relative Kinematic mode, this satellite reduction is also observed.

Figure 102 – Number of satellites used in GBAS and Kinematic Relative positioning for the 321/2023 flight.

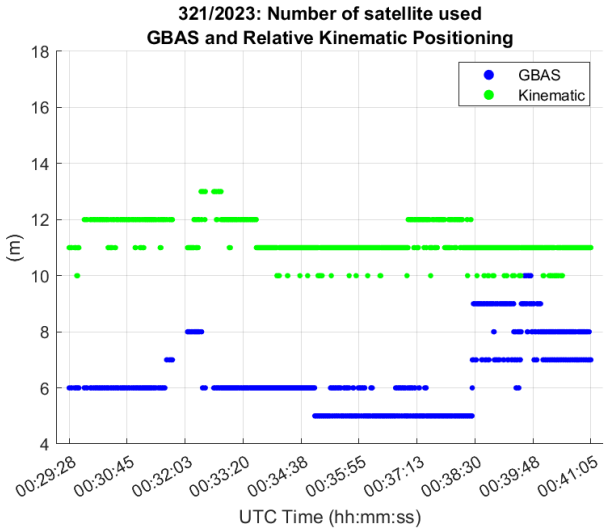
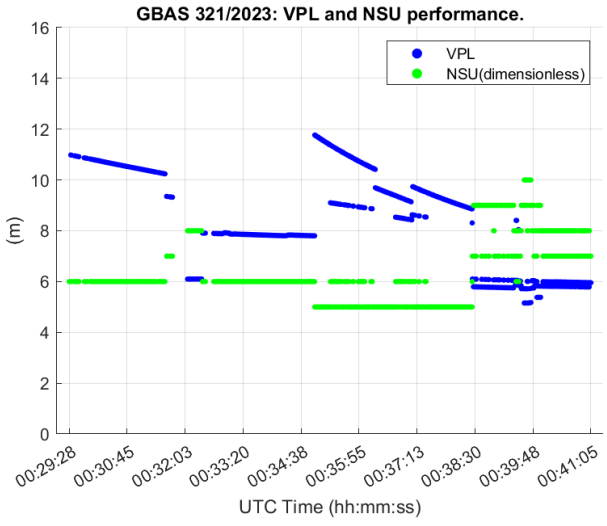


Figure 103 – Performance of VPL and NSU in GBAS positioning for day 145/2023.



7. CONCLUSIONS

This study investigated the introduction of new GNSS signals and satellite constellations planned for future GBAS services, focusing on their potential advantages and disadvantages for supporting precision approach operations. The experiments were conducted in Brazil, a low-latitude region characterized by the frequent occurrence of ionospheric irregularities, which affect GNSS GBAS signals and lead to the degradation of the performance requirements necessary for precision approach operations.

A GBAS DFDC architecture was implemented, based on the integration of GPS and Galileo signals (L1/E1 and L5/E5a), tracked by a network of six reference receivers. This configuration represents a prototype system named GBAS UNESP Experimental, which has been developed within the framework of the INCT GNSS-NavAer Project. The system is intended for aviation-focused research and for monitoring and assessing the impact of ionospheric effects on GNSS-based positioning.

Following the installation of all receivers in the GBAS UNESP Experimental architecture, a study was conducted to characterize the nominal multipath conditions at each station over a period of 11 days without ionospheric scintillation. The use of dual-frequency GNSS data allows for improved multipath estimation, which in this work was performed using two methodologies: the Carrier Minus Code (CMC) DFree linear combination, and the conventional multipath (MP) index determination algorithm, applied to both the L1/E1 and L5/E5a frequencies.

Among the stations, PRU2, located at the GBAS ground facility, exhibited the highest L1/E1 multipath indices, with a 95th percentile value of approximately 0.35 m and an uncertainty of 0.23 m in the 10°–30° elevation range—an angular sector typically most affected by multipath. Conversely, station MOR3 recorded the lowest L1/E1 multipath indices, with a 95th percentile of 0.25 m and a standard deviation of 0.15 m within the same elevation angle range. Notably, MOR3 was the only station that did not exhibit any multipath peaks during the 11-day observation period. In contrast, all other stations experienced multipath peaks exceeding 1 meter, with PRU2 registering values greater than 2 meters on certain days. Safety requirements for receivers, internet connectivity, and electrical power at GBAS reference stations often limit their location to less than ideal environments. Consequently, some installations such as PRU2 exhibit elevated multipath index.

The analysis also demonstrated that the L5/E5a carrier-phase exhibited greater resilience to multipath effects than the L1/E1 signal, with index values up to two times lower across all stations. Furthermore, the highest multipath peaks were consistently associated with satellites at elevation angles between 10° and 20°. While this pattern suggests that elevation masking could be employed to mitigate positioning errors in GBAS applications. Such a strategy was not adopted in this study, as the existing GNSS data quality monitors had already reduced the number of usable satellites, thereby constraining the satellite geometry available for positioning.

Another analysis conducted in this study involved the spatial distribution of multipath occurrences at each station. Given the daily repeatability of GPS satellite orbits, the multipath effect tends to manifest with similar signatures at approximately the same times and in the same regions.

In GBAS applications presented in this work, the UNESP Experimental GBAS architecture, employing two stations as aircraft proxies, enabled their use for performance monitoring. Since the STAV and STPZ stations are located approximately 10 km (West-East) and 13 km (North-South), respectively, from the ground stations, it was possible to evaluate CAT I GBAS performance using both single-frequency dual-constellation data and the ionosphere-free) combination.

GBAS performance was assessed during both high and low ionospheric scintillation periods. Across both conditions and at both stations used as airborne platforms, performance was found to be similar. For the single-frequency (SF) GBAS mode, the system met accuracy requirements in over 99% of the analyzed period, with position errors remaining within the limits defined for CAT I operations. Although the protection levels also satisfied the required performance thresholds, instances of integrity loss were noted at both STAV and STPZ, primarily due to vertical protection levels (VPL) exceeding the vertical alert limit. These integrity loss events, which compromise the continuity and availability of GBAS services, were mainly attributed to the performance of the data quality monitoring algorithms.

Conversely, when processing CAT I GBAS data using IFree mode, the performance was lower than SF mode. Operational conditions for GBAS were met for approximately 90% of the time; however, integrity loss events were significantly more frequent, with VPL values exceeding the alert threshold. Additionally, the 99th percentile of VPL was 17.55 m for STAV and 18.78 m for STPZ, both of which surpassed the vertical alert limit of 10 m.

Comparing the two GBAS modes, it becomes evident that even under ionospheric scintillation conditions, the SF L1 mode delivered superior performance, primarily due to the higher number of usable satellites. The requirement for GNSS data quality monitoring and the fact that not all GPS satellites transmit the L5 signal led to a reduced number of usable satellites in IFree mode compared to SF L1. Therefore, within the context of this study, the inclusion of an additional satellite constellation proved to be more beneficial than the addition of another frequency for differential GNSS positioning in GBAS applications.

On the other hand, the inclusion of the L5/E5a carrier-phase enabled the estimation of parameters related to ionospheric conditions on the days analyzed. Ionospheric gradients were estimated using the Time-Step Method for both ground-based and airborne stations. During periods of intense ionospheric scintillation, the gradients exhibited high values (exceeding 700 mm/km), while in periods of low scintillation, the gradients remained relatively low (below 200 mm/km).

In addition, the test statistic was conducted to compare the ionospheric delay observed at the ground station with that recorded aboard the aircraft. This monitoring did not reveal any significant variation in ionospheric delay between the ground and airborne stations. The absolute 95th percentile values for the ionospheric delay during the high scintillation period were 1.603 m at STAV and 0.952 m at STPZ. During the low scintillation period, the corresponding values were 1.601 m at STAV and 0.974 m at STPZ. These results suggest that STPZ exhibited a stronger correlation in ionospheric delay with the reference stations than STAV. Moreover, despite the occurrence of ionospheric scintillation, the estimated values of the Iono Test were similar across both periods analyzed.

The study also evaluated the performance of GBAS DFDC in kinematic mode using a GNSS receiver onboard of a UAV (drone) during periods of both high and low ionospheric scintillation. The flights were of short duration (17 minutes and 12 minutes), and performance was assessed by comparing coordinates obtained through GBAS processing with those derived from relative kinematic positioning, considered as reference. Results indicated that the low scintillation period yielded better performance in the vertical component, with 88.51% of epochs meeting CAT I availability requirements. In contrast, during the high scintillation scenario, performance decreased to 77.52% of the flight time. Additionally, kinematic GBAS performance during high scintillation was characterized by elevated VPL values, which exceeded the warning

threshold due to satellite loss induced by quality control mechanisms applied by the monitoring system.

7.1 Recommendations for Future Research

Regarding the GBAS DFDC research carried out in this study, several other investigations could be conducted to complement this study, such as:

- Determination of a multipath model for the reference stations and the aircraft based on both frequencies and constellations, using historical data from the GNSS stations of the GBAS UNESP Experimental prototype.
- Conduct extended experiments spanning multiple days of analysis to identify consistent patterns in ionospheric correlation and to rigorously assess GBAS performance.
- Application of the concepts of internal and external reliability in the detection, identification and adaptation of GNSS signal errors applied to the aircraft position estimation model. Techniques such as DIA (Detection, Identification and Adaptation), MDB (Minnimum Detectable Bias), Data Snopping and others can be used to monitor the integrity of the GBAS.
- Application of the methodology proposed for GAST E (Murphy et al., 2023), under conditions of high ionospheric scintillation, primarily using the Divergence Free linear combination, which was not used in this work for DGNSS positioning in GBAS.
- Implementation of an Ionospheric Scintillation Monitor, considering that GNSS receivers have the potential for high performance data collection. An ionospheric scintillation index monitor (S4 or other) in order to exclude or alert of satellites affected by strong scintillation. Another potential approach is the implementation of real-time monitoring using the Ion_Index software, which detects ionospheric irregularities as described by Pereira and Camargo (2016).
- Use of new GPS signals such as L1C and L2C, as well as the addition of other satellite constellations (GLONASS and BeiDou) to make GBAS Multifrequency and Multiconstellation, a more robust system to mitigate the effects of the ionosphere.

- To develop and investigate a novel stochastic modeling approach for positioning that allows for the dynamic assignment of different weights to the observations. This approach aims to account for varying levels of measurement reliability, particularly emphasizing measurements that are more influenced by ionospheric or other systematic errors. Such a model would enhance the accuracy and robustness of positioning solutions by effectively mitigating the impact of these systematic disturbances.
- Improving the GBAS implementation as GBAS simulation data processing in kinematic mode using UAVs.
- To investigate if the application of cycle slip corrections instead of just detection may improve the results and if it is feasible for real time; and
- Adapting the implementations developed in this study for use in eVTOL (electric vertical takeoff and landing) projects aimed at urban air mobility.

8. REFERENCES

BLEWITT, G. (1990). An automatic editing algorithm for GPS data. Geophysical research letters. vol. 17, no. 3, 1990, pp. 199-202.

CAAMANO, M., FELUX, M., CIRCIU, M. S., GERBETH, D. (2016). Multi-constellation Gb AS: How to benefit from a second constellation. *Proceedings of the IEEE/ION Position, Location and Navigation Symposium, PLANS 2016*, 833–841. https://doi.org/10.1109/PLANS.2016.7479779

CIRCIU, M. S. Integrity aspects for dual-frequency dual constelation GBAS Based Augmentation System GBAS (2020). Thesis – PhD in Engineering, Faculty of Electrical Engineering and Information Technology of the Rheinisch-Westf alischen Technische Hochschule Aachen, 2020.

CIRCIU, M. S., FELUX, M., REMI, P., YI, L., BELABBAS, B., & PULLEN, S. (2014). Evaluation of dual frequency GBAS performance using flight data. Institute of Navigation International Techinical Meeting, ITM 2014, 645–656.

CHRISTOVAM, A. L., PROL, F.S., HERNÁNDEZ-PAJARES, M., CAMARGO, P. O. (2023). Plasma bubble imaging by single-frequency GNSS measurements. GPS Solutions. 27, 124. https://doi.org/10.1007/s10291-023-01463-z

DE SOUZA, T. L, F., SILVA, W.C, SILVA, C. M., TSUCHIYA, I., MONICO, F. G. J. (2025). Development and Evaluation of a Multi-constellation Multi-frequency GBAS Prototype for Air Navigation. Proceedings of the International Technical Meeting of The Institute of Navigation, ITM, 2025-January, 378–400. https://doi.org/10.33012/2025.20029

EUROCAE (2013). M Minimum operational performance specification for global navigation satellite ground-based augmentation system ground equipment towards support category I operations. Tech Rep ED-114, European Organization for Civil Aviation Equipment.

EUROCONTROL (2019). PEGASUS GNSS Solution: Design Justification.

FARNWORTH, R. Aviation applications. In: TEUNISSEN, P.J.G.; MONTENBRUCK, O. Springer Handbook of Global Navigation Satellite Systems. Springer, 2017. p.877 – 903.

FELUX, M., CAAMANO, M., CIRCIU, M. S., GERBETH, D. (2019). Improved Ionospheric Monitoring for Future Dual-Frequency GBAS. Proceedings of the ISGNSS 2019.

FELUX, M., CIRCIU, M. S., BELABBAS, B., MEURER, M., STANISAK, M., MILNER, C., JIANG, Y., GUILBERT, A., PHILIPPI. A. (2016). Concept for a Dual Frequency Dual Constellation GBAS. HAL Id : hal-01272779.

FELUX, M., CIRCIU, M. S., LEE, J., HOLZAFEL, (2017a) Ionospheric Gradient Threat Mitigation in Future Dual Frequency GBAS F. International Journal of Aerospace Engineering Volume 2017, Article ID 4326018, 10 pages https://doi.org/10.1155/2017/4326018.

FELUX, M., CIRCIU, M. S., GERBETH, D., CAAMANO, M. (2017b) Future GBAS processing: Do we need an ionosphere-free mode? Paper presented International Symposium on GNSS (ISGNSS 2017). ISGNSS; Hongkong, China. [accessed Jul 8 2021]. https://elib. dlr.de/117741/1/Paper_Felux.pdf.

FELUX, M., DAUTERMANN, T., BECKER, H. GBAS landing system – precision approach guidance after ILS. Aircraft Engineering and Aerospace Technology, Vol. 85 Issue: 5, pp.382-388, 2013. https://doi.org/10.1108/AEAT-07-2012-0115.

FELUX, M., GRÄUPL, T., MÄURER, N., STANISAK, M. (2018). Transmitting GBAS messages via LDACS. AIAA/IEEE Digital Avionics Systems Conference - Proceedings, 2018-Septe. https://doi.org/10.1109/DASC.2018.8569836.

FELUX, M., LEE, J., & HOLZAPFEL, F. (2015). GBAS ground monitoring requirements from an airworthiness perspective. GPS Solutions, 19(3), 393–401. https://doi.org/10.1007/s10291-014-0398-0.

GERBETH, D., CIRCIU, M. S., CAAMANO, M., FELUX, M. (2016). Nominal performance of future dual frequency dual constellation GBAS. International Journal of Aerospace Engineering, 2016(June). https://doi.org/10.1155/2016/6835282.

GERBETH, D., CAAMANO, M., CIRCIU, M. S., FELUX, M., (2022). Airborne Ionospheric Gradient Monitoring for Dual-Frequency GBAS. *Proceedings of the 2022 International Technical Meeting of The Institute of Navigation*, Long Beach, California, January 2022, pp. 1110-1122. https://doi.org/10.33012/2022.18179.

INTERNATIONAL CIVIL AVIATION ORGANIZATION (ICAO). International Standards and Recommended Practices (SARPs). Annex 10 to the Convention of International Civil Aviation. Volume I -Radio Navigation Aids," Tech. Rep., Jul. 2018.

JIANG, Y., MILNER, C., & MACABIAU, C. (2017). Code carrier divergence monitoring for dual-frequency GBAS. GPS Solutions, 21(2), 769–781. https://doi.org/10.1007/s10291-016-0567-4.

KHANAFSEH, S., PULLEN, S., & WARBURTON, J. (2012). Carrier phase ionospheric gradient ground monitor for GBAS with experimental validation. Navigation, Journal of the Institute of Navigation, 59(1), 51–60. https://doi.org/10.1002/navi.3.

LEE, J., PULLEN, S., DATTA-BARUA, S., ENGE, P. (2007). Assessment of ionosphere spatial decorrelation for Global Positioning System-Based aircraft landing systems. Journal of Aircraft, vol. 44, n. 5, 2007. pp. 1662-1669.

LI, G., NING, B., OTSUKA, Y., ABDU, M. A., ABADI, P., LIU, Z., SPOGLI, L., & WAN, W. (2021). Challenges to Equatorial Plasma Bubble and Ionospheric Scintillation

Short-Term Forecasting and Future Aspects in East and Southeast Asia. In Surveys in Geophysics (Vol. 42, Issue 1). https://doi.org/10.1007/s10712-020-09613-5

MARINI-PEREIRA, L., PULLEN, S., MORAES, A. de O., SOUSASANTOS, J. (2021). Ground-Based Augmentation Systems Operation in Low Latitudes - Part 1: Challenges, Mitigations, and Future Prospects. Journal of Aerospace Technology and Management, 13, 1–24. https://doi.org/10.1590/jatm.v13.1236

MARINI-PEREIRA, L., MORAES, A. O., PULLEN, S. (2023). Advanced Warning of Threatening Equatorial Plasma Bubbles to Support GBAS in Low Latitudes. IEEE Transactions on Aerospace and Electronic Systems, 59(5), 4858–4869. https://doi.org/10.1109/TAES.2023.3243581

MONICO, J. F. G. Posicionamento pelo GNSS: descrição, fundamentos e aplicações. 2. Ed. São Paulo: UNESP, 2008.

MONICO, J. F. G., DE PAULA, E. R., MORAES, A. de O., COSTA, E., SHIMABUKURO, M. H., ALVES, D. B. M., SOUZA, J. R., CAMARGO, P. de O., PROL, F. D. S., VANI, B. C., PEREIRA, V. S. A., JUNIOR, P. S. de O., TSUCHIYA, I., AGUIAR, C. R. (2022). The GNSS NavAer INCT Project Overview and Main Results. Journal of Aerospace Technology and Management, 14, 1–23. https://doi.org/10.1590/jatm.v14.1249

MORAES, A. O., E. R. DE PAULA, M. T. A. H. MUELLA, AND W. J. PERRELLA (2014), On the second order statistics for GPS ionospheric scintillation modeling, Radio Sci., 49, 94–105, doi:10.1002/2013RS005270.

MORAES, A. O., VANI, B. C., COSTA, E., SOUSA, J., ABDU, M. A., RODRIGUES, F. et al. (2018). Ionospheric scintillation fading coefficients for the GPS L1, L2, and L5 frequencies. Radio Science, 53, 1165–1174. https://doi.org/ 10.1029/2018RS006653.

MUELLA, M. T. A. H., DE PAULA, E. R., KANTOR, I. J., REZENDE, L. F. C., & SMORIGO, P. F. (2009). Occurrence and zonal drifts of small-scale ionospheric irregularities over an equatorial station during solar maximum - Magnetic quiet and disturbed conditions. Advances in Space Research, 43(12), 1957–1973. https://doi.org/10.1016/j.asr.2009.03.017

MURPHY, T., HARRIS, M., McGRAW, G., WICHGERS, J., LAVIK, L., TOPLAND, M., TUFFAHA, M., SAITO, S. (2021). Alternative architecture for dual frequency multi-constellation GBAS. Proceedings of the 34th International Technical Meeting of the Satellite Division of the Institute of Navigation, ION GNSS+ 2021, 1334–1374. https://doi.org/10.33012/2021.18152

MURPHY, T., HARRIS, M., BALVEDI, G., MCGRAW, G., WICHGERS, J., LAVIK, L., TOPLAND, M., TUFFAHA, M., SAITO, S. (2023). Managing Long Time Constant and Variable Rate Carrier Smoothing for DFMC GBAS. Proceedings of the 36th International Technical Meeting of the Satellite Division of the Institute of Navigation, ION GNSS+ 2023, 925–946. https://doi.org/10.33012/2023.19433

PEREIRA, V. A. S., CAMARGO, P. O. (2016). Programa científico para o monitoramento em tempo real ou pós-processado das irregularidades ionosféricas e cintilação dos sinais GNSS. Boletim de Ciências Geodésicas, vol. 22, n. 2, 2016. pp. 282-302.

PEREIRA, V. A. S., CAMARGO, P. O. (2017). Brazilian active GNSS networks as systems for monitoring the ionosphere. *GPS Solutions*, pp. 1013–1025. https://doi.org/10.1007/s10291-016-0589-y

PEREIRA, V. A. S.; MONICO, J. F. G; CAMARGO., P. O. (2017). Procedimento geral para o desenvolvimento de Modelo De Risco Ionosférico para GBAS e principais modelos existentes. IV SBG - Simpósio Brasileiro de Geomática e II Jornadas Lusófonas Sobre Ciências e Tecnologias de Informação Geográfica/CTIG, 1–8. Retrieved from http://docs.fct.unesp.br/departamentos/cartografia/eventos/2017_IV_SBG/index_Artigos.htm.

PULLEN, S. Ground Based Augmentation Systems. In: TEUNISSEN, P.J.G.; MONTENBRUCK, O. Springer Handbook of Global Navigation Satellite Systems. Cham (Suiça): Springer, 2017. p.905 – 932.

PULLEN, S., CASSELL, R., JOHNSON, B., BRENNER, M., WEED, D., CYPRIANO, L., PERVAN, B., HARRIS, M., SAITA, S., LEE, J., CLARK, B., BEAUCHAMP, S., DENNIS, J. (2017). Impact of ionospheric anomalies on GBAS CAST D service and validation of relevant ICAO SARPs requirements. 30th International Technical Meeting of the Satellite Division of the Institute of Navigation, ION GNSS 2017, 3, 2085–2105. https://doi.org/10.33012/2017.15135.

ROBERT, E., JONAS, P., VUILLAUME, J., SALOS, D., HECKER, L., YAYA, P. (2018). Development of a European ionosphere threat model in support of GBAS deployment. 2018 IEEE/ION Position, Location and Navigation Symposium, PLANS 2018 - Proceedings, 1181–1190. https://doi.org/10.1109/PLANS.2018.8373503

ROTONDO, G. (2016). Processing and Integrity of DC/DF GBAS for CAT II/III Operations 2. Structure, 203–206.

ROTONDO, G., THEVENON, P., MILNER, C., MACABIAU, C., FELUX, M., HORNBOSTEL, A., CIRCIU, M. S. (2015). Methodology for determining pseudorange noise and multipath models for a multi-constellation, multi-frequency GBAS system. Institute of Navigation International Technical Meeting 2015, ITM 2015, 383–392.

RTCA. Radio Technical Commission for Aeronautics (2008). Minimum Operational Performance Standards for GPS Local Area Augmentation System Airborne Equipment Rept. SC-159, DO-253C, Washington, D.C, Dez., 2008.

SABATINI, R.; MOORE, T.; RAMASAMY, S. (2017) Global navigation satellite systems performance analysis and augmentation strategies in aviation. Progress in Aerospace Sciences, v. 95, p. 45-98, 2017. ISSN 0376-0421. https://doi.org/10.1016/j.paerosci.2017.10.002

SAITO, S., SUNDA, S., LEE, J., PULLEN, S., SUPRIADI, S., YOSHIHARA, T., LECAT, F. (2017). Ionospheric delay gradient model for GBAS in the Asia-Pacific region. GPS Solutions, 21(4), 1937–1947. https://doi.org/10.1007/s10291-017-0662-1.

SAITO, S., YOSHIHARA, T. (2017). Evaluation of extreme ionospheric total electron content gradient associated with plasma bubbles for GNSS Ground-Based Augmentation System. Radio Science, [s. l.], v. 52, n. 8, p. 951–962, 2017.

SAITO, S., YOSHIHARA, T. (2018). Impact assessment of ionospheric scintillation associated with plasma bubbles on GAST-D ground integrity monitors. Proceedings of the 31st International Technical Meeting of the Satellite Division of the Institute of Navigation, ION GNSS+ 2018, 2186–2194. https://doi.org/10.33012/2018.15854.

SAITO, S., ZUREIKAT, S., & YOSHIHARA, T. (2018). Preliminary results of impacts of ionospheric scintillations on GAST-D ground integrity monitors. *Proceedings of the 2018 International Technical Meeting of The Institute of Navigation, ITM 2018*, *2018-Janua*, 177–187. https://doi.org/10.33012/2018.15562

SEEBER, G. Satellite geodesy. 2nd ed. Berlin, New York: Walter de Gruyter, 2003.

SILVA, W. C., MONICO, J. F. G. "GBAS: fundamentals and availability analysis according to σ_{vig}" Journal of Geodetic Science, vol. 12, no. 1, 2022, pp. 22-37. https://doi.org/10.1515/jogs-2022-0132

SILVA, C. M., SILVA, W. C., SOUZA, F. T. L., MONICO, J. F. G., BALDEVI, G., GOUVEA, T. A. F., ALVES, D. B. M. GAST X e o Futuro do GBAS DFMC com uso do monitoramento ionosférico. In: XII Colóquio Brasileiro de Ciências Geodésicas & V Simpósio Brasileiro de Geomática. Curitiba, 2022. Anais [https://cbcg.ufpr.br/?page_id=2341], Curitiba, 2022.

SILVA, C. M. D., SILVA, W. C., DE SOUZA, F. T. L., MONICO, J. F. G., ALVES, D. B. M., TSUCHIYA, I., BALVEDI, G., MURPHY, T., SAITO, S., WICHGERS, J. Assessing the Performance of Dual-Frequency Multi-Constellation GBAS Architectures during Periods of Ionospheric Scintillation in Brazil. In: Proceedings of the 36th International Technical Meeting of the Satellite Division of The Institute of Navigation (ION GNSS+ 2023). 2023. p. 1855-1878. https://doi.org/10.33012/2023.19303

SONG, J., MILNER, C., SELMI, I. (2020). Signal deformation fault monitors for dual-frequency GBAS. Navigation, Journal of the Institute of Navigation, 67(2), 379–396. https://doi.org/10.1002/navi.360

STANISAK, M., LIPP, A., FEURLE, T. (2015). Possible VDB formatting for multi-constellation / multi-frequency GBAS services. 28th International Technical Meeting of the Satellite Division of the Institute of Navigation, ION GNSS 2015, 2(November), 1507–1518.

SUBIRANA, J. S., ZORNOZA, J. M. J., PAJARES, M. H. Code-Carrier Divergence Effect. 2012. Disponível em: https://gssc.esa.int/navipedia/index.php/Code-Carrier_Divergence_Effect. Acesso em 20/01/2021.

TAKASHASHI, H., PADILHA, A. L., COSTA, J. E. R., CECATTO, J. R., GONZALEZ, W. D., PAULA, E., VITORELLO, I., VELHO, H. C., SILVA, J. D. S., ABDU, M. A., MENDES JR., O., LAGO, A. D., NARDIN, C. M. D., SANTANNA, N., ALVES M. V., SOUZA, J. R. (2008). The first landmark of the Brazilian Space Weather Program. In: Proceedings of the Brazilian Decimetric Array Workshop. São José dos Campos – SP (Brazil).

TAKAHASHI, H., WRASSE, C. M., FIGUEIREDO, C. A. O. B., BARROS, D., ABDU, M. A., OTSUKA, Y., SHIOKAWA, K. (2018). Equatorial plasma bubble seeding by MSTIDs in the ionosphere. Progress in Earth and Planetary Science, 5(1). https://doi.org/10.1186/s40645-018-0189-2

TOSSAINT, M., SAMSON, J., TORAN, F., VENTURA-TRAVESET, J., HERNANDEZ- PAJARES, M.; JUAN, J. M.; SANZ, J.; RAMOS-BOSCH, P. The Stanford - ESA integrity diagram: A new tool for the user domain SBAS integrity assessment. Navigation, Journal of the Institute of Navigation, [s. l.], v. 54, n. 2, p. 153–162, 2007.

XU, X., NIE, Z., WANG, Z., & ZHANG, Y. (2020). A modified turboedit cycle-slip detection and correction method for dual-frequency smartphone GNSS observation. In Sensors (Switzerland) (Vol. 20, Issue 20, pp. 1–14). MDPI AG. https://doi.org/10.3390/s20205756

WANG, Z., YIN, Y., SONG, D., FANG, K., LI, Q., LI, X. (2020). Dual smoothing ionospheric gradient monitoring algorithm for dual-frequency BDS GBAS. Chinese Journal of Aeronautics. https://doi.org/10.1016/j.cja.2020.04.030.

WANG, J., & HUANG, D. (2023). Dual-frequency GPS Cycle Slip Detection and Repair Based on Dynamic Test. KSCE Journal of Civil Engineering, 27(12), 5329–5337. https://doi.org/10.1007/s12205-023-0388-2

YOON, M., LEE, J., PULLEN, S., GILLESPIE, J., MATHUR, N., COLE, R., DE SOUZA, J. R., DOHERTY, P., PRADIPTA, R. (2017). Equatorial Plasma Bubble Threat Parameterization to Support GBAS Operations in the Brazilian Region. Navigation, Journal of the Institute of Navigation, 64(3), 309–321. https://doi.org/10.1002/navi.203

YOON, M., KIM, D., PULLEN, S., LEE, J. (2019). Assessment and mitigation of equatorial plasma bubble impacts on category I GBAS operations in the Brazilian region. Navigation, Journal of the Institute of Navigation, 66(3), 643–659. https://doi.org/10.1002/navi.328

ZABALEGUI, P., DE MIGUEL, G., PEREZ, A., MENDIZABAL, J., Goya, J., ADIN, I. (2020). A Review of the Evolution of the Integrity Methods Applied in GNSS. IEEE Access, 8, 45813–45824. https://doi.org/10.1109/ACCESS.2020.2977455

APPENDIX

APPENDIX A – Partial view of the surroundings of the PRU2 station (reference date 04/23/2024).



APPENDIX B – Partial view of the surroundings of the PRU4 station (reference date 01/17/2024).



APPENDIX C – Partial view of the surroundings of the DMC1 station (reference date 01/20/2024).



APPENDIX D – Partial view of the surroundings of the MOR3 station (reference date 11/03/2024).



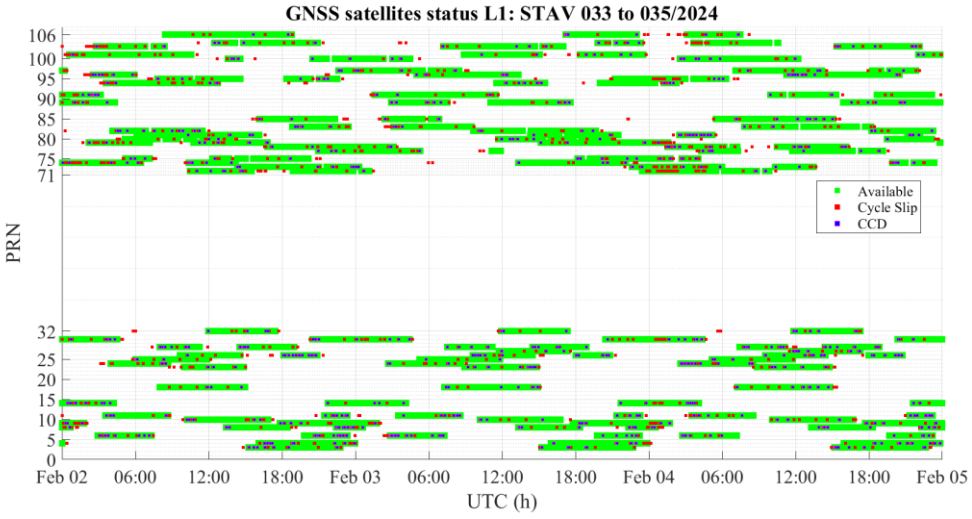
APPENDIX E – Partial view of the surroundings of the STAV station (reference date 04/13/2024).



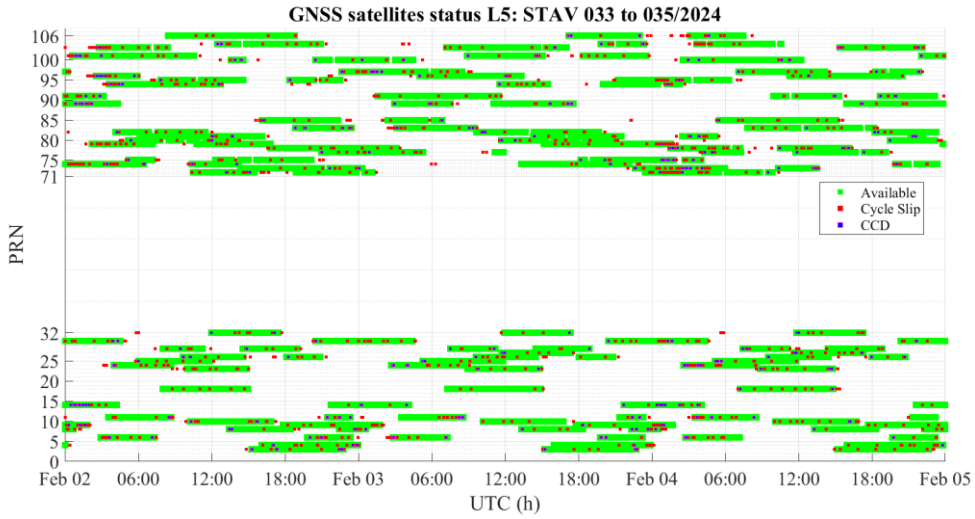
APPENDIX F – Partial view of the surroundings of the STPZ station (reference date 04/23/2024).



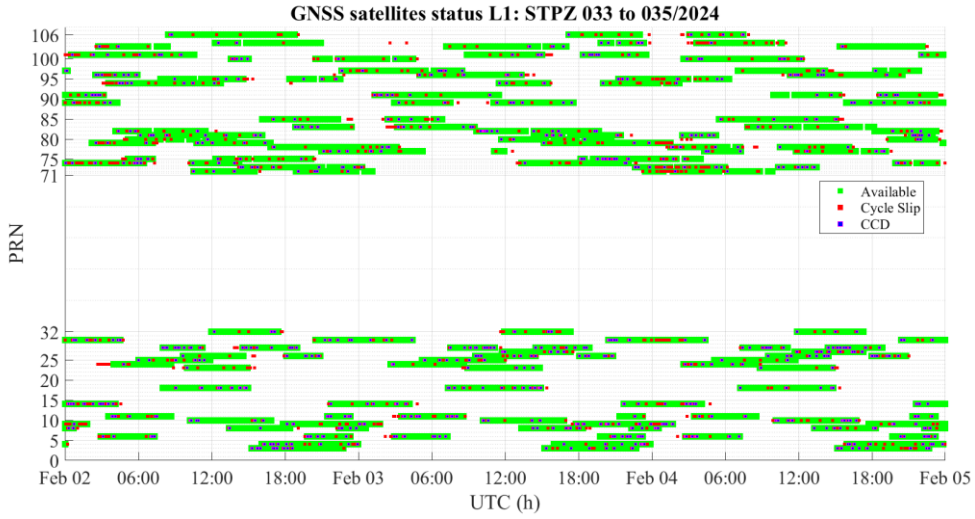
APÊNDICE G – Status of GNSS Signals on the L1/E1 Carrier-phase at the STAV station from Days 033 to 035 of 2024.



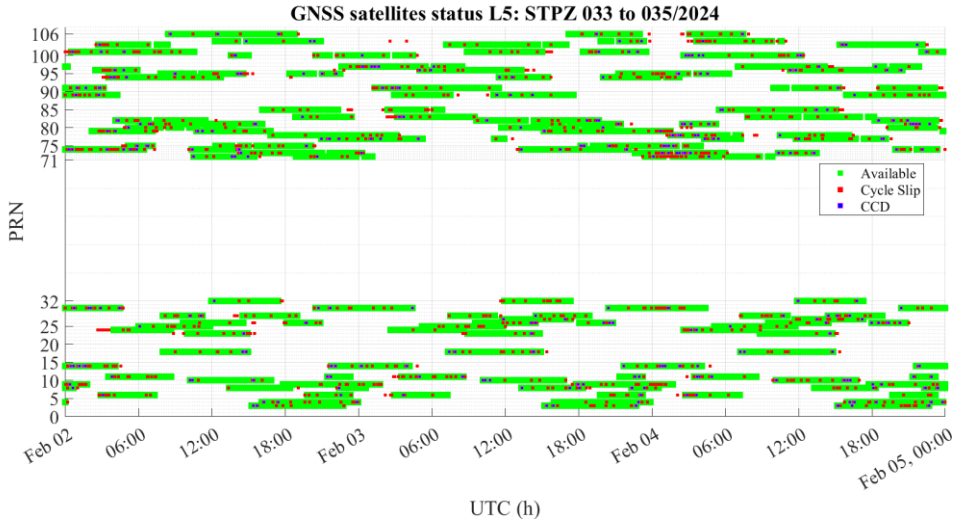
APÊNDICE H – Status of GNSS signals on the L5/E5a carrier-phase at the STAV station from days 033 to 035 of 2024.



APÊNDICE I – Status of GNSS Signals on the L1/E1 Carrier at the STPZ Station from Days 033 to 035 of 2024.



APÊNDICE J – Status of GNSS Signals on the L5/E5a Carrier-phase at the STPZ Station from Days 033 to 035 of 2024.



DADOS CURRICULARES

Nascimento 15/03/1985 – Coronel Fabriciano, MG

Filiação Lindomar Sarmento da Silva
Maria do Carmo Costa e Silva

2011 – 2017 Graduação
Bacharelado em Engenharia de Agrimensura e Cartográfica
Universidade Federal Rural do Rio de Janeiro – UFRRJ, campus Seropédica

Lattes https://lattes.cnpq.br/1318841862769161

ORCID https://orcid.org/0000-0001-5437-6976

2018 – 2020 Pós-Graduação
Mestrado em Ciências Cartográficas
Faculdade de Ciências e Tecnologia – Universidade Estadual Paulista "Júlio de Mesquita Filho" – UNESP, campus Presidente Prudente

2020 – 2025 Pós-Graduação
Doutorado em Ciências Cartográficas
Faculdade de Ciências e Tecnologia – Universidade Estadual Paulista "Júlio de Mesquita Filho" – UNESP, campus Presidente Prudente